AN EVALUATION OF THE NEED FOR CRITICALLY REFINED PURIFICATION PROCEDURES IN FLUORESCENT CARBON DOT SYNTHESES: THE RAMIFICATIONS OF THE UBIQUITOUS PRESENCE OF REACTION BY-PRODUCTS ON QUENCHOMETRIC AND LIGHT HARVESTING APPLICATIONS

A Dissertation

Presented to

the Faculty of the Graduate School

at the University of Missouri-Columbia

In Partial Fulfillment

of the Requirements for the Degree

Doctor of Philosophy

---

by

JEREMY BLAIR ESSNER

Professor Gary A. Baker, Dissertation Supervisor

MAY 2021

The undersigned, appointed by the Dean of the Graduate School, have examined the

dissertation entitled

AN EVALUATION OF THE NEED FOR CRITICALLY REFINED PURIFICATION PROCEDURES IN FLUORESCENT CARBON DOT SYNTHESES: THE RAMIFICATIONS OF THE UBIQUITOUS PRESENCE OF REACTION BY-PRODUCTS ON QUENCHOMETRIC AND LIGHT HARVESTING APPLICATIONS

presented by

Jeremy Blair Essner,

a candidate for the degree of Doctor of Philosophy of Chemistry,

and hereby certify that, in their opinion, it is worthy of acceptance.

Professor Gary A. Baker, Advisor and Committee Chair

Professor Michael Harmata, Departmental Member

Professor Justin R. Walensky, Departmental Member

Professor Matt R. Maschmann, External Member

This dissertation is dedicated to my son in heaven, Alexander Christian Essner, and my late grandfather, Floyd Preston Blair, who is keeping watch over my ACE until the day I am called home to meet him. You both are my guiding light in the darkness and my strength when I feel I have none.

ACKNOWLEDGEMENTS

First and foremost, I would like to thank God for my many blessings, for without Him nothing is possible. Secondly, my deepest gratitude goes out to my parents, Donald and Theresa Essner, and my sisters, Julia Essner and Andrea Arredondo (as well as her husband, Adam Arredondo), for their loving support and constant encouragement throughout my pursuits of higher education, a period of time that contains some of the darkest days of my life. Regardless of the poor decisions I made, their unconditional love and forgiveness, as well as constant reassurance, were the foundation in helping me address and begin to overcome the many personal obstacles I faced in addition to my graduate studies. I would not be writing this now if all of you were absent from my life. Additionally, I would also like to thank my parents for everything they have done and sacrificed over the years because, without their undying devotion to their children, I would not have made it this far in my education.

My sincerest appreciation goes out to my best friend and girlfriend, Jennifer Kist, who has remained by my side despite the melancholy place I allowed life to lead me to. Your steadfast love and encouragement have helped me climb out of the proverbial (emotional) hole I was in and get to the other side of the mountainous hurdles that life put in my path.

I would also like to thank all my extended family and friends, both old and new, for their support over the years. Special thanks go out to Matthew Seiler, Sean Adams, Bryan Lada, Matt Aksamit, Andrew Breshears, Jacob Scribner, and my wonderful neighbors, Cheryl and Thom Kleeschulte, whom I am blessed to call my dear friends.

Additionally, I thank all Baker group members, both past and present, for your support, the many intellectually stimulating conversations, the wonderful camaraderie, and all the

fun, and often wild times, we have shared over the years. It brings me great joy to call many of you friends, particularly, Nate Larm, Dustin Boogaart, Charlie Laber, and Chip Smith.

Last (but certainly not least), I must acknowledge and earnestly thank my advisor and mentor, Professor Gary Baker, for all the knowledge he has and continues to impart, as well as the numerous opportunities bestowed upon me, never-ending investments that have provided me with a solid platform to launch my individual academic career from.

TABLE OF CONTENTS

ACKNOWLEDGEMENTS ii

LIST OF SCHEMATICS AND FIGURES x

LIST OF TABLES l

LIST OF COMMONLY USED ACRONYMS li

ABSTRACT lii

CHAPTERS:

1. INTRODUCTION TO FLUORESCENT CARBON DOTS, THEIR SYNTHESIS AND APPLICATIONS, AND THE VEXING PURIFICATION CONUNDRUM 1

    References 12

2. BIOCOMPATIBLE FLUORESCENT CARBON DOTS DERIVED FROM THE UPCYCLING OF URINE TOWARDS CHROMOPHORIC TUNING FOR ENHANCED LIGHT HARVESTING 21

    Abstract 22

    Introduction 22

    Experimental 27

        Materials and Reagents 27

        Urine-derived Fluorescent Carbon Dot Syntheses 27

        Characterization Techniques 29

        Bioimaging Studies 30

        Cell Viability by Sulforhodamine B Assay 31

        Metal Quenching and Fluorescence Recovery Studies 32

    Results and Discussion 33

        Photophysical Characterizations 33

        Structural Characterizations 38

        Bioimaging Applications and Cytotoxicity Studies 41

Quenchometric Metal Ion Sensing and Fluorescence Recovery 43

Conclusions.....45

Acknowledgements.....46

References.....47

3. CATALYTIC CARBON DOT REDUCED BIMETALLIC NANOPARTICLES: SIZE AND SURFACE PLASMON RESONANCE TUNABILITY TOWARDS PLASMON-ENHANCED PHOTOVOLTAICS.....52

Abstract.....53

Introduction.....53

Experimental.....57

Materials and Reagents.....57

Citric Acid-derived Fluorescent Carbon Dot Synthesis.....57

Au@FCD Nanoparticle Syntheses.....58

Ag@FCD Nanoparticle Syntheses.....59

Au_xAg_{1-x}@FCD Nanoparticle Syntheses.....60

Characterization Techniques.....60

4-Nitrophenol (4-NP) Catalytic Studies.....61

Peroxidase-like Activity Studies.....61

Results and Discussion.....62

Photophysical and Structural Characterizations of the CA-derived FCDs.....62

Synthesis and Photophysical Properties of the Au@FCD Nanoparticles.....64

Synthesis and Photophysical Properties of the Ag@FCD Nanoparticles.....67

Synthesis and Photophysical Properties of the Au_xAg_{1-x}@FCD Bimetallic Nanoparticles.....68

Morphological and Compositional Analyses of the Au_xAg_{1-x}@FCD Nanoparticles.....70

Model Catalytic Application of the Au_xAg_{1-x}@FCD Nanoparticles.....72

Application of the Au@FCD Nanoparticles as Peroxidase Memetics 75

Conclusions 76

Acknowledgements 76

References 77

4. A FIELD MISLED: ARTIFACTS AND ERRORS ASSOCIATED WITH THE UBIQUITOUS PRESENCE OF FLUORESCENT IMPURITIES IN PURPORTEDLY "FLUORESCENT" CARBON NANODOTS 82

Abstract 83

Introduction 84

Experimental 86

Materials and Reagents 86

Fluorescent Carbon Dot Syntheses 87

Domestic Microwave Treatment of Citric Acid and Urea 88

Hydrothermal Treatments of Arginine and Citric Acid-Ethylenediamine 88

Electrochemical Oxidation of Graphite to GQDs 89

Fluorescent Carbon Dot Functionalization of GQDs 89

Fluorescent Carbon Dot Purification 90

Gold Nanoparticle Syntheses 91

Characterization Techniques 92

Cell Viability by Sulforhodamine B Assay 93

Metal Ion Quenching Studies 94

Approximate GQD Molecular Weight Calculation 95

Results and Discussion 95

Literature Survey of FCD Purification Methods 95

Luminescent Characterizations of the CA–U-derived Fractions 100

Dialysis Membrane Nanoscale Permeability Tracking with Au NPs 104

Electron Microscopic Imaging Analyses of CA–U-derived Fractions 105

Fractionation and Spectroscopic Properties of Arg- and CA–EDA-derived Samples 106

Effects of Fractionation on the Luminescent Properties of Bare and Functionalized GQDs.....108

Effects of Purification on Quenchometric Applications and Cell Viability Studies.....109

Improper Interpretation of Luminescent Characteristics due to Inner Filter Effects 112

Conclusions.....113

Acknowledgements.....114

References.....114

5. REACTION BY-PRODUCTS STRIKE AGAIN: EFFECTS OF MEMBRANE DIALYSIS ON THE PERFORMANCE OF CARBON-NANODOT-SENSITIZED MESOPOROUS-TiO_2-BASED PHOTOVOLTAIC DEVICES 126

Abstract.....127

Introduction.....127

Experimental.....131

Materials and Reagents.....131

Fluorescent Carbon Dot Syntheses and Purification 132

Thermal Treatment of Citric Acid in Ammonium Hydroxide.....132

Solvothermal Treatments of Arginine and Glutathione-Formamide.....134

Domestic Microwave Treatment of Citric Acid and Urea.....138

Acid Oxidation of Coal to GQDs.....139

Photovoltaic Device Preparation and Assembly.....140

Sensitized TiO_2 Film Characterizations.....142

Photovoltaic Device Characterizations.....143

CA–NH_4OH Dialysate-spiked Retentate Studies 144

Mass Spectrometric Analyses 144

Results and Discussion 145

Spectroscopic Studies of FCD Fraction Uptake by TiO_2.....145

PV Characterizations of TiO_2 Films Sensitized in CA–NH_4OH Fractions ...146

PV Characterizations of TiO_2 Sensitized in CA–NH_4OH Dial.-spiked Retent. Fractions.....151

Effects of 24 h Sensitization in CA–NH_4OH Fractions on PV Performance 154

Aging and Water-exposure Effects on PV Performance of As-synth. CA–NH_4OH Samples 154

PV Characterizations of TiO_2 Films Sensitized in Arg-derived Fractions 155

PV Characterizations of TiO_2 Films Sensitized in CA–U- and GSH–F-derived Fractions.....158

PV Characterizations of TiO_2 Films Sensitized in Coal-derived GQDs.....160

Mass Spectrometric Analyses of CA-based FCD Systems.....162

Conclusions.....167

Acknowledgements.....168

References.....168

6. CONCLUSIONS.....178

7. FUTURE OUTLOOKS 181

APPENDICES:

A. SUPPORTING FIGURES FOR CHAPTER 2 184

B. SUPPORTING FIGURES FOR CHAPTER 3 189

C. SUPPORTING FIGURES FOR CHAPTER 4 200

D. SUPPORTING FIGURES AND ANALYSES FOR CHAPTER 5.....224

Experimental Details and Analysis of Water-exposure Effects on CA–NH_4OH Samples 245

Experimental Details and Analysis of Aging Effects on CA–U-derived Samples....249

Experimental Details and Analysis of Aging Effects on GSH–F-derived Samples ..252

Experimental Details and Analysis of Aging Effects on GSH–F-sensitized Films ...256

Experimental Details and Analysis of Synthetic Temperature on GSH–F-derived Samples 259

E. SOLAR SIMULATOR SETUP AND OPERATION 268

Solar Simulator System Components 268

Solar Simulator System Setup and Calibration 273

Solar Simulator Operation 276

References 282

F. DETAILED PREPARATION AND OPERATION OF SENSITIZED SOLAR CELLS 283

Preparation of Substrates for use as Photovoltaic Electrodes 283

Photovoltaic Photoanode Preparation 284

Photovoltaic Cathode (Counter Electrode) Preparation 286

Electrolyte Preparation 287

Photovoltaic Device Assembly 287

Photovoltaic Device Architecture and Operation 289

References 291

G. INTERPRETATION AND ANALYSIS OF PHOTOVOLTAIC DATA 293

J-V Curves and Extracted Performance Metrics 293

External Quantum Efficiency 299

Chronoamperometry and Chronopotentiometry 301

Electrical Impedance Spectroscopy 304

References 306

VITA 308

LIST OF SCHEMATICS AND FIGURES

Scheme 1.1 (A) Representative structures of single-layer graphene quantum dots (GQDs), multi-layered carbon quantum dots (CQDs), and amorphous carbon nanodots (CNDs). Note, the CND structure is not meant to represent a specific molecule; its purpose is simply to convey a predominately amorphous structure of carbon atoms. (B) Representation of commonly observed fluorescent properties of these materials. Typically, as the size of the dot increases the emission wavelength redshifts, a phenomenon that can also occur via heteroatom doping and/or variation in surface functionality. Additionally, these dots frequently display excitation wavelength-dependent emission (*i.e.*, a red-edge effect) that is accompanied with a concomitant decrease in intensity. Schematic used with permission from reference 51. Copyright © 2017 Royal Society of Chemistry 2

Scheme 1.2 Schematical representation of a solar cell based on a mesoscopic, metal oxide film (*e.g.*, TiO_2) sensitized with FCDs showing the fundamental photovoltaic operation under illuminated conditions. The inset arbitrarily shows the appropriate band alignments in these devices 5

Scheme 1.3 (A) The origin of localized surface plasmon resonances: if particles are substantially smaller than the incident wavelength of light, they experience a relatively uniform electric field as the wave passes through them resulting in a collective oscillation of electrons. This electron resonance leads to drastically enhanced electric fields in the immediate area around the particle, as shown in panel B. Nanoparticle plasmon resonances can be exploited in various device architectures to enhance photon harvesting and device performance: (C) larger particles can act as light scattering centers at an interface while (D) smaller particles can act as light concentrators embedded within a film. Schematics

adapted with permission from references 62 and 63. Copyright © 2003 American Chemical Society and 2010 Nature Publishing Group.....7

Scheme 1.4 (A) Generalized formation of potential molecular fluorophores in citric acid-based FCD syntheses first proposed by Yang and coworkers,[91] in which the pyrolyzation of citric acid (CA) in the presence of common (di)amine-containing heteroatom dopants, such as (i) ethane diamines, (ii) propane diamines, or (iii) monoamines containing hydroxyl or thiol groups, yields the corresponding 2-pyridone-derived by-products. (B) Indeed, several fluorescent molecular by-products originating from the carbonization of CA-based precursor systems, which typically possess a 2-pyridone backbone, have been identified. Schematics adapted with permission from references 87 and 91. Copyright © 2015 Royal Society of Chemistry and 2018 Elsevier.....9

Scheme 2.1 Graphical abstract conceptualizing the thermal upcycling of human urine to biocompatible fluorescent carbon dots and their exploitation in bioimaging and quenchometric sensing applications 21

Figure 2.1 UV-vis spectra of the three different PD samples dispersed in water at a concentration of 0.1 mg mL^{-1}: UPDs (green curve), CPDs (magenta curve), and APDs (cyan curve). The inset photograph shows representative samples of these PDs at the same concentration viewed under ambient light.....35

Figure 2.2 (A) Excitation wavelength-dependent fluorescence emission spectra of APDs in water. Magnified emission spectra at longer excitation wavelengths are displayed in the inset. (B) Plotting the wavelength of maximum emission against the excitation wavelength for these PDs revealed redshifted emission for CPDs and APDs relative to UPDs at shorter

excitation wavelengths, particularly below 450 nm. The inset photographs show the fluorescence of (C) UPDs, (D) CPDs, and (E) APDs under blue (405 nm, upper beam) and green (532 nm, lower beam) laser pointer excitation. (F) Wavelength-dependent quantum yields measured at five different excitation wavelengths 36

Figure 2.3 (A) XRD patterns and (B) FTIR spectra showing the slight graphitic nature and surface functionalities of the PDs, respectively. The legend in panel A also corresponds to panel B 39

Figure 2.4 Representative TEM micrographs of (A) UPDs, (B) CPDs, and (C) APDs. Histograms with the average particle sizes (x-bar) are also shown with the inset of panel (C) further illustrates the bimodal particle size distribution of the APDs 40

Figure 2.5 Merged fluorescence micrographs of APD-incubated mice embryonic fibroblast (MEF) cells showing APD incorporation into the cellular cytoplasm. The cell micrographs combine the signal from DAPI staining of the nuclear material with APD-derived signal collected through a (A) FITC or (B) TRITC filter cube. (C) Summary of BT-474 cell viability for varying concentrations of the three kinds of PDs using a sulforhodamine B cell protein dye-binding assay.....42

Figure 2.6 (A) Metal screening test for all three PD types (0.05 mg mL^{-1}) against 11 different metal ions (Zn^{2+}, Sr^{2+}, Ba^{2+}, Mn^{2+}, Ca^{2+}, Sn^{2+}, Ni^{2+}, Fe^{3+}, Cu^{2+}, Pd^{2+}, and Hg^{2+}), each present at a concentration of 100 μM. (B) Representative plot of Hg^{2+} quenching of APD emission 44

Scheme 3.1 Graphical abstract highlighting the synthesis of CA-derived fluorescent carbon dots (FCDs) and their use as dual reducing and capping agents to produce Ag@FCD, Au@FCD, and Au_xAg_{1-x}@FCD NPs, the latter of which showed a high degree of spectroscopic tunability upon varying the Au:Ag ratio 52

Figure 3.1 Representative TEM micrographs of (A) Au@FCD and (D) Ag@FCD NPs. Shown are results for 0.3 mg mL^{-1}:0.35 mM and 0.3 mg mL^{-1}:0.30 mM FCDs:metal ratios for Au and Ag reductions, respectively. The SPR shifts of the resultant particles (panels B–F) show the smooth tunability afforded simply by changing the FCD:metal ratio. In the case of Au NPs (B and C), the SPR intensity initially increased, reaching a maximum at a 0.3 mg mL^{-1} FCD:0.45 mM Au ratio. The increase was also accompanied by a slight bathochromic shift. Higher Au:FCD ratios resulted in a continuous redshift with decreasing SPR intensity and substantial peak broadening, indicative of larger, more polydisperse NPs. On the other hand, the Ag NPs (E and F) displayed only a slight bathochromic shift in SPR, with increasing intensities as the Ag concentration was varied from 0.15 to 3 mM. The lower photographs correspond to the Au and Ag samples in panels B–C and E–F, respectively 65

Figure 3.2 (A) Normalized UV-vis absorbance of the bimetallic Au_xAg_{1-x}@FCD NPs showing that as the experimental Au:Ag ratio decreased the resultant SPR displayed a systematic hypsochromic shift. (B) Extracted SPR frequencies plotted *vs* the %Au, further demonstrating the smooth evolution in SPR wavelength as the Au:Ag ratio was modulated. The sample sets were replicated three times highlighting the reproducibility of the BMNPs (error bars denote one standard deviation from the mean), especially at the lower Au concentrations. (C) Photograph of a series of Au_xAg_{1-x}@FCD BMNP samples, illustrating

a palette of SPR transitions. The cuvettes correspond to the samples in panels A and B from 100% Ag (left) to 100% Au (right).....69

Figure 3.3 Representative TEM micrographs and their corresponding EDX spectra for (A and D) Au@FCDs, (B and E) bimetallic $Au_{0.5}Ag_{0.5}$@FCDs, and (C and F) Ag@FCDs. Interestingly, upon the slightest addition of silver, the NP's average size decreased by a factor of ~7 and remained relatively constant across the Au:Ag composition tested. (G) Plot showing the extent of alloying between Au and Ag (%Au measured) within the BMNPs *vs* the content predicted from the initial Au:Ag stoichiometry (*i.e.*, %Au theoretical). The dashed line represents the ideal case where the measured values directly correspond to reagent metallic ratios. In general, the measured content follows the prediction line. The slight enrichment with Au at higher initial Au% could be tentatively tied to a small amount of galvanic replacement in which Ag^0 is etched by Au^{3+}.....71

Figure 3.4 (A) Time-dependent UV-vis absorption spectra of the $NaBH_4$-assisted reduction of 4-NP catalyzed by the Au@FCD NPs. Spectra were acquired every 5 s but, for clarity, spectra are shown only for illustrative times. (B) Plots of $\ln(A_t/A_0)$ for 4-NP absorbance at 400 nm *vs* time for various metal NP@FCD catalysts. Each catalyst was tested within days of preparation 74

Scheme 4.1 Graphical abstract showing a representative FCD sample under dialysis highlighting the drastic quantity of small, molecular (highly fluorescent) by-products permeating the membrane, whose presence masks the true properties of FCDs and leads to misconceptions surrounding FCD emission when not sufficiently fractionated away.....82

Figure 4.1 (A) Trend showing the exponential rise in publications dealing with fluorescent carbon dots (FCDs) over the past decade. (B) A sampling of over 550 FCD publications categorized by their mode of purification. (C) An approximate molecular weight-to-size correlation suggesting that the use of <5 kDa molecular weight cut-off (MWCO) membranes is inadequate for purifying these materials. The pink and blue lines demarcate 1 kDa and 5 kDa MWCOs, respectively, while the purple area represents the average FCD size and ideal MWCOs that should be employed for membrane-based FCD purification. ‡This is an approximation; there is no universally correct correlation between a 2D particle size and a 3D molecular weight. The abbreviations in panel B are as follows: "Cent. & filt." = centrifugation and filtration (in no particular order); "Solv. extract." = solvent extraction; "MWCO unk." = MWCO for dialysis not reported; "EP" = electrophoretic separation; and "Chromatogr." = chromatographic separation. The bars labelled with specific MWCOs denote either dialysis or ultrafiltration as a means of purification.....96

Figure 4.2 Assessed fluorescence quantum yields of CA–U-derived samples following fractionation via (A) dialysis or (B) (ultra)filtration. The retent. results are represented by closed circles and dial./filtrate quantum yields are denoted by open circles. These sets of studies reveal that the smaller species permeating the membranes are associated with the majority of the fluorescence observed in the as-synth. samples while the retent. fractions show much weaker fluorescence 101

Figure 4.3 Sequence of photographs showing the progress of dialysis for microwave-generated CA–U (1:3) samples using a 1 kDa MWCO membrane. The rapid passage of colored material through the membrane vividly illustrates the fact that large quantities of

small molecular (non-nanoscale) by-products result from bottom-up microwave routes to FCDs 103

Figure 4.4 Representative TEM micrographs for the (A and C) retentate (retent.) and (B and D) dialysate (dial.) fractions resulting from (A–B) 1 kDa and (C–D) 50 kDa dialysis of samples produced by microwave treatment of CA–U (1:3). Some apparent FCDs are visible in the 1 kDa retent. (marked by cyan squares in panel A) but proved difficult to image due to the large quantity of by-product residues. While the 50 kDa retent. proved easier to image and the FCDs were more visually prominent, a significant amount of non-FCD material remained after purification. Some FCDs were visible in the 50 kDa dial. samples indicating that dialysis may not be capable of fully separating FCDs from organic molecular by-products 105

Figure 4.5 (A) Metal ion quenching studies conducted on the microwave-treated CA–U as-synth. sample and the corresponding retent. and dial. fractions. For the metal ions tested (Cu^{2+}, Fe^{3+}, or Hg^{2+}), the retent. fractions were quenched more strongly by 100 μM Hg^{2+} than their as-synth. or dial. counterparts, while the quenching in the presence of 100 μM Cu^{2+} or Fe^{3+} was essentially identical for all three fractions. (B) Stern-Volmer plots of Hg^{2+} titrations of CA–U-derived FCDs. These results reveal that improper purification can clearly impact the performance of the investigated material, in this case masking the analytical responsivity of the FCDs (the limit of detection for Hg^{2+} is 2–3 times better for the retent. fraction compared with the dial.). For all metal ion quenching studies, the concentration of the FCD fractions was “normalized” by adopting the same absorbance (~0.1) at the excitation wavelength (375 nm) employed in the fluorescence spectra acquisitions 110

Scheme 5.1 Graphical abstract highlighting the impact that molecular by-products generated in FCD syntheses have on photosensitizer applications, particularly when employed in photovoltaics 126

Figure 5.1 (A) Average *J*-*V* curves (with corresponding standard deviations) of illuminated devices employing TiO_2 films sensitized in 5 mg mL^{-1} CA–NH_4OH-derived fractions dispersed in 100% acetone or 50:50 vol% acetone:ethanol (denoted by "EtOH"). (B) Average device metrics. *Note, efficiency (η) is reported in percent and FF is a unitless parameter but both values are on the same scale as the left and right y-axes, respectively. (C) Average EQE and UV-vis absorbance (inset) spectra. (D) Photographs of representative films used in the devices. The performance of bare TiO_2 (black curves) is provided in all plots for comparison 147

Figure 5.2 (A–B) Average *J*-*V* curves (with corresponding standard deviations) of illuminated devices employing TiO_2 films sensitized in dial.-spiked (A) 5 mg mL^{-1} or (B) 1 mg mL^{-1} CA–NH_4OH retent. fractions dispersed in 100% acetone or 50:50 vol% acetone:ethanol (denoted by "EtOH"). Appropriate quantities of dial. fraction were spiked in the retent. solutions to yield concentrations of 1, 2.5, 5, 10, or 30 mg mL^{-1}. (C–F) Average EQE and absorbance spectra for the dial.-spiked (C and E) 5 mg mL^{-1} or (D and F) 1 mg mL^{-1} CA–NH_4OH retent. fraction with magnified versions of the EQE spectra provided as insets in panels C and D. (G–H) Photographs of representative films sensitized with dial.-spiked (G) 5 mg mL^{-1} or (H) 1 mg mL^{-1} CA–NH_4OH retent. fractions. The performance of bare TiO_2 (black curves) is provided in all plots for comparison 152

Figure 5.3 (A) Average *J-V* curves (with corresponding standard deviations) of illuminated devices employing TiO_2 films sensitized in 10 mg mL^{-1} Arg-derived fractions dispersed in EtOH. (B) Average device metrics. *Note, efficiency (η) is reported in percent and FF is a unitless parameter but both values are on the same scale as the left and right y-axes, respectively. (C) Average EQE and UV-vis absorbance spectra with a magnified version of the EQE spectra provided as an inset. (D) Photographs of representative films used in the devices. The performance of bare TiO_2 (black curves) is provided in all plots for comparison.....156

Figure A.1 Key suspected products of the metabolic breakdown of (A) asparagusic acid: (B) methanethiol, (C) dimethyl sulfide, (D) dimethyl disulfide, (E) dimethyl sulfoxide, and (F) dimethyl sulfone.....184

Figure A.2 (A) An extended pyrolysis time (24 h) of urine collected during the donor's unmodified diet phase generated a redshift in peak emission relative to the emission arising from a 12 h thermal treatment of the same urine (panel B). Specifically, the peak emission for the latter occurred at 392 nm under 325 nm excitation while the peak emission shifted to 445 under 350 nm excitation after an additional 12 h of pyrolysis. (C) The CPDs displayed a slight redshift in emission over the UPDs (12 h) but did not show as large of a redshift as the APDs (Figure 2.2A) or the UPDs from the 24 h pyrolysis. This loosely implies that a longer treatment time of the dietary-doped urine samples could lead to an even further redshift in emission. (D–E) TEM imaging analysis of the UPDs (24 h) confirmed that small, presumably carbonaceous, nanocrystals were still generated when a longer pyrolysis time was employed. Note, the abbreviation "F.I." used in the inset plots of panels A–C stands for fluorescence intensity.....185

Figure A.3 Confocal fluorescence micrograph of APD-labelled BT-474 (human mammary gland, ductal carcinoma) cells adhered to a 96-well plate 186

Figure A.4 (A) Quenching curves for UPDs (green), CPDs (magenta), and APDs (cyan) in the presence of Hg^{2+} (circles) and Cu^{2+} (triangles). Both metal ions showed fluorescence quenching with Hg^{2+} displaying stronger quenching over Cu^{2+}. Each respective metal quenched all three samples in a similar manner. (B–F) Quenching curves used for the determination of quenching constants and limit of detection (LOD) calculations. The color and shape schemes employed in panel A were kept consistent for all panels (*i.e.*, B–F). Note, the quenching curve used for the LOD calculation of APD quenching in the presence of Hg^{2+} is provided as panel B of Figure 2.6 187

Figure A.5 PD fluorescence signal recovery using EDTA to preferentially chelate Hg^{2+}, restoring the previously quenched fluorescent site to >90% of the original signal. Specifically, the (A) UPDs, (B) CPDs, and (C) APDs displayed 97.2%, 96.0%, and 93.6% recovery, respectively 188

Figure B.1 (A) Photophysical properties of the CA-derived FCDs employed in this work. Akin to other reported FCDs, these carbon dots displayed excitation wavelength-dependent emission and quantum yields (panel A inset). (B) Representative TEM micrograph of the CA-derived sample indicating that, presumably carbonaceous, nanodots, 30–60 nm (up to 100 nm) in size were produced. (C) FTIR spectrum of the CA-derived FCDs revealing that the nanocarbons possessed alcohol, carboxyl, epoxy, ester, and ether surface functionalities, moieties that account for the FCDs' high aqueous solubility. The FTIR peaks were assigned as such: stretching vibrations of O–H ($\nu_{O–H}$, 3600–3000 cm^{-1}),

stretching vibrations of C=O ($\nu_{C=O}$, 1800–1600 cm^{-1}), skeletal vibrations of aromatic groups ($\nu_{C=C}$, 1800–1600 cm^{-1}), stretching vibrations of C–O moieties ($\nu_{C–O–C}$ and $\nu_{C–OH}$, 1300–1000 cm^{-1}), and aliphatic carbon stretches ($\nu_{C–H}$ and $\nu_{=C–H}$, 2900, 1400, and 915 cm^{-1}). The outset panel to the right of panel C is an expanded plot of the area within the red box shown in panel C.....189

Figure B.2 UV-vis spectra of the resultant Au@FCD NP solutions when the concentration of Au salt was held constant at 0.3 mM and the FCD concentration was increased from 0.05 to 0.60 mg mL^{-1}. As the FCD concentration increased up to 0.30 mg mL^{-1}, the Au NP SPR appeared and hypsochromically shifted. For the three highest concentrations of FCDs, the Au NP SPR remained relatively constant in intensity and peak position 190

Figure B.3 Representative TEM micrographs of the resultant Au@FCD NPs when the FCD concentration was held at 0.3 mg mL^{-1} and the Au concentration was (A) 0.20 mM, (B) 0.35 mM, (C) 0.45 mM, or (D) 0.60 mM. Such FCD:Au ratios resulted in average quasi-spherical particle sizes of (A) 17.8 ± 6.4, (B) 26.7 ± 10.0, (C) 47.8 ± 20.7, and (D) 96.7 ± 29.9 nm, respectively. For the higher Au:FCD ratios, large hexagonal and trigonal Au plates formed with average particle sizes of 266.7 ± 99.3 and 528.8 ± 214.3 nm for Au concentrations of 0.45 and 0.60 mM, respectively. The higher Au:FCD ratios also produced much smaller quasi-spherical particles in the 5–20 nm regime as evidenced by the insets of panels C and D but these particles were less concentrated than the larger quasi-spherical particles and platelets.....191

Figure B.4 (A) Time-dependent UV-vis spectra of the room temperature Au reduction (0.3 mg mL^{-1} FCDs:0.35 mM $HAuCl_4$) showing that the reduction was near completion after 3

h. (B) Time-dependent fluorescence spectra (λ_{ex} = 350 nm) of the room temperature Au reduction (0.3 mg mL^{-1} FCDs:0.35 mM $HAuCl_4$). After the reduction, the Au@FCD NPs still retained approximately 25% of the original FCD fluorescence. Since $HAuCl_4$ did not show any absorbance or fluorescence features within the wavelength range of interest, the increase in absorbance and decrease in fluorescence intensity was solely attributed to the growth of Au NPs 192

Figure B.5 UV-vis spectra of the resultant Ag@FCD NP solutions when the concentration of Ag salt was held constant at 1.0 mM and the FCD concentration was increased from 0.05 to 0.60 mg mL^{-1}. In general, as the FCD concentration increased, the Ag NP SPR displayed a slight bathochromic shift. Interestingly, at the lowest concentration of FCDs (0.05 mg mL^{-1}), a broad shoulder centered at approximately 535 nm appeared in addition to the SPR peak at 396 nm, a feature that is indicative of larger Ag nanostructures with high polydispersity.....193

Figure B.6 Representative TEM micrographs of the resultant quasi-spherical Ag@FCD NPs when the FCD concentration was held at 0.3 mg mL^{-1} and the Ag concentration was (A) 0.30 mM, (B) 1.00 mM, or (C) 3.00 mM. Such FCD:Ag ratios resulted in average particle sizes of (A) 11.1 ± 9.9, (B) 6.9 ± 3.4, and (C) 6.0 ± 4.0 nm, respectively 194

Figure B.7 Resultant Au@FCD NP SPR as a function of the Au concentration within samples synthesized at 100 °C. Similar to the room temperature reductions of Au salt using FCDs, the 100 °C reductions resulted in a bathochromic shift of the SPR with increasing Au concentration, a transition indicative of the formation of larger Au NPs and further highlighting the degree of SPR tunability, even when using elevated temperatures.....195

Figure B.8 UV-vis spectrum of a control sample that was heated at 100 °C in the presence of 50:50 mol% Au:Ag but in the absence of FCDs. The lack of a discernable SPR peak provides further evidence that the CA-derived FCDs act as reducing agents towards Au_xAg_{1-x} NP formation.....195

Figure B.9 Representative TEM micrographs of the (A) $Au_{0.9}Ag_{0.1}$@FCD, (B) $Au_{0.7}Ag_{0.3}$@FCD, (C) $Au_{0.3}Ag_{0.7}$@FCD, and (D) $Au_{0.1}Ag_{0.9}$@FCD BMNPs. Interestingly, the size of the Au_xAg_{1-x} NPs decreased slightly with increasing Ag content. Specifically, size analyses of the imaged BMNPs yielded average particle sizes of 4.1 ± 1.4, 3.4 ± 0.9, 2.4 ± 0.8, and 1.9 ± 0.7 nm for the $Au_{0.9}Ag_{0.1}$@FCD, $Au_{0.7}Ag_{0.3}$@FCD, $Au_{0.3}Ag_{0.7}$@FCD, and $Au_{0.1}Ag_{0.9}$@FCD BMNPs, respectively.....196

Figure B.10 (A–B) Time-dependent UV-vis absorption spectra of the $NaBH_4$-assisted reduction of 4-NP catalyzed by (A) $Au_{0.5}Ag_{0.5}$@FCD NPs and (B) Ag@FCD NPs. (C) Plots of $\ln(A_t/A_0)$ of 4-NP absorbance at 400 nm *vs* time for various aged MNP@FCD catalysts.....197

Figure B.11 Normalized UV-vis absorption spectra of freshly prepared and aged (for 5 months in a lab drawer) MNP@FCD NPs highlighting the stability of the (A) Au@FCD, (B) $Au_{0.5}Ag_{0.5}$@FCD, and (C) Ag@FCD NPs. Comparison of the spectral profiles for fresh samples to those arising from their aged counterparts reveals that the Au@FCD NPs remained essentially unchanged after storing for 5 months while the aged $Au_{0.5}Ag_{0.5}$@FCD and Ag@FCD NPs displayed increased absorbance at longer wavelengths, features that likely stem from marginal particle aggregation.....198

Figure B.12 Concentration-dependent, peroxidase-mimicking activity of the Au@FCD NPs assessed by temporally monitoring absorbance changes of ABTS (0.805 mM) at 418 nm in the presence of 5.4 mM H_2O_2 and 3.0–48.3 μg mL^{-1} Au@FCD NPs. Note, the reported concentrations indicate the quantity of FCDs present in the Au@FCD aliquot added; the concentration of Au (in μM) within each Au@FCD sample is half the value of the corresponding FCD concentration (*e.g.*, the 24.2 μg mL^{-1} FCD sample contains 12.1 μM Au). Results of a control experiment using a 9.7 μg mL^{-1} solution of neat FCDs (*i.e.*, metal-free) are also provided (brown circles). While no activity was observed on this timescale for the "naked", metal-free FCDs, the Au@FCD NPs clearly showed higher activity with increasing nanocatalyst concentration 199

Figure C.1 Excitation wavelength-dependent emission of the microwave-generated, CA–U-derived (A) as-synth. sample and its filtrate fractions after ultrafiltration with (B) 1 kDa, (C) 10 kDa, or (D) 100 kDa MWCO membranes or bulk filtration with syringe filters of (E) 0.20 μm or (F) 0.45 μm pore size. The excitation wavelength-dependent emission profiles of all filtrate fractions were essentially identical to those of the as-synthesized sample indicating that the small organic material (<1 kDa) that traverses the membrane is associated with the majority of the observed fluorescence. Further, these results highlight that the common practice of purifying solely with a syringe filter is entirely inadequate 200

Figure C.2 Excitation wavelength-dependent emission of dialysis fractions stemming from membrane purification (MWCOs of 1, 3.5, 8, 15, and 50 kDa) of the CA–U-derived, microwave-generated sample, specifically the (A, C, E, G, and I) retent. and (B, D, F, H, and J) dial. fractions. Within each respective category (*i.e.*, retent., dial.), the fractions

displayed similar spectral characteristics to one another regardless of the membrane MWCO employed; however, the emission profiles in cross-category comparisons were markedly different, alluding to the existence of at least two distinct populations of fluorophores. Even further, when the emission was collected on fractions “normalized” to similar absorbance values in the near-UV region, the retent. fractions presented drastically lower emission intensities compared to the dial. fractions. That is, the y-axis maxima of the retent. emission plots are an order of magnitude lower than the maxima used for the plots of the dial. emission; the data were plotted as such to better show the spectral features of the retent. fractions. These results indicate that the retent. fractions, which should contain the desired FCDs (if present), are not nearly as fluorescent as once thought and that the majority of the fluorescence arises from small molecular species (<1 kDa) that permeate the membrane.....201

Figure C.3 Sequence of photographs showing the progress of dialysis for a microwave-generated, CA–U-derived sample after 48, 72, 96, and 120 h of dialysis. The images were collected immediately before replenishing the exchange solvent (*i.e.*, ultrapure water). These results highlight the sheer quantity of small molecular material (<1 kDa) that continues to permeate the membrane even after four additional 24 h dialysis periods against fresh exchange solvent.....202

Figure C.4 Sequence of photographs showing the dialysis progression of a 1 kDa CA–U retent. fraction dialyzed with a 50 kDa MWCO membrane. That is, the retent. fraction employed in this study was a microwave-generated, CA–U-derived parent (as-synth.) sample that had previously been extensively dialyzed with a 1 kDa MWCO membrane. These images further highlight that the resulting product consists of two size-disparate

species: one less than 1 kDa (*e.g.*, molecular/polymeric material) and the other greater than 50 kDa (*e.g.*, FCDs) 203

Figure C.5 Representative TEM micrographs of (A–B) citrate- and (D–E) $NaBH_4$-stabilized Au NPs. Corresponding histograms from the size analysis of the citrate- and $NaBH_4$-stabilized Au NPs are shown in panels C and F, respectively. The Au NPs were employed as a convenient means to clarify nanoscale membrane permeability for a given MWCO.....204

Figure C.6 UV-vis spectra of the dialysate (dial.) and ultrafiltration (filt.) fractions of the 14 nm citrate-stabilized and 6 nm $NaBH_4$-stabilized Au NPs compared to their parent (nonpurified) solutions. These benchmark experiments reveal that neither Au NP samples permeate the 50 kDa dialysis membrane, whereas minute quantities of both Au NP sizes pass through the 100 kDa ultrafiltration membrane, with the larger citrate-stabilized Au NPs mobilizing to a lesser extent. The inset panel is a magnified plot of the spectra for the dialysate and filtrate fractions to better highlight these revelations 205

Figure C.7 Representative TEM micrographs of the (A, B, E, and F) 1 kDa and (C, D, G, and H) 50 kDa MWCO retent. (panels A–D) and dial. (panels E–H) fractions from dialysis of the microwave-generated, CA–U-derived material. Some FCDs were visible in the 1 kDa MWCO retent. fraction but proved difficult to image due to the large quantity of film-forming, molecular by-products still present. Contrarily, FCDs were more prominent in the 50 kDa retent. fraction and were more easily imaged due to fewer (or no) by-product impurities still contaminating the fraction. However, some apparent FCDs were visible in the 50 kDa MWCO dial. fraction indicating that, in general, dialysis may be less than ideal

due to the difficulty in segregating the target FCDs from molecular (oligo- or polymeric) by-products, a scenario worsened by the potential for small, organic fluorophores to form supramolecular aggregates that resemble FCDs under TEM imaging 206

Figure C.8 Excitation wavelength-dependent emission of the hydrothermally treated, Arg-derived (A) as-synth. sample and its corresponding (B, D, and F) retent. and (C, E, and G) dial. fractions arising from the membrane MWCO-dependent dialysis study. All fractions had similar spectral characteristics to one another; however, the emission of the retent. fractions was drastically lower despite all fractions possessing similar absorbance values in the near-UV region. These results, in combination with the fluorescence quantum yield data (Figure C.10), further iterate that the majority of the photoluminescence arises from small molecular species (<1 kDa) and not FCDs 207

Figure C.9 Sequence of photographs showing the dialysis progression of a hydrothermally treated, Arg-derived sample dialyzed with a 1 kDa MWCO membrane. The continued mobilization of material through the membrane out to 24 h further highlights that a single dialysis treatment of <24 h is wholly insufficient to fully fractionate the target FCDs from small molecular by-products.....208

Figure C.10 Wavelength-dependent fluorescence quantum yields of hydrothermally synthesized, Arg-derived as-synth. samples and their corresponding retent. (closed circles) and dial. (open circles) fractions after dialysis for (A) 6 h and (B) 24 h with 1, 15, or 50 kDa MWCO membranes. Panel C compares the measured fluorescence quantum yields of the 24 h dial. fractions to those determined for retent. fractions after an additional 48 h of dialysis (72 h in total with the exchange solvent replenished every 24 h). The results clearly

show that 6 h of dialysis is insufficient, as evidenced by the quantum yields of the retent. fractions continually decreasing with longer dialysis periods, trends that further support the notion that the majority of the observed fluorescence of the as-synth. sample originates from material constituting the dial. fraction (*i.e.*, by-products).....209

Figure C.11 Excitation wavelength-independent emission of hydrothermally treated, CA–EDA-derived (A) as-synth. samples and their corresponding (B, D, and F) retent. and (C, E, and G) dial. fractions from the membrane MWCO-dependent dialysis study. All fractions had similar spectral characteristics to one another although the emission of the retent. fractions was drastically lower even for samples with comparable absorbance values. These trends are consistent with the other systems explored in this work and, again, allude to small molecular species (<1 kDa) accounting for the majority of observed emission 210

Figure C.12 Fluorescence quantum yields of a hydrothermally synthesized, nonpurified CA–EDA-derived sample (*i.e.*, as-synth.) and its corresponding 72 h retent. (closed circles) and 24 h dial. fractions (open circles). The results are consistent with all other dialysis studies and clearly show that the retent. fractions consist of less photoluminescent species, whereas the majority of the fluorescence of the as-synth. sample originates from species comprising the dial. fractions. The excitation wavelength (λ_{ex}) employed for these quantum yield assessments was 350 nm for all fractions 211

Figure C.13 UV-vis spectra of as-synth. samples from syntheses that employed (A) CA–U or (B) CA–EDA as precursors, as well as the spectra of their corresponding retent. and dial. fractions that were obtained after dialysis of the as-synth. samples with 1 or 50 kDa

MWCO membranes. Stark spectral differences between the retent. and dial. fractions were evident, where the latter fractions displayed identical features to their corresponding as-synth. sample, indicating that the species constituting the dial. fractions dominate the observed spectral properties of their respective parent, as-synth. sample 212

Figure C.14 Excitation wavelength-dependent emission of an electrochemically produced, graphite-derived (A) as-synth. sample and its corresponding (B, D, and F) retent. and (C, E, and G) dial. fractions obtained from a membrane MWCO-dependent (1, 15, and 50 kDa) dialysis study. While all fractions had similar spectral characteristics to one another, the results highlight that top-down approaches are not exempt from purification due to small photoluminescent by-products generated in situ during FCD synthesis.....213

Figure C.15 Excitation wavelength-dependent emission of a (A) hydrothermally PEG-N-functionalized (1.5 kDa) sample and its corresponding (B, D, and F) retent. and (C, E, and G) dial. fractions obtained from a membrane MWCO-dependent (1, 15, and 50 kDa) dialysis study. These results highlight that the products from FCD functionalization reactions are not solely comprised of passivated FCDs but also contain small fluorescent molecular species (<1 kDa), thus indicating that postfunctionalization purification is an absolute necessity. Note, the parent sample employed in this study was electrochemically synthesized from graphite rods 214

Figure C.16 Excitation wavelength-dependent emission of a (A) hydrothermally PEI-functionalized (1.2 kDa) sample and its corresponding (B, D, and F) retent. and (C, E, and G) dial. fractions obtained from a membrane MWCO-dependent (1, 15, and 50 kDa) dialysis study. Consistent with the fluorescence results obtained from the dialysis study of

the PEG-N-functionalized sample, these results further reveal that postfunctionalization purification is essential to adequately separate the putatively functionalized FCDs from molecular (oligo- or polymeric) by-products. Note, the parent sample employed in this study was electrochemically synthesized from graphite rods.....215

Figure C.17 Excitation wavelength-dependent fluorescence quantum yields assessed for the (A) electrochemically synthesized (non-functionalized), (B) PEG-N-functionalized (1.5 kDa), and (C) PEI-functionalized (1.2 kDa) materials, as well as their respective retent. (closed circles) and dial. (open circles) fractions. The resultant values highlight that even for top-down syntheses and their subsequent functionalization, adequate purification is a necessity after the initial synthesis as well as postfunctionalization 216

Figure C.18 (A) Excitation wavelength-dependent fluorescence quantum yields determined for an electrochemically synthesized (as-synth.) sample and its filtrate fractions obtained upon ultrafiltration (denoted by "UF") of the as-synth. sample with 1, 10, or 100 kDa MWCO membranes. The observed trends further highlight the need for adequate purification. (B) Excitation wavelength-dependent fluorescence quantum yields of the as-prepared PEG-N-functionalized (1.5 kDa) and PEI-functionalized (1.2 kDa) materials and their corresponding filtrate fractions after ultrafiltration with a 1 kDa MWCO membrane. The results clearly show that highly fluorescent by-products are indeed generated, necessitating fractionation from the target, functionalized FCDs. The excitation wavelength-dependent quantum yields of the electrochemically synthesized (as-synth.) parent sample are included in panel B for comparison.....217

Figure C.19 Metal ion quenching studies of a hydrothermally treated, CA–EDA-derived as-synth. sample and its corresponding retent. and dial. fractions. In general, Cu^{2+} and Fe^{3+} induced little to no quenching for all fractions while Hg^{2+} quenched the emission of the retent. fraction more strongly than the as-synth. and dial. fractions. These results are consistent with the quenching studies of the microwave-generated CA–U-derived materials 218

Figure C.20 Toxicity of microwave-generated, CA–U-derived (A) retent. and (B) dial. fractions toward mice embryonic fibroblasts. Although distinctive fraction- or membrane MWCO-dependent trends were not apparent for either fraction, minimal toxicity was observed for concentrations at or below 0.3 mg mL^{-1} while slight toxicities arose for concentrations of 1 mg mL^{-1}, regardless of the fraction. The toxicity of the as-synth., parent sample is provided in both panels for comparison.....219

Figure C.21 Toxicity of microwave-generated, CA–U-derived (A) retent. and (B) dial. fractions toward human breast cancer cells (T-47D). Both retent. and dial. fractions for all membrane MWCOs studied had no toxic effects on this specific cell line. The toxicity of the as-synth., parent sample is provided in both panels for comparison 220

Figure C.22 Toxicity of microwave-generated, CA–U-derived (A) retent. and (B) dial. fractions towards HeLa cells. For this cell line, the fractions did not display any concentration-, membrane MWCO-, or fraction-dependent trends in toxicity. The toxicity of the as-synth., parent sample is provided in both panels for comparison 221

Figure C.23 Photographic comparison of (A and C) as-synth. samples to (B and D) 50 kDa retent. fractions for the (A–B) CA–U- and (C–D) Arg-derived materials under white light

(left panels) and 354-nm UV light (right panels). This composite illustrates the misleading fluorescence results that arise when the samples are not properly diluted to a similar concentration (or absorbance value); that is, at higher concentrations, the samples will appear to fluoresce at longer (redder) wavelengths. However, this dubious observation is simply an artifact of the inner filter effect, arising from the (near complete) reabsorption of blue to green emission and the illumination of the already orange-, red-, or brown-colored solutions 222

Figure C.24 Excitation wavelength-dependent emission spectra of a hydrothermally generated, Arg-derived (A) as-synth. sample as well as (B) 10-fold diluted and (C) 100-fold diluted solutions. The results appear to indicate that the fluorescence blueshifts as the sample is diluted, which might lead one to believe that the samples emit redder wavelengths with increasing concentration. However, this apparent bathochromic shift simply arises from inner filter effects that lead to attenuation of the intense blue edge and subsequently render the weakly emitting red edge the only emission visible. (D) Plotting the wavelength of maximum emission (extracted from panels A–C) as a function of the excitation wavelength further highlights the perceived but deceptive emission shift 223

Figure D.1 (A) UV-vis and (B) fluorescence spectra of an as-synth. sample derived from GSH–F as well as its corresponding retent. and dial. fractions obtained after dialyzing with a 50 kDa MWCO membrane. The results further corroborate the need for adequate purification as the absorbance and emission profiles drastically change upon dialysis. Specifically, the as-synth. sample displays strong blue emission which decreased as the highly fluorescent by-products were removed leading to even stronger blue emission for the dial. fraction and the emergence of distinct red-emitting species (presumably FCDs) in

the retent. fraction (see inset photograph). Normalized (C) absorbance and (D) fluorescence spectra of the retent. fractions compared to the results reported in the literature reveal the synthetic consistency of the published protocol. The data in panels C and D was reproduced with permission from reference 86 of Chapter 5. Copyright © 2019 Elsevier.....224

Figure D.2 Temporal uptake of 5 mg mL^{-1} CA–NH_4OH-derived (A) as-synth., (B) dial., and (C) retent. fractions (dispersed in acetone) by TiO_2 films, monitored with UV-vis spectroscopy. Panel D shows that the majority of uptake occurred within the first 2 h of sensitization with the retent. fraction showing higher apparent uptake, evidenced by more strongly absorbing films; however, this observation could arise from a larger extinction coefficient inherent to the adsorbed species. Additionally, continued but slowed uptake of the different fractions was observed after the initial, rapid adsorption during the first 2 h of sensitization. Given the spectral similarities between TiO_2 films sensitized with the as-synth. and dial. fractions, the species constituting the dial. fraction clearly account for the majority of the as-synth. product composition, materials that dominate adsorption and the resultant spectral features of the sensitized films 225

Figure D.3 Temporal uptake of 10 mg mL^{-1} Arg-derived (A) as-synth., (B) syringe-filtered as-synth. (as-synth. filt.), (C) dial., and (D) retent. fractions (dispersed in EtOH) by TiO_2 films, monitored with UV-vis spectroscopy. Panel E shows that over 50% of the sensitizer uptake occurred within the first 2 h of sensitization, however, appreciable uptake still occurred up to 12 h with minimal to no additional uptake occurring after 24 h of sensitization. In fact, the two as-synth. fractions showed a slight decrease from 12 to 24 h, indicating undesirable sensitizer desorption. These fractions, as well as the retent. fraction, also showed absorbance decreases from 8 to 12 h total sensitization time. The widely

varying values of ln(A_t/A_0) for the studied fractions are attributed to drastically different extinction coefficients for the species comprising each fraction but could also arise from varying degrees of uptake 226

Figure D.4 Temporal uptake of aqueous 10 mg mL^{-1} CA–U-derived (A) as-synth., (B) dial., and (C) retent. fractions by TiO_2 films, monitored with UV-vis spectroscopy. Panel D shows that the majority of sensitizer uptake occurred within the first 2 h of sensitization with additional but minimal uptake occurring out to 24 h of total sensitization time. Interestingly, the dial. and retent. fractions showed almost identical uptake, both temporally and in terms of raw absorbance, while the as-synth. fraction showed a comparable trend in temporal uptake but yielded higher overall absorbance, the origin of which is currently unclear.....227

Figure D.5 Temporal uptake of GSH–F-derived (A) as-synth., (B) dial., and (C) retent. fractions by TiO_2 films, monitored with UV-vis spectroscopy. Note, the as-synth. and dial. fractions were dispersed in 50:50 vol% formamide:water at unknown concentrations while the retent. fraction was dispersed in 100% water at 10 mg mL^{-1}. Panel D shows that sensitizer uptake occurred rapidly within the first 4–6 h of sensitization and began to slow after 6 h but never fully levelled off, with sensitizing species still adsorbing out to 24 h of total sensitization time. Interestingly, the as-synth. and retent. uptakes were essentially identical despite the unknown concentration of the former, the different solvent systems employed, and the minor differences observed for the two fractions in their absorbance peaks between 600 and 750 nm. Additionally, substantially lower absorbance was observed for films sensitized in the dial. fraction, an occurrence that could stem from the concentration differences between the fractions since the concentration of the dial. fraction

was not assessable due to residual formamide. However, given the stark differences in film color between the fractions (Figure D.20), the lower absorbance likely arises from markedly lower extinction coefficients for the species comprising the dial. fraction 228

Figure D.6 TiO_2-subtracted (A) EQE and (B) absorbance (abs.) spectra of TiO_2 films that were sensitized in 5 mg mL^{-1} CA–NH_4OH-derived fractions in 100% acetone or 50:50 vol% acetone:ethanol (denoted by "EtOH"). The inset plot in panel A shows normalized (norm.) spectra for the TiO_2-subtracted (TiO_2-sub.) EQE spectra. Clearly, the photocurrent generated by species in the as-synth. fraction predominately originates from reaction by-products comprising the dial. fraction. Additionally, chromophoric but nonphotocurrent-generating, by-product species exist within the dial. fraction evidenced by lower absorbance for films sensitized in ethanolic solutions compared to those sensitized in 100% acetone yet the former films yielded comparable performance to the latter. Furthermore, the above results indicate that the photocurrent generated by the as-synth. and dial. fractions is likely produced by the species responsible for the shoulder observed at 450 nm in the absorbance spectra. Conversely, the retent. fractions generated substantially lower photocurrent despite having markedly higher absorbance. Moreover, the maximum EQE for the retent. fraction is hypsochromically shifted by 20 nm relative to the maxima observed for the as-synth. and dial. fractions 229

Figure D.7 (A) Average *J*-*V* curves (with corresponding standard deviations) of illuminated devices employing TiO_2 films that were sensitized in 10 mg mL^{-1} CA–NH_4OH-derived fractions dispersed in 100% acetone or 50:50 vol% acetone:ethanol (denoted by "EtOH"). (B) Average device metrics. *Note, efficiency (η) is reported in percent and FF is a unitless parameter but both values are on the same scale as the left and

right y-axes, respectively. (C) Average EQE and (D) UV-vis absorbance spectra with their corresponding TiO_2-subtracted counterparts provided in panels E and F, respectively. A magnified plot of the EQE from 350 to 550 nm, photographs of representative films used in the devices, and a plot of normalized (norm.) spectra for the TiO_2-subtracted (TiO_2-sub.) EQE spectra are provided in the insets of panels C, D, and E, respectively. The conclusions drawn from the above results are similar to those arrived at for the 5 mg mL^{-1} fractions; that is, device performance, mainly the photocurrent, arises from reaction by-products, specifically, species responsible for the absorbance shoulder at 450 nm and the yellow-orange color of the films. The performance of bare TiO_2 (black curves) is provided in all relevant plots for comparison.....230

Figure D.8 (A) Average *J-V* curves (with corresponding standard deviations) of illuminated devices employing TiO_2 films that were sensitized in 30 mg mL^{-1} CA–NH_4OH-derived fractions dispersed in 100% acetone or 50:50 vol% acetone:ethanol (denoted by "EtOH"). (B) Average device metrics. *Note, efficiency (η) is reported in percent and FF is a unitless parameter but both values are on the same scale as the left and right y-axes, respectively. (C) Average EQE and (D) UV-vis absorbance spectra with their corresponding TiO_2-subtracted counterparts provided in panels E and F, respectively. A magnified plot of the EQE from 350 to 550 nm, photographs of representative films used in the devices, and a plot of normalized (norm.) spectra for the TiO_2-subtracted (TiO_2-sub.) EQE spectra are provided in the insets of panels C, D, and E, respectively. The conclusions drawn from the above results are similar to those arrived at for the 5 and 10 mg mL^{-1} fractions; that is, device performance, mainly the photocurrent, arises from reaction by-products, specifically, species responsible for the absorbance shoulder at 450 nm and the

yellow-orange color of the films. The performance of bare TiO_2 (black curves) is provided in all relevant plots for comparison 231

Figure D.9 Comparative analysis of the results for the 5, 10, and 30 mg mL^{-1} CA–NH_4OH-derived (A–E) as-synth. and (F–J) dial. fractions. (A and F) Average *J-V* curves (with corresponding standard deviations) of illuminated devices employing TiO_2 films that were sensitized in the above fractions ("EtOH" denotes samples dispersed in 50:50 vol% acetone:ethanol). (B and G) Average device metrics. *Note, efficiency (η) is reported in percent and FF is a unitless parameter but both values are on the same scale as the left and right y-axes, respectively. (C and H) Average EQE and (D and I) UV-vis absorbance spectra with their corresponding TiO_2-subtracted counterparts provided as panel insets. (E and J) Photographs of representative films used in the devices. The performance of bare TiO_2 (black curves) is provided in all relevant plots for comparison 233

Figure D.10 (A) Average *J-V* curves (with corresponding standard deviations) of illuminated devices employing TiO_2 films that were sensitized in dial.-spiked, 5 mg mL^{-1} CA–NH_4OH-derived retent. solutions dispersed in 100% acetone or 50:50 vol% acetone:ethanol (denoted by "EtOH"). Appropriate quantities of the dial. fraction were spiked in 5 mg mL^{-1} retent. samples to yield 1, 2.5, 5, 10, or 30 mg mL^{-1} concentrations of the dial. species. (B) Average device metrics. *Note, efficiency (η) is reported in percent and FF is a unitless parameter but both values are on the same scale as the left and right y-axes, respectively. (C) Average EQE and (D) absorbance spectra with their corresponding TiO_2-subtracted counterparts shown in panels F and G. (E) Photographs of representative films sensitized in the dial.-spiked, 5 mg mL^{-1} CA–NH_4OH retent. solutions. A magnified plot of the EQE from 350 to 550 nm and a plot of normalized (norm.) spectra for the TiO_2-

subtracted (TiO_2-sub.) EQE spectra are provided in the insets of panels C and F, respectively. The performance of bare TiO_2 (black curves) is provided in all plots for comparison.....234

Figure D.11 (A) Average *J-V* curves (with corresponding standard deviations) of illuminated devices employing TiO_2 films that were sensitized in dial.-spiked, 1 mg mL^{-1} CA–NH_4OH-derived retent. solutions dispersed in 100% acetone or 50:50 vol% acetone:ethanol (denoted by "EtOH"). Appropriate quantities of the dial. fraction were spiked in the 1 mg mL^{-1} retent. samples to yield 1, 2.5, 5, 10, or 30 mg mL^{-1} concentrations of the dial. species. (B) Average device metrics. *Note, efficiency (η) is reported in percent and FF is a unitless parameter but both values are on the same scale as the left and right y-axes, respectively. (C) Average EQE and (D) absorbance spectra with their corresponding TiO_2-subtracted counterparts shown in panels F and G. (E) Photographs of representative films sensitized in the dial.-spiked, 1 mg mL^{-1} CA–NH_4OH retent. solutions. A magnified plot of the EQE from 350 to 550 nm and a plot of normalized (norm.) spectra for the TiO_2-subtracted (TiO_2-sub.) EQE spectra are provided in the insets of panels C and F, respectively. The performance of bare TiO_2 (black curves) is provided in all plots for comparison.....235

Figure D.12 Select comparisons of the results from the CA–NH_4OH dial. spiking studies. (A) Device metrics for TiO_2 films sensitized in 1 or 5 mg mL^{-1} retent. fractions spiked with 10 mg mL^{-1} dial. compared to films sensitized in a 10 mg mL^{-1} as-synth. fraction, which nominally contained 0.1 and 9.9 mg mL^{-1} retent. and dial. species, respectively. (B) Device metrics for TiO_2 films sensitized in 1 or 5 mg mL^{-1} retent. fractions spiked with dial. to a concentration of 30 mg mL^{-1} compared to films sensitized in ethanolic 30 mg mL^{-1} as-

synth. fraction, which nominally contained 0.3 and 29.7 mg mL^{-1} retent. and dial. species, respectively. (C) Average UV-vis absorbance spectra for the films employed in the devices summarized in panel B. These results clearly show that synergistic effects between the dial. and retent. species exist, where an optimized nanocarbon content leads to improved device performance, as widely reported in the literature. Furthermore, higher concentrations of the retent. fraction appear to diminish the apparent "selectivity" observed in ethanolic solutions, evidenced by increased film absorbance when sensitized in higher retent. content, even when in the presence of 50% ethanol (denoted by "EtOH").....237

Figure D.13 Comparison of 2 h *vs* 24 h uptake for CA–NH_4OH-derived as-synth. fractions. (A) Average *J-V* curves (with corresponding standard deviations) of illuminated devices employing TiO_2 films that were sensitized in 5, 10, or 30 mg mL^{-1} CA–NH_4OH-derived as-synth. fractions dispersed in 100% acetone or 50:50 vol% acetone:ethanol (denoted by "EtOH"). (B) Average device metrics. *Note, efficiency (η) is reported in percent and FF is a unitless parameter but both values are on the same scale as the left and right y-axes, respectively. (C) Average EQE and (D) UV-vis absorbance spectra with their corresponding TiO_2-subtracted counterparts provided in panels E and F, respectively. A magnified plot of the EQE from 350 to 550 nm, photographs of representative films used in the devices, and a plot of normalized (norm.) spectra for the TiO_2-subtracted (TiO_2-sub.) EQE spectra are provided in the insets of panels C, D, and E, respectively. The results clearly show that longer sensitization times negatively impacted device performance despite an increased uptake of chromophoric material, effects that were concentration dependent and, thus, most prominent for the 30 mg mL^{-1} as-synth. fraction. The

performance of bare TiO_2 (black curves) is provided in all relevant plots for comparison 238

Figure D.14 Concentration-dependent comparison of 2 h *vs* 24 h uptake for CA–NH_4OH-derived as-synth. fractions. (A) Average *J-V* curves (with corresponding standard deviations) of illuminated devices employing TiO_2 films that were sensitized in 5 or 30 mg mL^{-1} CA–NH_4OH-derived as-synth. fractions dispersed in 100% acetone or 50:50 vol% acetone:ethanol (denoted by "EtOH"). (B) Average device metrics. *Note, efficiency (η) is reported in percent and FF is a unitless parameter but both values are on the same scale as the left and right y-axes, respectively. (C) Average EQE and (D) absorbance spectra with their corresponding TiO_2-subtracted counterparts shown in panels F and G. (E) Photographs of representative films. A magnified plot of the EQE from 350 to 550 nm and a plot of normalized (norm.) spectra for the TiO_2-subtracted (TiO_2-sub.) EQE spectra are provided in the insets of panels C and F, respectively. The results clearly show that longer sensitization times led to diminished performance. Although, this observation is not solely a product of increased uptake, specifically, of nanocarbons, since 2 h sensitizations in 5 or 30 mg mL^{-1} as-synth. fractions yielded comparable performance to one another and 24 h sensitizations in ethanolic solutions produced similar decreases in performance as their 100% acetone counterparts. Therefore, the observed decreases in performance upon longer sensitizations may arise from TiO_2-induced degradation of the photoactive species. The performance of bare TiO_2 (black curves) is provided in all relevant plots for comparison 239

Figure D.15 Fraction-dependent comparison of 2 h *vs* 24 h uptake for CA–NH_4OH-derived samples. (A) Average *J-V* curves (with corresponding standard deviations) of illuminated

devices employing TiO_2 films that were sensitized in 30 mg mL^{-1} CA–NH_4OH-derived as-synth. and dial. fractions dispersed in 100% acetone. (B) Average device metrics. *Note, efficiency (η) is reported in percent and FF is a unitless parameter but both values are on the same scale as the left and right y-axes, respectively. (C) Average EQE and (D) absorbance spectra with their corresponding TiO_2-subtracted counterparts shown in panels E and F. A magnified plot of the EQE from 350 to 550 nm, photographs of representative films used in the devices, and a plot of normalized (norm.) spectra for the TiO_2-subtracted (TiO_2-sub.) EQE spectra are provided in the insets of panels C, D, and E, respectively. Akin to the other 24 h sensitization studies, longer sensitization led to diminished performance for the 30 mg mL^{-1} as-synth. and dial. fractions, however, the decrease observed in the latter was not nearly as prominent as that for the former, implying the nanocarbons may be playing a role in TiO_2-induced degradation of the photoactive species. The performance of bare TiO_2 (black curves) is provided in all relevant plots for comparison.....241

Figure D.16 Aging effects of CA–NH_4OH samples. (A) Average *J*-*V* curves (with corresponding standard deviations) of illuminated devices employing TiO_2 films that were sensitized in fresh or aged (>1 week old) 30 mg mL^{-1} CA–NH_4OH-derived as-synth. fractions dispersed in 100% acetone or 50:50 vol% acetone:ethanol (denoted by "EtOH"). (B) Average device metrics. *Note, efficiency (η) is reported in percent and FF is a unitless parameter but both values are on the same scale as the left and right y-axes, respectively. (C) Average EQE and (D) absorbance spectra with their corresponding TiO_2-subtracted counterparts shown in panels E and F. A magnified plot of the EQE from 350 to 550 nm, photographs of representative films used in the devices, and a plot of normalized (norm.)

spectra for the TiO_2-subtracted (TiO_2-sub.) EQE spectra are provided in the insets of panels C, D, and E, respectively. While not staggering, slight aging effects were observed in the 30 mg mL^{-1} as-synth. fractions. Although, when the same samples were sensitized in the presence of EtOH, the minor decrease in performance was not apparent. Such an observation implies the lower performance likely does not originate from degradation of the photoactive species but stems from the degradation of another species that is only present in a sufficient enough concentration to induce a negative impact in the 30 mg mL^{-1} as-synth. fraction, which could be the nanocarbons or an unidentified reaction by-product. The performance of bare TiO_2 (black curves) is provided in all relevant plots for comparison.....242

Figure D.17 Effects of water exposure on CA–NH_4OH samples. (A) Average *J-V* curves (with corresponding standard deviations) of illuminated devices employing TiO_2 films that were sensitized in 30 mg mL^{-1} CA–NH_4OH-derived as-synth. fractions dispersed in 100% acetone. (B) Average device metrics. *Note, efficiency (η) is reported in percent and FF is a unitless parameter but both values are on the same scale as the left and right y-axes, respectively. (C) Average EQE and (D) absorbance spectra with their corresponding TiO_2-subtracted counterparts shown in panels F and G. The inset in panel D illustrates the effects that water exposure (right) has on the acetone-dispersed solutions (left). (E) Photographs of representative films. A magnified plot of the EQE from 350 to 550 nm and a plot of normalized (norm.) spectra for the TiO_2-subtracted (TiO_2-sub.) EQE spectra are provided in the insets of panels C and F, respectively. The performance of bare TiO_2 (black curves) is provided in all relevant plots for comparison. The experimental details for these studies and an in-depth analysis of the results are provided below 244

Figure D.18 TiO_2-subtracted (A) EQE and (B) absorbance (abs.) spectra for 10 mg mL^{-1} Arg fractions in EtOH. The inset plot in panel A shows normalized (norm.) spectra for the TiO_2-subtracted (TiO_2-sub.) EQE spectra. Clearly, photocurrent generation from the retent. fraction is negatively impacted by a species present in the dial. fraction since the photocurrent produced by the as-synth. fractions is only slightly higher than that created by the dial. fraction. Note, "as-synth. filt." represents the as-synth. sample that was passed through a 0.20 μm pore size syringe filter 247

Figure D.19 Aging effects of CA–U-derived samples. (A) Average *J-V* curves (with corresponding standard deviations) of illuminated devices employing TiO_2 films that were sensitized in fresh or aged (>1 month old) 10 mg mL^{-1} CA–U-derived fractions dispersed in water. (B) Average device metrics. *Note, efficiency (η) is reported in percent and FF is a unitless parameter but both values are on the same scale as the left and right y-axes, respectively. (C) Average EQE and (D) absorbance spectra with their corresponding TiO_2-subtracted counterparts shown in panels E and F. A magnified plot of the EQE from 350 to 550 nm, photographs of representative films used in the devices, and a plot of normalized (norm.) spectra for the TiO_2-subtracted (TiO_2-sub.) EQE spectra are provided in the insets of panels C, D, and E, respectively. The performance of bare TiO_2 (black curves) is provided in all relevant plots for comparison. The experimental details for these studies and an in-depth analysis of the results are provided below 248

Figure D.20 Aging effects of GSH–F-derived samples. (A) Average *J-V* curves (with corresponding standard deviations) of illuminated devices employing TiO_2 films that were sensitized in fresh or aged (>1 week old) solutions of the GSH–F-derived fractions. (B) Average device metrics. *Note, efficiency (η) is reported in percent and FF is a unitless

parameter but both values are on the same scale as the left and right y-axes, respectively. (C) Average EQE and (D) absorbance spectra with their corresponding TiO_2-subtracted counterparts shown in panels E and F. A magnified plot of the EQE from 350 to 550 nm, photographs of representative films used in the devices, and a plot of normalized (norm.) TiO_2-subtracted (TiO_2-sub.) EQE spectra are provided in the insets of panels C, D, and E, respectively. Magnified plots of the EQE and absorbance from 550 to 750 nm are shown in panels G and H with their corresponding TiO_2-subtracted counterparts shown in panels I and J, respectively. The performance of bare TiO_2 (black curves) is provided in all relevant plots for comparison. The experimental details for these studies and an in-depth analysis of the results are provided below 251

Figure D.21 Effects of aging on GSH–F-sensitized TiO_2 films. (A) Average *J-V* curves (with corresponding standard deviations) of illuminated devices employing TiO_2 films that were sensitized in fresh or aged (>2 months old) films sensitized with the GSH–F-derived fractions. (B) Average device metrics. *Note, efficiency (η) is reported in percent and FF is a unitless parameter but both values are on the same scale as the left and right y-axes, respectively. (C) Average EQE and (D) absorbance spectra with their corresponding TiO_2-subtracted counterparts shown in panels E and F. A magnified plot of the EQE from 350 to 550 nm, photographs of representative films used in the devices, and a plot of normalized (norm.) spectra for the TiO_2-subtracted (TiO_2-sub.) EQE spectra are provided in the insets of panels C, D, and E, respectively. Magnified plots of the EQE and absorbance from 550 to 750 nm are shown in panels G and H with their corresponding TiO_2-subtracted counterparts shown in panels I and J, respectively. The performance of bare TiO_2 (black

curves) is provided in all relevant plots for comparison. The experimental details for these studies and an in-depth analysis of the results are provided below 255

Figure D.22 Effects of synthesis temperature on GSH–F-derived fractions. (A) Average *J-V* curves (with corresponding standard deviations) of illuminated devices employing TiO_2 films that were sensitized in GSH–F-derived samples synthesized at either 180 or 200 °C. (B) Average device metrics. *Note, efficiency (η) is reported in percent and FF is a unitless parameter but both values are on the same scale as the left and right y-axes, respectively. (C) Average EQE and (D) absorbance spectra with their corresponding TiO_2-subtracted counterparts shown in panels E and F. A magnified plot of the EQE from 350 to 550 nm, photographs of representative films employed in the devices, and a plot of normalized (norm.) spectra for the TiO_2-subtracted (TiO_2-sub.) EQE spectra are provided in the insets of panels C, D, and E, respectively. Magnified plots of the EQE and absorbance from 550 to 750 nm are shown in panels G and H with their corresponding TiO_2-subtracted counterparts shown in panels I and J, respectively. The performance of bare TiO_2 (black curves) is provided in all relevant plots for comparison. The experimental details for these studies and an in-depth analysis of the results are provided below 258

Figure D.23 Average *J-V* curves (with corresponding standard deviations) of devices employing TiO_2 films that were sensitized in an aqueous, 10 mg mL^{-1}, coal-derived retent. fraction that purportedly contains GQDs. (B) Average device metrics. *Note, efficiency (η) is reported in percent and FF is a unitless parameter but both values are on the same scale as the left and right y-axes, respectively. (C) Average EQE spectrum of the devices (left y-axis) and average absorbance spectrum of the films employed within (right y-axis). A representative photograph of the sensitized TiO_2 films is provided in the inset. (D) Plot

of the normalized EQE spectra. The performance of bare TiO_2 (black curves) is provided in all relevant plots for comparison. Clearly, the highly graphitic nanocarbons negatively impacted PV action, decreasing the performance well below that of bare TiO_2 and generating near-zero power conversion efficiency, despite the intense uptake or high extinction coefficient of the material. Furthermore, the graphitic nanocarbons produced essentially no photocurrent and, in fact, substantially decreased the photocurrent arising from TiO_2 and hypsochromically shifted the EQE peak by 20 nm 262

Figure D.24 Mass spectra of (A) CA and (B–C) CA–U precursor solutions from a *m/z* range of (B) 100–242 and (C) 246–807 263

Figure D.25 Mass spectra of (A–B) CA–NH_4OH and (C–D) CA–U as-synth. fractions from *m/z* ranges of (A) 86–242, (B) 247–512, (C) 46–242, and (D) 251–470. An asterisk (*) next to a peak or peak assignment indicates that the peak was also observed in the precursor spectra 264

Figure E.1 (A) Photograph of the solar simulator system employed in all the studies discussed within this dissertation. (B–C) Schematical representation of the components comprising the solar simulator system shown in panel A. Specifically, panels B (solid lines) and C (dashed lines) represent the instrumentation/modules on the lower breadboard and upper shelf, respectively, where the provided identifiers correspond to the elements listed in Table E.1 268

Figure E.2 (A) Schematic representation of the origin of various air mass (AM) classifications, specifically, AM0, 1, 1.5D, and 1.5G, which are the solar radiation at the top of the Earth's atmosphere at the Zenith angle, solar radiation at the Earth's surface at

the Zenith angle, direct solar radiation at the Earth's surface at a 48.2° angle (relative to Zenith), and both direct and diffuse solar radiation at the Earth's surface at a 48.2° angle (relative to Zenith), respectively. The solar radiation spectra arising from AM0 and AM1.5 conditions are shown in yellow and red, respectively, in panel B, with simulated spectra of these conditions (*i.e.*, AM0, AM1.5D, AM1.5G) provided in panel C. AM1.5G filters employed in photovoltaic characterizations are designed to mimic the blue "AM1.5 Global" spectrum shown in panel C. Panels B and C were used with permission from references 1 and 2, respectively. Copyright © 2007 Robert A. Rohde (panel B) and Copyright © 2010 Christiana Honsberg and Stuart Bowden (panel C; original work and data from SMARTS modeling program used at the National Renewable Energy Laboratory) 270

Figure E.3 (A) Ideally, an incident beam of light irradiating from the lamp would possess uniform power across the entire beam. (B) Realistically though, the power magnitude of the incident beam is more conically shaped; that is, a Gaussian distribution with high power at the center and decreasing power away from the apex. (C) Therefore, the goal is to align the lamps and collimate the emanating light such that a more uniform power distribution (*i.e.*, dome-shaped) is achieved.....274

Figure E.4 For proper alignment of the 300 W arc lamp, the (A) actual arc and the (B) arc image created by the back reflector mirror need to be (C) superimposed in such a manner that the "hot spots" of the electrodes (tip of point electrode) do not lie directly over the larger curved anode.....275

Scheme F.1 Schematic representation of the components of a fully assembled sensitized solar cell 290

Figure G.1 (A) Schematic of representative *J*-*V* curves of a photovoltaic device collected under dark and illuminated conditions with major device metrics and their origins shown, specifically, short-circuit current density (J_{SC}), open-circuit voltage (V_{OC}), theoretical power output (P_{theo}), maximum power output (P_{max}), current density at P_{max} (J_{max}), and voltage at P_{max} (V_{max}). Additionally, the equations for calculation of fill factor (FF) and efficiency (η), as well as the approximation of shunt (R_{SH}) and series (R_S) resistances, are also provided in the inset. Such photovoltaic devices can be modeled by simple equivalent circuits such as that shown in panel B 294

Figure G.2 The maximum power density output of a device can be determined by plotting the product of the current and voltage values *vs* the original voltage values. A near parabolic curve should be obtained where the apex of the curve equates to the maximum power output 297

Figure G.3 Critical information regarding charge transport properties can be inferred from the *J*-*V* response under dark conditions by plotting the dark current density on a log scale *vs* a specified voltage range 299

Figure G.4 Schematic representation of external quantum efficiency (EQE) for a device with a dye-sensitized semiconductor photoanode. EQE is a direct measure of how efficiently the device converts incident photons to electrons, and then current, at each wavelength. Ideally, the observed EQE peaks will correspond to the characteristic UV-vis absorption peaks of the photoactive sensitizer.....300

Figure G.5 Chronoamperometry provides vital information about device charge transport, namely, temporal stability of photocurrent, whether the photocurrent production is limited by diffusion, and, if so, what the diffusion coefficient of the electrolyte is. As the illumination is continually interrupted, a stable device will have the same current response during each illumination period; that is, a drop in photocurrent will not be observed over multiple dark/illuminated cycles. Conversely, if a decay in photocurrent is visible during each illumination period then the device's photocurrent production is limited by electrolyte diffusion. In this scenario, the photocurrent decay can be plotted *vs* time$^{-0.5}$ as shown in the outset plot and the apparent diffusion coefficient can be extracted from an appropriate fitting of the curve.....302

Figure G.6 Similar to chronoamperometry, chronopotentiometry can provide critical information regarding device stability and charge transport properties, specifically, the decay in the photovoltage can be used to determine the recombination lifetime of electrons within the electrolyte.....303

Figure G.7 (A) Schematic representation of a Nyquist plot obtained from the electrical impedance spectroscopic characterization of a dye-sensitized solar cell. The resulting Nyquist plot from such characterizations will typically consist of three semicircles which arise from: (i) the charge transfer resistance at the counter electrode (kHz region), (ii) the charge transfer resistance in the photoanode (Hz region), and (iii) the finite Warburg impedance (mHz region). The semicircles will be shifted to the right, or to higher resistance values, depending on the electrolyte and contact resistance. Plotting the same data in a Bode phase plot and extracting the peak frequency of the 2nd semicircle provides information about the electron lifetime within the semiconductor film. (B) The Nyquist

plot can also be modeled by a resistor and two RC circuits in series, with one RC circuit containing a finite-Warburg Impedance element, Z_W. R_S corresponds to the resistance of the electrolyte and the electric contacts while the two RC circuits (Q = capacitor, C, of variable capacitance) represent the charge transfer resistances at the counter electrode/electrolyte interface (R_{CTCE}) and the dye/semiconductor/electrolyte (photoanode) interface (R_{CTPA}) as well as the double layer capacitances at each interface (Q) 305

LIST OF TABLES

Table 2.1 Reference fluorophores used to determine quantum yield (Φ) values.....29

Table 4.1 Reference fluorophores used to determine quantum yield (Φ) values.....93

Table D.1 Photovoltaic metrics for all device sets in Chapter 5 and Appendix D.....265

Table E.1 Major components comprising the solar simulator system.....269

LIST OF COMMONLY USED ACRONYMS

APD: Carbon dot derived from urine collected during an asparagus-enriched diet

Arg: L-arginine

BMNP: Bimetallic nanoparticle

CA: Citric acid

CA–U: Citric acid-urea

CPD: Carbon dot derived from urine collected during a vitamin C-supplemented diet

CQD: Carbon quantum dot

DAPI: 4′,6-diamidino-2-phenylindole

EQE: External quantum efficiency

η: Power conversion efficiency

FCD: Fluorescent carbon dot

FF: Fill factor

FITC: Fluorescein isothiocyanate

GQD: Graphene quantum dot

GSH–F: Glutathione-formamide

J_{SC}: Short-circuit current density

MEF: Mouse embryonic fibroblast

MNP: Metal nanoparticle (typically monometallic)

MTT: 3-(4,5-dimethylthiazol-2-yl)-2,5-diphenyltetrazolium bromide

MWCO: Molecular weight cut-off

NP: Nanoparticle

PD: Pee dot (*i.e.*, carbon dot derived from urine)

PV: Photovoltaic

SPR: Surface plasmon resonance

SRB: Sulforhodamine B

TRITC: Tetramethylrhodamine

UPD: Carbon dot derived from unmodified urine

V_{OC}: Open-circuit voltage

AN EVALUATION OF THE NEED FOR CRITICALLY REFINED PURIFICATION PROCEDURES IN FLUORESCENT CARBON DOT SYNTHESES: THE RAMIFICATIONS OF THE UBIQUITOUS PRESENCE OF REACTION BY-PRODUCTS ON QUENCHOMETRIC AND LIGHT HARVESTING APPLICATIONS

Jeremy B. Essner

Professor Gary A. Baker, Dissertation Supervisor

ABSTRACT

Fluorescent carbon dots constitute a novel and intriguing class of nanocarbons that display unique optical properties and can be purportedly generated from virtually any carbon-containing source. For example, the thermal pyrolysis of human urine results in the formation of fluorescent nanocarbons, whose spectroscopic properties are dependent on the diet of the urine donor, a scenario potentially leading to heteroatom doping of the carbonaceous nanomaterials. Furthermore, these nanocarbons' alluring electron donor/acceptor capabilities afford their implementation as dual reducing and capping agents towards the formation of metal nanoparticle/carbon dot composites that possess a high degree of optical tunability. The ability to modulate the spectroscopic properties of both these materials holds promise for exploitation in solar energy harvesting applications as green sensitizers and plasmonic enhancers. However, these nanocarbons' distinguishing luminescent properties, whose origin continues to elude the field, has recently come under scrutiny due to the presence of highly fluorescent, molecular by-products generated in route to the target nanocarbon, resulting in the widespread misrepresentation of their emission characteristics. Thus, this detrimental issue of insufficient by-product removal and the subsequent effects on reported nanocarbon luminescence, as well as common applications, namely, quenchometric detection and photosensitizers, are addressed here, providing a

path forward for arriving at a fundamental understanding of these promising nanocarbons and their true properties.

Chapter 1: Introduction to Fluorescent Carbon Dots, their Synthesis and Applications, and the Vexing Purification Conundrum

Nanoscale carbons (*e.g.*, fullerenes, graphenes, carbon nanotubes, nanodiamonds) possess a range of highly attractive properties, including electrical conductivity, chemical inertness, high thermal stability, and tunability (*e.g.*, textural properties, doping), that have prompted intensive research into these carbonaceous nanomaterials in recent years. Within this family of nanoscale carbons, the recently established fluorescent carbon dot (FCD), often separated into subgroups such as graphene quantum dots (GQDs), carbon quantum dots (CQDs), and carbon nanodots (CNDs; Scheme 1.1A), and typically sized below 10 nm, displays unique and useful optical features generally not observed in its nanocarbon cousins,[1-19] such as tunable emission color, excellent photostability, and, most notably, excitation wavelength-dependent fluorescence (Scheme 1.1B). Furthermore, FCDs offer high aqueous solubility and an alluring eco-friendliness (*e.g.*, biocompatibility, low cytotoxicity) making them preferential nanomaterials over conventional semiconductor-based quantum dots, such as CdX (X = S, Se, Te).

Since the serendipitous discovery of FCDs over a decade ago during the purification of crude carbon nanotubes, researchers have increasingly reported alternate synthetic pathways for generating FCDs from myriad carbon sources. These various synthetic techniques for producing FCDs are broadly lumped into two camps: top-down and bottom-up. Top-down approaches, such as arc discharge,[7] laser ablation,[20-21] and electrochemical oxidation,[22-26] involve the cleavage of macroscale, relatively pure (typically, graphitic)

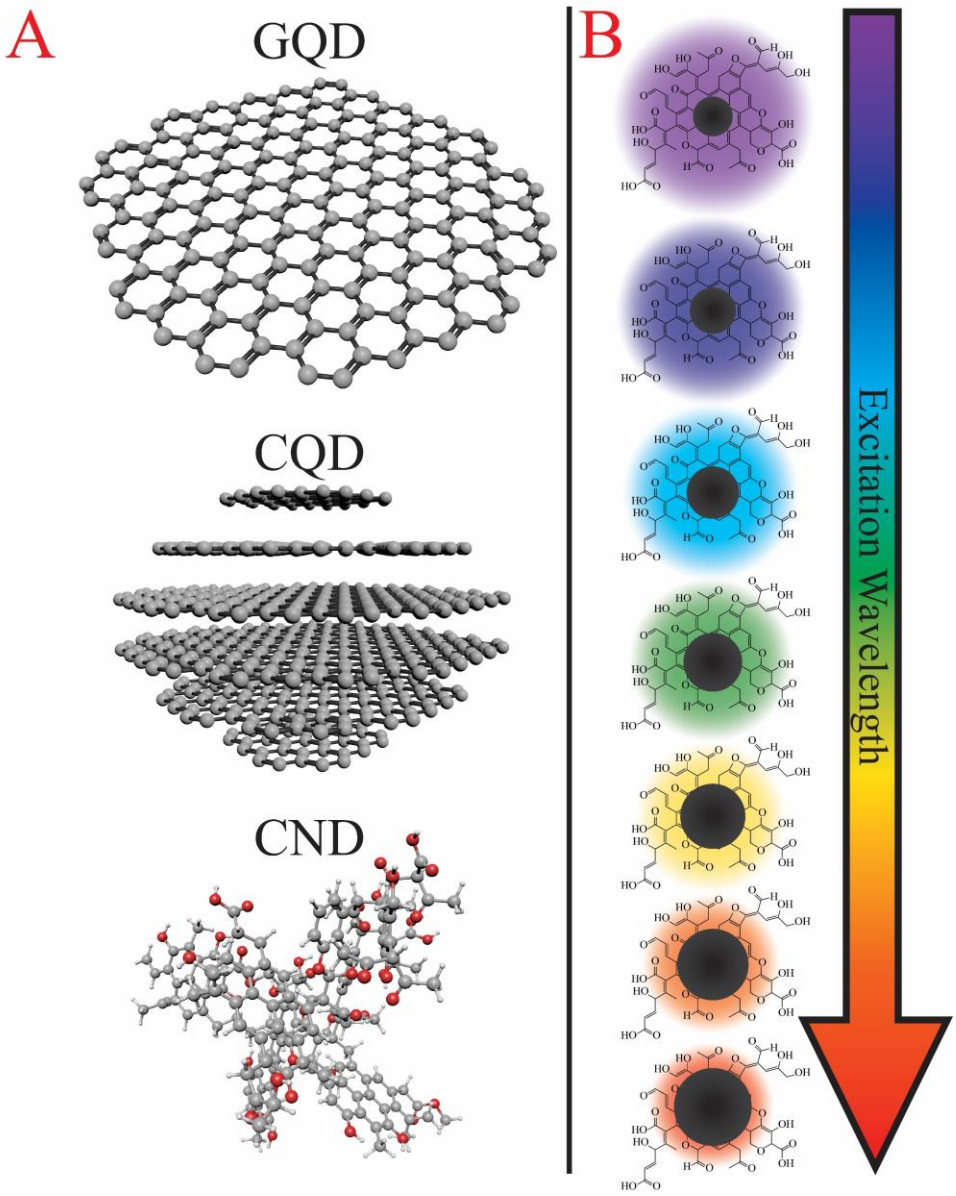

Scheme 1.1 (A) Representative structures of single-layer graphene quantum dots (GQDs), multi-layered carbon quantum dots (CQDs), and amorphous carbon nanodots (CNDs). Note, the CND structure is not meant to represent a specific molecule; its purpose is simply to convey a predominately amorphous structure of carbon atoms. (B) Representation of commonly observed fluorescent properties of these materials. Typically, as the size of the dot increases the emission wavelength redshifts, a phenomenon that can also occur via heteroatom doping and/or variation in surface functionality. Additionally, these dots frequently display excitation wavelength-dependent emission (*i.e.*, a red-edge effect) that is accompanied with a concomitant decrease in intensity. Schematic used with permission from reference 51.

carbon fragments into smaller and smaller particles, eventually resulting in few to multilayer, crystalline FCDs. Conversely, bottom-up methods comprise chemical or mechanical assembly of the FCDs, in an essentially atom-by-atom or molecule-by-molecule fashion, from carbon-containing molecular precursors, an approach that overwhelmingly yields FCDs that are highly amorphous in nature. Examples of these tactics include combustion or thermal treatment,[27] and templated,[28] microwave-assisted,[12] or hydrothermal growth.[29] Thus, the literature suggests that FCDs can be produced through an appropriate treatment of virtually any carbon-containing precursor such as citrates[12, 27, 30-34] and saccharides (*e.g.*, glucose, chitosan).[35-41] Unfortunately, despite the "green" nature of FCDs, many of these synthetic protocols employed unsustainable precursors, organic solvents, harsh acidic/alkaline conditions, high synthetic temperatures, or extensive pre- or posttreatments. Therefore, with environmental sustainability concerns ever increasing, a shift toward developing greener pathways for FCD synthesis occurred, where more benign carbon sources and synthetic methods that did not necessitate subsequent functionalization steps were explored. For instance, greener carbonization strategies such as the microwave, thermal, or hydrothermal treatment of various sustainable precursors (*e.g.*, citric acid,[11-12] urea[12]) or even low-value waste materials (*e.g.*, grass,[13] fruit peels,[14-17] coffee grounds,[42] biomass[13, 43-45]) have been aggressively pursued. Additionally, the carbonization of human hair[46-48] and even human urine[49] or animal feces[50] have been reported to result in the formation of FCDs.

In addition to FCDs' putative fluorescent properties and the growing library of inexpensive, facile preparation protocols reported, these material's ability to function as electron donors or acceptors coupled with their ease of (bio)conjugation, account for their

increasing interest as candidates in a number of applications ranging from fluorescence sensing to bioimaging[1-4]. Of these numerous applications, the exploitation of FCDs' properties in various photovoltaic (PV) solar cell architectures is of particular interest since their inexpensive synthesis and greener nature makes them promising additives within, or even full replacements to the often scare, costly, and toxic materials found in, state-of-the-art PV devices.[4-6, 51] In the last few decades, one of the most widely explored PV architectures is the dye-sensitized solar cell (DSSC), which was pioneered by Michael Grätzel in 1991 and has been rightfully dubbed the Grätzel cell.[52] The heart of these photoelectrochemical cells is the photoanode, which consists of a metal oxide film, typically a mesoporous network of interconnecting TiO_2 nanoparticles, that is deposited on a glass substrate precoated with a transparent conductive oxide (*e.g.*, fluorine-doped tin oxide or FTO) and then sensitized with a chromophore, such as the industry standard, Ru-centered organometallic dye (N719), a unique design in which light absorption and charge separation processes occur within different device constituents, contrary to conventional solid-state devices based on a PN junction. Fabrication of a complete cell is then accomplished by sandwiching a redox-active electrolyte (*e.g.*, I^-/I_3^- in acetonitrile) between the photoanode and a cathode, or counter electrode, that is typically a thin Pt film also deposited on an FTO-coated glass substrate. A schematic of the generic device architecture, albeit with FCD sensitizers, is shown in Scheme 1.2. The detailed operation of these devices is provided in Appendix F but, briefly, assuming appropriate energy alignments between the individual components, the sensitizer absorbs incident radiation, promoting an electron from the highest occupied molecular orbital (HOMO) or valence band (VB) to the lowest unoccupied molecular orbital (LUMO) or conduction band (CB). The excited-state

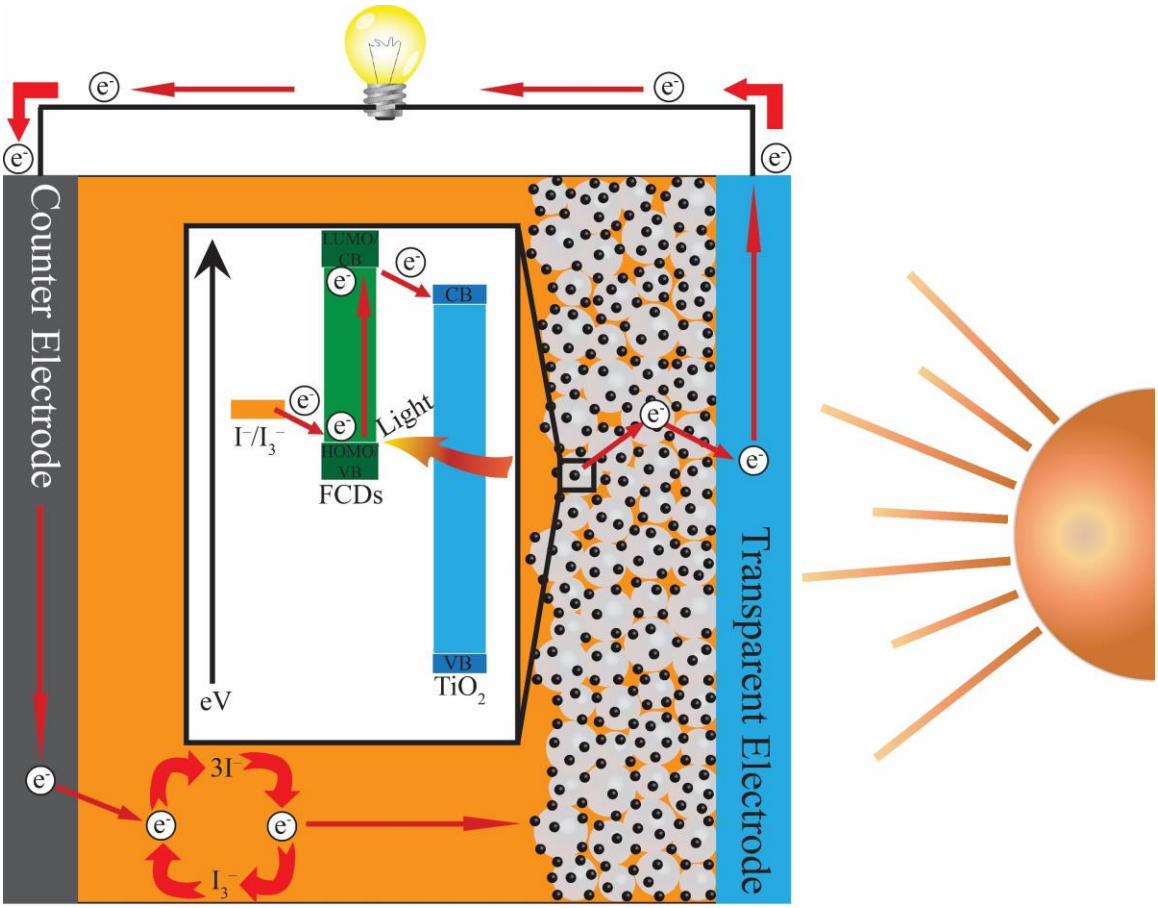

Scheme 1.2 Schematical representation of a solar cell based on a mesoscopic, metal oxide film (*e.g.*, TiO_2) sensitized with FCDs showing the fundamental photovoltaic operation under illuminated conditions. The inset arbitrarily shows the appropriate band alignments in these devices.

electron is then injected into the semiconductor's CB and percolates through the film to the FTO layer, from which it leaves the device to do external work before returning through the counter electrode to reduce the electrolyte's redox couple, the component that sustains the entire process by shuttling charge carriers back and forth between the electrodes.

While state-of-the-art Grätzel cells have been reported to yield a power conversion efficiency, or simply efficiency (η), over 12%, this promising performance is obtained using costly organometallic dyes such as N719, that rely on rapid metal-to-ligand charge transfers from the Ru center, an element of particularly low terrestrial abundance.

Therefore, there is increasing interest in replacing these high-performing but unsustainable dyes with low-cost sensitizers derived from abundant sources such as Zn-centered porphyrins or metal-free dyes.[53] In addition to these desirable attributes, ideal replacement sensitizers need to possess intense, broadband optical absorption, conjugated chemical bonds to allow electrical conductivity between the absorption center and metal oxide scaffold, and appropriate surface functionality (typically carboxylic acid moieties) to afford strong covalent attachment (*i.e.*, chemisorption) and electrical continuity to the metal oxide. FCDs, which often have high absorption cross sections, graphitic islands/cores (*i.e.*, inherent conjugation), and chemisorption-capable functionalities, represent a promising alternative to conventional sensitizers, however, devices employing these nanocarbon sensitizers have yet to crest an η of approximately 0.5% since these material's strongest absorption is typically limited to wavelengths below 400 nm leading to insufficient light absorption in the visible region, a regime that constitutes about 43% of incident solar radiation.

One potential avenue to overcome these optical hurdles and increase device efficiency is to introduce heteroatoms (*e.g.*, O, N, S, Si, B, P) into the FCD core or functional periphery, a doping strategy that has been demonstrated to bathochromically shift (*i.e.*, redshift) both the observed absorption and luminescent properties.[54-57] Despite the promising effects on optical properties, these doped nanocarbon sensitizers have yet to produce an η beyond 1%.[51, 58-61] An alternate approach to improving performance is to incorporate (noble) metal nanoparticles (MNPs) in the photoanode architecture since the intrinsic optical properties of these materials (*i.e.*, localized surface plasmon resonance or LSPR) allow them to function as light-concentrating antennae or light-scattering centers,

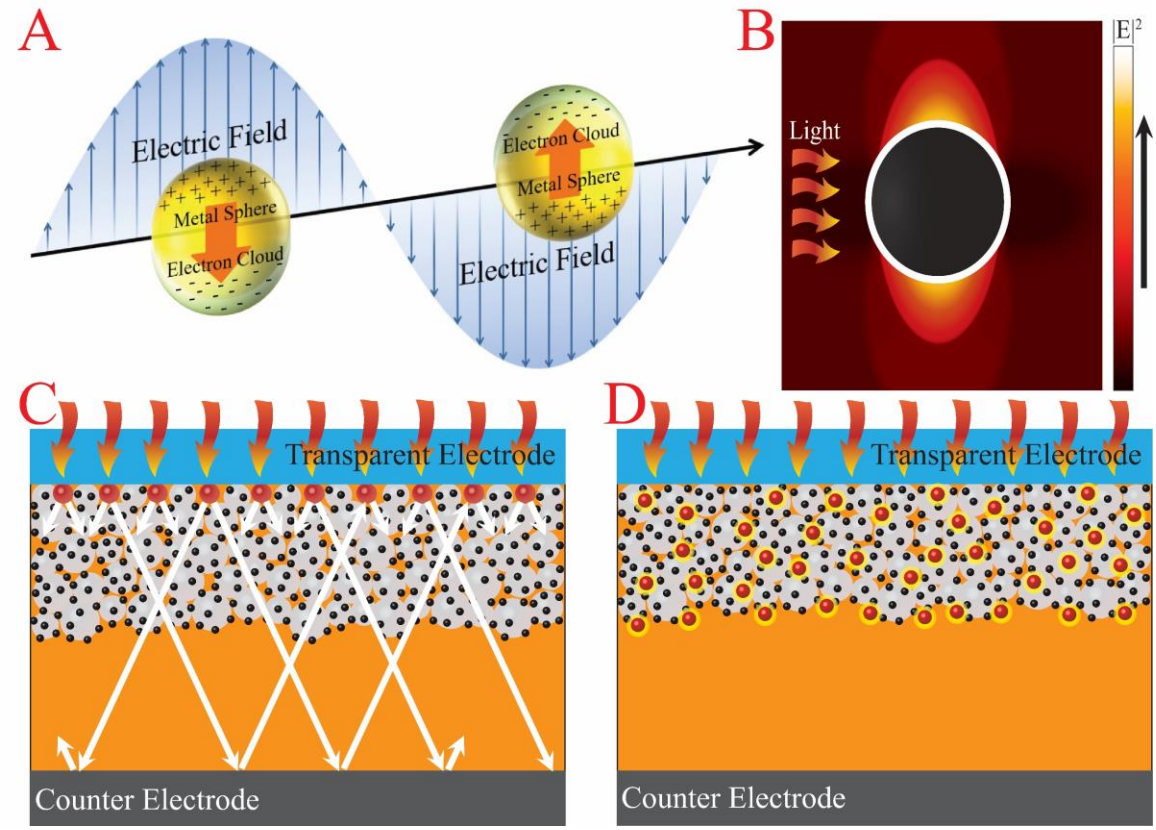

Scheme 1.3 (A) The origin of localized surface plasmon resonances: if particles are substantially smaller than the incident wavelength of light, they experience a relatively uniform electric field as the wave passes through them resulting in a collective oscillation of electrons. This electron resonance leads to drastically enhanced electric fields in the immediate area around the particle, as shown in panel B. Nanoparticle plasmon resonances can be exploited in various device architectures to enhance photon harvesting and device performance: (C) larger particles can act as light scattering centers at an interface while (D) smaller particles can act as light concentrators embedded within a film. Schematics adapted with permission from references 62 and 63. Copyright © 2003 American Chemical Society and 2010 Nature Publishing Group.

scenarios that positively augment photon absorption by the photoanode (Scheme 1.3).[62-63] Towards this auspicious efficiency enhancing strategy, FCDs have recently shown promise as dual reducing and stabilizing agents in the formation of Au and Ag MNPs,[35, 38-39, 64-71] owing to their intrinsic ability to act as electron donors/acceptors.[72] Additionally,

heteroatom-doped FCDs have shown similar functionalities in the growth of MNPs,[73] thus, the implementation of these doped-FCD/MNP composites as photoactive sensitizers may lead to substantial enhancements in device performance, however, such tactics have seen little exploration to date. Therefore, much work is still required to thoroughly understand the fundamental intricacies of these carbonaceous nanomaterials and their subsequent applications.

Due to the facile preparation and promising characteristics of FCDs, research on these materials has exploded in the last few years, although the majority of these works simply focused on altering the carbon source or synthetic protocol. Thus, knowledge of the particle growth mechanisms and their exact chemical structure, how this final composition influences their observed properties, and the effects these properties induce on application-based studies are all still severely lacking. Furthermore, the unbridled enthusiasm and extremely rapid pace of research has naturally led to numerous uncritical, uncorroborated, and detrimental claims and misconceptions entering the publication record, a very real barrier preventing maturation of the field, especially given the fact that the purification of FCDs is frequently inadequate, unsubstantiated, or missing altogether. Several researchers have already alluded to the fact that, in order to elucidate the true origin of FCD fluorescence, efficient separation procedures to reduce sample complexity are urgently needed.[74-77] Exacerbating the issue is the mounting evidence that the fluorescence associated with FCDs originates significantly from molecular/oligomeric by-products, such as 2-pyridone derivatives,[78] that are generated alongside the nanoscale carbons,[32, 78-83] where the properties of aggregated molecular by-products resemble the reported properties of FCDs,[84-86] making a unified purification approach all the more pressing.

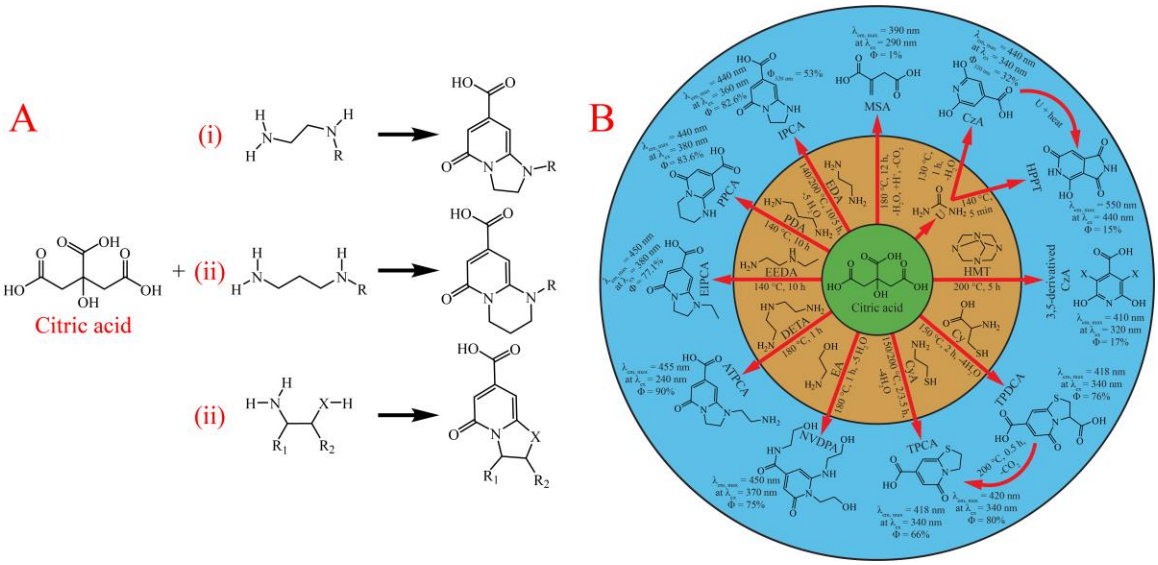

Scheme 1.4 (A) Generalized formation of potential molecular fluorophores in citric acid-based FCD syntheses first proposed by Yang and coworkers,[91] in which the pyrolyzation of citric acid (CA) in the presence of common (di)amine-containing heteroatom dopants, such as (i) ethane diamines, (ii) propane diamines, or (iii) monoamines containing hydroxyl or thiol groups, yields the corresponding 2-pyridone-derived by-products. (B) Indeed, several fluorescent molecular by-products originating from the carbonization of CA-based precursor systems, which typically possess a 2-pyridone backbone, have been identified. Schematics adapted with permission from references 87 and 91. Copyright © 2015 Royal Society of Chemistry and 2018 Elsevier.

Indeed, as shown in Scheme 1.4 above, a handful of fluorescent, molecular species,[87] such as methylenesuccinic acid (MSA),[84] citrazinic acid (CzA),[88] 4-hydroxy-1*H*-pyrrolo[3,4-*c*] pyridine-1,3,6(2*H*,5*H*)-trione (HPPT),[89] N-(2-hydroxyethyl)-2-oxo-1-vinyl-6-(vinyl-amino)-1,2-dihydropyridine-4-carboxamide (NVDPA),[90] 5-oxo-1,2,3,5-tetrahydro-imidazo[1,2-*a*]pyridine-7-carboxylic acid (IPCA),[88, 91] 1-(2-aminoethyl)-5-oxo-1,2,3,5-tetrahydroimidazo[1,2-a]pyridine-7-carboxylic acid (ATPCA),[92] 5-oxo-3,5-dihydro-2*H*-thiazolo[3,2-*a*]pyridine-7-carboxylic acid (TPCA),[93-94] and 5-oxo-3,5-dihydro-2*H*-thiazolo[3,2-*a*]pyridine-3,7-dicarboxylic acid (TPDCA)[84, 93] have been identified for the thermal degradation of citric acid (CA)[84] and CA reacted with N or S dopants such as urea

(U),[88-89] ethanolamine (EA),[90] ethylenediamine (EDA),[88, 91] diethylenetriamine (DETA),[92] cysteine (Cy),[84, 93] or cysteamine (Cya),[93-94] respectively. Additionally, non-FCD studies have generated these exact (or structurally related) molecular fluorophores through the reaction of CA with similar N- or S-containing precursors.[95-99] Furthermore, Chang and co-workers recently demonstrated that FCD samples require ~120 h of purification via membrane dialysis, even when refreshing the exchange solvent multiple times per day, to fully remove these small molecular by-products,[100] a duration and routine rarely reported in the literature. Despite mounting evidence, the improper and insufficient purification of FCD samples remains unsettlingly common, necessitating a reassessment and unification of employed purification practices.

Furthermore, FCDs are often haphazardly classified or given invented names or acronyms to give the false impression that a novel material has been introduced. Indeed, nearly a dozen names have emerged in the literature to designate these fluorescent nanocarbons, such as GQDs, CQDs, CNDs, carbon dots, C-dots, carbogenic dots, carbon nanoclusters, polymer dots, nitrogen-rich quantum dots, and graphitic carbon nitride dots, although several of these titles can be consolidated into a few subclasses. Specifically, it has been proposed that only three categories (*i.e.*, GQDs, CQDs, CNDs) are sufficient to categorize all FCDs, where the segregation is based on the chemical, physical, and photophysical properties specific to each subclass. For the purposes of this dissertation, all nanocarbons studied within these works will simply be referred to as fluorescent carbon dots (FCDs), although materials derived from graphitic sources are often designated as GQDs.

Herein, Chapter 2 details the green synthesis of FCDs through the upcycling of human urine, where a diet fortified with vitamin C or asparagus resulted in changes to the observed photophysical properties, potentially due to heteroatom doping of the resultant FCDs, while Chapter 3 describes the fabrication of plasmonic bimetallic NP/FCD composites using CA-derived FCDs as dual reducing and stabilizing agents. The original intention was to employ the urine-derived FCDs and MNP/FCD composites as sensitizers in PV applications to investigate potential enhancements in performance metrics for reasons mentioned above, however, in route to achieving these goals, the observation that highly fluorescent by-products were produced during FCD syntheses, in combination with emerging literature arriving at similar conclusions, altered the pathway of these works. Specifically, these observations led to the exploration of the resulting photophysical properties of carefully separated (via membrane dialysis) FCD fractions, samples that were generated by following previously reported, representative FCD synthetic protocols, as detailed in Chapter 4. The results disseminated in this work unequivocally demonstrate the dire need for an adequate, unified purification protocol to arrive at meaningful, error-free results, especially regarding luminescent characterizations of FCDs. Given the insufficient purification practices plaguing the field, particularly in PV applications of FCDs, Chapter 5 describes the effects that careful fractionation of FCD samples had on the PV performance of devices containing photoanodes sensitized with the various FCD fractions. The results of these studies indicated that reaction by-products can contribute substantially to or negatively impact the photovoltaic action observed in FCD-sensitized devices, corroborating the conclusions in Chapter 4, and providing additional, undisputable

evidence that standardized purification procedures need to be implemented immediately alongside the execution of remedial studies to evaluate the validity of previous claims.

References

1. Baker, S. N.; Baker, G. A., Luminescent Carbon Nanodots: Emergent Nanolights. *Angew. Chem. Int. Ed.* **2010**, *49*, 6726–6744.

2. Ding, C.; Zhu, A.; Tian, Y., Functional Surface Engineering of C-dots for Fluorescent Biosensing and In Vivo Bioimaging. *Acc. Chem. Res.* **2013**, *47*, 20–30.

3. Li, H.; Kang, Z.; Liu, Y.; Lee, S.-T., Carbon Nanodots: Synthesis, Properties and Applications. *J. Mater. Chem.* **2012**, *22*, 24230–24253.

4. Shen, J.; Zhu, Y.; Yang, X.; Li, C., Graphene Quantum Dots: Emergent Nanolights for Bioimaging, Sensors, Catalysis and Photovoltaic Devices. *Chem. Commun.* **2012**, *48*, 3686–3699.

5. Wang, J.; Xin, X.; Lin, Z., Cu_2ZnSnS_4 Nanocrystals and Graphene Quantum Dots for Photovoltaics. *Nanoscale* **2011**, *3*, 3040–3048.

6. Zhang, Z.; Zhang, J.; Chen, N.; Qu, L., Graphene Quantum Dots: An Emerging Material for Energy-related Applications and Beyond. *Energy Environ. Sci.* **2012**, *5*, 8869–8890.

7. Xu, X.; Ray, R.; Gu, Y.; Ploehn, H. J.; Gearheart, L.; Raker, K.; Scrivens, W. A., Electrophoretic Analysis and Purification of Fluorescent Single-walled Carbon Nanotube Fragments. *J. Am. Chem. Soc.* **2004**, *126*, 12736–12737.

8. Hu, S.; Liu, J.; Yang, J.; Wang, Y.; Cao, S., Laser Synthesis and Size Tailor of Carbon Quantum Dots. *J. Nanopart. Res.* **2011**, *13*, 7247–7252.

9. Liu, H.; Ye, T.; Mao, C., Fluorescent Carbon Nanoparticles Derived from Candle Soot. *Angew. Chem. Int. Ed.* **2007**, *46*, 6473–6475.

10. Tian, L.; Ghosh, D.; Chen, W.; Pradhan, S.; Chang, X.; Chen, S., Nanosized Carbon Particles from Natural Gas Soot. *Chem. Mater.* **2009**, *21*, 2803–2809.

11. Dong, Y.; Shao, J.; Chen, C.; Li, H.; Wang, R.; Chi, Y.; Lin, X.; Chen, G., Blue Luminescent Graphene Quantum Dots and Graphene Oxide Prepared by Tuning the Carbonization Degree of Citric Acid. *Carbon* **2012**, *50*, 4738–4743.

12. Qu, S.; Wang, X.; Lu, Q.; Liu, X.; Wang, L., A Biocompatible Fluorescent Ink based on Water-soluble Luminescent Carbon Nanodots. *Angew. Chem. Int. Ed.* **2012**, *51*, 12215–12218.

13. Liu, S.; Tian, J.; Wang, L.; Zhang, Y.; Qin, X.; Luo, Y.; Asiri, A. M.; Al-Youbi, A. O.; Sun, X., Hydrothermal Treatment of Grass: A Low-cost, Green Route to Nitrogen-doped, Carbon-rich, Photoluminescent Polymer Nanodots as an Effective Fluorescent Sensing Platform for Label-Free Detection of Cu(II) Ions. *Adv. Mater.* **2012**, *24*, 2037–2041.

14. Lu, W.; Qin, X.; Liu, S.; Chang, G.; Zhang, Y.; Luo, Y.; Asiri, A. M.; Al-Youbi, A. O.; Sun, X., Economical, Green Synthesis of Fluorescent Carbon Nanoparticles and their use as Probes for Sensitive and Selective Detection of Mercury(II) Ions. *Anal. Chem.* **2012**, *84*, 5351–5357.

15. Zhou, J.; Sheng, Z.; Han, H.; Zou, M.; Li, C., Facile Synthesis of Fluorescent Carbon Dots using Watermelon Peel as a Carbon Source. *Mater. Lett.* **2012**, *66*, 222–224.

16. Vikneswaran, R.; Ramesh, S.; Yahya, R., Green Synthesized Carbon Nanodots as a Fluorescent Probe for Selective and Sensitive Detection of Iron(III) Ions. *Mater. Lett.* **2014**, *136*, 179–182.

17. Prasannan, A.; Imae, T., One-pot Synthesis of Fluorescent Carbon Dots from Orange Waste Peels. *Ind. Eng. Chem. Res.* **2013**, *52*, 15673–15678.

18. Li, L.; Wu, G.; Yang, G.; Peng, J.; Zhao, J.; Zhu, J.-J., Focusing on Luminescent Graphene Quantum Dots: Current Status and Future Perspectives. *Nanoscale* **2013**, *5*, 4015–4039.

19. Zheng, X. T.; Ananthanarayanan, A.; Luo, K. Q.; Chen, P., Glowing Graphene Quantum Dots and Carbon Dots: Properties, Syntheses, and Biological Applications. *Small* **2015**, *11*, 1620–1636.

20. Hu, S.-L.; Niu, K.-Y.; Sun, J.; Yang, J.; Zhao, N.-Q.; Du, X.-W., One-step Synthesis of Fluorescent Carbon Nanoparticles by Laser Irradiation. *J. Mater. Chem.* **2009**, *19*, 484–488.

21. Sun, Y.-P.; Zhou, B.; Lin, Y.; Wang, W.; Fernando, K. A. S.; Pathak, P.; Meziani, M. J.; Harruff, B. A.; Wang, X.; Wang, H.; Luo, P. G.; Yang, H.; Kose, M. E.; Chen, B.; Veca, L. M.; Xie, S.-Y., Quantum-sized Carbon Dots for Bright and Colorful Photoluminescence. *J. Am. Chem. Soc.* **2006**, *128*, 7756–7757.

22. Li, H.; He, X.; Kang, Z.; Huang, H.; Liu, Y.; Liu, J.; Lian, S.; Tsang, C. H. A.; Yang, X.; Lee, S.-T., Water-soluble Fluorescent Carbon Quantum Dots and Photocatalyst Design. *Angew. Chem. Int. Ed.* **2010**, *49*, 4430–4434.

23. Ming, H.; Ma, Z.; Liu, Y.; Pan, K.; Yu, H.; Wang, F.; Kang, Z., Large Scale Electrochemical Synthesis of High Quality Carbon Nanodots and their Photocatalytic Property. *Dalton Trans.* **2012**, *41*, 9526–9531.

24. Zhao, Q.-L.; Zhang, Z.-L.; Huang, B.-H.; Peng, J.; Zhang, M.; Pang, D.-W., Facile Preparation of Low Cytotoxicity Fluorescent Carbon Nanocrystals by Electrooxidation of Graphite. *Chem. Commun.* **2008**, 5116–5118.

25. Zheng, L.; Chi, Y.; Dong, Y.; Lin, J.; Wang, B., Electrochemiluminescence of Water-soluble Carbon Nanocrystals Released Electrochemically from Graphite. *J. Am. Chem. Soc.* **2009**, *131*, 4564–4565.

26. Zhou, J.; Booker, C.; Li, R.; Zhou, X.; Sham, T.-K.; Sun, X.; Ding, Z., An Electrochemical Avenue to Blue Luminescent Nanocrystals from Multiwalled Carbon Nanotubes (MWCNTs). *J. Am. Chem. Soc.* **2007**, *129*, 744–745.

27. Bourlinos, A. B.; Stassinopoulos, A.; Anglos, D.; Zboril, R.; Georgakilas, V.; Giannelis, E. P., Photoluminescent Carbogenic Dots. *Chem. Mater.* **2008**, *20*, 4539–4541.

28. Yang, Y.; Wu, D.; Han, S.; Hu, P.; Liu, R., Bottom-up Fabrication of Photoluminescent Carbon Dots with Uniform Morphology via a Soft-hard Template Approach. *Chem. Commun.* **2013**, *49*, 4920–4922.

29. Shi, Q.-Q.; Li, Y.-H.; Xu, Y.; Wang, Y.; Yin, X.-B.; He, X.-W.; Zhang, Y.-K., High-yield and High-solubility Nitrogen-doped Carbon Dots: Formation, Fluorescence Mechanism and Imaging Application. *RSC Adv.* **2014**, *4*, 1563–1566.

30. Essner, J. B.; Laber, C. H.; Baker, G. A., Carbon Dot Reduced Bimetallic Nanoparticles: Size and Surface Plasmon Resonance Tunability for Enhanced Catalytic Applications. *J. Mater. Chem. A* **2015**, *3*, 16354–16360.

31. Bourlinos, A. B.; Stassinopoulos, A.; Anglos, D.; Zboril, R.; Karakassides, M.; Giannelis, E. P., Surface Functionalized Carbogenic Quantum Dots. *Small* **2008**, *4*, 455–458.

32. Krysmann, M. J.; Kelarakis, A.; Dallas, P.; Giannelis, E. P., Formation Mechanism of Carbogenic Nanoparticles with Dual Photoluminescence Emission. *J. Am. Chem. Soc.* **2011**, *134*, 747–750.

33. Wang, L.; Zhu, S.-J.; Wang, H.-Y.; Qu, S.-N.; Zhang, Y.-L.; Zhang, J.-H.; Chen, Q.-D.; Xu, H.-L.; Han, W.; Yang, B.; Sun, H.-B., Common Origin of Green Luminescence in Carbon Nanodots and Graphene Quantum Dots. *ACS Nano* **2014**, *8*, 2541–2547.

34. Laber, C. H.; Essner, J. B.; Scott, T. A.; Polo-Parada, L.; Baker, G. A., Domestic Pressure Cooker as Inexpensive Hydrothermal Vessel: Demonstrated Utility for Eco-friendly Synthesis of Non-toxic Carbon Dots. *Nano-Struct. Nano-Objects* **2016**, *6*, 52–58.

35. Choi, Y.; Ryu, G. H.; Min, S. H.; Lee, B. R.; Song, M. H.; Lee, Z.; Kim, B.-S., Interface-controlled Synthesis of Heterodimeric Silver–Carbon Nanoparticles Derived from Polysaccharides. *ACS Nano* **2014**, *8*, 11377–11385.

36. Yang, Y.; Cui, J.; Zheng, M.; Hu, C.; Tan, S.; Xiao, Y.; Yang, Q.; Liu, Y., One-step Synthesis of Amino-functionalized Fluorescent Carbon Nanoparticles by Hydrothermal Carbonization of Chitosan. *Chem. Commun.* **2012**, *48*, 380–382.

37. Chowdhury, D.; Gogoi, N.; Majumdar, G., Fluorescent Carbon Dots Obtained from Chitosan Gel. *RSC Adv.* **2012**, *2*, 12156–12159.

38. Shen, L.-M.; Chen, M.-L.; Hu, L.-L.; Chen, X.-W.; Wang, J.-H., Growth and Stabilization of Silver Nanoparticles on Carbon Dots and Sensing Application. *Langmuir* **2013**, *29*, 16135–16140.

39. Shen, L.-M.; Chen, Q.; Sun, Z.-Y.; Chen, X.-W.; Wang, J.-H., Assay of Biothiols by Regulating the Growth of Silver Nanoparticles with C-dots as Reducing Agent. *Anal. Chem.* **2014**, *86*, 5002–5008.

40. Yang, Z.-C.; Wang, M.; Yong, A. M.; Wong, S. Y.; Zhang, X.-H.; Tan, H.; Chang, A. Y.; Li, X.; Wang, J., Intrinsically Fluorescent Carbon Dots with Tunable Emission Derived from Hydrothermal Treatment of Glucose in the Presence of Monopotassium Phosphate. *Chem. Commun.* **2011**, *47*, 11615–11617.

41. Tang, L.; Ji, R.; Cao, X.; Lin, J.; Jiang, H.; Li, X.; Teng, K. S.; Luk, C. M.; Zeng, S.; Hao, J.; Lau, S. P., Deep Ultraviolet Photoluminescence of Water-soluble Self-passivated Graphene Quantum Dots. *ACS Nano* **2012**, *6*, 5102–5110.

42. Hsu, P.-C.; Shih, Z.-Y.; Lee, C.-H.; Chang, H.-T., Synthesis and Analytical Applications of Photoluminescent Carbon Nanodots. *Green Chem.* **2012**, *14*, 917–920.

43. Krysmann, M. J.; Kelarakis, A.; Giannelis, E. P., Photoluminescent Carbogenic Nanoparticles Directly Derived from Crude Biomass. *Green Chem.* **2012**, *14*, 3141–3145.

44. Briscoe, J.; Marinovic, A.; Sevilla, M.; Dunn, S.; Titirici, M., Biomass-derived Carbon Quantum Dot Sensitizers for Solid-state Nanostructured Solar Cells. *Angew. Chem. Int. Ed.* **2015**, *54*, 4463–4468.

45. Qin, X.; Lu, W.; Asiri, A. M.; Al-Youbi, A. O.; Sun, X., Green, Low-cost Synthesis of Photoluminescent Carbon Dots by Hydrothermal Treatment of Willow Bark and their Application as an Effective Photocatalyst for Fabricating Au Nanoparticles-reduced Graphene Oxide Nanocomposites for Glucose Detection. *Catal. Sci. Techol.* **2013**, *3*, 1027–1035.

46. Sun, D.; Ban, R.; Zhang, P.-H.; Wu, G.-H.; Zhang, J.-R.; Zhu, J.-J., Hair Fiber as a Precursor for Synthesizing of Sulfur- and Nitrogen-co-doped Carbon Dots with Tunable Luminescence Properties. *Carbon* **2013**, *64*, 424–434.

47. Wang, J.; Peng, F.; Lu, Y.; Zhong, Y.; Wang, S.; Xu, M.; Ji, X.; Su, Y.; Liao, L.; He, Y., Large-scale Green Synthesis of Fluorescent Carbon Nanodots and their use in Optics Applications. *Adv. Opt. Mater.* **2015**, *3*, 103–111.

48. Liu, S.-S.; Wang, C.-F.; Li, C.-X.; Wang, J.; Mao, L.-H.; Chen, S., Hair-derived Carbon Dots Toward Versatile Multidimensional Fluorescent Materials. *J. Mater. Chem. C* **2014**, *2*, 6477–6483.

49. Essner, J. B.; Laber, C. H.; Ravula, S.; Polo-Parada, L.; Baker, G. A., Pee-dots: Biocompatible Fluorescent Carbon Dots Derived from the Upcycling of Urine. *Green Chem.* **2016**, *18*, 243–250.

50. D'Angelis do E. S. Barbosa, C.; Corrêa, J. R.; Medeiros, G. A.; Barreto, G.; Magalhães, K. G.; de Oliveira, A. L.; Spencer, J.; Rodrigues, M. O.; Neto, B. A. D., Carbon Dots (C-dots) from Cow Manure with Impressive Subcellular Selectivity Tuned by Simple Chemical Modification. *Chem. Eur. J.* **2015**, *21*, 5055–5060.

51. Essner, J. B.; Baker, G. A., The Emerging Roles of Carbon Dots in Solar Photovoltaics: A Critical Review. *Environ. Sci.: Nano* **2017**, *4*, 1216–1263.

52. Oregan, B.; Grätzel, M., A Low-cost, High-efficiency Solar-cell based on Dye-sensitized Colloidal TiO_2 Films. *Nature* **1991**, *353*, 737–740.

53. Shalini, S.; Balasundaraprabhu, R.; Kumar, T. S.; Prabavathy, N.; Senthilarasu, S.; Prasanna, S., Status and Outlook of Sensitizers/Dyes used in Dye Sensitized Solar Cells (DSSC): A Review. *Int. J. Energy Res.* **2016**, *40*, 1303–1320.

54. Barman, M. K.; Patra, A., Current Status and Prospects on Chemical Structure Driven Photoluminescence Behaviour of Carbon Dots. *J. Photochem. Photobio. C* **2018**, *37*, 1–22.

55. Chen, B. B.; Liu, M. L.; Li, C. M.; Huang, C. Z., Fluorescent Carbon Dots Functionalization. *Adv. Colloid Interface Sci.* **2019**, *270*, 165–190.

56. Yan, F.; Sun, Z.; Zhang, H.; Sun, X.; Jiang, Y.; Bai, Z., The Fluorescence Mechanism of Carbon Dots, and Methods for Tuning their Emission Color: A Review. *Microchim. Acta* **2019**, *186*, 583.

57. Zhao, Q.; Song, W.; Zhao, B.; Yang, B., Spectroscopic Studies of the Optical Properties of Carbon Dots: Recent Advances and Future Prospects. *Mater. Chem. Front.* **2020**, *4*, 472–488.

58. Carolan, D.; Rocks, C.; Padmanaban, D. B.; Maguire, P.; Svrcek, V.; Mariotti, D., Environmentally Friendly Nitrogen-doped Carbon Quantum Dots for Next Generation Solar Cells. *Sustain. Energy Fuels* **2017**, *1*, 1611–1619.

59. Marinovic, A.; Kiat, L. S.; Dunn, S.; Titirici, M.-M.; Briscoe, J., Carbon-nanodot Solar Cells from Renewable Precursors. *ChemSusChem* **2017**, *10*, 1004–1013.

60. Wang, H.; Sun, P.; Cong, S.; Wu, J.; Gao, L.; Wang, Y.; Dai, X.; Yi, Q.; Zou, G., Nitrogen-doped Carbon Dots for "Green" Quantum Dot Solar Cells. *Nanoscale Res. Lett.* **2016**, *11*, 27.

61. Zhang, Q.; Zhang, G.; Sun, X.; Yin, K.; Li, H., Improving the Power Conversion Efficiency of Carbon Quantum Dot-sensitized Solar Cells by Growing the Dots on a TiO_2 Photoanode In Situ. *Nanomaterials* **2017**, *7*, 130.

62. Atwater, H. A.; Polman, A., Plasmonics for Improved Photovoltaic Devices. *Nat. Mater.* **2010**, *9*, 205–213.

63. Kelly, K. L.; Coronado, E.; Zhao, L. L.; Schatz, G. C., The Optical Properties of Metal Nanoparticles: The Influence of Size, Shape, and Dielectric Environment. *J. Phys. Chem. B* **2003**, *107*, 668–677.

64. Wang, X.; Long, Y.; Wang, Q.; Zhang, H.; Huang, X.; Zhu, R.; Teng, P.; Liang, L.; Zheng, H., Reduced State Carbon Dots as both Reductant and Stabilizer for the Synthesis of Gold Nanoparticles. *Carbon* **2013**, *64*, 499–506.

65. Mandani, S.; Sharma, B.; Dey, D.; Sarma, T. K., Carbon Nanodots as Ligand Exchange Probes in Au@C-dot Nanobeacons for Fluorescent Turn-on Detection of Biothiols. *Nanoscale* **2015**, *7*, 1802–1808.

66. Liu, S.; Yu, B.; Zhang, T., Nitrogen-doped Carbon Nanodots as a Reducing Agent to Synthesize Ag Nanoparticles for Non-enzymatic Hydrogen Peroxide Detection. *RSC Adv.* **2014**, *4*, 544–548.

67. Choi, H.; Ko, S.-J.; Choi, Y.; Joo, P.; Kim, T.; Lee, B. R.; Jung, J.-W.; Choi, H. J.; Cha, M.; Jeong, J.-R.; Hwang, I.-W.; Song, M. H.; Kim, B.-S.; Kim, J. Y., Versatile Surface Plasmon Resonance of Carbon-dot-supported Silver Nanoparticles in Polymer Optoelectronic Devices. *Nat. Photonics* **2013**, *7*, 732–738.

68. Liu, R.; Liu, J.; Kong, W.; Huang, H.; Han, X.; Zhang, X.; Liu, Y.; Kang, Z., Adsorption Dominant Catalytic Activity of a Carbon Dots Stabilized Gold Nanoparticles System. *Dalton Trans.* **2014**, *43*, 10920–10929.

69. Ran, X.; Sun, H.; Pu, F.; Ren, J.; Qu, X., Ag Nanoparticle-decorated Graphene Quantum Dots for Label-free, Rapid and Sensitive Detection of Ag^+ and Biothiols. *Chem. Commun.* **2013**, *49*, 1079–1081.

70. Jaiswal, A.; Gautam, P. K.; Ghosh, S. S.; Chattopadhyay, A., Carbon Dots Mediated Room-temperature Synthesis of Gold Nanoparticles in Poly(ethylene glycol). *J. Nanopart. Res.* **2013**, *16*, 2188.

71. Luo, P.; Li, C.; Shi, G., Synthesis of Gold@Carbon Dots Composite Nanoparticles for Surface Enhanced Raman Scattering. *Phys. Chem. Chem. Phys.* **2012**, *14*, 7360–7366.

72. Wang, X.; Cao, L.; Lu, F.; Meziani, M. J.; Li, H.; Qi, G.; Zhou, B.; Harruff, B. A.; Kermarrec, F.; Sun, Y.-P., Photoinduced Electron Transfers with Carbon Dots. *Chem. Commun.* **2009**, 3774–3776.

73. Nozaki, T.; Kakuda, T.; Pottathara, Y. B.; Kawasaki, H., A Nanocomposite of N-doped Carbon Dots with Gold Nanoparticles for Visible Light Active Photosensitisers. *Photochem. Photobio. Sci.* **2019**, *18*, 1235–1241.

74. Qi, B.-P.; Bao, L.; Zhang, Z.-L.; Pang, D.-W., Electrochemical Methods to Study Photoluminescent Carbon Nanodots: Preparation, Photoluminescence Mechanism and Sensing. *ACS Appl. Mater. Interfaces* **2016**, *8*, 28372–28382.

75. Hu, Q.; Meng, X.; Chan, W., An Investigation on the Chemical Structure of Nitrogen and Sulfur Codoped Carbon Nanoparticles by Ultra-performance Liquid Chromatography-tandem Mass Spectrometry. *Anal. Bioanal. Chem.* **2016**, *408*, 5347–5357.

76. Demchenko, A. P.; Dekaliuk, M. O., The Origin of Emissive States of Carbon Nanoparticles Derived from Ensemble-averaged and Single-molecular Studies. *Nanoscale* **2016**, *8*, 14057–14069.

77. Sarswat, P. K.; Free, M. L., Light Emitting Diodes based on Carbon Dots Derived from Food, Beverage, and Combustion Wastes. *Phys. Chem. Chem. Phys.* **2015**, *17*, 27642–27652.

78. Ehrat, F.; Bhattacharyya, S.; Schneider, J.; Löf, A.; Wyrwich, R.; Rogach, A. L.; Stolarczyk, J. K.; Urban, A. S.; Feldmann, J., Tracking the Source of Carbon Dot Photoluminescence: Aromatic Domains versus Molecular Fluorophores. *Nano Lett.* **2017**, *17*, 7710–7716.

79. Zhu, S.; Zhao, X.; Song, Y.; Lu, S.; Yang, B., Beyond Bottom-up Carbon Nanodots: Citric-acid Derived Organic Molecules. *Nano Today* **2016**, *11*, 128–132.

80. Essner, J. B.; Kist, J. A.; Polo-Parada, L.; Baker, G. A., Artifacts and Errors Associated with the Ubiquitous Presence of Fluorescent Impurities in Carbon Nanodots. *Chem. Mater.* **2018**, *30*, 1878–1887.

81. Righetto, M.; Privitera, A.; Fortunati, I.; Mosconi, D.; Zerbetto, M.; Curri, M. L.; Corricelli, M.; Moretto, A.; Agnoli, S.; Franco, L.; Bozio, R.; Ferrante, C., Spectroscopic Insights into Carbon Dot Systems. *J. Phys. Chem. Lett.* **2017**, *8*, 2236–2242.

82. Hsu, Y.-F.; Chen, Y.-H.; Chang, C.-W., The Spectral Heterogeneity and Size Distribution of the Carbon Dots Derived from Time-resolved Fluorescence Studies. *Phys. Chem. Chem. Phys.* **2016**, *18*, 30086–30092.

83. Obadiya, T.; Uppala, H.; Sidebottom, D., Fluorescent Carbon Particles Formed from Concentrated Glucose Solutions. *MRS Adv.* **2019**, *4*, 67–72.

84. Khan, S.; Sharma, A.; Ghoshal, S.; Jain, S.; Hazra, M. K.; Nandi, C. K., Small Molecular Organic Nanocrystals Resemble Carbon Nanodots in terms of their Properties. *Chem. Sci.* **2018**, *9*, 175–180.

85. Reckmeier, C. J.; Schneider, J.; Xiong, Y.; Häusler, J.; Kasák, P.; Schnick, W.; Rogach, A. L., Aggregated Molecular Fluorophores in the Ammonothermal Synthesis of Carbon Dots. *Chem. Mater.* **2017**, *29*, 10352–10361.

86. Gude, V.; Das, A.; Chatterjee, T.; Mandal, P. K., Molecular Origin of Photoluminescence of Carbon Dots: Aggregation-induced Orange-red Emission. *Phys. Chem. Chem. Phys.* **2016**, *18*, 28274–28280.

87. Xiong, Y.; Schneider, J.; Ushakova, E. V.; Rogach, A. L., Influence of Molecular Fluorophores on the Research Field of Chemically Synthesized Carbon Dots. *Nano Today* **2018**, *23*, 124–139.

88. Schneider, J.; Reckmeier, C. J.; Xiong, Y.; von Seckendorff, M.; Susha, A. S.; Kasák, P.; Rogach, A. L., Molecular Fluorescence in Citric Acid-based Carbon Dots. *J. Phys. Chem. C* **2017**, *121*, 2014–2022.

89. Kasprzyk, W.; Świergosz, T.; Bednarz, S.; Walas, K.; Bashmakova, N. V.; Bogdał, D., Luminescence Phenomena of Carbon Dots Derived from Citric Acid and Urea – A Molecular Insight. *Nanoscale* **2018**, *10*, 13889–13894.

90. Das, A.; Gude, V.; Roy, D.; Chatterjee, T.; De, C. K.; Mandal, P. K., On the Molecular Origin of Photoluminescence of Nonblinking Carbon Dot. *J. Phys. Chem. C* **2017**, *121*, 9634–9641.

91. Song, Y.; Zhu, S.; Zhang, S.; Fu, Y.; Wang, L.; Zhao, X.; Yang, B., Investigation from Chemical Structure to Photoluminescent Mechanism: A Type of Carbon Dots from the Pyrolysis of Citric Acid and an Amine. *J. Mater. Chem. C* **2015**, *3*, 5976–5984.

92. Liu, X.; Li, H.-B.; Shi, L.; Meng, X.; Wang, Y.; Chen, X.; Xu, H.; Zhang, W.; Fang, X.; Ding, T., Structure and Photoluminescence Evolution of Nanodots during Pyrolysis of Citric Acid: From Molecular Nanoclusters to Carbogenic Nanoparticles. *J. Mater. Chem. C* **2017**, *5*, 10302–10312.

93. Shi, L.; Yang, J. H.; Zeng, H. B.; Chen, Y. M.; Yang, S. C.; Wu, C.; Zeng, H.; Yoshihito, O.; Zhang, Q., Carbon Dots with High Fluorescence Quantum Yield: The Fluorescence Originates from Organic Fluorophores. *Nanoscale* **2016**, *8*, 14374–14378.

94. Zhang, J.; Yang, L.; Yuan, Y.; Jiang, J.; Yu, S.-H., One-pot Gram-scale Synthesis of Nitrogen and Sulfur Embedded Organic Dots with Distinctive Fluorescence Behaviors in Free and Aggregated States. *Chem. Mater.* **2016**, *28*, 4367–4374.

95. Kasprzyk, W.; Bednarz, S.; Bogdał, D., Luminescence Phenomena of Biodegradable Photoluminescent Poly(diol citrates). *Chem. Commun.* **2013**, *49*, 6445–6447.

96. Kasprzyk, W.; Bednarz, S.; Zmudzki, P.; Galica, M.; Bogdal, D., Novel Efficient Fluorophores Synthesized from Citric Acid. *RSC Adv.* **2015**, *5*, 34795–34799.

97. Kim, J. P.; Xie, Z.; Creer, M. H.; Liu, Z.; Yang, J., Citrate-based Fluorescent Materials for Low-cost Chloride Sensing in the Diagnosis of Cystic Fibrosis. *Chem. Sci.* **2017**, *8*, 550–558.

98. Wang, H.-X.; Yang, Z.; Liu, Z.-G.; Wan, J.-Y.; Xiao, J.; Zhang, H.-L., Facile Preparation of Bright-fluorescent Soft Materials from Small Organic Molecules. *Chem. Eur. J.* **2016**, *22*, 8096–8104.

99. Kokorina, A. A.; Bakal, A. A.; Sapelkin, A. V.; Sukhorukov, G. B.; Goryacheva, I. Y., High Luminescent Fluorophore Synthesized at Atmospheric Pressure from Citric Acid and Ethylenediamine, International Symposium on Optics and Biophotonics VI: Saratov Fall Meeting 2018. *SPIE* **2019**, Vol. 11067.

100. Chen, C.-Y.; Tsai, Y.-H.; Chang, C.-W., Evaluation of the Dialysis Time Required for Carbon Dots by HPLC and the Properties of Carbon Dots after HPLC Fractionation. *New J. Chem.* **2019**, *43*, 6153–6159.

Chapter 2: Biocompatible Fluorescent Carbon Dots Derived from the Upcycling of Urine Towards Chromophoric Tuning for Enhanced Light Harvesting†

†This chapter is based on a submitted and accepted peer-reviewed manuscript in *Green Chem*. The information contained herein is adapted with permission from Essner, J. B.; Laber, C. H.; Ravula, S.; Polo-Parada, L.; Baker, G. A., Pee-dots: Biocompatible Fluorescent Carbon Dots Derived from the Upcycling of Urine. *Green Chem.* **2016**, *18*, 243–250. Copyright © 2016 Royal Society of Chemistry.

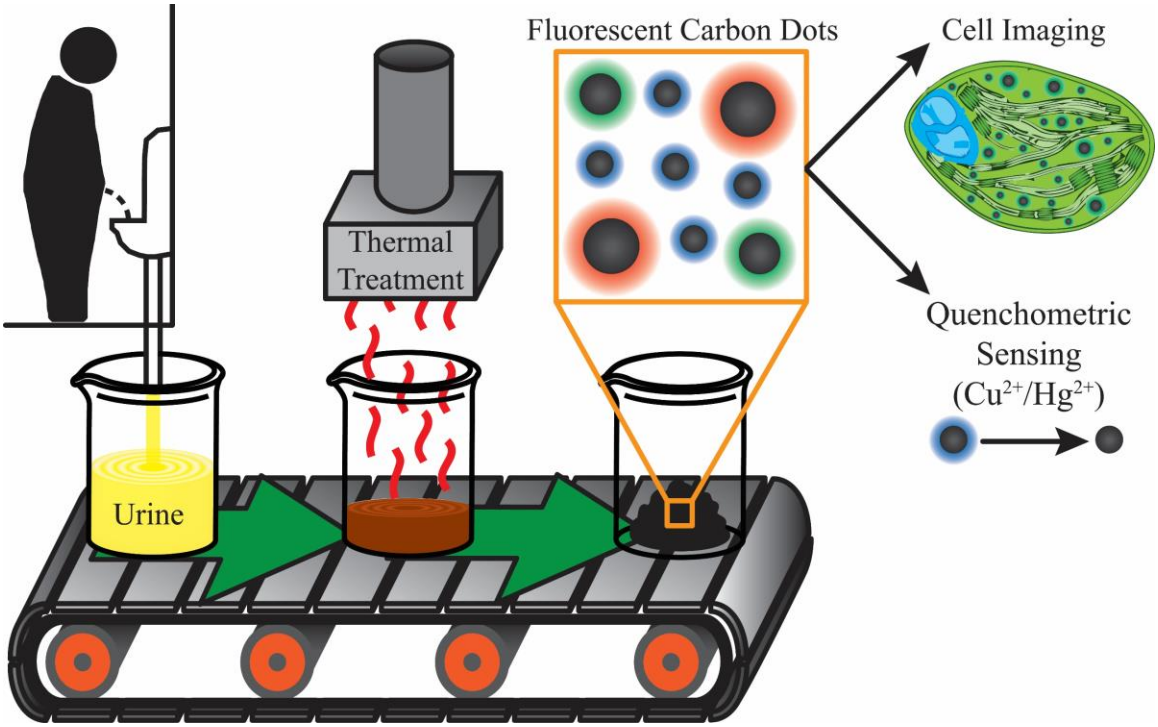

Scheme 2.1 Graphical abstract conceptualizing the thermal upcycling of human urine to biocompatible fluorescent carbon dots and their exploitation in bioimaging and quenchometric sensing applications.

Abstract

An easy, economic, one-step synthetic route to water-soluble fluorescent carbon dots derived from the thermal upcycling of urine is demonstrated. These "pee-dots" (PDs), which primarily comprise hydrophile-decorated amorphous carbon, exhibit bright, stable, excitation wavelength-dependent fluorescence in aqueous solution and are shown to be useful nanoscale labels in cell imaging applications. Cytotoxicity studies demonstrate that these PDs are benign toward model cell lines, even at concentrations as high as 500 μg mL^{-1}. Notably, this approach converts an otherwise useless, negatively valued by-product of human life into a value-added nanoscale product while simultaneously pasteurizing the waste stream. The reported PDs proved to be effective nanoprobes for the fluorescence-based detection of heavy metal ions of environmental concern, particularly Cu^{2+} and Hg^{2+} ions, which were found to be strong quenchers of their fluorescence. Interestingly, the optical properties and nanoscale dimensions of the PDs are a direct reflection of the diet (*e.g.*, vitamin C or asparagus (sulfur) fortified) followed by the urine donor.

Introduction

The fluorescent carbon nanodot (FCD) is a recently established form of nanocarbon which displays unique and valuable optical properties (*e.g.*, excitation wavelength-dependent fluorescence, excellent photostability) compared with its carbonaceous cousins, the fullerenes, graphenes, carbon nanotubes, and nanodiamonds.[1-6] Variously (and often arbitrarily) referred to as carbon quantum dots (CQDs) or graphene quantum dots (GQDs), sometimes depending on their level of crystallinity, FCDs offer an attractive eco-friendliness (*e.g.*, biocompatibility, inertness, low cytotoxicity) not shared with other conventional quantum dots, particularly semiconductor-based quantum dots such as CdX

(X = S, Se, Te). These properties, plus their ability to act as electron donors or acceptors coupled with their ease of (bio)conjugation, account for their growing interest as candidates in a number of applications ranging from sensing and bioimaging[1-4] to incorporation within photovoltaic devices.[4-6] From the time of their serendipitous discovery a decade ago during the purification of crude carbon nanotubes, researchers have increasingly explored various synthetic pathways for generating FCDs from myriad carbon sources using a wide variety of means. Synthetic approaches for making FCDs can broadly be lumped into two camps: top-down and bottom-up approaches. Top-down approaches, examples of which consist of arc discharge,[7] laser ablation,[8-9] and electrochemical oxidation,[10-14] involve the cleavage of "large" (macroscale) relatively pure carbon fragments into smaller and smaller particles, eventually resulting in GQDs if the carbon source is highly graphitic in nature to begin with. Bottom-up approaches, on the other hand, essentially involve assembling the FCDs in an atom-by-atom or molecule-by-molecule fashion from carbon-containing molecular precursors, tactics that overwhelmingly yield FCDs that are highly amorphous in nature. Examples of bottom-up methods include combustion or thermal treatment,[15] and templated,[16] microwave-assisted,[17] or hydrothermal growth.[18] Unfortunately, many of these synthetic procedures (both top-down and bottom-up) involve high temperatures, acidic/alkaline conditions, organic solvents, and/or extensive pre- and posttreatment steps which do not embrace the principles of green chemistry. With environmental sustainability becoming an increasing concern, a shift toward developing greener pathways to FCDs is occurring, both in terms of the use of more benign carbon sources as well as employing synthetic methods such as low-temperature thermal treatment and hydrothermal reactions which do not necessitate subsequent functionalization steps. For instance, it has recently

been shown that FCDs can be generated through the carbonization of various food wastes, including spent coffee grounds and certain fruit peels (*e.g.*, watermelon, pomelo).[19-21] The recouping of spent foods via carbonization to FCDs could have the added benefit of reclaiming a waste stream that might otherwise simply find its way into already-overflowing landfills.

Another area of great environmental concern, and one which relates to the conversion of waste material(s) into more valuable products (*i.e.*, "upcycling"), is waste remediation, especially of human sewage. The lack of clean, potable water is one of the most significant worldwide health issues, affecting billions of people who do not have access to safe drinkable water, including devastating numbers who die tragically each year after consuming contaminated water.[22] Even in densely populated and industrialized areas, contaminates are increasingly entering waste streams due to human activity.[22] In general, conventional wastewater treatments and the further development of these treatment facilities to generate a cleaner end-product are intensive and expensive enterprises.[22] Identifying cheaper means for converting human waste streams into more environmentally friendly forms and their upcycling to value-added by-products are of particular importance. For example, it has already been shown that biochar and activated carbon can be produced from cattle manure.[23-24] More recently, Wei *et al*. showed that FCDs could be synthesized via the hydrothermal treatment of shredded office paper.[25] Given these examples, it is entirely plausible that, under the appropriate conditions, raw sewage waste, which primarily comprises cellulose, fecal matter, and urine, can be converted into useful carbon-based materials, adding value and rendering the sewage harmless whilst eliminating certain time-consuming steps in the purification process.

To this end, it should be pointed out that the solid portion of sewage waste can be usefully employed as a source of fuel or fertilizer (indeed, cow/chicken manure has been used as fertilizer for centuries),[26] however, the remaining liquid portion ("yellow water" containing urine) currently finds essentially no useful applications. In fact, despite comprising just 1% of the volume of domestic wastewater, urine contributes the majority of chemical nutrients: 80% of the nitrogen and nearly half of the phosphates. These nutrients must be removed through multiple energy-intensive steps before the water is clean enough to release back into our rivers and oceans, if they are not to wreck the ecosystem downstream (*e.g.*, algal blooms). Worse, conventional Western plumbing involves the staggeringly wasteful dilution of urine with vast quantities of drinking water (which then combines with "grey water" from household sinks, baths, and wash machines) plus rainwater to make the removal process unnecessarily inefficient and costly. In order to close the nutrient cycle, some have proposed "pee cycling",[27-28] which entails the diversion and pasteurization of human urine for fertilizer, as a possible option for sustainable living. Although this is something of a minority pursuit so far, a number of countries (among them, Sweden, Finland, Denmark, and the Netherlands) are seriously experimenting with this concept, highlighting an evolving mindset regarding how we should utilize energy and resources in our daily lives.

Urine contains a significant amount of urea (~9 g L^{-1}) as a nitrogenous breakdown product of protein metabolism, in addition to lesser quantities of salts (Cl^-, Na^+, K^+) and heterocyclic species (*e.g.*, creatinine, uric acid), suggesting potential as an otherwise discarded carbon source for making nitrogen-doped FCDs. Indeed, Qu *et al*. reported on FCDs displaying a fairly high quantum yield (14% under 420 nm excitation) produced by

microwave irradiation of an aqueous solution of urea and citric acid.[17] Finding a productive use for raw urine is attractive not only for deriving economic benefit but also for relieving the current burden placed upon current wastewater treatment, a problem emerging in developed countries today.

The concept of upcycling of waste to prepare industrially significant carbon-based materials has gained significant traction recently. A key early example is the inspiring work of Pol in which conductive carbon microspheres were prepared from waste plastics, including high density polyethylene grocery bags and polystyrene disposable drinking cups, using a solvent-free autogenic process.[29] The Tour group showed that cheap and even negatively valued sources ranging from Girl Scout cookies to a cockroach leg could be transformed into pristine graphene using a chemical vapor deposition route.[30] Similarly, Müller *et al*. showed that well-ordered graphene monolayers could be grown via liquid precursor deposition using human fingerprint residues with identical quality as those derived from ultrapure precursors.[31] Other prominent examples of value-added carbons include hierarchical micro-/mesoporous carbons produced by pyrolysis of used cigarette filters[32] and FCDs made from the hydrothermal treatment of grass[33] or the pyrolysis of hair.[34] Most recently, researchers successfully carbonized dehydrated human urine in a tube furnace under nitrogen at 700–1100 °C to prepare heteroatom (*e.g.*, N, S, Si, P) doped porous carbons that were electrocatalytic for the oxygen reduction reaction (ORR).[35] The current work adds significantly to the scope of these noteworthy efforts by describing a simple approach for upcycling urine into useful FCDs that display negligible cytotoxicity and show excellent potential for both cellular imaging and fluorescence-based sensing applications.

Experimental

Materials and Reagents

All experiments were carried out using Ultrapure Millipore water polished to a resistivity of 18.2 MΩ·cm. All human urine used was collected from a single source (*i.e.*, one person). The vitamin C tablets and asparagus were both purchased from a local grocery store. The 96-well plates and the chloride salts of Cu^{2+} (lab grade), Fe^{3+} (ACS grade, >98%), Sr^{2+} (ACS grade, >99%), Ba^{2+} (>99%), and Ca^{2+} (99.999%), were obtained from Fisher Scientific (Pittsburg, PA). Sulforhodamine B (SRB), fetal bovine serum (FBS), cell culture media, phosphate-buffered saline (PBS), trichloroacetic acid, acetic acid, ethylenediaminetetraacetic acid (EDTA), the chloride salts of Ni^{2+} (98%), Hg^{2+} (ACS >99.5%), Sn^{2+} (≥99.995% trace metal basis), and Mn^{2+} (99.99% trace metals basis), as well as the sulfate salt of Cu^{2+} (≥98.0%), were all purchased from Sigma-Aldrich (St. Louis, MO). The acetate salt of Pd^{2+} (>99.95% Pd) and the anhydrous chloride salt of Zn^{2+} (99.95% metals basis) were acquired from Strem Chemicals (Newburyport, MA) and Alfa Aesar (Ward Hill, MA), respectively. All chemicals were used as received. Dialysis tubing (132105, Spectra/Por® 7, 1 kDa molecular weight cut-off or MWCO) was purchased from Repligen® (formerly Spectrum Labs®, Rancho Dominguez, CA). Mice embryonic fibroblast (MEF) cells were obtained from colleagues within the Dalton Cardiovascular Center while the human mammary gland, ductal carcinoma cells (BT-474) were acquired from the American Type Culture Collection (ATCC® HTB-20™).

Urine-derived Fluorescent Carbon Dot Syntheses

Roughly one liter of urine was collected for each of the three different dietary conditions investigated: unmodified diet, vitamin C supplemented, and asparagus-rich diet. Since

numerous excretions were required to acquire this volume, urine was pooled over the course of several days (collected between mid-morning and mid-afternoon) and homogenized to ensure a representative sample. To fortify the diet with vitamin C, four 500 mg vitamin C tablets (Nature Made®) were taken at 2 h intervals, with vitamin C-enriched urine collected 4 h and 6 h after consumption of the first tablet. To set the conditions for sulfur-enriched urine, approximately one pound of fresh and locally sourced asparagus was lightly steamed and consumed, collecting all urine within 6 h of its ingestion. This exercise was repeated several times over the course of a couple days, much to the student's chagrin.

To initiate FCD synthesis, 450 g of a particular urine sample was dehydrated in a heated round-bottom flask that was immersed within an improvised sand bath consisting of an anodized aluminum, round cake pan (Fat Daddio's®) filled with copper-coated airgun BBs (0.177 caliber; Crosman® Copperhead®). Temperature control was achieved to within 2 °C using a digital stirring hotplate (Super-Nuova™; Thermo Scientific™) connected to a J-type thermocouple immersed in the BBs. Stirring was provided at 300 rpm using a PTFE-coated, magnetic stir bar. The dehydrated residues were heated for an additional 12 h at 200 °C to yield a black char that readily resuspended in water. As the liquid evaporated, the urine gradually darkened from yellow to burnt orange and, finally, a viscous brown solution. Throughout the carbonization process, the material evolved in appearance, eventually becoming coal black. Following the carbonization step, the solid was reconstituted using 60 mL of water. The suspension was centrifuged at 5k rpm for 30 min and filtered using a 0.45 µm nylon syringe filter (Fisherbrand®, 09-719D) to remove large particles, after which the resulting solution was dialyzed for 12 h against 1.5 L of water

(changing the dialysis water three times throughout) using a 1 kDa MWCO cellulose dialysis membrane. A portion of each dialyzed sample was lyophilized to obtain a solid product for XRD analysis.

Characterization Techniques

Absorbance and steady-state fluorescence data were collected on a Varian Cary® Bio 50 UV-vis spectrophotometer and Varian Cary® Eclipse spectrofluorometer, respectively. For the studies discussed in this chapter, all spectroscopic data were blank subtracted and, when applicable, all fluorescence emission data were also dilution corrected. Excitation wavelength-dependent quantum yield values (Φ) were calculated using the following equation:

$$\Phi_S = \Phi_R \left[\frac{F_S}{F_R}\right]\left[\frac{OD_R}{OD_S}\right]\left[\frac{n_S^2}{n_R^2}\right]$$

where *R* and *S* stand for reference and sample respectively, *F* stands for integrated fluorescence intensity (calculated over the wavelength range of interest), *OD* stands for optical density (at the excitation wavelength, λ, used in the fluorescent measurements), and *n* stands for refractive index. Specifically, quinine sulfate, coumarin 153, fluorescein, rhodamine B, and cresyl violet were employed as reference fluorophores with all relevant fluorophore parameters utilized for the quantum yield determinations provided in Table 2.1 below.

Table 2.1 Reference fluorophores used to determine quantum yield (Φ) values.

Fluorophore	**Excitation λ (nm)**	**Solvent**	***n***	**Φ_R (%)**	**Reference**
Quinine sulfate	350	0.1 M H_2SO_4	1.343	58	[36]
Coumarin 153	421	Ethanol	1.366	38	[37]
Fluorescein	470	0.1 M NaOH	1.336	91	[38]
Rhodamine B	514	Water	1.334	31	[39]
Cresyl violet	580	Methanol	1.332	53	[36]

Raman spectra were collected on a Renishaw® Raman spectrometer employing a laser, operating at an incident wavelength of 514.5 nm. The samples were drop-casted on a clean Si wafer and allowed to air-dry at room temperature. The X-ray diffraction patterns were recorded at 25 °C by a Rigaku® PXRD system using Cu Kα radiation (λ = 1.5418 Å) at 40 kV and 44 mA with the spectral range of 2θ from 10° to 80°. The samples were drop-casted on a glass slide and allowed to air-dry at room temperature. Transmission electron microscopy (TEM) studies were conducted on carbon coated copper grids (Ted Pella, Inc., 01822-F, support films, ultrathin carbon type-A, 400 mesh copper grid) using a FEI® Tecnai™ (F30 G2, Twin) microscope operated at a 300 keV electron acceleration voltage.

Bioimaging Studies

For the fluorescent imaging studies, freshly isolated MEF cells were cultured in a 35 mm glass culture dish in the presence of each type of PD (0.2 mg mL^{-1}). The cells were fixed with a 70% ethanol solution for 10 min and mounted with Prolong™ Gold Antifade Mountant (Invitrogen) for imaging. Cells were observed and photographed using an inverted microscope Olympus® X-71 with Normanski and fluorescence optics using 4, 10, 20, or 40× lenses and a black and white (QImaging Retiga EXi) or color (Axiocam MRc5, Carl Zeiss) camera. Confocal micrographs were obtained using an Olympus® Fluoview™ 1200 laser scanning (Olympus® America) IX83 microscope with appropriate lenses. Fluorescence micrographs shown in Figure 2.5 combine the signal from 4',6-diamidino-2-phenylindole (DAPI) staining of the nuclear material with APD-derived signal collected through (A) FITC (excitation/emission: 479 nm/524 nm) or (B) TRITC (excitation/emission: 543 nm/593 nm) filter cubes (Semrock, Inc., Rochester, NY).

Cell Viability by Sulforhodamine B Assay

Cell viabilities were evaluated based on the colorimetric sulforhodamine B (SRB) assay, as it produces more consistent results (standard error of measurement or coefficient of variation) for adherent cell cultures over the more commonly employed colorimetric assay based on the light-sensitive, tetrazolium dye, 3-(4,5-dimethylthiazol-2-yl)-2,5-diphenyl-tetrazolium bromide (MTT). After the addition of PDs, cell viability was quantified using the SRB assay as described previously.[40-41] This cell protein dye-binding assay is based on the measurement of protein content of surviving cells as an index to determine cell growth, inhibition, and cell viability. Briefly, 8×10^3 cells (BT-474) dispersed in 100 μL culture media were seeded into each well of a 96-well plate and incubated overnight at 37 °C in a 10% CO_2 atmosphere, after which the culture media was removed and the cells were washed with 100 μL of serum-free medium (Dulbecco's Modified Eagle Medium: Nutrient Mixture F-12). The cells were then treated in 5% FBS culture medium for 48 h in the presence of 1, 3, 10, or 30 μL of a 5 mg mL^{-1} PD stock solution; the final volume in each well always totaled 100 μL. Following PD exposure, the medium was removed and surviving, or adherent, cells were fixed, in situ, by adding 100 μL of PBS solution and 100 μL of 50% cold trichloroacetic acid. The cells were then incubating at 4 °C for 1 h, after which they were washed with ice-cold water five times and dried. Cells were stained by adding 50 μL of a 4% SRB solution (in 1 vol% acetic acid) for 8 min at room temperature. Unbound dye was removed by washing the cells five times with cold 1% acetic acid and the cells were then dried. Bound SRB was solubilized with 150 μL of 10 mM Tris buffer solution (pH 7.4) and the absorbance of the resulting solutions at 560 nm was collected

with a microplate reader. Three separate wells were used for each PD concentration and every solubilized SRB solution was measured in triplicate.

Metal Quenching and Fluorescence Recovery Studies

Stock solutions of the various metal salts with concentrations of at least 5 mM were generated, which were then diluted to 3.1 mM. The PD concentration was kept constant at 0.05 mg mL^{-1} throughout all studies. For the metal screening tests, 100 µL of each 3.1 mM metal salt solution was added to separate cuvettes containing 3 mL of a 0.05 mg mL^{-1} PD solution. Fluorescence and UV-vis spectra were collected before and after the metal additions. For the quenching titrations, the emission of the metal-free FCD solution (3 mL) was first collected then a 10 µL addition of a 31 µM aqueous solution of Hg^{2+} or Cu^{2+} was added to give a metal ion concentration of ~100 nM and the emission was re-collected. This process was repeated nine additional times resulting in a final Hg^{2+} or Cu^{2+} concentration of 1 µM. Next, nine separate 10.5 µL additions of a 310 µM aqueous solution of Hg^{2+} or Cu^{2+} were added to give metal ion concentrations of ~2–10 µM, after which nine separate 11 µL additions of a 3.1 mM aqueous solution of Hg^{2+} or Cu^{2+} were added to give metal ion concentrations of ~20–100 µM. Emission spectra were collected after each aliquot of Hg^{2+} or Cu^{2+} was added. For the fluorescence recovery studies, three separate cuvettes per sample were treated in the following manner:

Cuvette 1: 3 × 100 µL water

Cuvette 2: 1 × 100 µL water followed by 2 × 100 µL 6.4 mM EDTA

Cuvette 3: 1 × 100 µL 3.1 mM $HgCl_2$ followed by 2 × 100 µL 6.4 mM EDTA

Fluorescence and UV-vis spectra were collected after each 100 µL addition. After the EDTA additions, the cuvettes were vigorously shook prior to collecting the spectra. This

process of shaking then collecting was repeated until the fluorescence emission stabilized. Again, all spectroscopic data were blank subtracted and all fluorescence spectra were dilution corrected when applicable. Additionally, the fluorescence emission data for the metal screening and recovery studies were corrected for inner filter effects through the approximate correction factor below:

$$F_{corr} = F_{obs}\left(10^{\frac{A_{ex}+A_{em}}{2}}\right)$$

where F_{corr} is the corrected fluorescence, F_{obs} is the observed (blank subtracted and dilution corrected) fluorescence, A_{ex} is the absorbance of the sample at the excitation wavelength (*i.e.*, 450 nm), and A_{em} is the absorbance at each wavelength over the emission range collected (*i.e.*, 460–800 nm). The fluorescence data for the titration quenching studies was not inner filter corrected as the metals (Hg^{2+}/Cu^{2+}) used for these studies showed no measurable absorbance over 460–800 nm even at concentrations much higher (*e.g.*, 1 mM) than those used in the titrations (maximum concentration of 100 μM).

Results and Discussion

Photophysical Characterizations

The thermal treatment of human urine collected from an unmodified diet indeed affords upcycling of the negatively valued waste into useful FCDs, referred to as "pee-dots" (PDs) herein. In addition to carbonizing raw urine derived from an unmodified diet, the test subject volunteered to consume large quantities of either vitamin C supplements or asparagus, on separate occasions over the course of several days, in an attempt to alter the properties of the urine by doping with excess ascorbic acid or sulphur-containing compounds, respectively. The motivation for this "dietary doping" experiment was to attempt to alter the optical features of the resulting carbon dots by either incorporation of

an additional, known carbon source in the urine or, in the case of an asparagus-rich diet, S-doping of the final nanocarbon, as heteroatom doping has been reported to bathochromically shift the observed absorbance and fluorescence. Indeed, the pungent, disagreeable smell associated with "asparagus-urine" derives from metabolic breakdown products of asparagusic acid. Although the exact mechanisms by which asparagusic acid is metabolized are not completely understood, it is known that asparagusic acid is digested to various sulfur-containing compounds like methanethiol, dimethyl sulfide, and dimethyl sulfoxide.[42-45] Figure A.1 of Appendix A summarizes the primary, suspected breakdown products of asparagusic acid. Throughout the remainder of this chapter, FCDs derived from an unmodified diet will be referred to as UPDs ("unmodified pee-dots"), those derived from a diet heavily supplemented with vitamin C as CPDs, and those upcycled from asparagus-urine as APDs.

Detailed synthetic procedures can be found under "Fluorescent Carbon Dot Syntheses" in the "Experimental" section above. Briefly though, collected urine was dehydrated at atmospheric pressure on a hotplate, followed by a carbonization step at 200 °C for 12 h to yield a black char material that readily redispersed in water. In addition to these experiments, undoped urine samples were also treated for an extended period of 24 h with representative results summarized in Figure A.2 (panels A, D, and E). Following PD purification, which comprised centrifugation, filtration, and dialysis steps, orange to dark brown solutions were obtained depending upon the precise nature of the initial urine, as shown in the inset of Figure 2.1 below. Reports on FCDs generally show featureless UV-vis absorbance spectra in which the absorbance sharply rises as the wavelength decreases toward the UV region,[1, 9, 15] an observation generally attributed to π-π* transitions of

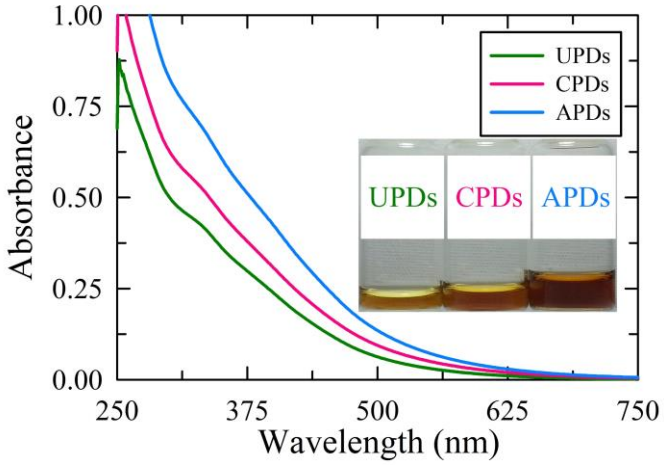

Figure 2.1 UV-vis spectra of the three different PD samples dispersed in water at a concentration of 0.1 mg mL^{-1}: UPDs (green curve), CPDs (magenta curve), and APDs (cyan curve). The inset photograph shows representative samples of these PDs at the same concentration viewed under ambient light.

aromatic sp^2 domains.[17-18, 46-48] The PDs display similar spectral profiles to those typically reported, although all three samples display two weak shoulders (Figure 2.1). The UPDs exhibit a shoulder near 330 nm with a minor shoulder at 390 nm. The CPDs show similar features at 330 and 385 nm, as do the APDs at approximately 325 and 400 nm. The citric acid-urea-derived FCDs described by Qu and co-workers, which were reported to possess a largely graphitic character, displayed two broad absorption peaks at 340 and 405 nm characteristic of an aromatic, pi system.[17] The shoulders present in the absorbance spectra of the PDs appear at similar wavelengths as the characteristic peaks for the citric acid-urea-derived FCDs, pointing to a minor graphitic character for the PDs.

All three PD samples displayed fluorescent properties akin to known FCDs, such as excitation wavelength-dependent emission, with the APDs showing the most redshifted emission for a given excitation wavelength. As shown in Figure 2.2A, APDs show their peak emission intensity at 500 nm which coincides with 425 nm excitation. In comparison,

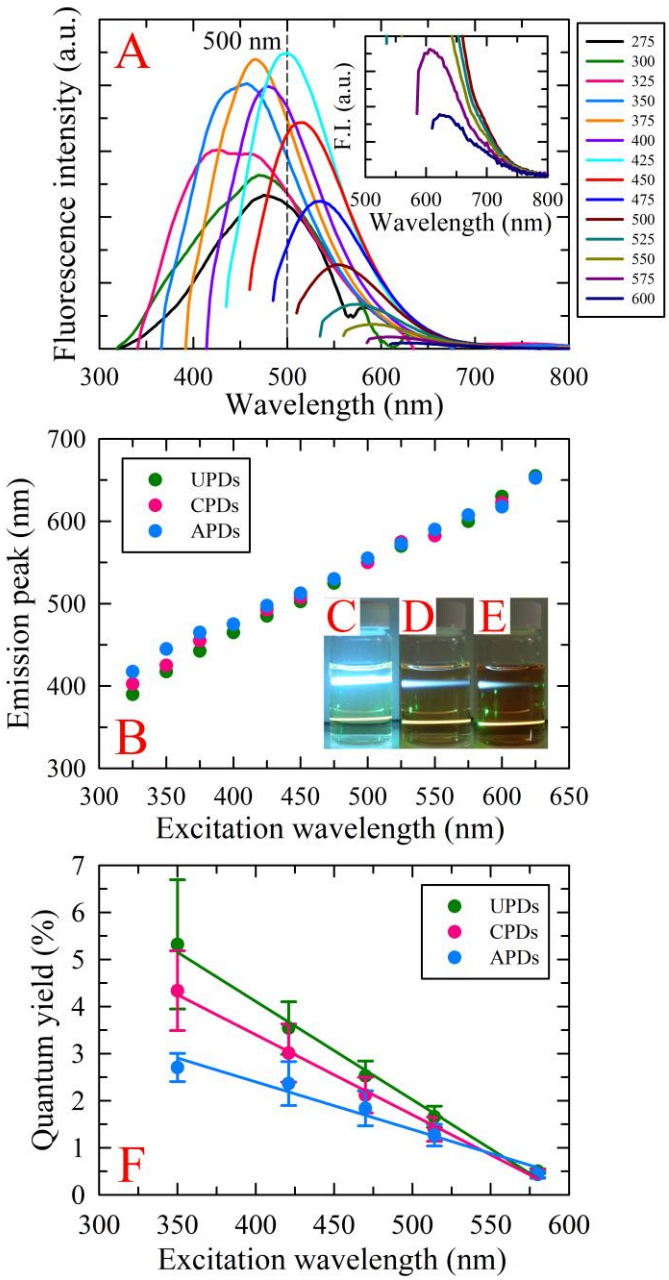

Figure 2.2 (A) Excitation wavelength-dependent fluorescence emission spectra of APDs in water. Magnified emission spectra at longer excitation wavelengths are displayed in the inset. (B) Plotting the wavelength of maximum emission against the excitation wavelength for these PDs revealed redshifted emission for CPDs and APDs relative to UPDs at shorter excitation wavelengths, particularly below 450 nm. The inset photographs show the fluorescence of (C) UPDs, (D) CPDs, and (E) APDs under blue (405 nm, upper beam) and green (532 nm, lower beam) laser pointer excitation. (F) Wavelength-dependent quantum yields measured at five different excitation wavelengths.

CPDs (Figure A.2C) and UPDs (Figure A.2B) display their highest emission intensities at 427 nm and 392 nm, which correspond to 350 nm and 325 nm excitation, respectively. This easily observable redshift in the emission for the APDs can be traced to the dietary presence and putative incorporation of sulfur into the PDs. A comparison between the wavelength-dependent fluorescence features of the PDs can be made on the basis of a plot illustrating the dependence of the maximum emission wavelength on the excitation wavelength, as shown in Figure 2.2B. These data reveal that, to a lesser extent, the CPDs also show a slight redshift relative to UPDs and, moreover, that the redshift is predominant at lower excitation wavelengths, particularly in the UV regime. Indeed, when the excitation wavelength exceeds 450 nm, the emission-excitation profiles for all three PDs begin to converge.

To make direct comparisons with fluorescence quantum yields (Φ) previously reported in the open literature, Φ for these samples were determined under 350 nm excitation using quinine sulfate as the reference fluorophore. Although this is the most popular choice for the determination of FCD Φ by a wide margin, it is not a particularly meaningful one given the limitations of 350 nm (*i.e.*, UV) excitation in prospective bioimaging applications. That is to say, a high Φ value measured for 350 nm excitation does not necessarily translate to a high Φ for excitation at longer wavelengths better suited to cellular imaging, a feature underlined by the characteristic drop in the fluorescence intensity from FCDs as the excitation wavelength increases. To better elucidate this behavior, we performed a multi-excitation wavelength Φ study for the three kinds of PDs using excitation wavelengths of 350, 421, 470, 514, and 580 nm. To the best of our knowledge, this is the first time such a study has been carried out for a multiplicity of excitation wavelengths for FCDs. In fact,

only rarely have Φ for FCDs been measured at more than a single excitation wavelength.[17] Our results presented in Figure 2.2F demonstrate a clear trend of diminishing Φ values as the excitation wavelength increases. Overall, UPDs display the highest Φ (5.3% at 350 nm), with CPDs and APDs presenting lower values, although their maximal Φ similarly occur at 350 nm excitation, with Φ of 4.3% and 2.7%, respectively. Despite this situation, at an excitation wavelength of 580 nm, all three samples display similar Φ values (UPDs: 0.50 ± 0.05%, CPDs: 0.44 ± 0.09%, APDs: 0.43 ± 0.07%), an outcome likely related to the redshifted emission associated with the APDs. It should also be noted that the fluorescence emission of UPDs prepared by thermal treatment for 24 h displays a greater redshift compared with samples treated for 12 h. For a 24 h thermal step, the peak emission was observed at 445 nm under 350 nm excitation (Figure A.2A) while the corresponding UPDs prepared by a 12 h thermal process peaks at 392 nm under 325 nm excitation (Figure A.2B).

Structural Characterizations

To define the nature of the carbon comprising the different PDs, X-ray diffraction (XRD) patterns and Raman spectra were collected for the lyophilized materials. The powder XRD patterns for all three samples reveal a broad band at approximately 22° with a d-spacing between the (002) planes of 0.37–0.38 nm, indicating that the PDs consist of weakly graphitic crystallinity (Figure 2.3A). This d-spacing also indicates the presence of functional groups on the surface of the slightly graphitic sheets within the dot. This kind of behaviour has been observed in the literature and shows that the PDs are highly amorphous in nature but do possess a slight graphitic nature.[49] The Raman spectra (data not shown) gave no evidence for their graphitic nature, consistent with earlier reports on other FCDs.[50] Although no Raman peaks were discernible for the PDs, the steady increase

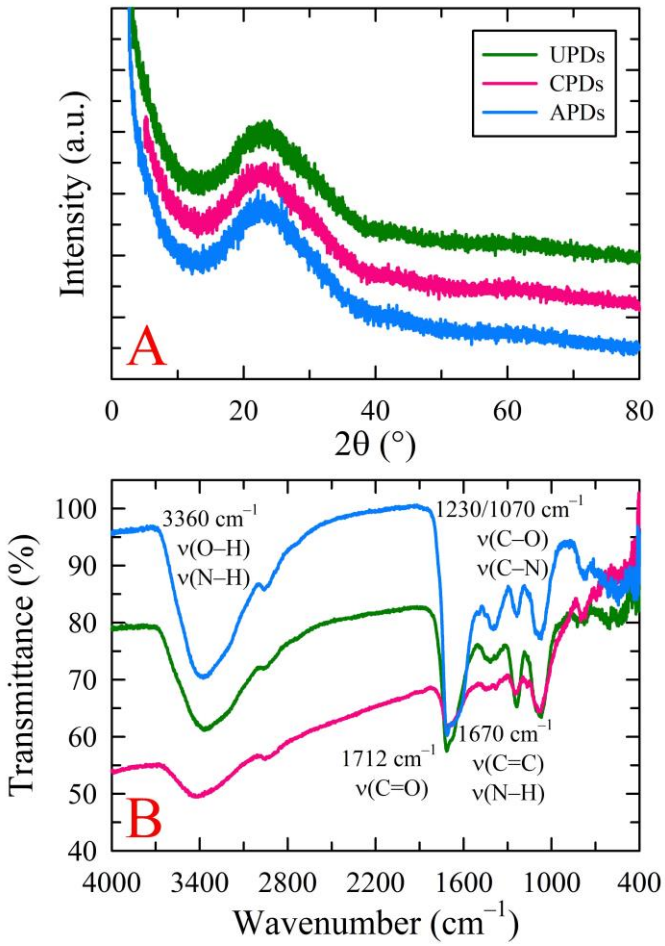

Figure 2.3 (A) XRD patterns and (B) FTIR spectra showing the slight graphitic nature and surface functionalities of the PDs, respectively. The legend in panel A also corresponds to panel B.

in intensity with increasing Raman shift has been observed in other FCDs and most certainly arises from their luminescence, which could obscure weak graphitic signals.[51]

Fourier-transform infrared (FTIR) spectra for the three different PDs (Figure 2.3B) indicate that the PDs are functionalized with carboxyl, carbonyl, hydroxyl, epoxy, and amine moieties. The large, broad absorption band near 3400 cm^{-1} is assigned to the stretching vibrations of O–H (ν_{O-H}) and N–H (ν_{N-H}). The well-defined absorbance bands at 1712 cm^{-1} and 1670 cm^{-1} are ascribed to the stretching vibrations of C=O ($\nu_{C=O}$) and the

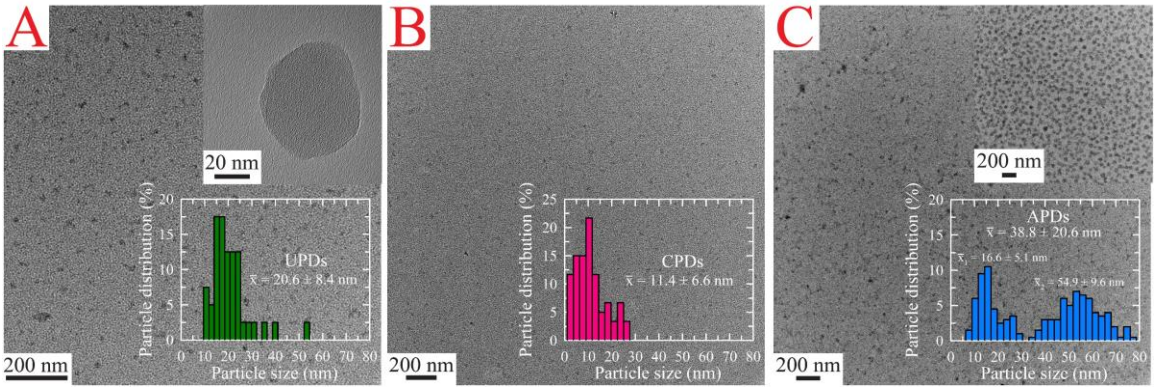

Figure 2.4 Representative TEM micrographs of (A) UPDs, (B) CPDs, and (C) APDs. Histograms with the average particle sizes (x-bar) are also shown with the inset of panel (C) further illustrates the bimodal particle size distribution of the APDs.

skeletal vibrations of aromatic groups ($\nu_{C=C}$) or NH/NH_2 deformation (ν_{N-H}), respectively. The peaks at 1230 and 1070 cm^{-1} arise from the different stretching modes of carboxylic, ester, ether, and alcohol moieties (ν_{C-O-C} and ν_{C-OH}), while the peaks near 2950 and 1400 cm^{-1} are assigned to aliphatic carbon vibrations (ν_{C-H}). These chemical functionalities account for the excellent water dispersibility of the PDs while also providing evidence for some degree of conjugation, consistent with the slightly graphitic character suggested by the XRD results.

Representative TEM micrographs for the UPDs, CPDs, and APDs, along with histograms of the PDs size distributions, are provided in Figure 2.4. Panel A of Figure 2.4 reveals that the thermal treatment of unmodified urine results in UPDs varying in size between 10 and 30 nm, with a few errant particles as large as about 55 nm. The inset provided in Figure 2.4A displays a single, large quasi-spherical dot approximately 55 nm in diameter; given that no discernible lattice fringes are observed, this micrograph further supports the earlier notion that these PDs are primarily amorphous in nature. The average size of the CPDs is roughly half that of the UPDs (Figure 2.4B). Interestingly, the APDs display a bimodal size distribution, with one distribution centered near 17 nm and a second

particle size near 55 nm (Figure 2.4C). An unanticipated finding, it appears that dietary doping can influence not only the optical properties of the PDs but their size distribution as well.

Bioimaging Applications and Cytotoxicity Studies

The three different PDs were next explored for bioimaging studies using mice embryonic fibroblast (MEF) cells (Figure 2.5) and human mammary gland, ductal carcinoma cells (BT-474; Figure A.3). Despite their modest Φ values under visible light excitation (in the range of a few percent), the PDs proved fully capable of fluorescently staining both cell lines, demonstrating their potential in cell imaging. The fluorescence micrographs of MEF cells incubated with APDs confirms that APDs can be endocytosed by MEF cells and that the dots distribute throughout the cell cytoplasm (Figure 2.5; panels A and B). Because PDs are compatible with common excitation sources spanning the visible spectrum, they offer many options for multicolor and multiplex detection. In demonstration of this, we show in Figure 2.5A and 2.5B that fluorescence signal can be monitored in either the green (FITC filter set) or the red (TRITC) spectral regions, providing contrast to the blue-fluorescing 4',6-diamidino-2-phenylindole (DAPI) stain known to bind strongly to A-T rich regions in DNA. Cytotoxicity screening *vs* the BT-474 cancer cell line was also carried out using a sulforhodamine B colorimetric assay for PD concentrations ranging from 0.05 to 1.5 mg mL^{-1} (Figure 2.5C). There was full retention of cell viability at concentrations of 0.15 mg mL^{-1} for all three types of PDs. Further, the cytotoxicities of UPDs and CPDs were found to be negligible at PD concentrations as high as 0.5 mg mL^{-1}. Even at the highest PD concentration studied (*i.e.*, 1.5 mg mL^{-1}; it should be noted that prior studies of FCD cytotoxicity have rarely included concentrations beyond 0.5 mg mL^{-1}), BT-474 cell

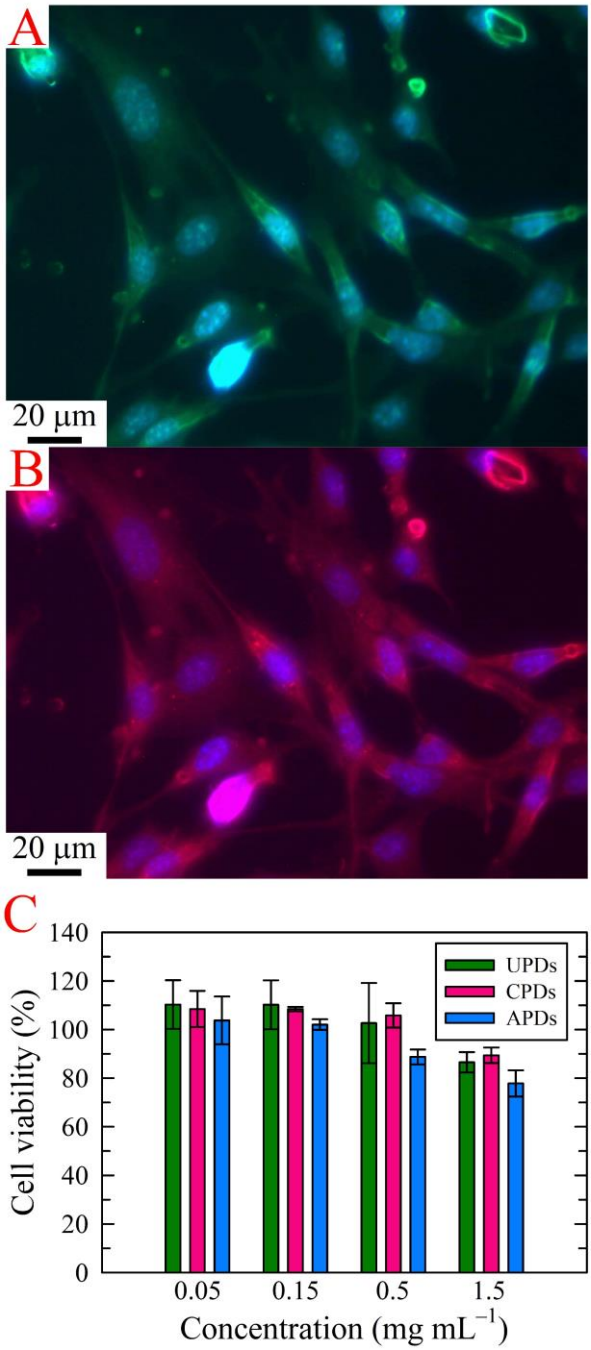

Figure 2.5 Merged fluorescence micrographs of APD-incubated mice embryonic fibroblast (MEF) cells showing APD incorporation into the cellular cytoplasm. The cell micrographs combine the signal from DAPI staining of the nuclear material with APD-derived signal collected through a (A) FITC or (B) TRITC filter cube. (C) Summary of BT-474 cell viability for varying concentrations of the three kinds of PDs using a sulforhodamine B cell protein dye-binding assay.

cultures retained 90% of their viability. In fact, some of this apparent decrease in cell survival can be attributed to the osmotic shock associated with addition of relatively large volumes of the PD stocks (which were prepared in deionized water) to the 96-well plates used in the cytotoxicity screening. The resulting change in cell culture media osmolality can induce cell rupture, which is not related to PD toxicity as such. Measurements at the lower PD concentrations were not subject to this artifact since miniscule volumes of PD solution were required for these concentrations. Regardless, the PDs appear to be highly biocompatible, even at concentrations that are well in excess of those required for cellular imaging studies.

Quenchometric Metal Ion Sensing and Fluorescence Recovery

A final set of experiments investigated the utility of PDs in fluorescence-based metal ion sensing (Figure 2.6 and A.4). In these experiments, PD fluorescence quenching behaviour was screened against 11 different metal ions: Zn^{2+}, Sr^{2+}, Ba^{2+}, Mn^{2+}, Ca^{2+}, Sn^{2+}, Ni^{2+}, Fe^{3+}, Cu^{2+}, Pd^{2+}, and Hg^{2+} (Figure 2.6A). All three types of PD responded in a similar manner to each individual metal ion. The metal ions Zn^{2+}, Sr^{2+}, Ba^{2+}, Mn^{2+}, and Ca^{2+} showed no quenching of PD emission whilst Sn^{2+} and Ni^{2+} showed relatively weak quenching. The remaining metal ions (Fe^{3+}, Cu^{2+}, Pd^{2+}, and Hg^{2+}) all produced much stronger fluorescence quenching, with Pd^{2+} and Hg^{2+} displaying the strongest quenching capabilities of the metals tested, irrespective of the PD identity. Since the strongest quencher (Pd^{2+}) is an unlikely environmental contaminant in most waters, we focused our attention on investigating Hg^{2+} detection. Figure 2.6B provides a representative Stern–Volmer plot of Hg^{2+}-induced quenching of APD fluorescence, where F_0 and F represent the fluorescence intensities in the absence and presence of Hg^{2+}, respectively. Following the 3σ convention, the limit of

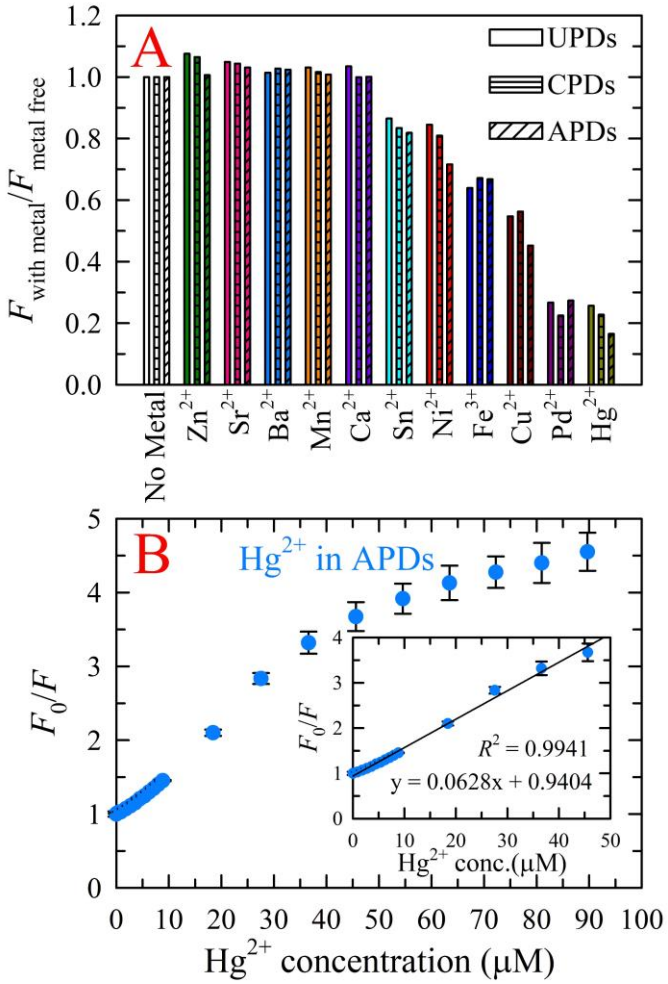

Figure 2.6 (A) Metal screening test for all three PD types (0.05 mg mL^{-1}) against 11 different metal ions (Zn^{2+}, Sr^{2+}, Ba^{2+}, Mn^{2+}, Ca^{2+}, Sn^{2+}, Ni^{2+}, Fe^{3+}, Cu^{2+}, Pd^{2+}, and Hg^{2+}), each present at a concentration of 100 μM. (B) Representative plot of Hg^{2+} quenching of APD emission.

detection (LOD) for a particular metal ion was determined as the Hg^{2+} concentration corresponding to a signal that differed from that of the metal-free result by thrice the standard deviation of the signal in the absence of metal. LOD values were estimated in the low micromolar range for both Hg^{2+} and Cu^{2+} ions. Specifically, for UPDs, the calculated LODs were 2.7 μM and 3.4 μM for Hg^{2+} and Cu^{2+}, respectively, while the corresponding Hg^{2+} (Cu^{2+}) LOD values for CPDs and APDs were 1.8 μM (1.7 μM) and 2.7 μM (2.9 μM), respectively.

In addition to showing quenchometric sensing capabilities for priority, heavy-metal-ion pollutants, the fluorescence signal was almost completely (94–97%) recoverable through the addition of a strong metal-chelating agent, ethylenediaminetetraacetic acid (EDTA), to Hg^{2+}-quenched samples (Figure A.5).[33] An excess of EDTA (>4:1 EDTA:Hg^{2+} molar ratio) is required to achieve the greatest signal recovery, indicating that while a majority of the Hg^{2+} ions may be loosely interacting with the functional groups at the PD surface, some fraction are apparently bound with a high affinity.

Conclusions

To sum, analytically useful and biocompatible FCDs can be facilely derived from the thermal upcycling of human urine. The synthesized pee dots were found to be effective nanoscale labels, illustrated in the multiplexed fluorescence imaging of mice embryonic fibroblast cells, whilst showing no apparent cytotoxicity at concentrations approaching 1.5 mg mL^{-1}. These dots also proved to be excellent nanosensors for fluorescence quenching-based detection of priority, heavy-metal-ion pollutants of environmental interest like mercuric (Hg^{2+}). The fluorescence signal was fully recoverable using EDTA as a chelator, suggesting the potential for immobilization of the dots within reusable paper test strips for water quality monitoring, for example.

The current work represents one of the few instances where fluorescent quantum yields of FCDs have been measured at a multiplicity of wavelengths. The findings reveal a marked decrease in quantum yield with excitation wavelength, suggesting a need to shift away from reporting quantum yields at a single excitation wavelength (*e.g.*, 350 nm) or, at the very least, to employing visible excitation wavelengths better matched to target applications such as bioimaging, sensing, and photovoltaics for which the FCDs are being

proposed for immediate exploitation. Moreover, this observation points to the need to specify the precise optical conditions employed when making meaningful comparisons between quantum yields and other optical properties commonly reported in the literature, a guideline not always followed. Pragmatically, another consequence of these findings is that FCDs that yield the highest emission under ultraviolet or blue emission may not necessarily be those best suited for practical bioimaging, particularly given the excitation of cellular autofluorescence in these spectral regions.

Intriguingly, we have also demonstrated that the fluorescent, size, and sensory characteristics of the carbon dots can be modulated by simple dietary modifications of the urine donor. For instance, intentional consumption of sulphur-containing foodstuffs (*i.e.*, asparagus) was shown to lead to measurable redshifts in the fluorescence emission from the dots. Furthermore, although highly speculative, this result suggests the enticing notion that an extension of this approach might possibly be used to assess the diet and general health of urine donors in resource-limited settings, as such will be reflected in the optical features of the subsequent dots produced to some extent. In any case, compelling evidence that urine can be upcycled into a useful carbonaceous product in a process that could potentially combine, simplify, or remove steps in wastewater treatment is provided. Within a larger context, the work adds momentum to research aimed at upcycling low or negatively valued waste into useful and compelling nanocarbons.

Acknowledgements

This work was supported by the Interdisciplinary Intercampus (IDIC) Research Program at the University of Missouri. We thank Dr. Tommi White and the MU Electron Microscopy Core Facility for the provision of imaging resources. We are grateful to Prof.

Jian “Javen” Lin (Department of Mechanical & Aerospace Engineering) for stimulating discussions on the future of this exciting area.

References

1. Baker, S. N.; Baker, G. A., Luminescent Carbon Nanodots: Emergent Nanolights. *Angew. Chem. Int. Ed.* **2010**, *49*, 6726–6744.

2. Ding, C.; Zhu, A.; Tian, Y., Functional Surface Engineering of C-dots for Fluorescent Biosensing and In Vivo Bioimaging. *Acc. Chem. Res.* **2013**, *47*, 20–30.

3. Li, H.; Kang, Z.; Liu, Y.; Lee, S.-T., Carbon Nanodots: Synthesis, Properties and Applications. *J. Mater. Chem.* **2012**, *22*, 24230–24253.

4. Shen, J.; Zhu, Y.; Yang, X.; Li, C., Graphene Quantum Dots: Emergent Nanolights for Bioimaging, Sensors, Catalysis and Photovoltaic Devices. *Chem. Commun.* **2012**, *48*, 3686–3699.

5. Wang, J.; Xin, X.; Lin, Z., Cu_2ZnSnS_4 Nanocrystals and Graphene Quantum Dots for Photovoltaics. *Nanoscale* **2011**, *3*, 3040–3048.

6. Zhang, Z.; Zhang, J.; Chen, N.; Qu, L., Graphene Quantum Dots: An Emerging Material for Energy-related Applications and Beyond. *Energy Environ. Sci.* **2012**, *5*, 8869–8890.

7. Xu, X.; Ray, R.; Gu, Y.; Ploehn, H. J.; Gearheart, L.; Raker, K.; Scrivens, W. A., Electrophoretic Analysis and Purification of Fluorescent Single-walled Carbon Nanotube Fragments. *J. Am. Chem. Soc.* **2004**, *126*, 12736–12737.

8. Hu, S.-L.; Niu, K.-Y.; Sun, J.; Yang, J.; Zhao, N.-Q.; Du, X.-W., One-step Synthesis of Fluorescent Carbon Nanoparticles by Laser Irradiation. *J. Mater. Chem.* **2009**, *19*, 484–488.

9. Sun, Y.-P.; Zhou, B.; Lin, Y.; Wang, W.; Fernando, K. A. S.; Pathak, P.; Meziani, M. J.; Harruff, B. A.; Wang, X.; Wang, H.; Luo, P. G.; Yang, H.; Kose, M. E.; Chen, B.; Veca, L. M.; Xie, S.-Y., Quantum-sized Carbon Dots for Bright and Colorful Photoluminescence. *J. Am. Chem. Soc.* **2006**, *128*, 7756–7757.

10. Li, H.; He, X.; Kang, Z.; Huang, H.; Liu, Y.; Liu, J.; Lian, S.; Tsang, C. H. A.; Yang, X.; Lee, S.-T., Water-soluble Fluorescent Carbon Quantum Dots and Photocatalyst Design. *Angew. Chem. Int. Ed.* **2010**, *49*, 4430–4434.

11. Ming, H.; Ma, Z.; Liu, Y.; Pan, K.; Yu, H.; Wang, F.; Kang, Z., Large Scale Electrochemical Synthesis of High Quality Carbon Nanodots and their Photocatalytic Property. *Dalton Trans.* **2012**, *41*, 9526–9531.

12. Zhao, Q.-L.; Zhang, Z.-L.; Huang, B.-H.; Peng, J.; Zhang, M.; Pang, D.-W., Facile Preparation of Low Cytotoxicity Fluorescent Carbon Nanocrystals by Electrooxidation of Graphite. *Chem. Commun.* **2008**, 5116–5118.

13. Zheng, L.; Chi, Y.; Dong, Y.; Lin, J.; Wang, B., Electrochemiluminescence of Water-soluble Carbon Nanocrystals Released Electrochemically from Graphite. *J. Am. Chem. Soc.* **2009**, *131*, 4564–4565.

14. Zhou, J.; Booker, C.; Li, R.; Zhou, X.; Sham, T.-K.; Sun, X.; Ding, Z., An Electrochemical Avenue to Blue Luminescent Nanocrystals from Multiwalled Carbon Nanotubes (MWCNTs). *J. Am. Chem. Soc.* **2007**, *129*, 744–745.

15. Bourlinos, A. B.; Stassinopoulos, A.; Anglos, D.; Zboril, R.; Georgakilas, V.; Giannelis, E. P., Photoluminescent Carbogenic Dots. *Chem. Mater.* **2008**, *20*, 4539–4541.

16. Yang, Y.; Wu, D.; Han, S.; Hu, P.; Liu, R., Bottom-up Fabrication of Photoluminescent Carbon Dots with Uniform Morphology via a Soft-hard Template Approach. *Chem. Commun.* **2013**, *49*, 4920–4922.

17. Qu, S.; Wang, X.; Lu, Q.; Liu, X.; Wang, L., A Biocompatible Fluorescent Ink based on Water-soluble Luminescent Carbon Nanodots. *Angew. Chem. Int. Ed.* **2012**, *51*, 12215–12218.

18. Shi, Q.-Q.; Li, Y.-H.; Xu, Y.; Wang, Y.; Yin, X.-B.; He, X.-W.; Zhang, Y.-K., High-yield and High-solubility Nitrogen-doped Carbon Dots: Formation, Fluorescence Mechanism and Imaging Application. *RSC Adv.* **2014**, *4*, 1563–1566.

19. Hsu, P.-C.; Shih, Z.-Y.; Lee, C.-H.; Chang, H.-T., Synthesis and Analytical Applications of Photoluminescent Carbon Nanodots. *Green Chem.* **2012**, *14*, 917–920.

20. Lu, W.; Qin, X.; Liu, S.; Chang, G.; Zhang, Y.; Luo, Y.; Asiri, A. M.; Al-Youbi, A. O.; Sun, X., Economical, Green Synthesis of Fluorescent Carbon Nanoparticles and their use as Probes for Sensitive and Selective Detection of Mercury(II) Ions. *Anal. Chem.* **2012**, *84*, 5351–5357.

21. Zhou, J.; Sheng, Z.; Han, H.; Zou, M.; Li, C., Facile Synthesis of Fluorescent Carbon Dots using Watermelon Peel as a Carbon Source. *Mater. Lett.* **2012**, *66*, 222–224.

22. Shannon, M. A.; Bohn, P. W.; Elimelech, M.; Georgiadis, J. G.; Marinas, B. J.; Mayes, A. M., Science and Technology for Water Purification in the Coming Decades. *Nature* **2008**, *452*, 301–310.

23. Cao, X.; Ma, L.; Gao, B.; Harris, W., Dairy-manure Derived Biochar Effectively Sorbs Lead and Atrazine. *Environ. Sci. Technol.* **2009**, *43*, 3285–3291.

24. Qian, Q.; Machida, M.; Tatsumoto, H., Textural and Surface Chemical Characteristics of Activated Carbons Prepared from Cattle Manure Compost. *Waste Manage.* **2008**, *28*, 1064–1071.

25. Wei, J.; Zhang, X.; Sheng, Y.; Shen, J.; Huang, P.; Guo, S.; Pan, J.; Liu, B.; Feng, B., Simple One-step Synthesis of Water-soluble Fluorescent Carbon Dots from Waste Paper. *New J. Chem.* **2014**, *38*, 906–909.

26. Werther, J.; Ogada, T., Sewage Sludge Combustion. *Prog. Energy Combust. Sci.* **1999**, *25*, 55–116.

27. Larson, S., National Geographic, Is "Pee-cycling" the Next Wave in Sustainable Living? http://news.nationalgeographic.com/news/2014/02/140202-peecycling-urine-human-waste-compost-fertilizer/ (accessed May 10, 2015).

28. Lawton, G., Pee-cycling. *New Scientist* December 23-30, **2006**, *192*, pp 45–47.

29. Pol, V. G., Upcycling: Converting Waste Plastics into Paramagnetic, Conducting, Solid, Pure Carbon Microspheres. *Environ. Sci. Technol.* **2010**, *44*, 4753–4759.

30. Ruan, G.; Sun, Z.; Peng, Z.; Tour, J. M., Growth of Graphene from Food, Insects, and Waste. *ACS Nano* **2011**, *5*, 7601–7607.

31. Müller, F.; Grandthyll, S.; Gsell, S.; Weinl, M.; Schreck, M.; Jacobs, K., Graphene from Fingerprints: Exhausting the Performance of Liquid Precursor Deposition. *Langmuir* **2014**, *30*, 6114–6119.

32. Minzae, L.; Gil-Pyo, K.; Hyeon Don, S.; Soomin, P.; Jongheop, Y., Preparation of Energy Storage Material Derived from a used Cigarette Filter for a Supercapacitor Electrode. *Nanotechnology* **2014**, *25*, 345601.

33. Liu, S.; Tian, J.; Wang, L.; Zhang, Y.; Qin, X.; Luo, Y.; Asiri, A. M.; Al-Youbi, A. O.; Sun, X., Hydrothermal Treatment of Grass: A Low-cost, Green Route to Nitrogen-doped, Carbon-rich, Photoluminescent Polymer Nanodots as an Effective Fluorescent Sensing Platform for Label-Free Detection of Cu(II) Ions. *Adv. Mater.* **2012**, *24*, 2037–2041.

34. Liu, S.-S.; Wang, C.-F.; Li, C.-X.; Wang, J.; Mao, L.-H.; Chen, S., Hair-derived Carbon Dots Toward Versatile Multidimensional Fluorescent Materials. *J. Mater. Chem. C* **2014**, *2*, 6477–6483.

35. Chaudhari, N. K.; Song, M. Y.; Yu, J.-S., Heteroatom-doped Highly Porous Carbon from Human Urine. *Sci. Rep.* **2014**, *4*, 5221.

36. Lakowicz, J. R., *Principles of Fluorescence Spectroscopy*. 3rd ed.; Springer: 2006.

37. Jones, G.; Jackson, W. R.; Choi, C. Y.; Bergmark, W. R., Solvent Effects on Emission Yield and Lifetime for Coumarin Laser Dyes. Requirements for a Rotatory Decay Mechanism. *J. Phys. Chem.* **1985**, *89*, 294–300.

38. Porrès, L.; Holland, A.; Pålsson, L.-O.; Monkman, A.; Kemp, C.; Beeby, A., Absolute Measurements of Photoluminescence Quantum Yields of Solutions using an Integrating Sphere. *J. Fluoresc.* **2006**, *16*, 267–273.

39. Magde, D.; Rojas, G. E.; Seybold, P. G., Solvent Dependence of the Fluorescence Lifetimes of Xanthene Dyes. *Photochem. Photobiol.* **1999**, *70*, 737–744.

40. Skehan, P.; Storeng, R.; Scudiero, D.; Monks, A.; McMahon, J.; Vistica, D.; Warren, J. T.; Bokesch, H.; Kenney, S.; Boyd, M. R., New Colorimetric Cytotoxicity Assay for Anticancer-drug Screening. *J. Natl. Cancer Inst.* **1990**, *82*, 1107–1112.

41. Rubinstein, L. V.; Shoemaker, R. H.; Paull, K. D.; Simon, R. M.; Tosini, S.; Skehan, P.; Scudiero, D. A.; Monks, A.; Boyd, M. R., Comparison of In Vitro Anticancer-drug-screening Data Generated with a Tetrazolium Assay versus a Protein Assay against a Diverse Panel of Human Tumor Cell Lines. *J. Natl. Cancer Inst.* **1990**, *82*, 1113–1117.

42. Mitchell, S. C., Food Idiosyncrasies: Beetroot and Asparagus. *Drug Metab. Dispos.* **2001**, *29*, 539–543.

43. Pelchat, M. L.; Bykowski, C.; Duke, F. F.; Reed, D. R., Excretion and Perception of a Characteristic Odor in Urine after Asparagus Ingestion: A Psychophysical and Genetic Study. *Chem. Senses* **2011**, *36*, 9–17.

44. Waring, R. H.; Mitchell, S. C.; Fenwick, G. R., The Chemical Nature of the Urinary Odour Produced by man after Asparagus Ingestion. *Xenobiotica* **1987**, *17*, 1363–1371.

45. White, R., Occurrence of S-methyl Thioesters in Urines of Humans after they have Eaten Asparagus. *Science* **1975**, *189*, 810–811.

46. Mao, Y.; Bao, Y.; Yan, L.; Li, G.; Li, F.; Han, D.; Zhang, X.; Niu, L., pH-switched Luminescence and Sensing Properties of a Carbon Dot-Polyaniline Composite. *RSC Adv.* **2013**, *3*, 5475–5482.

47. Xie, M.; Su, Y.; Lu, X.; Zhang, Y.; Yang, Z.; Zhang, Y., Blue and Green Photoluminescence Graphene Quantum Dots Synthesized from Carbon Fibers. *Mater. Lett.* **2013**, *93*, 161–164.

48. Zhang, W. F.; Zhu, H.; Yu, S. F.; Yang, H. Y., Observation of Lasing Emission from Carbon Nanodots in Organic Solvents. *Adv. Mater.* **2012**, *24*, 2263–2267.

49. Dong, Y.; Shao, J.; Chen, C.; Li, H.; Wang, R.; Chi, Y.; Lin, X.; Chen, G., Blue Luminescent Graphene Quantum Dots and Graphene Oxide Prepared by Tuning the Carbonization Degree of Citric Acid. *Carbon* **2012**, *50*, 4738–4743.

50. Philippidis, A.; Spyros, A.; Anglos, D.; Bourlinos, A. B.; Zbořil, R.; Giannelis, E. P., Carbon-dot Organic Surface Modifier Analysis by Solution-state NMR Spectroscopy. *J. Nanopart. Res.* **2013**, *15*, 1777.

51. Ye, R.; Xiang, C.; Lin, J.; Peng, Z.; Huang, K.; Yan, Z.; Cook, N. P.; Samuel, E. L. G.; Hwang, C.-C.; Ruan, G.; Ceriotti, G.; Raji, A.-R. O.; Martí, A. A.; Tour, J. M., Coal as an Abundant Source of Graphene Quantum Dots. *Nat. Commun.* **2013**, *4*, 2943.

Chapter 3: Catalytic Carbon Dot Reduced Bimetallic Nanoparticles: Size and Surface Plasmon Resonance Tunability Towards Plasmon-Enhanced Photovoltaics†

†This chapter is based on a submitted and accepted peer-reviewed manuscript in *J. Mater. Chem.* A. The information contained herein is adapted with permission from Essner, J. B.; Laber, C. H.; Baker, G. A., Carbon Dot Reduced Bimetallic Nanoparticles: Size and Surface Plasmon Resonance Tunability for Enhanced Catalytic Applications. *J. Mater. Chem.* A **2015**, *3*, 16354–16360. Copyright © 2015 Royal Society of Chemistry.

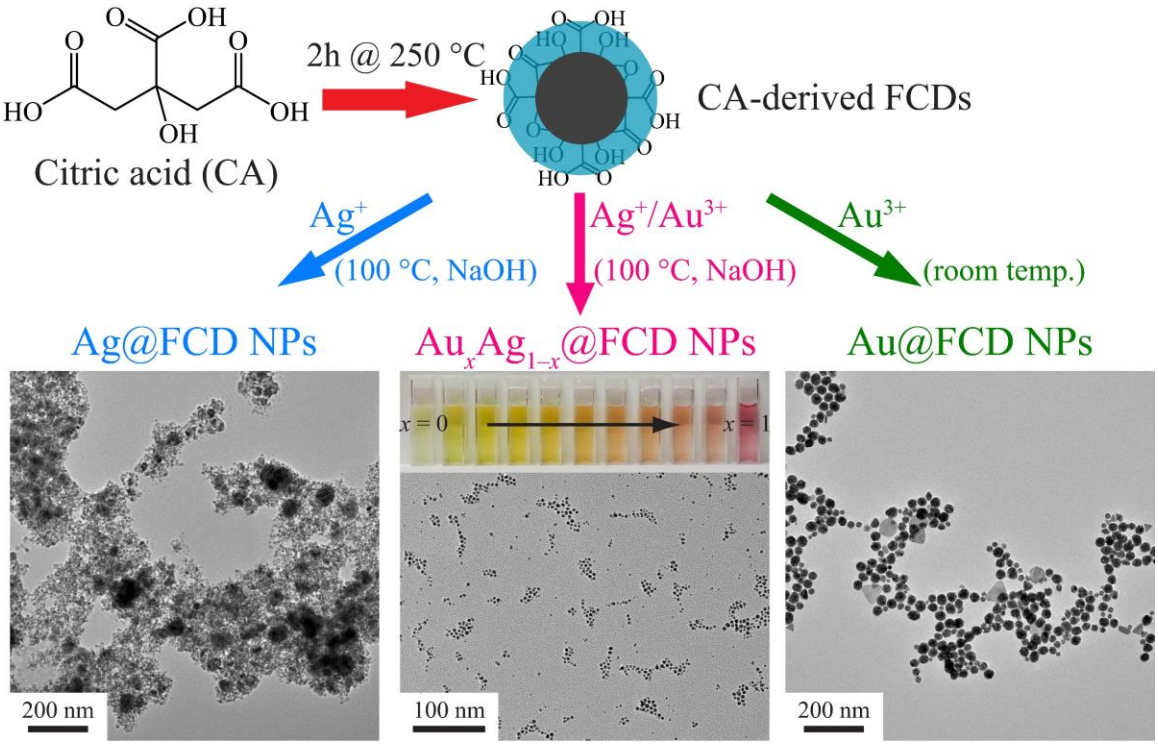

Scheme 3.1 Graphical abstract highlighting the synthesis of CA-derived fluorescent carbon dots (FCDs) and their use as dual reducing and capping agents to produce Ag@FCD, Au@FCD, and Au_xAg_{1-x}@FCD NPs, the latter of which showed a high degree of spectroscopic tunability upon varying the Au:Ag ratio.

Abstract

A simple and green route toward monometallic (Au or Ag) and alloyed bimetallic AuAg nanoparticles using CA-derived FCDs as the reducing and stabilizing agent is reported. Simple variation in the initial FCD:metal ratio yields a smoothly tunable surface plasmon resonance and the resulting nanomaterials show excellent catalytic activity for 4-nitrophenol reduction, which is fully preserved following 5 months of storage. Furthermore, the Au@FCD catalyst demonstrated intrinsic peroxidase-like activity.

Introduction

Metal nanoparticles, especially those consisting of Au or Ag, have received increasing attention in recent years owing to their attractive electronic, thermal, optical, and chemical properties, making them applicable in a wide range of fields such as catalysis, biomedicine, photovoltaics, antimicrobials, and surface-enhanced Raman spectroscopy (SERS).[1-6] In particular, the observed properties of these monometallic nanoparticles (hereafter, referred to as MNPs) are greatly influenced by their size, shape, crystal structure, and composition, characteristics that also dictate how these particles interact with incident light. When the size of the nanoparticle is substantially smaller than the wavelength of incident light, it experiences a relatively uniform electric field, resulting in a collective oscillation of conduction electrons. This gives rise to an energy-dependant resonance known as the surface plasmon resonance (SPR). When incorporated into photovoltaic (PV) solar cells, these MNPs can behave as light-concentrating antennae or light-scattering centers, depending on their size or morphology, which leads to increased photon absorption and device performance.[7] Furthermore, the optoelectronic properties of the MNPs can be

altered or enhanced by incorporating other metals into their structure or by the formation of composites or heterostructures. Indeed, bimetallic NPs (BMNPs) have shown enhanced properties over their monometallic counterparts because of a synergetic coupling between the individual metals' SPRs.[8-10] The addition of this second metal can improve the electronic and absorption properties, giving rise to SPR bands lying intermediate between the individual MNP SPRs, thereby enhancing catalytic, antimicrobial, and, in particular, PV prospects for the material. Recently, Haldar *et al*. reported on the synthesis of Au@Ag bimetallic core-shell NPs with varying Au core diameters.[9] These researchers showed that the catalytic efficiency toward the reduction of 4-nitrophenol (4-NP) varied with the Au core size, however, the bimetallic core-shell NPs were still up to 12 times more active than their monometallic Au counterparts. In a similar vein, our group recently demonstrated a green, sunlight-assisted approach toward the generation of bimetallic AuAg alloys decorated onto 3-aminopropyl-functionalized magnesium phyllosilicate nanoclay sheets.[10] In this work, the BMNP-decorated aminoclays possessed superior catalytic and antibacterial activity compared to their pure Ag or Au NP decorated analogs.

Historically, approaches such as laser ablation[11] and chemical reduction (*e.g.*, $NaBH_4$,[12-13] hydrazine[14]) have been commonly employed to generate MNPs but these methods required either timely, complex, resource-limited equipment, or hazardous chemicals to carry out the reduction. This scenario impelled researchers to shift toward simple, environmentally friendly, and cost-effective approaches for synthesizing various MNPs, including consideration of phytochemicals found in plant and fruit extracts as the reducing and stabilizing agents.[15-24] For example, Nadagouda *et al*. presented a greener synthetic approach for generating both Au and Ag NPs using blackberry, blueberry,

pomegranate, and turmeric extracts, taking advantage of the electron-donating capabilities of the antioxidants present in the extracts.[19] Use of these greener reducing agents has also recently been extended to the formation of bimetallic AuAg NPs. For example, Kumari *et al*. used pomegranate juice to generate both alloyed AuAg and core-shell Au@Ag NPs.[25] Recently, FCDs prepared by various methods have shown promise as reducing agents towards the formation of Au and Ag NPs,[26-36] owing to their intrinsic ability to act as electron donors/acceptors.[37] For instance, Luo and co-workers demonstrated that electrochemically synthesized FCDs functioned as reducing and stabilizing agents in the preparation of Au@FCD nanocomposites that displayed tunable particle diameters by varying the chloroauric acid:FCD ratio.[36] Similarly, Shen *et al*. reported the reductive capabilities of hydrothermally synthesized FCDs for Ag NP growth where the resultant Ag NP size varied when the silver nitrate:FCD ratio was altered.[35] Owing to the enticing prospects of FCDs as additives or replacements to costly components in PV devices, in particular, in sensitized metal oxide solar cells, as well as the established efficiency-enhancing capabilities of MNPs via exploitation of their SPRs, these MNP/FCD composites may hold promise as low-cost, green materials toward improved PV performance.

Since the serendipitous discovery of FCDs over a decade ago, research into their formation and application has grown exponentially due to their many attractive optical and physical properties, including large red-edge effects (*i.e.*, excitation wavelength-dependant emission), electron-donating/accepting capabilities, high aqueous solubility, extreme photostability, and low cytotoxity.[38-49] Despite the "green" nature of FCDs, in general, many synthetic approaches, such as arc-discharge,[39] laser ablation,[40] and acid oxidations,[41-

[42] often involve unsustainable precursors, harsh acidic/alkaline conditions, high synthetic temperatures, or extensive pre- or posttreatments, which are inconsistent with the principles of green chemistry. Therefore, greener synthetic strategies such as microwave, thermal, or hydrothermal treatment of various sustainable precursors (*e.g.*, citric acid,[43-44] urea[44]) or low-value waste materials such as grass,[45] fruit peels (*e.g.*, pomelo,[46] watermelon,[47] banana,[48] orange[49]), and, even human urine,[50] are being aggressively pursued. For example, Dong *et al*. recently demonstrated that either FCDs or graphene oxide could be selectively generated through a simple thermal degradation of solid citric acid, where the degree of carbonization dictated the resultant product.[43]

In this chapter, the thermal degradation of solid citric acid (CA) to produce FCDs following methods slightly modified from that reported by Dong and co-workers is described. The resultant FCDs were competent reducing agents for the thermally assisted formation of Ag NPs as well as the ambient-temperature synthesis of Au NPs. Similar to previous reports,[35-36] varying the FCD:metal salt ratio resulted in different MNP sizes and morphologies, an influence reflected in the observed SPRs. Interestingly, the FCDs were also effective for the co-reduction of both Au and Ag salts to synthesize Au_xAg_{1-x}@FCD BMNPs. To the best of our knowledge, this is the first example of BMNP formation using FCDs as the reducing and stabilizing agent. Due to the synergistic effect of the two metals' SPRs, the Au_xAg_{1-x}@FCD BMNPs showed marked improvements in the catalytic reduction of 4-nitrophenol (4-NP) over their monometallic Au@FCD NPs counterpart. Perhaps more surprisingly, the Ag@FCD NPs possessed catalytic activities comparable to that of the $Au_{0.5}Ag_{0.5}$@FCD NPs.

Experimental

Materials and Reagents

All experiments were carried out using Ultrapure Millipore water polished to a resistivity of 18.2 MΩ·cm. Anhydrous citric acid (791725, 99.5%), silver(I) nitrate (204390, 99.9999%), gold(III) chloride hydrate ($HAuCl_4$, 254169, 99.995%), sodium hydroxide (306576, 99.99%), sodium borohydride (480886, 99.99%), 4-nitrophenol (241326, ≥99%), 2,2′-azino-bis(3-ethylbenzothiazoline-6-sulfonic acid) diammonium salt (ABTS, 11557, 98%), and hydrogen peroxide (216763, 30 wt%) were purchased from Sigma-Aldrich (St. Louis, MO). All chemicals were used as received. Dialysis tubing (132105, Spectra/Por® 7, 1 kDa molecular weight cut-off or MWCO) was purchased from Repligen® (formerly Spectrum Labs®, Rancho Dominguez, CA).

Citric Acid-derived Fluorescent Carbon Dot Synthesis

In a typical synthesis, 50 g of solid, anhydrous citric acid (CA) and a PTFE-coated, magnetic stir bar were added to a round bottom flask. The round bottom was placed into an improvised sand bath consisting of an anodized aluminum, round cake pan (Fat Daddio's®) filled with copper-coated airgun BBs (0.177 caliber; Crosman® Copperhead®) and the CA was thermally decomposed at 250 °C (300 rpm) for 2 h, with temperature control achieved to within 2 °C using a digital stirring hotplate (Super-Nuova™; Thermo Scientific™) connected to a J-type thermocouple immersed in the BBs. The resultant dark red product was dissolved in 50 mL of water and then centrifuged for 30 min at 5k rpm to remove any larger particles. The supernatant was transferred to a cellulose dialysis membrane (1 kDa MWCO) and dialyzed for 48 h against 1.5 L of water, replenishing the exchange solvent with a fresh 1.5 L aliquot of water after 24 h. Upon completion of

dialysis, the dark orange solution was lyophilized and stored in a drawer until needed. A 5 mg mL^{-1}, aqueous stock solution of the CA-derived FCDs was prepared and employed for all characterizations and MNP syntheses, diluting as needed.

Au@FCD Nanoparticle Syntheses

For the nanoparticle syntheses discussed here, as well as in the next two sections, all metal ion reductions were conducted in 20 mL borosilicate glass scintillation vials (Fisherbrand™ 03-337-7). Initially, a broad range of FCD to chloroauric acid ($HAuCl_4$; hereafter, simply referred to as Au) ratios were tested for Au reduction at various temperatures (100 °C, 60 °C, 40 °C, and room temperature). While Au NP formation appeared to occur at all tested temperatures and an increase in reaction temperature resulted in more rapid reduction, the FCDs adequately reduced Au at room temperature over a 1–4 h period. Therefore, all subsequent Au reductions were carried out at room temperature. For the Au reductions, a 2 mg mL^{-1} aqueous solution of the FCDs was prepared and two series of room temperature Au reductions were generated; one in which the Au concentration was kept constant with increasing FCD additions and another in which the FCD concentration was kept constant with increasing Au additions. For the constant Au series, the concentration of Au was held at 0.3 mM while increasing amounts of FCDs were added to generate concentrations of 0.05, 0.15, 0.30, 0.45, and 0.60 mg mL^{-1}. Conversely, for the other series, the FCD concentration was held constant at 0.30 mg mL^{-1} and the Au concentration was increased from 0.10 to 0.60 mM in 0.05 mM increments. For all metal reductions conducted at elevated temperatures (including the Ag and AuAg reductions discussed below), scintillation vials containing the FCD solutions were heated in a circular, anodized aluminum reaction block (Chemglass® CG-1991-03) with temperature control

achieved to within 2 °C using a digital stirring hotplate (Super-Nuova™; Thermo Scientific™) connected to a J-type thermocouple inserted in the thermowell of the reaction block.

Ag@FCD Nanoparticle Syntheses

Similar to the Au reductions, a broad range of FCD to $AgNO_3$ (hereafter, simply referred to as Ag) ratios were tested for Ag reduction at various temperatures (100 °C, 90 °C, 70 °C, 50 °C, 30 °C, and room temperature). Unfortunately, no apparent Ag NP formation occurred at any of the tested temperatures. Based on related literature,[35] the addition of NaOH, at final concentrations of 1, 10, and 20 mM, was tested at all of the above temperatures. While the addition of NaOH promoted the reduction of Ag at all tested temperatures, it was found that temperatures >80 °C and NaOH concentrations of 20 mM resulted in the optimal formation of Ag NPs. Therefore, for all subsequent Ag reductions, the NaOH concentration was held constant at 20 mM and a reduction temperature of 100 °C was employed. To initiate the formation of Ag@FCD NPs, the alkaline FCD solution was heated at 100 °C for 15 min and then various aliquots of Ag were added, heating the samples at 100 °C for an additional 15 min. Akin to the Au reductions, two series of Ag reductions were generated; one in which the Ag concentration was held constant with increasing FCD additions and another in which the FCD concentration was kept constant with increasing Ag additions. For the constant Ag series, the concentration of Ag was held at 1 mM while increasing amounts of FCDs were added to generate concentrations of 0.05, 0.15, 0.30, 0.45, and 0.60 mg mL^{-1}. For the constant FCD series, the concentration of FCDs was maintained at 0.3 mg mL^{-1} while increasing amounts of Ag were added to generate concentrations of 0.15, 0.30, 1.0, 1.5, and 3.0 mM.

Au_xAg_{1-x}@FCD Nanoparticle Syntheses

First, 7 mL of a 0.43 mg mL^{-1}, aqueous FCD solution was heated at 100 °C for 15 min to allow for thermal equilibration. NaOH was then added to $HAuCl_4$ to produce gold hydroxide, $Au(OH)_4^-$, after which the $Au(OH)_4^-$ and $AgNO_3$ solutions were simultaneously added to the hot FCD solution and allowed to react for 15 min. Specifically, aliquots of 10 mM $Au(OH)_4^-$ and 10 mM $AgNO_3$ were simultaneously injected into the hot FCD solution to generate Au:Ag ratios of 90:10, 80:20, 70:30, 60:40, 50:50, 40:60, 30:70, 20:80, and 10:90, where the combined metal salt concentrations in the final samples always totaled 1 mM. For example, to generate a 50:50 Au:Ag sample, 0.5 mL of 10 mM $HAuCl_4$ was added to 2 mL of 100 mM NaOH and the alkaline Au solution was then injected, alongside 0.5 mL of 10 mM $AgNO_3$, into the hot FCD solution. In all instances, the final FCD and NaOH concentrations were held constant at 0.3 mg mL^{-1} and 20 mM, respectively.

Characterization Techniques

Absorbance and steady-state fluorescence spectra were acquired with a Varian Cary® Bio 50 UV-vis spectrophotometer and a Varian Cary® Eclipse spectrofluorometer, respectively, using PMMA cuvettes. 4-Nitrophenol catalytic and peroxidase mimetic studies were conducted in quartz microcuvettes (1 mL) and PMMA cuvettes, respectively, monitoring the reaction rates using the same Cary® spectrophotometer. Transmission electron microscopy (TEM) studies were conducted on carbon coated copper grids (Ted Pella, Inc., 01822-F, support films, ultrathin carbon type-A, 400 mesh copper grid) using a FEI® Tecnai™ (F30 G2, Twin) microscope operated at a 300 keV electron acceleration voltage.

4-Nitrophenol (4-NP) Catalytic Studies

For the catalytic rate studies, 400 µL of 0.2 M $NaBH_4$, 400 µL of 0.2 mM 4-NP (1000:1 $NaBH_4$:4-NP mole ratio), and 20 µL of the catalysts (Au (or Ag)@FCDs and Au_xAg_{1-x} @FCDs; 0.2 mM metal concentration) were combined in a 1 mL microcuvette and UV-vis spectra were collected every 5 s until the characteristic 4-NP peak at 400 nm disappeared. More specifically, the as-synthesized Ag@FCD NP and Au_xAg_{1-x}@FCD BMNP samples were diluted 5-fold using water. Since the Au@FCD NPs did not contain NaOH and were at a lower overall metal concentration then the other samples, these catalysts were only diluted 1.25-fold using 20 mM NaOH to keep the base (4 mM in MNP solutions; 97.6 µM in cuvettes) and metal concentrations (0.2 mM stocks; 4.9 µM in cuvettes) similar in all samples. Within these diluted samples, the highest FCD concentration (0.24 mg mL^{-1}) was present within the Au@FCD NPs due to the smaller dilution factor. Therefore, for the FCD control studies, a 2 mg mL^{-1} stock solution of FCDs was diluted 8.3-fold to generate a 0.24 mg mL^{-1} solution and 20 µL of this solution was used in place of the nanocatalyst composites. Prior to use, the 0.2 mM stock solution of 4-NP was degassed for 20 min to remove any dissolved gases, minimizing the induction time. In addition, freshly prepared (less than 3 h old) $NaBH_4$ was used in all catalytic studies.

Peroxidase-like Activity Studies

For conducting the peroxidase mimetic studies, select volumes of MNP@FCD solution (ranging from 15.6 to 500 µL) plus 100 µL of 25 mM ABTS were mixed in disposable PMMA cuvettes and diluted with deionized water to bring the total volume to 3.1 mL. To initiate the reaction, a 5 µL droplet of 30 wt% H_2O_2 was carefully pipetted onto the side of the cuvette and gently mixed by manually inverting the cuvette twice. This procedure

resulted in concentrations of 0.805 mM ABTS and 5.4 mM H_2O_2. The peroxidase-like activity was assessed by monitoring the absorbance at 418 nm over a 45 min period, collecting data points every 30 s. A control experiment was carried out using neat FCDs at a concentration of 9.7 μg mL^{-1}. While no activity was observed on this timescale for unmodified FCDs, as shown in Figure B.12, Au@FCDs clearly produced pronounced activities that increased with nanocatalyst concentration. The concentrations listed in Figure B.12 denote the concentration of FCDs within the aliquot of Au@FCDs added. Specifically, the different samples contained the following concentrations of FCDs and Au in μg mL^{-1} and μM, respectively (assuming both are uniformly dispersed): 3.0 and 1.5, 6.0 and 3.0, 12.1 and 6.0, 24.2 and 12.1, and 48.3 and 24.2. Note, no activity was observed for Ag@FCDs or $Au_{0.5}Ag_{0.5}$@FCDs over the time period monitored; that is, 24 h after initiating the reaction.

Results and Discussion

Photophysical and Structural Characterizations of the CA-derived FCDs

The detailed experimental procedures and characterizations of the FCDs employed in this work are provided in "Citric Acid-derived Fluorescent Carbon Dot Synthesis" under the "Experimental" section above and Figure B.1 of Appendix B, respectively. Briefly, 50 g of solid CA was thermally decomposed at 250 °C for 2 h. The resultant dark red product was redispersed in deionized water, centrifuged, dialyzed, and then lyophilized. The CA-derived FCDs displayed properties akin to those of previously reported FCDs.[38, 47, 49] Specifically, the FCDs showed increasing absorbance with decreasing wavelength (Figure B.1A, dashed black line), which arises from the π-π^* transition of aromatic sp^2 domains and is likely due to the broad size distribution of FCDs produced.[47, 49] Similar to other

reported FCDs,[38, 47] the CA-derived FCDs displayed excitation wavelength-dependent emission with a maximum emission occurring near 470 nm under 350 nm excitation (Figure B.1A). The emission intensity increased as the excitation wavelength was increased from 300 to 350 nm, after which it decreased and redshifted. The decrease in emission is further highlighted and quantified by the excitation wavelength-dependent quantum yields (Figure B.1A, inset). The resultant CA-derived FCDs were slightly larger than those typically reported in the literature (*e.g.*, 1–10 nm),[38] ranging in size from 30 to 60 nm with some dots reaching 100 nm (Figure B.1B).

Fourier-transform infrared (FTIR) spectroscopic analysis indicated that the FCDs possessed hydroxyl, carboxyl, and epoxide moieties, accounting for their hydrophilicity and excellent dispersibility in water (Figure B.1C).[43] The large, broad absorption bands between 3600 and 3000 cm^{-1} were assigned to the stretching vibrations of O–H (ν_{O-H}). Well-defined absorbance bands appeared between 1800 cm^{-1} and 1600 cm^{-1} that were ascribed to the stretching vibrations of C=O ($\nu_{C=O}$) and the skeletal vibrations of aromatic groups ($\nu_{C=C}$). The various peaks between 1300 and 1000 cm^{-1} arose from the different stretching modes of carboxylic, ester, ether, and alcohol moieties (ν_{C-O-C} and ν_{C-OH}), while the peaks near 2900, 1400, and 915 cm^{-1} were attributed to aliphatic carbons (ν_{C-H} and $\nu_{=C-H}$). The presence of these functionalities account for the long-term dispersibility of FCDs in water. Due to these surface functionalities and based on previous literature reports,[26-36] we posited that the CA-derived FCDs would likely function as reducing, as well as capping, agents in the formation of MNPs. After optimizing the reaction conditions (details can be found in the "Au@FCD Nanoparticle Syntheses" and "Ag@FCD Nanoparticle Syntheses" subsections under the "Experimental" section above), it was revealed that FCDs were

capable of directly reducing $HAuCl_4$ to Au NPs at room temperature, whereas Ag reduction required alkaline conditions and elevated temperatures with the most promising results achieved using 20 mM NaOH (pH>10) and a reaction temperature of 100 °C.

Synthesis and Photophysical Properties of the Au@FCD Nanoparticles

For the room temperature reduction of Au, various ratios of FCDs:Au were tested in two fashions: 1) using a constant FCD concentration for varying Au precursor additions and 2) maintaining a constant Au concentration for varying FCD additions. A given concentration of Au (0.3 mM) with increasing amounts of FCDs (0.05–0.60 mg mL^{-1}) resulted in increased SPR intensities accompanied by a blueshift (indicative of smaller Au NPs) until the FCD concentration reached 0.30 mg mL^{-1}, after which the SPR intensities remained relatively constant and presented a negligible shift in wavelength (Figure B.2). On the other hand, for a given concentration of FCDs (0.30 mg mL^{-1}) in the presence of increasing amounts of Au (0.10–0.60 mM; 0.05 mM increments), the SPR increased and drastically redshifted (indicative of larger Au NPs) pointing towards the potential tunability of the resultant Au NPs (Figure 3.1B and C). Specifically, between Au concentrations of 0.10 and 0.35 mM, slight bathochromic shifts arose accompanied by increases in SPR intensity while for Au concentrations greater than 0.35 mM, large bathochromic shifts in the SPR were apparent. At these higher concentrations of Au, the SPR intensities increased up to 0.45 mM, after which the SPRs decreased and substantial peak broadening occurred, features that are indicative of larger, more polydisperse Au NPs. Based on these results, the CA-derived FCDs appear to function effectively as both reducing and stabilizing agents. The results also indicate the clear potential for fine-tuning the Au SPR (Figure 3.1C), and concurrently the Au NP size, simply by varying the FCD:Au ratio.

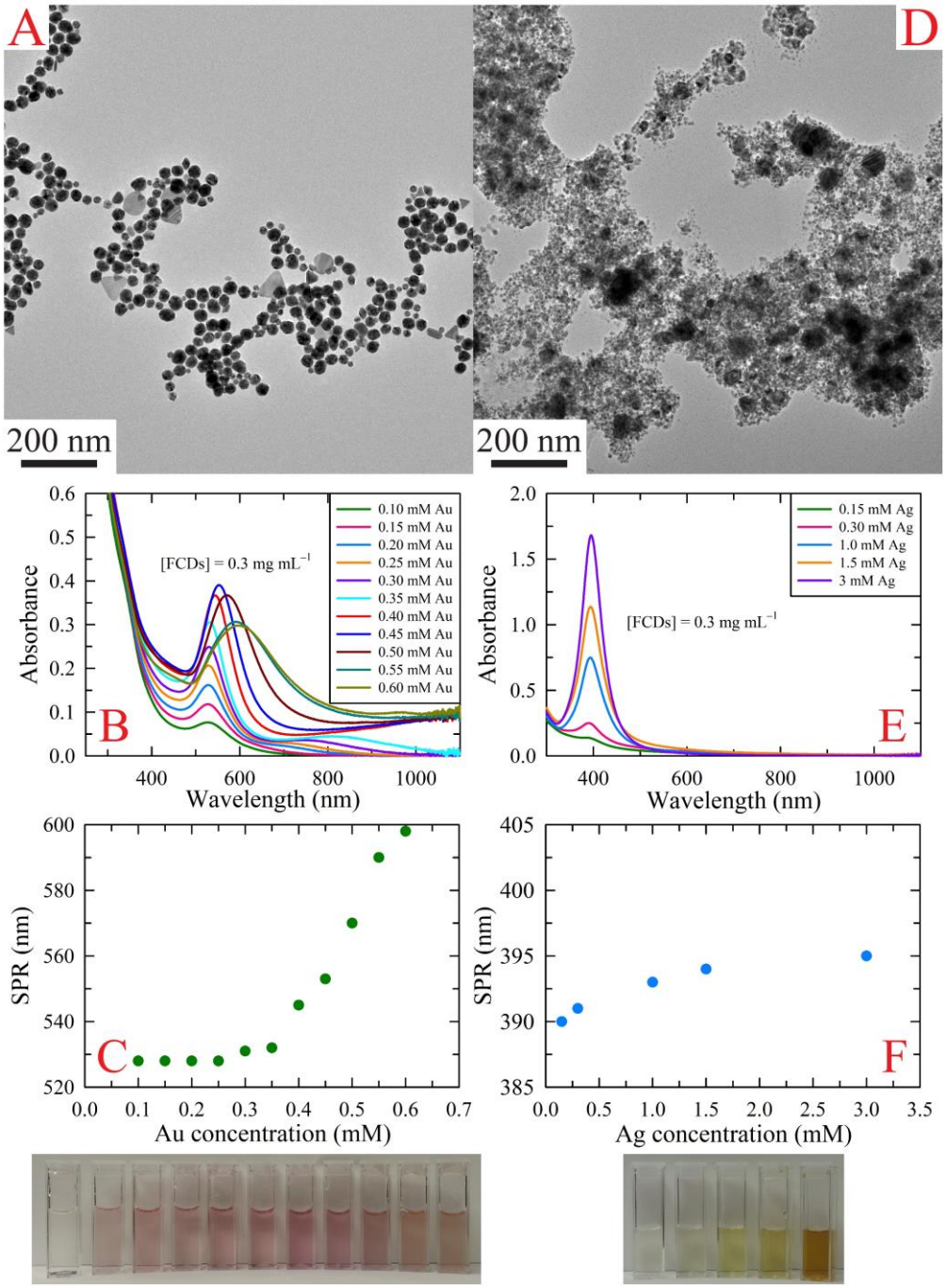

Figure 3.1 Representative TEM micrographs of (A) Au@FCD and (D) Ag@FCD NPs. Shown are results for 0.3 mg mL^{-1}:0.35 mM and 0.3 mg mL^{-1}:0.30 mM FCDs:metal ratios for Au and Ag reductions, respectively. The SPR shifts of the resultant particles (panels B–F) show the smooth tunability afforded simply by changing the FCD:metal ratio. In the case of Au NPs (B and C), the SPR intensity initially increased, reaching a maximum at a 0.3 mg mL^{-1} FCD:0.45 mM Au ratio. The increase was also accompanied by a slight

bathochromic shift. Higher Au:FCD ratios resulted in a continuous redshift with decreasing SPR intensity and substantial peak broadening, indicative of larger, more polydisperse NPs. On the other hand, the Ag NPs (E and F) displayed only a slight bathochromic shift in SPR, with increasing intensities as the Ag concentration was varied from 0.15 to 3 mM. The lower photographs correspond to the Au and Ag samples in panels B–C and E–F, respectively.

The SPR bathochromic shifts and peak broadening were attributed to increases in particle size and higher degrees of polydispersity, respectively, as evidenced in Figure B.3. For example, the 0.20 mM, 0.35 mM, 0.45 mM, and 0.60 mM Au concentrations resulted in 17.8 ± 6.4, 26.7 ± 10.0, 47.8 ± 20.7, and 96.7 ± 29.9 nm quasi-spherical particles, respectively. The 0.3 mg mL^{-1}:0.35 mM FCD:Au ratio is also shown in Figure 3.1A. Moreover, for higher concentrations of Au, large hexagonal and trigonal plates formed, with a higher amount of plate formation occurring with increasing Au:FCD ratios. Although sample stability initially appeared to decrease for higher Au concentrations, the samples could be easily redispersed and the sedimentation was actually linked to the presence of large Au nanoplates which settled from solution within a couple days. Indeed, the 0.45 mM and 0.60 mM Au concentrations afforded 266.7 ± 99.3 and 528.8 ± 214.3 nm plates with approximate quasi-spherical:plate ratios of 1:5 and 1:2, respectively. The increasing formation of large hexagonal and trigonal plates translated to substantial peak broadening within the UV-vis spectra and bathochromic shifts of the SPR, resulting in a color transition of the solutions from red to blue/purple. Interestingly, the higher Au concentrations still produced a population of small Au NPs in the 5–20 nm size range (Figure B.3C and D insets), however, these particles were relatively rare in these samples.

To gain additional insight into the reduction process and the photophysical characteristics of the Au@FCDs, the room temperature reduction of 0.3 mg mL^{-1}

FCDs:0.35 mM Au samples was monitored via UV-vis and fluorescence spectroscopies (Figure B.4). After 180 min, the intensity of the SPR band (absorbance at 544 nm) was still increasing, although the SPR growth rate had begun to slow, indicating that the Au reduction was nearing completion (Figure B.4A inset; left vertical axis). Throughout the reduction, the SPR remained consistently near 544 nm (Figure B.4A inset; right vertical axis), elucidating that the increase in absorbance was due to the growth of additional NPs of a similar size rather than new species possessing different optical characteristics. Intriguingly, despite the intrinsic quenching nature of Au, the Au@FCDs retained ~25% of the original fluorescence from the FCD parent solution (Figure B.4B). The inset plot of Figure B.4B shows that, initially, the fluorescence rapidly decreased but eventually stabilized. Over the monitoring period, the wavelength of maximum emission from the FCDs remained relatively constant near 460 nm.

Synthesis and Photophysical Properties of the Ag@FCD Nanoparticles

Similar to the case for Au reduction, various FCD:Ag ratios were tested at room temperature for potential reduction to Ag NPs. In this case, no Ag NP formation was evident even after a week's time. Based on its past use in promoting noble metal reduction,[26, 35] various concentrations of NaOH (1, 10, or 20 mM) were added and elevated temperatures were employed (30, 50, 70, 90, or 100 °C) in an attempt to drive Ag^+ reduction. Although some Ag NP formation was evident at lower temperatures and modest NaOH concentrations, the best results (on the basis of narrow and intense SPR bands) were achieved at 100 °C using 20 mM NaOH. Under these conditions, various FCD:Ag ratios were assayed. The Ag reductions displayed a decreased SPR dependency on FCD:metal ratios compared to their Au reduction counterparts. When the FCD concentration was held

constant (0.3 mg mL^{-1}) and increasing amounts of Ag were added (0.15–3.0 mM), the SPR intensity drastically increased (indicative of increased Ag NP formation) whilst showing negligible shift in wavelength (Figure 3.1E and F). On the other hand, when the Ag concentration was held constant at 1.0 mM and increasing amounts of FCDs (0.05 to 0.60 mg mL^{-1}) were added, the SPR intensity again increased but displayed a small hypsochromic shift followed by a slight bathochromic shift (Figure B.5). In spite of this slight SPR shift, an increasing Ag:FCD ratio apparently generated slightly smaller Ag NPs (Figure B.6). A size analysis, conducted by counting over 200 particles per sample, resulted in mean particle sizes of 11.1 ± 9.9, 6.9 ± 3.4, and 6.0 ± 4.0 nm for the 0.30 mM, 1.0 mM, and 3.0 mM Ag concentrations, respectively. A representative TEM micrograph for the Ag@FCD sample derived from a 0.3 mg mL^{-1}:0.30 mM FCD:Ag sample is also shown in Figure 3.1D.

Synthesis and Photophysical Properties of the Au_xAg_{1-x}@FCD Bimetallic Nanoparticles

Both the Ag@FCD and Au@FCD NPs, due to their plasmonic nature, hold prospects for SERS and, in particular, PV applications, but to further enhance the applicability of these MNPs@FCDs, attempts to simultaneously reduce both Ag and Au salts to generate Au_xAg_{1-x}@FCD BMNPs were explored. The fact that Ag reduction for the generation of Ag@FCDs was only obtainable under basic conditions required that the synthetic approach be tailored in order to arrive at BMNPs. Firstly, NaOH was added to $HAuCl_4$ to produce gold hydroxide, $Au(OH)_4^-$. The FCD solution was then heated at 100 °C for 15 min to allow for thermal equilibration. Lastly, $Au(OH)_4^-$ and $AgNO_3$ solutions were simultaneously injected into the hot FCD solution and were allowed to react for 15 min. In all instances, the FCD, NaOH, and total metal salt concentrations were held constant at 0.3

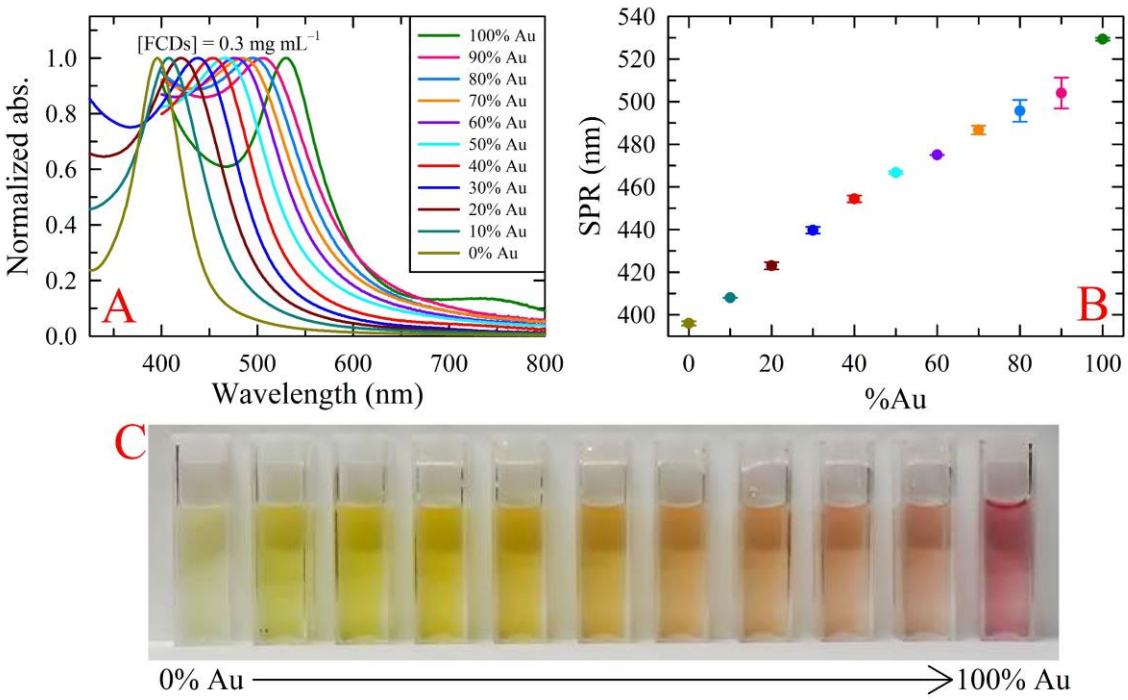

Figure 3.2 (A) Normalized UV-vis absorbance of the bimetallic Au_xAg_{1-x}@FCD NPs showing that as the experimental Au:Ag ratio decreased the resultant SPR displayed a systematic hypsochromic shift. (B) Extracted SPR frequencies plotted *vs* the %Au, further demonstrating the smooth evolution in SPR wavelength as the Au:Ag ratio was modulated. The sample sets were replicated three times highlighting the reproducibility of the BMNPs (error bars denote one standard deviation from the mean), especially at the lower Au concentrations. (C) Photograph of a series of Au_xAg_{1-x}@FCD BMNP samples, illustrating a palette of SPR transitions. The cuvettes correspond to the samples in panels A and B from 100% Ag (left) to 100% Au (right).

mg mL^{-1}, 20 mM, and 1 mM, respectively. Aliquots of 10 mM $HAuCl_4$ and 10 mM $AgNO_3$ were mixed to generate Au:Ag ratios of 90:10, 80:20, 70:30, 60:40, 50:50, 40:60, 30:70, 20:80, and 10:90 (Figure 3.2A). For example, to generate the 50:50 Au:Ag BMNP sample, 0.5 mL of 10 mM $HAuCl_4$ was added to 2 mL of 100 mM NaOH which was simultaneously injected, alongside 0.5 mL of 10 mM $AgNO_3$, into 7 mL of hot FCD solution (0.43 mg mL^{-1}). Samples containing 100% Ag were made in analogous fashion, whereas the

preparation of 100% Au samples involved no addition of NaOH, in accordance with the Au@FCD preparation method described earlier. It is noteworthy that the use of $Au(OH)_4^-$ in the absence of Ag at 100 °C led solely to the formation of large gold plates. As the Au:Ag ratio decreased, the SPR uniformly blueshifted, consistent with the presence of BMNPs (Figure 3.2A and B).[10, 14, 25]

Reminiscent of the room temperature reduction of 0.6 mM Au, use of 1 mM Au at 100 °C yielded highly unstable particles that displayed a broad, redshifted SPR. For this reason, the 100% Au results reported in Figure 3.2 were generated using 0.25 mM Au. Given this observation, the effect of Au concentration on the resultant SPR was also investigated for 100 °C reductions (Figure B.7), where the results of these studies again reiterate the strong control over the SPR made possible by simply varying the ratio of Au:FCDs. To verify that the FCDs were indeed responsible for the reduction of the BMNPs, a control reaction was performed for a 50:50 Au:Ag sample in the absence of FCDs (Figure B.8). The lack of both a SPR band and a visible change in solution color indicated that the FCDs were solely responsible for accomplishing metal ion reduction.

Morphological and Compositional Analyses of the Au_xAg_{1-x}@FCD Nanoparticles

Both the Au@FCD and Ag@FCD NPs displayed larger particle sizes than all their bimetallic counterparts (Figure 3.3A–C and Figure B.9). Interestingly, upon the addition of 10% Ag, the average particle size dramatically decreased from 30.0 ± 6.0 nm for the Au@FCD NPs to 4.1 ± 1.4 nm for the $Au_{0.9}Ag_{0.1}$@FCD NPs. Increasing the Ag:Au ratio within the BMNPs led to further decreased particle size. For the $Au_{0.7}Ag_{0.3}$@FCD, $Au_{0.5}Ag_{0.5}$@FCD, $Au_{0.3}Ag_{0.7}$@FCD, and $Au_{0.1}Ag_{0.9}$@FCD BMNPs, the average particle sizes were 3.4 ± 0.9, 3.3 ± 1.1, 2.4 ± 0.8, and 1.9 ± 0.7 nm, respectively. Although a small

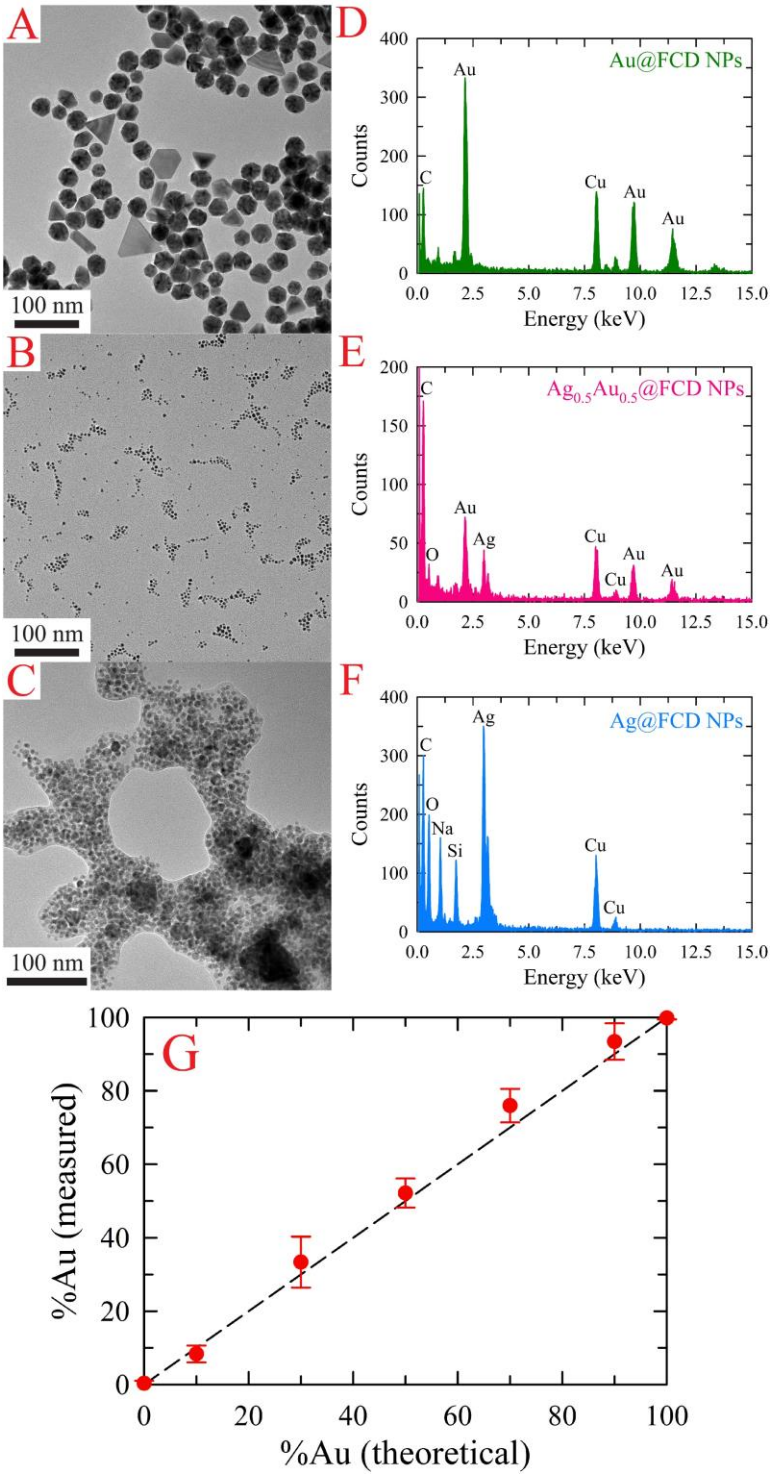

Figure 3.3 Representative TEM micrographs and their corresponding EDX spectra for (A and D) Au@FCDs, (B and E) bimetallic $Au_{0.5}Ag_{0.5}$@FCDs, and (C and F) Ag@FCDs. Interestingly, upon the slightest addition of silver, the NP's average size decreased by a factor of ~7 and remained relatively constant across the Au:Ag composition tested. (G)

Plot showing the extent of alloying between Au and Ag (%Au measured) within the BMNPs *vs* the content predicted from the initial Au:Ag stoichiometry (*i.e.*, %Au theoretical). The dashed line represents the ideal case where the measured values directly correspond to reagent metallic ratios. In general, the measured content follows the prediction line. The slight enrichment with Au at higher initial Au% could be tentatively tied to a small amount of galvanic replacement in which Ag^0 is etched by Au^{3+}.

decrease in particle size was present, the dependence of the SPR maximum on the Au:Ag ratio was primarily related to different levels of alloying and, therefore, synergistic plasmonic cooperation between the two metals.

Energy-dispersive X-ray (EDX) microanalysis of Au_xAg_{1-x}@FCD NPs was performed to reveal the average composition of the BMNPs (Figure 3.3D–F). As expected, the Au peaks became less prominent as the Au:Ag ratio decreased, whereas the Ag peaks became dominant. Figure 3.3G shows that the actual composition of the Au_xAg_{1-x}@FCD NPs was nominally the same as the starting Au:Ag ratios, although for Au:Ag fractions greater than 20:80, a slight enrichment in Au arose, possibly due to minor galvanic replacement of Ag with Au. Note, the Cu peaks observed in the EDX spectra arose from the copper grids employed for imaging.

Model Catalytic Application of the Au_xAg_{1-x}@FCD Nanoparticles

The catalytic activities of the MNPs@FCDs were studied through the model reduction of 4-nitrophenol (4-NP) to 4-aminophenol (4-AP) using $NaBH_4$ as the reducing agent. The reaction kinetics of the catalytic conversion were monitored via UV-vis spectroscopy. The aqueous solution of 4-NP displays little (pale yellow) to no color with an absorbance band at 320 nm. Upon the addition of $NaBH_4$, the solution immediately turns dark yellow due to the formation of the 4-nitrophenolate ion (4-NPO). The formation of 4-NPO results in an

increased absorbance accompanied by a bathochromic shift to 400 nm. To test for catalytic activities, UV-vis spectra were collected every 5 s following injection of $NaBH_4$ to monitor the decreasing absorbance at 400 nm (*i.e.*, loss of 4-NP). The 4-NP to 4-AP conversion was unaltered in the presence of the CA-derived FCDs (5.8 μg mL^{-1}) even after 30 min, demonstrating that unmodified FCDs are not catalysts for this reaction (Figure 3.4B; only shown out to 450 s). Upon addition of MNPs@FCDs to the 4-NPO solution, however, a prompt drop in absorbance at 400 nm was observed within seconds, indicating the rapid conversion of 4-NP to 4-AP (Figures 3.4A and B.10A–B). The complete reduction of 4-NP to 4-AP was observed within 120 s, 150 s, and >1000 s for Ag@FCDs, $Ag_{0.5}Au_{0.5}$@FCDs, and Au@FCDs, respectively. The reduction mechanism can be explained through the Langmuir-Hinshelwood mechanism, in which the analyte of interest (4-NPO) adsorbs on the surface of the MNPs, while the MNPs also react with the BH_4^- to form a metal hydride. The metal hydride then reacts with the sorbed analyte (4-NPO), facilitating its reduction. Due to the slow transfer of electrons from the metal hydride to 4-NPO, it is considered the rate determining step of the reaction.[51] This lag phase or induction time (t_o) in the reaction rate was minimized by degassing the 4-NP solution for 20 min to remove any dissolved oxygen. Despite this preventative measure, lag phases were still observed in the Au@FCD NP samples. In these studies, excess amounts (1000-fold) of $NaBH_4$ (0.2 M, 0.4 mL) compared to 4-NP were used (0.2 mM, 0.4 mL) so that the conversions would follow a pseudo-first-order rate law. Under these conditions, the apparent rate constants (k_{app}) for each catalyst can be estimated from the slopes of the linear correlation of $\ln(A_t/A_o)$ *vs* time, where A_o is the initial absorbance and A_t is the absorbance at time (t). The k_{app} values for Ag@FCD, $Ag_{0.5}Au_{0.5}$@FCD, and Au@FCD catalysts were

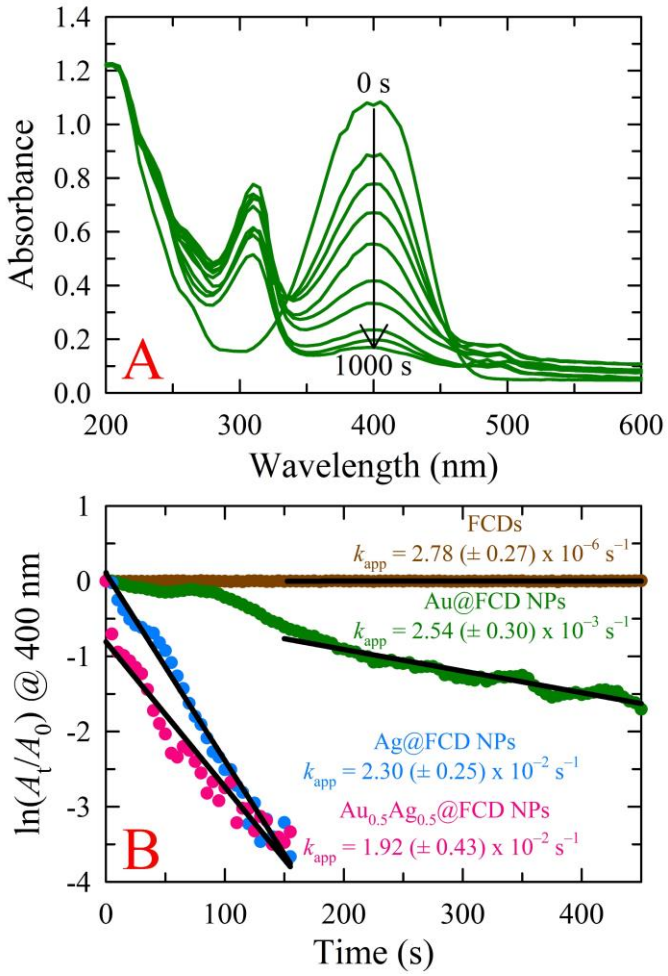

Figure 3.4 (A) Time-dependent UV-vis absorption spectra of the $NaBH_4$-assisted reduction of 4-NP catalyzed by the Au@FCD NPs. Spectra were acquired every 5 s but, for clarity, spectra are shown only for illustrative times. (B) Plots of $\ln(A_t/A_0)$ for 4-NP absorbance at 400 nm *vs* time for various metal NP@FCD catalysts. Each catalyst was tested within days of preparation.

2.30 (± 0.25) x 10^{-2} s^{-1}, 1.92 (± 0.43) x 10^{-2} s^{-1}, and 2.54 (± 0.30) x 10^{-3} s^{-1}, respectively (Figure 3.4B). Thus, the $Ag_{0.5}Au_{0.5}$@FCD and Ag@FCD catalysts showed improved activities (faster 4-NP reduction) over the Au@FCD NPs, an outcome attributed to their smaller sizes and, therefore, higher surface areas.

All three types of metal NPs@FCDs retained their catalytic activities after months of storage in a lab drawer. Even after 5 months of casual, ambient storage, the apparent rate

constants for 4-NP reduction were completely preserved. In fact, surprisingly, the Ag@FCD and $Ag_{0.5}Au_{0.5}$@FCD NPs displayed statistically meaningful *increases* in their catalytic rates. The k_{app} for the 5-month aged Ag@FCD, $Ag_{0.5}Au_{0.5}$@FCD, and Au@FCD catalysts were 3.83 (± 0.30) x 10^{-2} s^{-1}, 2.69 (± 0.39) x 10^{-2} s^{-1}, and 2.98 (± 0.22) x 10^{-3} s^{-1}, respectively (Figure B.10C). Since the aged Ag@FCD and $Ag_{0.5}Au_{0.5}$@FCD NPs showed improved catalytic rates over their freshly prepared NPs counterparts, UV-vis studies were conducted on both the aged and freshly prepared NPs to monitor any optical changes (Figure B.11). The Au@FCD NPs remained essentially unchanged after 5 months while the aged $Au_{0.5}Ag_{0.5}$@FCD and Ag@FCD NPs displayed increased absorbance at longer wavelengths, possibly due to minor nanoparticle aggregation. The slight particle aggregation upon prolonged storage may have resulted in catalytic "hotspots", accounting for the marginal increase in catalytic activity of the aged Ag@FCD and $Ag_{0.5}Au_{0.5}$@FCD NPs. Due to the surprisingly high catalytic rate of the Ag@FCD NPs and gold's established reputation as a good catalyst for this reaction, the improved catalytic rates of the BMNPs could be attributed to a synergistic effect of Au and Ag nano-domains within the individual particles, in line with results reported recently by Ravula *et al*.[10]

Application of the Au@FCD Nanoparticles as Peroxidase Memetics

Lastly, the potential of the MNP@FCD samples as peroxidase mimetics toward oxidation of the peroxidase substrate 2,2'-azino-bis(3-ethylbenzothiazoline-6-sulfonic acid) diammonium salt (ABTS) using H_2O_2 was examined. While neither $Ag_{0.5}Au_{0.5}$@FCDs nor Ag@FCDs displayed any measurable peroxidase-like activity within 24 h of prospective catalyst addition, the Au@FCDs demonstrated clear activity. As summarized in Figure B.12, addition of Au@FCDs triggered the formation of the green colored ABTS oxidation

product which was monitored spectrophotometrically at 418 nm. A control experiment carried out using CA-derived FCDs alone did not yield noticeable peroxidase-like activity. A dramatic increase in the catalytic velocity was observed in the time-dependent absorption profiles as the Au@FCD content was increased, validating the intrinsic peroxidase-like activity of the Au@FCDs in contrast with the naked FCDs. Among other things, these data open the possibility of using hybrid FCDs for selective glucose detection by coupling with glucose oxidase, for example.

Conclusions

In summary, a simple and green approach towards the synthesis of MNPs/BMNPs using FCDs as the reducing and stabilizing agent has been demonstrated. The resultant SPR of the various MNPs and BMNPs showed a systematic tunability indicating that the size of NPs can be easily controlled simply by varying the FCD:metal ratio. The Au_xAg_{1-x}@FCD metal compositions were nominally the same as the starting stoichiometric ratios, pointing to the efficacy of this nanoscale preparation. Notably, the Ag@FCD NPs and Au_xAg_{1-x} @FCD BMNPs displayed remarkably enhanced catalytic activities over Au@FCD for 4-nitrophenol reduction, highlighting the potential of these materials in various catalytic applications. Finally, the Au@FCD NPs showed peroxidase-like activity not seen in the unmodified FCDs nor in their Ag@FCD and Au_xAg_{1-x}@FCD analogs. Looking forward, these materials possess tantalizing potentials for exploitation in additional areas such as surface-enhanced spectroscopies and, most notably, plasmon-assisted photovoltaics.

Acknowledgements

The authors kindly thank Drs. Tommi White and Thomas Lam of the MU Electron Microscopy Core Facility for their assistance with all nanoparticle imaging.

References

1. Saha, S.; Pal, A.; Kundu, S.; Basu, S.; Pal, T., Photochemical Green Synthesis of Calcium-alginate-stabilized Ag and Au Nanoparticles and their Catalytic Application to 4-Nitrophenol Reduction. *Langmuir* **2009**, *26*, 2885–2893.

2. Qi, J.; Dang, X.; Hammond, P. T.; Belcher, A. M., Highly Efficient Plasmon-enhanced Dye-sensitized Solar Cells through Metal@Oxide Core–Shell Nanostructure. *ACS Nano* **2011**, *5*, 7108–7116.

3. Standridge, S. D.; Schatz, G. C.; Hupp, J. T., Distance Dependence of Plasmon-enhanced Photocurrent in Dye-sensitized Solar Cells. *J. Am. Chem. Soc.* **2009**, *131*, 8407–8409.

4. Sharma, V. K.; Yngard, R. A.; Lin, Y., Silver Nanoparticles: Green Synthesis and their Antimicrobial Activities. *Adv. Colloid Interface Sci.* **2009**, *145*, 83–96.

5. Chernousova, S.; Epple, M., Silver as Antibacterial Agent: Ion, Nanoparticle, and Metal. *Angew. Chem. Int. Ed.* **2013**, *52*, 1636–1653.

6. Mu, Z.; Zhao, X.-W.; Xie, Z.; Zhao, Y.; Zhong, Q.-F.; Bo, L.; Gu, Z.-Z., In Situ Synthesis of Gold Nanoparticles (AuNPs) in Butterfly Wings for Surface Enhanced Raman Spectroscopy (SERS). *J. Mater. Chem. B* **2013**, *1*, 1607–1613.

7. Atwater, H. A.; Polman, A., Plasmonics for Improved Photovoltaic Devices. *Nat. Mater.* **2010**, *9*, 205–213.

8. Chang, H.; Kang, H.; Yang, J.-K.; Jo, A.; Lee, H.-Y.; Lee, Y.-S.; Jeong, D. H., Ag Shell–Au Satellite Hetero-nanostructure for Ultra-sensitive, Reproducible, and Homogeneous NIR SERS Activity. *ACS Appl. Mater. Interfaces* **2014**, *6*, 11859–11863.

9. Haldar, K. K.; Kundu, S.; Patra, A., Core-size-dependent Catalytic Properties of Bimetallic Au/Ag Core–Shell Nanoparticles. *ACS Appl. Mater. Interfaces* **2014**, *6*, 21946–21953.

10. Ravula, S.; Essner, J. B.; La, W. A.; Polo-Parada, L.; Kargupta, R.; Hull, G. J.; Sengupta, S.; Baker, G. A., Sunlight-assisted Route to Antimicrobial Plasmonic Aminoclay Catalysts. *Nanoscale* **2015**, *7*, 86–91.

11. Lee, I.; Han, S. W.; Kim, K., Production of Au-Ag Alloy Nanoparticles by Laser Ablation of Bulk Alloys. *Chem. Commun.* **2001**, 1782–1783.

12. Liz-Marzan, L. M.; Philipse, A. P., Stable Hydrosols of Metallic and Bimetallic Nanoparticles Immobilized on Imogolite Fibers. *J. Phys. Chem. A* **1995**, *99*, 15120–15128.

13. Kariuki, N. N.; Luo, J.; Maye, M. M.; Hassan, S. A.; Menard, T.; Naslund, H. R.; Lin, Y.; Wang, C.; Engelhard, M. H.; Zhong, C.-J., Composition-controlled Synthesis of Bimetallic Gold−Silver Nanoparticles. *Langmuir* **2004**, *20*, 11240–11246.

14. Chen, D.-H.; Chen, C.-J., Formation and Characterization of Au-Ag Bimetallic Nanoparticles in Water-in-oil Microemulsions. *J. Mater. Chem.* **2002**, *12*, 1557–1562.

15. Kharissova, O. V.; Dias, H. V. R.; Kharisov, B. I.; Pérez, B. O.; Pérez, V. M. J., The Greener Synthesis of Nanoparticles. *Trends Biotechnol.* **2013**, *31*, 240–248.

16. Mittal, A. K.; Chisti, Y.; Banerjee, U. C., Synthesis of Metallic Nanoparticles using Plant Extracts. *Biotechnol. Adv.* **2013**, *31*, 346–356.

17. Bankar, A.; Joshi, B.; Kumar, A. R.; Zinjarde, S., Banana Peel Extract Mediated Novel Route for the Synthesis of Silver Nanoparticles. *Colloids Surf. A* **2010**, *368*, 58–63.

18. Bankar, A.; Joshi, B.; Ravi Kumar, A.; Zinjarde, S., Banana Peel Extract Mediated Synthesis of Gold Nanoparticles. *Colloids Surf. B* **2010**, *80*, 45–50.

19. Nadagouda, M. N.; Iyanna, N.; Lalley, J.; Han, C.; Dionysiou, D. D.; Varma, R. S., Synthesis of Silver and Gold Nanoparticles using Antioxidants from Blackberry, Blueberry, Pomegranate, and Turmeric Extracts. *ACS Sustain. Chem. Eng.* **2014**, *2*, 1717–1723.

20. Xu, H.; Wang, L.; Su, H.; Gu, L.; Han, T.; Meng, F.; Liu, C., Making Good use of Food Wastes: Green Synthesis of Highly Stabilized Silver Nanoparticles from Grape Seed Extract and their Antimicrobial Activity. *Food Biophys.* **2014**, *10*, 12–18.

21. Rao, A.; Mahajan, K.; Bankar, A.; Srikanth, R.; Kumar, A. R.; Gosavi, S.; Zinjarde, S., Facile Synthesis of Size-tunable Gold Nanoparticles by Pomegranate (*Punica granatum*) Leaf Extract: Applications in Arsenate Sensing. *Mater. Res. Bull.* **2013**, *48*, 1166–1173.

22. Ganesh Kumar, V.; Dinesh Gokavarapu, S.; Rajeswari, A.; Stalin Dhas, T.; Karthick, V.; Kapadia, Z.; Shrestha, T.; Barathy, I. A.; Roy, A.; Sinha, S., Facile Green Synthesis of Gold Nanoparticles using Leaf Extract of Antidiabetic Potent *Cassia auriculata*. *Colloids Surf. B* **2011**, *87*, 159–163.

23. Kahrilas, G. A.; Wally, L. M.; Fredrick, S. J.; Hiskey, M.; Prieto, A. L.; Owens, J. E., Microwave-assisted Green Synthesis of Silver Nanoparticles using Orange Peel Extract. *ACS Sustain. Chem. Eng.* **2013**, *2*, 367–376.

24. Alam, M. N.; Das, S.; Batuta, S.; Roy, N.; Chatterjee, A.; Mandal, D.; Begum, N. A., *Murraya koenegii* Spreng. Leaf Extract: An Efficient Green Multifunctional Agent for the Controlled Synthesis of Au Nanoparticles. *ACS Sustain. Chem. Eng.* **2014**, *2*, 652–664.

25. Meena Kumari, M.; Jacob, J.; Philip, D., Green Synthesis and Applications of Au–Ag Bimetallic Nanoparticles. *Spectrochim. Acta A* **2015**, *137*, 185–192.

26. Shen, L.-M.; Chen, Q.; Sun, Z.-Y.; Chen, X.-W.; Wang, J.-H., Assay of Biothiols by Regulating the Growth of Silver Nanoparticles with C-dots as Reducing Agent. *Anal. Chem.* **2014**, *86*, 5002–5008.

27. Wang, X.; Long, Y.; Wang, Q.; Zhang, H.; Huang, X.; Zhu, R.; Teng, P.; Liang, L.; Zheng, H., Reduced State Carbon Dots as both Reductant and Stabilizer for the Synthesis of Gold Nanoparticles. *Carbon* **2013**, *64*, 499–506.

28. Mandani, S.; Sharma, B.; Dey, D.; Sarma, T. K., Carbon Nanodots as Ligand Exchange Probes in Au@C-dot Nanobeacons for Fluorescent Turn-on Detection of Biothiols. *Nanoscale* **2015**, *7*, 1802–1808.

29. Liu, S.; Yu, B.; Zhang, T., Nitrogen-doped Carbon Nanodots as a Reducing Agent to Synthesize Ag Nanoparticles for Non-enzymatic Hydrogen Peroxide Detection. *RSC Adv.* **2014**, *4*, 544–548.

30. Choi, H.; Ko, S.-J.; Choi, Y.; Joo, P.; Kim, T.; Lee, B. R.; Jung, J.-W.; Choi, H. J.; Cha, M.; Jeong, J.-R.; Hwang, I.-W.; Song, M. H.; Kim, B.-S.; Kim, J. Y., Versatile Surface Plasmon Resonance of Carbon-dot-supported Silver Nanoparticles in Polymer Optoelectronic Devices. *Nat. Photonics* **2013**, *7*, 732–738.

31. Choi, Y.; Ryu, G. H.; Min, S. H.; Lee, B. R.; Song, M. H.; Lee, Z.; Kim, B.-S., Interface-controlled Synthesis of Heterodimeric Silver–Carbon Nanoparticles Derived from Polysaccharides. *ACS Nano* **2014**, *8*, 11377–11385.

32. Liu, R.; Liu, J.; Kong, W.; Huang, H.; Han, X.; Zhang, X.; Liu, Y.; Kang, Z., Adsorption Dominant Catalytic Activity of a Carbon Dots Stabilized Gold Nanoparticles System. *Dalton Trans.* **2014**, *43*, 10920–10929.

33. Ran, X.; Sun, H.; Pu, F.; Ren, J.; Qu, X., Ag Nanoparticle-decorated Graphene Quantum Dots for Label-free, Rapid and Sensitive Detection of Ag^+ and Biothiols. *Chem. Commun.* **2013**, *49*, 1079–1081.

34. Jaiswal, A.; Gautam, P. K.; Ghosh, S. S.; Chattopadhyay, A., Carbon Dots Mediated Room-temperature Synthesis of Gold Nanoparticles in Poly(ethylene glycol). *J. Nanopart. Res.* **2013**, *16*, 2188.

35. Shen, L.-M.; Chen, M.-L.; Hu, L.-L.; Chen, X.-W.; Wang, J.-H., Growth and Stabilization of Silver Nanoparticles on Carbon Dots and Sensing Application. *Langmuir* **2013**, *29*, 16135–16140.

36. Luo, P.; Li, C.; Shi, G., Synthesis of Gold@Carbon Dots Composite Nanoparticles for Surface Enhanced Raman Scattering. *Phys. Chem. Chem. Phys.* **2012**, *14*, 7360–7366.

37. Wang, X.; Cao, L.; Lu, F.; Meziani, M. J.; Li, H.; Qi, G.; Zhou, B.; Harruff, B. A.; Kermarrec, F.; Sun, Y.-P., Photoinduced Electron Transfers with Carbon Dots. *Chem. Commun.* **2009**, 3774–3776.

38. Baker, S. N.; Baker, G. A., Luminescent Carbon Nanodots: Emergent Nanolights. *Angew. Chem. Int. Ed.* **2010**, *49*, 6726–6744.

39. Xu, X.; Ray, R.; Gu, Y.; Ploehn, H. J.; Gearheart, L.; Raker, K.; Scrivens, W. A., Electrophoretic Analysis and Purification of Fluorescent Single-walled Carbon Nanotube Fragments. *J. Am. Chem. Soc.* **2004**, *126*, 12736–12737.

40. Hu, S.; Liu, J.; Yang, J.; Wang, Y.; Cao, S., Laser Synthesis and Size Tailor of Carbon Quantum Dots. *J. Nanopart. Res.* **2011**, *13*, 7247–7252.

41. Liu, H.; Ye, T.; Mao, C., Fluorescent Carbon Nanoparticles Derived from Candle Soot. *Angew. Chem. Int. Ed.* **2007**, *46*, 6473–6475.

42. Tian, L.; Ghosh, D.; Chen, W.; Pradhan, S.; Chang, X.; Chen, S., Nanosized Carbon Particles from Natural Gas Soot. *Chem. Mater.* **2009**, *21*, 2803–2809.

43. Dong, Y.; Shao, J.; Chen, C.; Li, H.; Wang, R.; Chi, Y.; Lin, X.; Chen, G., Blue Luminescent Graphene Quantum Dots and Graphene Oxide Prepared by Tuning the Carbonization Degree of Citric Acid. *Carbon* **2012**, *50*, 4738–4743.

44. Qu, S.; Wang, X.; Lu, Q.; Liu, X.; Wang, L., A Biocompatible Fluorescent Ink based on Water-soluble Luminescent Carbon Nanodots. *Angew. Chem. Int. Ed.* **2012**, *51*, 12215–12218.

45. Liu, S.; Tian, J.; Wang, L.; Zhang, Y.; Qin, X.; Luo, Y.; Asiri, A. M.; Al-Youbi, A. O.; Sun, X., Hydrothermal Treatment of Grass: A Low-cost, Green Route to Nitrogen-doped, Carbon-rich, Photoluminescent Polymer Nanodots as an Effective Fluorescent Sensing Platform for Label-Free Detection of Cu(II) Ions. *Adv. Mater.* **2012**, *24*, 2037–2041.

46. Lu, W.; Qin, X.; Liu, S.; Chang, G.; Zhang, Y.; Luo, Y.; Asiri, A. M.; Al-Youbi, A. O.; Sun, X., Economical, Green Synthesis of Fluorescent Carbon Nanoparticles and their use as Probes for Sensitive and Selective Detection of Mercury(II) Ions. *Anal. Chem.* **2012**, *84*, 5351–5357.

47. Zhou, J.; Sheng, Z.; Han, H.; Zou, M.; Li, C., Facile Synthesis of Fluorescent Carbon Dots using Watermelon Peel as a Carbon Source. *Mater. Lett.* **2012**, *66*, 222–224.

48. Vikneswaran, R.; Ramesh, S.; Yahya, R., Green Synthesized Carbon Nanodots as a Fluorescent Probe for Selective and Sensitive Detection of Iron(III) Ions. *Mater. Lett.* **2014**, *136*, 179–182.

49. Prasannan, A.; Imae, T., One-pot Synthesis of Fluorescent Carbon Dots from Orange Waste Peels. *Ind. Eng. Chem. Res.* **2013**, *52*, 15673–15678.

50. Essner, J. B.; Laber, C. H.; Ravula, S.; Polo-Parada, L.; Baker, G. A., Pee-dots: Biocompatible Fluorescent Carbon Dots Derived from the Upcycling of Urine. *Green Chem.* **2016**, *18*, 243–250.

51. Wunder, S.; Polzer, F.; Lu, Y.; Mei, Y.; Ballauff, M., Kinetic Analysis of Catalytic Reduction of 4-Nitrophenol by Metallic Nanoparticles Immobilized in Spherical Polyelectrolyte Brushes. *J. Phys. Chem. C* **2010**, *114*, 8814–8820.

Chapter 4: A Field Misled: Artifacts and Errors Associated with the Ubiquitous Presence of Fluorescent Impurities in Purportedly "Fluorescent" Carbon Nanodots†

†This chapter is based on a submitted and accepted peer-reviewed manuscript in *Chem. Mater*. The information contained herein is adapted with permission from Essner, J. B.; Kist, J. A.; Polo-Parada, L.; Baker, G. A., Artifacts and Errors Associated with the Ubiquitous Presence of Fluorescent Impurities in Carbon Nanodots. *Chem. Mater*. **2018**, *30*, 1878–1887. Copyright © 2018 American Chemical Society.

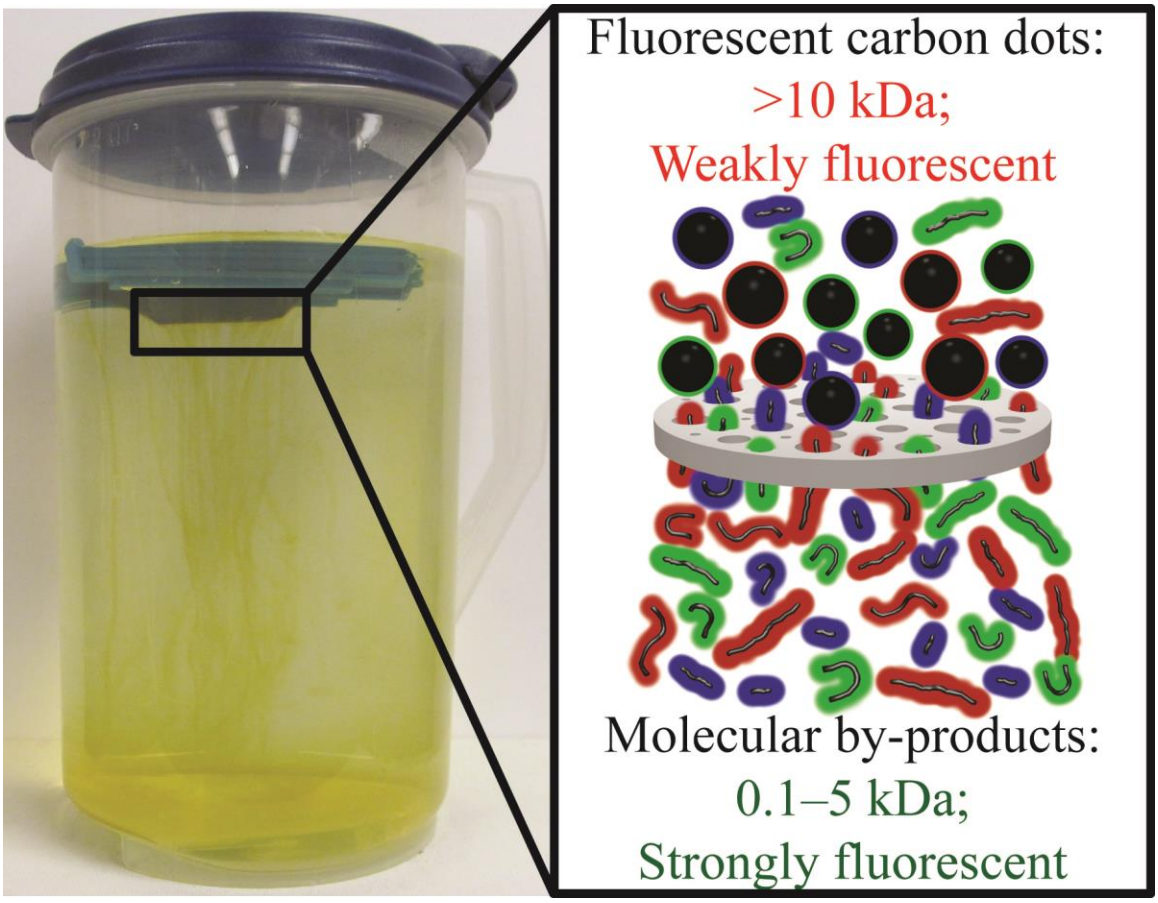

Scheme 4.1 Graphical abstract showing a representative FCD sample under dialysis highlighting the drastic quantity of small, molecular (highly fluorescent) by-products permeating the membrane, whose presence masks the true properties of FCDs and leads to misconceptions surrounding FCD emission when not sufficiently fractionated away.

Abstract

Fluorescent carbon dots have attracted tremendous attention owing to their superlative optical properties which suggest opportunities for replacing conventional fluorescent materials in various application fields. Not surprisingly, the rapid pace of publication has been accompanied by a host of critical issues, errors, controversies, and misconceptions associated with these emergent materials, which present significant barriers to elucidating their true nature, substantially hindering the extensive exploitation of these nanomaterials. Of particular interest are expedient, bottom-up pathways to carbon dots starting from molecular precursors (*e.g.*, citric acid, amino acids, alkylamines), although such routes are associated with the generation of a ubiquity of small molecular weight or oligomeric fluorescent by-products. A primary obstacle to progress is the inadequacy of purification in reported studies, an omission which gives rise to misconceptions about the nature and characteristics of the carbon dots. In this work, a series of carbon dot syntheses using facile, hydrothermal and microwave routes employing citric acid (paired with urea or ethylenediamine as a nitrogen source) is explored, followed by dialysis or ultrafiltration purification steps. Careful comparison and analysis of the optical properties of the resulting purification products (*i.e.*, dialysate/filtrate *vs* retentate fractions) affirms the formation of molecular fluorophores (potentially oligomeric or polymeric in nature) during bottom-up chemical syntheses, species that produce the majority of the observed emission from unpurified carbon dot samples. Clear evidence is provided showing that the fluorescent impurities produced as by-products of carbon dot synthesis must be rigorously removed to obtain reliable results. On the basis of these findings, the inadequate purification in many reports calls into question published work, suggesting that many previous studies will need

to be carefully revisited using more rigorous purification protocols. Of course, deficiencies in purification in prior studies only add to the ongoing debate on carbon dot structure and the origin of their emission. Moving forward, rigorous and consistent purification steps will need to be uniformly implemented, a tactical change that will help pave the way toward the development of carbon dots as next-generation agents for cellular imaging, solid-state and full-color lighting, photovoltaics, catalysis, and (bio)sensing.

Introduction

Nanoscale carbons are associated with a range of attractive properties, including electrical conductivity, biocompatibility, high thermal stability, and tunability (*e.g.*, textural properties, doping), forming the subject of intensive research in recent years. The newest addition to the family of nanoscale carbons consists of fluorescent carbon dots (FCDs). Typically sized below 10 nm, FCDs display unique and useful optical features (*e.g.*, excitation wavelength-dependent fluorescence, tunable emission color, high photostability) not seen with their nanocarbon relatives (*i.e.*, fullerenes, graphenes, carbon nanotubes, nanodiamonds), while also offering biocompatibility, inertness, and low cytotoxicity, which make them preferable to conventional semiconductor-based quantum dots (*e.g.*, CdS).[1-8] Moreover, FCDs can be synthesized using a wide variety of top-down or bottom-up approaches. The literature suggests that FCDs can be produced as a result of appropriate thermal treatment of virtually any carbon-containing precursor, with examples including citrates,[9-15] saccharides (*e.g.*, glucose, chitosan),[16-22] food waste,[23-28] biomass,[29-32] human hair,[33-35] and even human urine[36] or animal feces.[37] Due to their facile preparation and promising characteristics, research on FCDs has exploded recently but, unfortunately, the unbridled enthusiasm and extremely rapid pace of research has naturally led to a

number of uncritical, unsubstantiated, and detrimental claims and misconceptions entering the publication record. In many instances, revisiting prior work with more scientific rigor is warranted, paying closer attention to consistency, purification, proper characterization, and sometimes nomenclature. Cayuela *et al*. recently published a highlight stressing the urgency for consistency in FCD research, proposing a unified nomenclature in the classification of fluorescent nanocarbons.[38] We agree with these authors, particularly given how frequently FCDs are haphazardly classified or given invented names or acronyms to give the false impression that a novel material is being introduced. Currently, nearly a dozen names are (sometimes arbitrarily) used for fluorescent nanocarbons: graphene quantum dots (GQDs), carbon quantum dots (CQDs), carbon nanodots (CNDs), carbon dots, C-dots, carbogenic dots, carbon nanoclusters, polymer dots, nitrogen-rich quantum dots (N-dots), and graphitic carbon nitride dots, although several of these can be consolidated into a few subclasses. Indeed, Cayuela *et al*. proposed that only three categories (GQDs, CQDs, and CNDs) are necessary to sufficiently categorize all FCDs, based on the chemical, physical, and photophysical properties specific to each subclass.

Beyond troubling nomenclature inconsistencies, a very real barrier preventing maturation of the field is the fact that the purification of FCDs is frequently inadequate, unsubstantiated, or missing altogether. Several researchers have already alluded to the fact that, in order to elucidate the true origin of FCD fluorescence, efficient separation procedures are urgently needed to reduce sample complexity.[39-42] Worse, recent evidence suggests that the fluorescence associated with FCDs may originate significantly from organic (*e.g.*, oligomeric) by-products generated alongside FCDs.[43-46] Despite mounting evidence, the improper and insufficient purification of FCD samples remains common,

making a unified purification approach all the more pressing. In response to this need, we report on the nanoscale features, photophysical properties, and cytotoxicities of representative FCDs made via top-down and bottom-up strategies. By evaluating the FCD fractions resulting from extensive purification using membrane dialysis (*i.e.*, retentate (retent.), dialysate (dial.)), alongside unfractionated, as-synthesized (as-synth.) samples, we unequivocally demonstrate the importance of adequate purification to generate meaningful, error-free results, particularly in regard to luminescent characterizations. Indeed, the results suggest that inconsistencies and errors in published work are widespread and in need of re-evaluation. Moving forward, standardized purification procedures taking into account these findings will need to be implemented and remedial studies to gauge the veracity of previous claims will also be warranted in many instances.

Experimental

Materials and Reagents

All experiments were carried out using Ultrapure Millipore water polished to a resistivity of 18.2 MΩ·cm unless otherwise stated. Anhydrous citric acid (791725, ≥99.5%), urea (U5378), ethylenediamine (E26266, ≥99%), sodium hydroxide (306576, 99.99% trace metals basis), sodium chloride (S7653, ≥99.5%), bis(3-aminopropyl) terminated polyethylene glycol (452572, M_n ~1,500 kDa), gold(III) chloride hydrate (520918, ≥99.9% trace metal basis), sodium borohydride (480886, 99.99% trace metal basis), sodium citrate tribasic dihydrate (C7254, ≥98%), quinine hemisulfate salt monohydrate (referred to as quinine sulfate; 22640, >98.0%), coumarin 153 (01511, ≥99.0%), fluorescein sodium salt (F6377), sulforhodamine B (SRB), cell culture media, phosphate-buffered saline (PBS), trichloroacetic acid, acetic acid, the chloride salt of Hg^{2+} (ACS >99.5%), and the sulfate

salt of Cu^{2+} (≥98.0%) were all purchased from Sigma-Aldrich (St. Louis, MO). Rhodamine 610 (rhodamine B) chloride (06101) was acquired from Exciton, Inc. (Dayton, OH). Branched polyethylenimine (bPEI) (06088, ≥99%, M_n ~1,200 kDa) was purchased from Polysciences, Inc. (Warrington, PA). L-arginine (BP2505500, ≥99%, free base), Fisherbrand™ syringe filters with 0.45 μm (09-719D) and 0.20 μm (09-719C) pore sizes, 96-well plates, and the chloride salt of Fe^{3+} (ACS >98%) were obtained from Fisher Scientific (Pittsburg, PA). Ethanol (2716, 200 proof) and graphite rods (40766, 99.9995% metals basis) were procured from Decon Labs, Inc., (King of Prussia, PA) and Alfa Aesar (Ward Hill, MA), respectively. Regenerated cellulose dialysis membranes with molecular weight cut-offs (MWCOs) of 1, 3.5, 8, 15, and 50 kDa (Spectra/Por® 7, 132105, 132111, 132116, 132124, and 132130, respectively) were acquired from Repligen® (formerly Spectrum Labs®, Rancho Dominguez, CA). Ultrafiltration filter membranes with MWCOs of 1, 10, and 100 kDa (13312, 13612, and 14412, respectively) were purchased from Millipore (St. Charles, MO). Mice embryonic fibroblasts (MEF), human mammary gland epithelial cells derived from a ductal carcinoma, metastatic pleural effusion site (T-47D; ATCC® HTB-133™), and human epithelial cells derived from a cervical adenocarcinoma (HeLa; ATCC® CCL-2™) were acquired from colleagues within the Dalton Cardiovascular Research Center. All chemicals were used as received.

Fluorescent Carbon Dot Syntheses

Representative microwave,[13-14, 47-51] hydrothermal,[52-58] and electrochemical[59-65] synthetic routes were explored to elucidate possible shortcomings and misconceptions from previous literature reports.

Domestic Microwave Treatment of Citric Acid and Urea

Following a common and widely reported protocol,[13-14, 47-51] FCDs were synthesized from citric acid (CA) and urea (U) in a 1:3 CA:U molar ratio using a 900 W Frigidaire domestic microwave oven. Specifically, 6 g of CA and 6 g of U were dissolved in 20 mL of water in a round bottom flask stabilized in a beaker and the solution was treated in the microwave on the default power setting (100% power) for 5 min, forming a charred, porous product. The resultant carbonaceous material was dissolved in 50 mL of water and the round bottom flask was rinsed with two additional 50 mL aliquots of water to ensure adequate removal of all the product. The three 50 mL fractions of the product were thoroughly homogenized resulting in 150 mL of final sample which was purified following the procedures outlined in the "Fluorescent Carbon Dot Purification" section below.

Hydrothermal Treatments of Arginine and Citric Acid-Ethylenediamine

Two hydrothermal approaches using different FCD precursors were explored: (i) L-arginine[52-53] and (ii) CA and ethylenediamine (EDA).[54-58]

(i) For the FCDs derived from L-arginine (Arg), a 3 M aqueous solution of Arg was made by dissolving 26.13 g of Arg in 50 mL of water. Due to this concentration being beyond the solubility limit of Arg, the saturated solution was vigorously shaken and 10 mL was rapidly pipetted into a 23 mL Teflon-lined stainless-steel autoclave. The solution was then hydrothermally treated at 180 °C for 9 h in a programmable oven.

(ii) For the CA–EDA-derived FCDs, 0.42 g of CA and 536 µL of EDA were dissolved in 10 mL of water in a 23 mL Teflon-lined stainless-steel autoclave which was then hydrothermally treated at 200 °C for 5 h in a programmable oven.

Both syntheses were repeated 5 additional times and the six samples of each type of FCD were thoroughly homogenized. The homogenized samples were purified following the procedures outlined in the "Fluorescent Carbon Dot Purification" section below.

Electrochemical Oxidation of Graphite to GQDs

FCDs were synthesized through an electrochemical route using graphite rods as both the cathode and anode submersed in 100 mL of an ethanol/water (95:5 v/v) mixture containing 0.4 g of NaOH, similar to previously reported procedures.[59-65] The synthesis was conducted at constant voltage (60 V) for 4 h using an Agilent® DC Power Supply (E3612A). During the synthesis the solution changed from clear to yellow to orange and finally to dark brown. Note, the measured current varied from 200 to 400 mA throughout the synthesis. The resultant samples were either functionalized prior to purification or directly purified following the procedures outlined in the respective "Fluorescent Carbon Dot Functionalization of GQDs" or "Fluorescent Carbon Dot Purification" sections below.

Fluorescent Carbon Dot Functionalization of GQDs

The electrochemically synthesized FCDs were functionalized with two commonly employed passivating agents, namely bis(3-aminopropyl) terminated polyethylene glycol (PEG-N; 1.5 kDa) and branched polyethylenimine (bPEI; 1.2 kDa).[66-69] To functionalize the FCDs, 5 mL of the as-synth. material (after centrifugation; see "Fluorescent Carbon Dot Purification" section) was combined with 5 mL of a 20 mM solution of either PEG-N or bPEI in a 23 mL Teflon-lined stainless-steel autoclave and the mixtures were hydrothermally treated at 180 °C for 12 h in a programmable oven. After treatment, the products were diluted with 10 mL of water. For each passivating agent, functionalization was conducted on four additional aliquots of the as-synth., electrochemically derived

sample, thoroughly homogenizing the five samples of each type of passivated FCD prior to purification following the procedures outlined in the "Fluorescent Carbon Dot Purification" section below.

Fluorescent Carbon Dot Purification

All as-synth. FCD samples (excluding the functionalized FCDs) were centrifuged at 5k rpm for 30 min, decanting the supernatant and discarding any sediment. The samples were then dialyzed using 1, 3.5, 8, 15, or 50 kDa MWCO cellulose membranes. Initially, the samples were dialyzed for 24 h against 0.5 or 1.0 L of exchange solvent to obtain a more concentrated dial. fraction for further studies. After this, the samples were dialyzed for an additional three to five days against 1.5 L of solvent, replenishing the exchange solvent every 24 h. The duration of dialysis varied with the synthetic approach but all samples were dialyzed until the exchange solvent was visually clear to the eye and did not display any observable fluorescence using blue (405 nm) and green (532 nm) laser pointers. For the microwave- and hydrothermally synthesized FCDs, the samples were dialyzed against ultrapure water while the electrochemically synthesized and functionalized FCDs were dialyzed against 100:0 and 50:50 vol% ethanol:water solutions, respectively. Note, for the Arg-derived FCDs, aliquots of the retent. and dial. fractions were pulled off 6 h into the initial 24 h dialysis for further analysis. Additionally, more concentrated samples were used to acquire the pictures of the time-dependent dialyses to clearly illustrate the rapid mobilization of by-products. Select as-synth. samples were also subjected to (ultra)filtration using Fisherbrand™ syringe filters (0.20 μm or 0.45 μm pore size) or a Millipore® 5121 Amicon® ultrafiltration system (model 8010) employing 1, 10, or 100 kDa MWCO filter membranes. The filtrates were retained for further analysis.

Gold Nanoparticle Syntheses

Benchmark dialysis and ultrafiltration experiments were conducted on gold nanoparticles (Au NPs) of two different size regimes (12–16 nm and 5–7 nm) to clarify nanoscale membrane permeability. To generate the larger Au NPs, a sodium citrate reduction known as the Turkevich method[70-74] was employed. Specifically, 1 mL of 5 mM $HAuCl_4$ was diluted in 18 mL of water and the solution was brought to a boil in a round bottom flask placed in a water bath. Temperature control was achieved to within 2 °C using a digital stirring hotplate (Super-Nuova™; Thermo Scientific™) connected to a J-type thermocouple immersed in the water bath. Once boiling, 1 mL of a 0.5% sodium citrate solution was added under stirring provided by a PTFE-coated, magnetic stir bar spinning at 300 rpm. The solution was heated until a color change was observed (typically, clear/light yellow to purple), after which the round bottom flask was removed and allowed to cool to ambient temperature. During this cooling period, the solution color changed from dark purple to dark red. Water was added to the Au NP solution to bring the volume back to 20 mL, accounting for any solvent losses during boiling. To generate the smaller size regime of Au NPs, reduction of Au^{3+} was accomplished with sodium borohydride ($NaBH_4$) in the absence of a conventional capping, a protocol recently reported by the Astruc group.[75] Specifically, 1 mL of freshly prepared 50 mM aqueous $NaBH_4$ was added to 19 mL of 0.25 mM $HAuCl_4$ (1 mL of 5 mM $HAuCl_4$ in 18 mL of water) at ambient temperature and under magnetic stirring (PTFE-coated, magnetic stir bar spinning at 300 rpm). Upon $NaBH_4$ addition, the solution rapidly changed from faint yellow to orange and over a few hours the solution color transitioned to dark orange/red. The $NaBH_4$-generated Au NPs were allowed to ripen for 24 h prior to use. Both Au NP solutions were subjected to dialysis

(against 0.5 L water) or ultrafiltration using 50 kDa or 100 kDa MWCO membranes, respectively.

Characterization Techniques

Absorbance and steady-state fluorescence spectra were collected on a Hitachi U-3000 or Varian Cary® Bio 50 UV-vis spectrophotometer and a Horiba Jobin Yvon Fluorolog®-3 or Varian Cary® Eclipse spectrofluorometer, respectively. All measurements were conducted at ambient temperature using 1 cm (1.4 mL or 4 mL) fluorescence quartz cuvettes and all samples were diluted to an absorbance at 350 nm of 0.1 or lower to minimize inner filter effects. All spectroscopic data were blank subtracted. Additionally, when applicable, the fluorescence spectra were corrected for dilution and inner filter effects, with the latter accounted for through the approximate correction factor below:

$$F_{corr} = F_{obs}\left(10^{\frac{A_{ex}+A_{em}}{2}}\right)$$

where F_{corr} is the corrected fluorescence values, F_{obs} is the observed (blank subtracted and dilution corrected) fluorescence, A_{ex} is the absorbance of the sample at the excitation wavelength (*i.e.*, 375 nm), and A_{em} is the absorbance at each wavelength over the emission range collected (*i.e.*, 385–650 nm). Excitation wavelength-dependent quantum yield (Φ) values were calculated using the following equation:

$$\Phi_S = \Phi_R\left[\frac{F_S}{F_R}\right]\left[\frac{OD_R}{OD_S}\right]\left[\frac{n_S^2}{n_R^2}\right]$$

where *R* and *S* stand for reference and sample respectively, *F* stands for integrated fluorescence intensity (calculated over the wavelength range of interest), *OD* stands for optical density (at the excitation wavelength, λ, used in the fluorescent measurements), and *n* stands for refractive index. Specifically, quinine sulfate, coumarin 153, fluorescein, and

rhodamine B were employed as reference fluorophores with all relevant fluorophore parameters utilized for the quantum yield determinations provided in Table 4.1 below.

Table 4.1 Reference fluorophores used to determine quantum yield (Φ) values.

Fluorophore	**Excitation λ (nm)**	**Solvent**	***n***	**Φ_R (%)**	**Reference**
Quinine sulfate	350	0.1 M H_2SO_4	1.343	58	[76]
Coumarin 153	421	Ethanol	1.366	38	[77]
Fluorescein	470	0.1 M NaOH	1.336	91	[78]
Rhodamine B	514	Water	1.334	31	[79]

Transmission electron microscopy (TEM) studies were conducted on carbon coated copper grids (Ted Pella, Inc., 01814-F, support films, carbon type-B, 400 mesh copper grid) using a FEI® Tecnai™ (F30 G2, Twin) microscope operated at a 300 keV electron acceleration voltage.

Cell Viability by Sulforhodamine B Assay

The cell viabilities were evaluated based on the sulforhodamine B (SRB) colorimetric assay, as described in the literature.[80-81] For the assay, solutions of freshly isolated mice embryonic fibroblasts (MEF), human mammary gland epithelial cells derived from a ductal carcinoma, metastatic pleural effusion site (T-47D; ATCC® HTB-133™), and human epithelial cells derived from a cervical adenocarcinoma (HeLa; ATCC® CCL-2™) were seeded into each well of a 96-well plate (5–8 × 10^3 cells in 100 μL of Dulbecco's Modified Eagle Medium/Newborn Calf Serum culture media) and allowed to adhere to the wells for 24 h at 37 °C in a 10% CO_2 atmosphere. The cells were then treated with 100 μL of various FCD concentrations (0.002–2 mg mL^{-1} in saline solution, previously prepared by dissolving 9 g NaCl in 1 L water) for 24 h at 37 °C in a 10% CO_2 atmosphere. After FCD treatment, the media was removed, the cells were washed twice with PBS solution, and the surviving or adherent cells were fixed in situ by adding 100 μL of PBS and 100 μL of 50%

cold trichloroacetic acid followed by an incubation period of 1 h at 4 °C. Lastly, the cells were washed with ice-cold water five times, dried, and then stained according to the SRB colorimetric assay protocol. The protocol involves staining the cells using 50 μL of 4% SRB (in 1 vol% acetic acid solution) for 8 min at room temperature. Any unbound dye was removed by washing the cells five times with cold 1% acetic acid and the stained cells were then dried. The absorbance of the dried stained cells was measured at 560 nm using a microplate reader. Each FCD concentration was tested in triplicate (at minimum).

Metal Ion Quenching Studies

Stock solutions of the various metal salts with concentrations of at least 5 mM were generated, which were then diluted to 3.1 mM. The as-synth. samples and their dial. and retent. fractions were diluted to an absorbance of approximately 0.1 at 375 nm, where all absorbance values were 0.09 ± 0.03. For the metal screening tests, 100 μL of the 3.1 mM metal salt solutions was added to a cuvette containing 3 mL of the above diluted solutions. For the quenching titrations, the emission of the metal-free FCD solution (3 mL) was first collected then a 10 μL addition of a 31 μM aqueous solution of Hg^{2+} was added to give a Hg^{2+} concentration of ~100 nM and the emission was re-collected. This process was repeated nine additional times resulting in a final Hg^{2+} concentration of 1 μM. Next, nine separate 10.5 μL additions of a 310 μM aqueous solution of Hg^{2+} were added to give Hg^{2+} concentrations of ~2–10 μM, after which nine separate 11 μL additions of a 3.1 mM aqueous solution of Hg^{2+} were added to give Hg^{2+} concentrations of ~20–100 μM. Emission spectra were collected after each aliquot of Hg^{2+} was added. Again, spectroscopic data for all quenching studies were blank subtracted and all fluorescence spectra were dilution corrected, however, the spectra from the quenching titrations were not inner filter

corrected as the metal (Hg^{2+}) used for these studies showed no measurable absorbance over 375–800 nm even at concentrations much higher (1 mM) than those used in the titrations (maximum concentration of 100 μM).

Approximate GQD Molecular Weight Calculation

The approximate molecular weights of GQDs ranging in size from 1 to 20 nm (presented in Figure 4.1C) were calculated from the equation below using the density of carbon atoms in graphene (*i.e.*, 3.21 x 10^{15} C atoms cm^{-2}).[82] For simplicity, the calculation was based on completely spherical GQDs absent any heteroatom doping or functional groups.

$$MW_{Approx}\ (kDa) = GQD\ Area * \left(3.21 \text{ x } 10^{15}\ \frac{C\ atoms}{cm^2}\right) * Carbon\ Molar\ Mass$$

$$MW_{Approx}\ (kDa) = \pi\left(\frac{10\ nm}{2}\right)^2 \times \left(\frac{1\ cm^2}{1 \text{ x } 10^{14}\ nm^2}\right) \times \left(3.21 \text{ x } 10^{15}\ \frac{C\ atoms}{cm^2}\right) \times \left(\frac{12.01\ Da}{C\ atom}\right)$$

$$MW_{Approx}\ (kDa) = 30{,}279\ Da \times \left(\frac{1 \text{ x } 10^{-3}\ kDa}{1\ Da}\right)$$

$$MW_{Approx}\ (kDa)\ of\ a\ 10\ nm\ GQD = 30.28\ kDa$$

Results and Discussion

Literature Survey of FCD Purification Methods

Since the serendipitous discovery of nanoscale fluorescent carbons by Xu *et al*. in 2004,[83] the number of articles published has grown exponentially (Figure 4.1A), with the total number of publications exceeding 3,500 by the end of 2016. In accordance with the recommendations by Cayuela *et al*., the publications have been segregated into three FCD subclasses (*i.e.*, CQDs, GQDs, CNDs) and are categorized according to their published classification, with the exception that the CND subclass encompasses the terms carbon nanodots, carbon dots, C-dots, and carbogenic dots. Figure 4.1B shows a random sampling of more than 550 FCD publications, which are sorted according to the reported purification

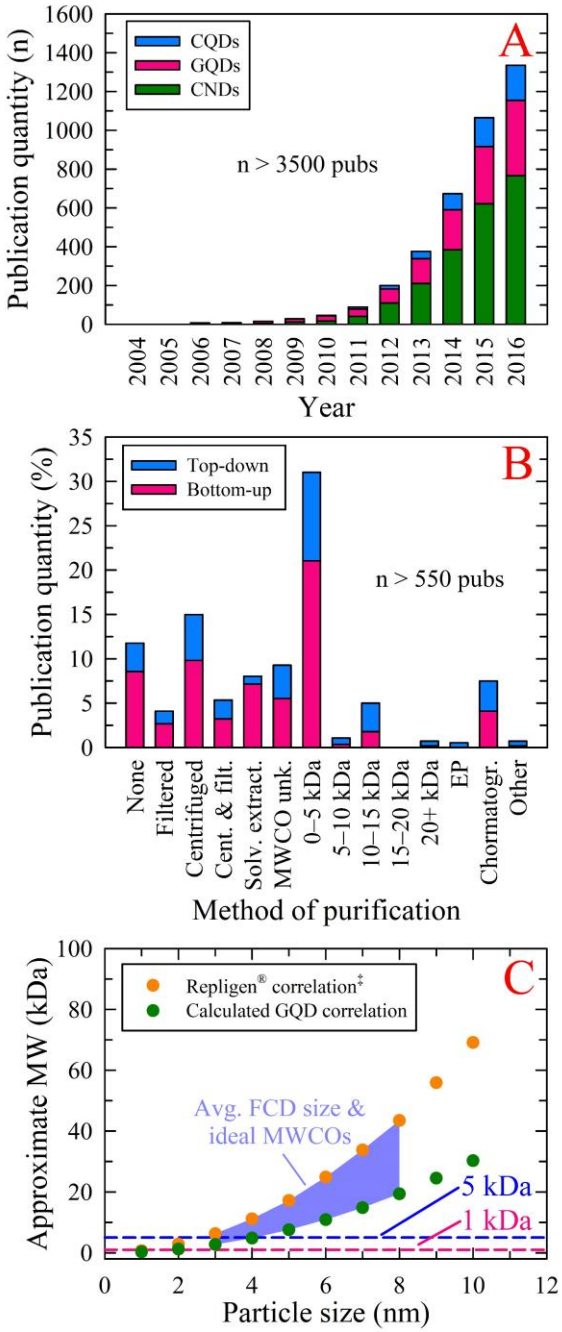

Figure 4.1 (A) Trend showing the exponential rise in publications dealing with fluorescent carbon dots (FCDs) over the past decade. (B) A sampling of over 550 FCD publications categorized by their mode of purification. (C) An approximate molecular weight-to-size correlation suggesting that the use of <5 kDa molecular weight cut-off (MWCO) membranes is inadequate for purifying these materials. The pink and blue lines demarcate 1 kDa and 5 kDa MWCOs, respectively, while the purple area represents the average FCD

size and ideal MWCOs that should be employed for membrane-based FCD purification. ‡This is an approximation; there is no universally correct correlation between a 2D particle size and a 3D molecular weight. The abbreviations in panel B are as follows: “Cent. & filt.” = centrifugation and filtration (in no particular order); “Solv. extract.” = solvent extraction; “MWCO unk.” = MWCO for dialysis not reported; “EP” = electrophoretic separation; and “Chromatogr.” = chromatographic separation. The bars labelled with specific MWCOs denote either dialysis or ultrafiltration as a means of purification.

and further categorized by the synthetic camp (top-down *vs* bottom-up). The experimental details for over 300 of these publications are summarized in the supporting information of our published *Chem. Mater.* article.[84] Note, many of the reported dialysis or ultrafiltration purification protocols also include centrifugation and/or filtration steps prior to membrane separation. Figure 4.1B illustrates a wide range of purification methods used in published FCD reports. As demonstrated herein, more than half of these reports employ purification procedures that are assuredly inadequate. In fact, ~12% of these representative examples perform no purification whatsoever. To make matters worse, some go so far as to make the false claim that avoiding purification is an advantage in some misguided belief that FCDs are the sole product generated. Considering that bottom-up approaches utilize molecular or ill-defined (*e.g.*, food waste) carbon sources, the chemical transformations taking place during synthesis may parallel those that transpire in the roasting of coffee,[85-87] malting of grain,[88-92] or the boiling of sugar-protein solutions (*e.g.*, wort) where non-enzymatic browning (*e.g.*, Maillard reaction, caramelization) occurs, for example. These carbonization reactions are exceedingly complex and can produce thousands of identifiable compounds, including melanoidins and other oligomeric or polymeric products, making side-product formation during FCD synthesis a certainty. Indeed, recent reports have shown that mild thermal treatment of common FCD precursors can yield highly fluorescent

materials that are molecular in nature (*e.g.*, polymers, soft gels) and display fluorescence quantum yields >60%.[93-97] These observations are in accord with recent reports that attribute observed fluorescence to organic fluorophore side-products,[43-46] making the notion of exclusive formation of FCDs by bottom-up approaches extremely improbable. In fact, earlier reports suggested the low temperature production of highly fluorescent polymeric products while significantly higher temperatures were required to generate a "carbogenic core", a feature associated with a substantially lower fluorescence quantum yield.[12, 43] We note that while top-down approaches might be deduced to result in more well-defined products and fewer impurities (most are derived from graphite, after all), this does not exempt them from the need for purification, which becomes even more critical when postsynthetic functionalization steps are involved.

Given the above discussion, a full 20% of the surveyed literature (Figure 4.1B) employs only centrifugation or bulk filtration (*i.e.*, excluding membrane ultrafiltration using a defined molecular weight cut-off, MWCO) yielding insufficiently purified FCDs. To efficiently remove starting materials and putative molecular by-products, a purification approach involving either chromatographic separation or dialysis with an appropriate MWCO membrane is required. Unfortunately, nearly 30% of the surveyed literature performed dialysis with a membrane MWCO of 5 kDa or below (Figure 1B), with 1 kDa and 3.5 kDa MWCOs being the most popular choices. In reality, larger MWCOs should be employed to ensure efficient removal of large oligomeric or polymeric by-products. Figure 4.1C presents a highly approximate correlation between molecular weight and colloid size for FCDs. The upper limit of the shaded region in Figure 4.1C was adapted from a Repligen® (formerly Spectrum Labs®) technical note[98] and the lower limit is based on

calculations for an unfunctionalized GQD using the density of carbon atoms found in graphene,[82] as described in the "Approximate GQD Molecular Weight Calculation" subsection of the "Experimental" section above. Given that the average FCD size culled from the references compiled in Figure 4.1B falls in the 3–8 nm range, with recent estimates suggesting that the approximate molecular weights of 3–10 nm GQDs fall in the 15–30 kDa range,[99-100] purification with larger MWCO membranes is desired to comprehensively remove organic, molecular (especially, polymeric, supramolecular, or aggregated) impurities and by-products, while retaining the desired nanoscale FCD fraction. Indeed, notable examples exist in which 20 kDa+ MWCO membranes were employed for purification without losing the target FCDs.[101-102]

At this point, it must be stated that nanoscale imaging (TEM or AFM analysis) of a colloidal dispersion coupled with a steady-state fluorescence study of the same sample is incapable of determining the origin of the emission (*i.e.*, molecular *vs* nanoscale). Consider, for example, the following hypothetical scenario: Unbeknownst to an investigator, a colleague spikes a low concentration of an organic laser dye into their dispersion of well-defined but non-fluorescent nanoparticles. Absent any possible quenching or excessive scattering, the sample will emit brightly, as for a solution of the fluorescent dye itself. Meanwhile, TEM imaging will reveal the presence of well-defined nanoparticles. Being organic in nature (low Z-contrast), dilute, and small (typical laser dyes have molecular weights from 300 to 500 Da), the TEM will provide no indication that the laser dye is present at all. Our hypothetical investigator can hardly be blamed for believing they have evidently generated fluorescent nanoparticles. Of course, we know she or he has been the unwitting victim of a laboratory prank. This contrived scenario, in fact, provides a

surprisingly apt cautionary tale when interpreting the origin of luminescence from an FCD-containing sample. Thus, without adequate purification, one can neither confidently claim that FCDs are the primary product nor that the origin of the observed photoluminescence derives primarily from FCDs. In fact, to date, there is little direct evidence that the dots themselves fluoresce,[41] let alone proof they are the sole or even principal photoluminescent species present. Further complicating the matter, it was recently shown that, upon drying, small organic compounds can form nanocrystals whose properties are disconcertingly reminiscent of FCDs,[103] calling into question many published results on FCDs.

Luminescent Characterizations of the CA–U-derived Fractions

To further elucidate possible shortcomings and misconceptions arising from previous literature reports on FCD synthesis, representative microwave,[13-14, 47-51] hydrothermal,[52-58] and electrochemical[59-65] synthetic routes were evaluated, with particular emphasis placed on the microwave-generated samples. Detailed experimental procedures for these representative routes are provided in "Fluorescent Carbon Dot Syntheses" under the "Experimental" section above. The microwave-generated samples, synthesized from citric acid (CA) and urea (U) in a 1:3 CA:U molar ratio (denoted as CA–U), were subjected to dialysis (1, 3.5, 8, 15, or 50 kDa MWCO membranes) or (ultra)filtration purification protocols (1, 10, or 100 kDa MWCO membranes; or 0.20 or 0.45 μm pore size syringe filters), after which the retent., dial., and filtrate fractions were characterized by their steady-state fluorescence (Figures C.1 and C.2) and wavelength-dependant quantum yields (Figure 4.2).

All the microwave-generated CA–U samples (*i.e.*, retent., dial., filtrates) displayed the commonly reported excitation wavelength-dependant emission with the dial. (Figure C.2B,

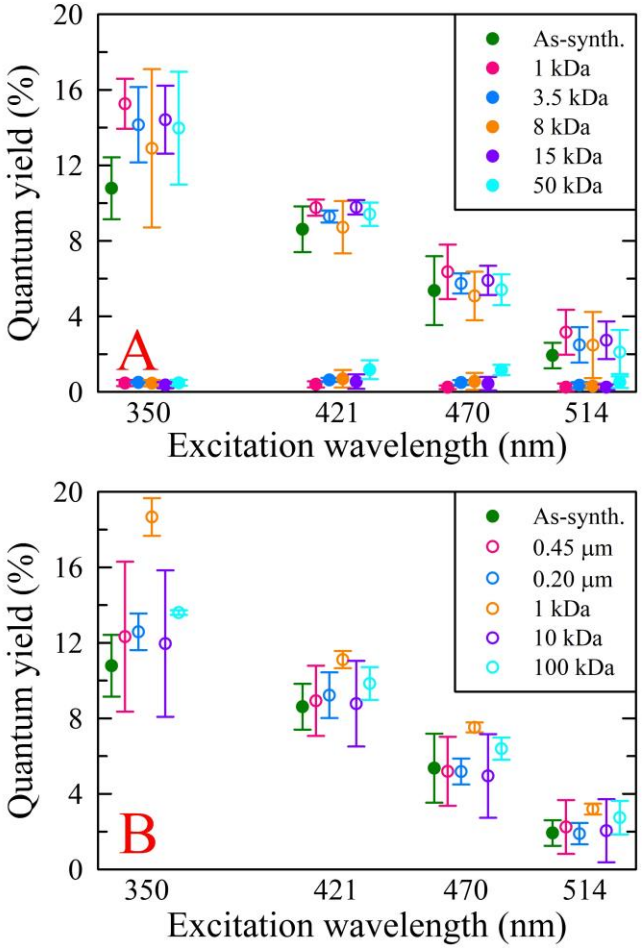

Figure 4.2 Assessed fluorescence quantum yields of CA–U-derived samples following fractionation via (A) dialysis or (B) (ultra)filtration. The retent. results are represented by closed circles and dial./filtrate quantum yields are denoted by open circles. These sets of studies reveal that the smaller species permeating the membranes are associated with the majority of the fluorescence observed in the as-synth. samples while the retent. fractions show much weaker fluorescence.

D, F, H, J) and filtrate (Figure C.1B–F) fractions displaying similar spectral features to the as-synth., nonpurified samples (Figure C.1A) while the retent. fractions (Figure C.2A, C, E, G, I) produced drastically weaker emission for samples of relatively comparable absorptivity. In general, all samples universally showed diminishing fluorescence emission with increasing excitation wavelength. To better elucidate this behavior, multiexcitation

wavelength fluorescence quantum yield determinations were made using excitation wavelengths of 350, 421, 470, and 514 nm. The results, summarized in Figure 4.2, are consistent with our previous observations that as the excitation wavelength increases, the calculated quantum yield generally decreases markedly.[9, 15, 36] Figure 4.2A shows that regardless of the membrane MWCO chosen for dialysis, the measured quantum yields of the retent. fractions (closed circles) were drastically lower than those of the as-synth. samples as well as those of the dial. fractions (open circles), which gave similar quantum yields. From these results, we can infer that in popular microwave-generated FCD samples there exist at least two distinct populations of fluorophores: a population of molecular (<1 kDa) species responsible for the majority of the observed fluorescence and a population of low quantum yield emitters much larger in size (≥50 kDa). We note that emission from aqueous dispersions of graphene oxide has been proposed to arise from quasi-molecular fluorophores, akin to polycyclic aromatic compounds coupled to the graphitic surface.[104-105] It is currently not possible to rule out a similar quasi-molecular involvement in FCD emission arising from organic fluorophore coupling at the carbon surface. The exact origin and nature of FCD emission remains elusive, although historically the observed FCD fluorescence has been variously attributed to a size-dependent quantum confinement effect and surface functionalities/defects.[1] However, there is mounting evidence that certain FCDs are not in fact quantum emitters and indeed not even "dots",[106] but are, instead, supramolecular clusters comprising an assembly of individual monomeric organic fluorophores contributing the bulk of the observed fluorescence.[40, 46, 106] In this light, the two distinct populations of fluorophores each likely consist of a range of fluorophores that combine to produce the observed bulk fluorescence. Similar conclusions can be drawn

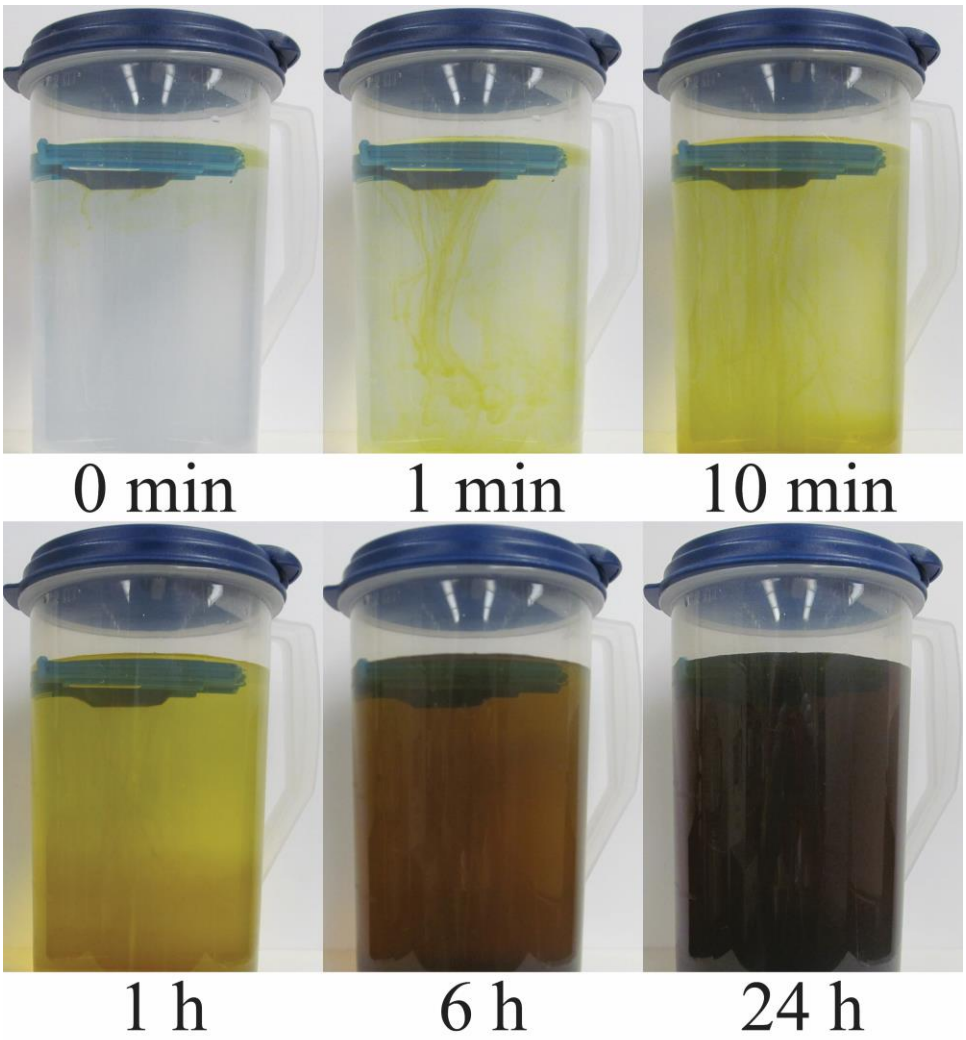

Figure 4.3 Sequence of photographs showing the progress of dialysis for microwave-generated CA–U (1:3) samples using a 1 kDa MWCO membrane. The rapid passage of colored material through the membrane vividly illustrates the fact that large quantities of small molecular (non-nanoscale) by-products result from bottom-up microwave routes to FCDs.

from the (ultra)filtration studies of the microwave-produced CA–U samples, where the quantum yields measured for the filtrates (Figure 4.2B) were comparable to or higher than those of as-synth. material. This clearly demonstrates that the common practice of purifying with a syringe filter (*e.g.*, 0.20 μm) is wholly inadequate, offering essentially no purification whatsoever. Figures 4.3 and C.3 further highlight the rapid mobilization of

small molecular weight species through a 1 kDa membrane during dialysis of a microwave-produced CA–U (1:3) sample. It is noteworthy that when the retent. from this 1 kDa dialysis was subjected to further dialysis with a 50 kDa MWCO membrane (Figure C.4), no colored species were observed permeating the membrane after 24 h, further supporting the notion that two distinct, size-disparate populations are generated for microwave treatment of molecular species such as CA–U.

Dialysis Membrane Nanoscale Permeability Tracking with Au NPs

To clarify nanoscale membrane permeability for a given MWCO, we performed benchmark experiments involving the dialysis (50 kDa MWCO) and ultrafiltration (100 kDa MWCO) of well-defined ~14 nm citrate-stabilized[70-74] Au nanoparticles (Au NPs) compared with ~6 nm borohydride-stabilized Au NPs[75]. TEM micrographs of these Au NPs are provided in Figure C.5. Conveniently, the localized surface plasmon resonance of the Au NPs allowed us to track permeation through the membrane. Comparison of UV-vis spectra collected on the dial. and filtrate fractions (Figure C.6) with spectra for nonfractionated, parent Au NP samples reveals that neither 6 nm nor 14 nm Au NPs pass through the 50 kDa dialysis membrane, whereas small amounts of both Au NP sizes permeate the 100 kDa ultrafiltration membrane, with the larger citrate-stabilized Au NPs mobilizing to a lesser extent. This outcome suggests that nanoparticles in the 5–15 nm regime will not traverse a 50 kDa MWCO membrane but may begin to pass a 100 kDa MWCO membrane. Given a mean reported size of 3–8 nm for FCDs, dialyses with a membrane MWCO below 20 kDa is not recommended because there is potential for retention of molecular by-products in addition to the FCD fraction.

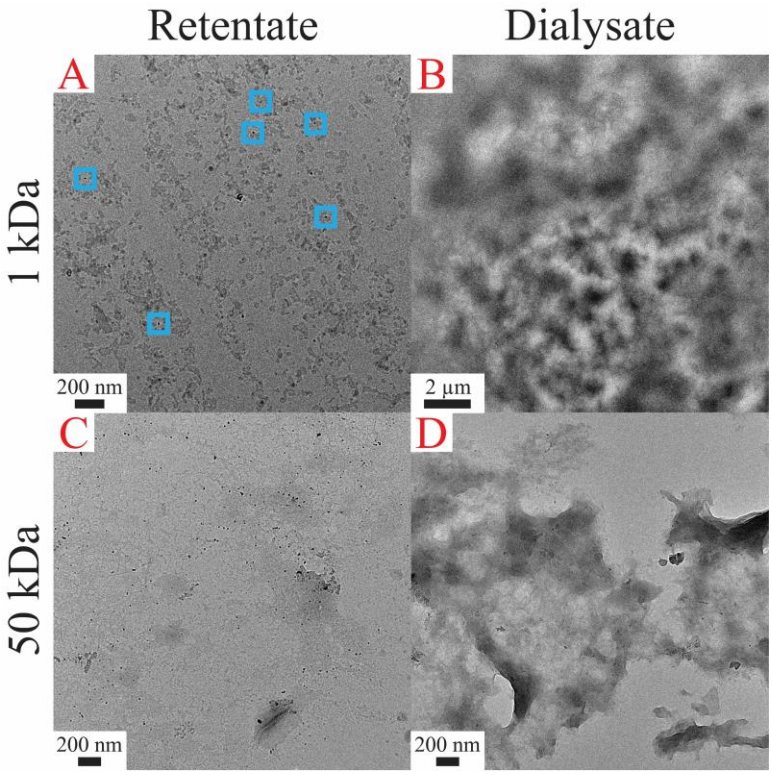

Figure 4.4 Representative TEM micrographs for the (A and C) retentate (retent.) and (B and D) dialysate (dial.) fractions resulting from (A–B) 1 kDa and (C–D) 50 kDa dialysis of samples produced by microwave treatment of CA–U (1:3). Some apparent FCDs are visible in the 1 kDa retent. (marked by cyan squares in panel A) but proved difficult to image due to the large quantity of by-product residues. While the 50 kDa retent. proved easier to image and the FCDs were more visually prominent, a significant amount of non-FCD material remained after purification. Some FCDs were visible in the 50 kDa dial. samples indicating that dialysis may not be capable of fully separating FCDs from organic molecular by-products.

Electron Microscopic Imaging Analyses of CA–U-derived Fractions

Figure 4.4 presents representative TEM micrographs of the retent. (A and C) and dial. (B and D) fractions resulting from 1 kDa and 50 kDa MWCO membrane dialysis of microwave-generated CA–U material. Both retent. fractions appear to contain FCDs, however, the dots are often sequestered within amorphous deposits of undesired organic material, particularly for dialysis using a 1 kDa MWCO membrane (Figure 4.4A),

demonstrating that 1 kDa is completely insufficient for removing organic residues. Unfortunately, even when employing a 50 kDa MWCO membrane (Figure 4.4C), non-FCD impurities still appeared on the TEM grid for the retent. sample, suggesting that even this high a MWCO membrane may not provide adequate purification. Both dial. fractions appear to contain primarily organic by-products that produced thin films on the grid, especially when dialyzing against a 1 kDa membrane (Figure 4.4B). No FCDs were observed in the 1 kDa dial., although the "polymer-like" coating would surely obscure their observation, were they present. FCD-like structures were occasionally observed in the 50 kDa dial. (Figure 4.4D), although they were rare. Overall, these TEM studies demonstrate that dialysis against membranes having a MWCO < 50 kDa is most assuredly insufficient, although dialysis, in general, may be less than ideal due to the difficulty of separating the target FCDs from molecular (oligo- or polymeric) by-products, a situation exacerbated by the possibility for supramolecular association of small, organic fluorophores.[40, 46, 106] Additional representative TEM micrographs of the retent. and dial. fractions resulting from the 1 kDa and 50 kDa MWCO membrane dialysis of the microwave-generated CA–U material are provided in Figure C.7.

Fractionation and Spectroscopic Properties of Arg- and CA–EDA-derived Samples

To ascertain the prevalence of fluorescent organic impurities (by-products) using other synthetic routes, the fluorescence properties of products resulting from a hydrothermal synthesis using L-arginine (Arg)[52-53] or citric acid and ethylenediamine (CA–EDA)[54-58] plus an electrochemical preparation from graphite[59-65] were explored next. The details for these synthetic routes can be found in "Fluorescent Carbon Dot Syntheses" under the "Experimental" section. All samples were subjected to dialysis as per the microwave

synthesized FCDs, with the omission of the 3.5 kDa and 8 kDa MWCO membranes earlier shown to be inadequate for FCD purification. In general, as was the case for the CA–U microwave FCDs, all samples displayed excitation wavelength-dependant emission (Figures C.8 and C.14) and fluorescence quantum yields (Figures C.10 and C.17A), again indicating a distribution of fluorophores, with the smaller species being the most photoluminescent. Contrastingly, the hydrothermally derived CA–EDA samples displayed excitation wavelength-independent emission (Figure C.11), a known but rarer feature of FCD photoluminescence[1, 50, 107] thought to arise from a more homogeneous fluorophore composition. In spite of this key difference, the results for hydrothermal CA–EDA-derived products reinforce the conclusion that small organic molecular by-products produce a majority of the observed fluorescence and not nanoscale carbons (Figure C.12). Further evidence that two spectroscopically distinct species are generated is provided in Figure C.13, where the UV-vis spectra for the retent. fractions from 1 kDa or 50 kDa MWCO membrane dialysis of CA–U- (panel A) and CA–EDA-derived (panel B) FCDs are markedly different from the parent samples and the corresponding dial. fractions. Specifically, for the CA–U retent. fractions, the shoulders at 250 nm and 275 nm are no longer evident, whereas for the CA–EDA retent. fractions, the peak wavelength blueshifts by approximately 10 nm.

We note that in prior reports employing dialysis for FCD purification, the duration or conditions of dialysis are frequently inadequate. Although a number of factors influence the dialysis rate, standard protocols call for a 16–24 h period of dialysis with multiple changes of the exchange solvent throughout.[108] Many reports involving FCD dialysis fail to meet these standards, halting the dialysis, prematurely, for example. To shed light on

this questionable practice, fractions of the dial. and retent. from Arg-derived hydrothermal samples were collected after dialysis for 6, 24, or 72 h (in the latter case, the exchange solvent was changed every 24 h) and fluorescence quantum yields were measured (Figure C.10). During the early stages of dialysis, the quantum yields of the retent. and dial. fractions were relatively similar. Over time, however, the quantum yield associated with the retent. began to drop off, regardless of the chosen MWCO membrane. These results are further corroborated by time-lapse photos of the Arg-derived FCDs undergoing dialysis with a 1 kDa MWCO membrane (Figure C.9). Clearly, these results demonstrate that 6 h of dialysis is inadequate, regardless of the membrane MWCO employed, urging researchers to not only employ an adequately large MWCO but also to allow dialysis to proceed for at least 24 h, preferably with frequent changes of the exchange solvent. Indeed, time-lapse photos of CA–U FCD dialysis (Figures 4.3 and C.3) reinforce this notion as well.

Effects of Fractionation on the Luminescent Properties of Bare and Functionalized GQDs

Graphitized CQDs/GQDs are often functionalized with an amine-containing passivating agent, such as bis(3-aminopropyl) terminated polyethylene glycol (PEG-N)[66, 69] or branched polyethylenimine (bPEI),[67-68] to improve their fluorescence features. Problematically, however, the majority of these reports perform no purification following functionalization, suggesting that the observed fluorescence enhancement may derive, at least in part, from organic fluorescent impurities generated in situ. In fact, to date, there is little irrefutable evidence that the observed fluorescence from FCD samples actually originates from the CQD/GQD core or surface functionality on the dot and not from side-reactions or degradation of the passivating agent used for surface functionalization. To

highlight this uncertainty, electrochemically synthesized FCDs were hydrothermally treated with PEG-N (1.5 kDa) or bPEI (1.2 kDa) to functionalize the nanodots and the resulting samples were subjected to dialysis and ultrafiltration purification. The fluorescence emission spectra of the "functionalized" samples (Figures C.15 and C.16) showed similar excitation-wavelength dependence as the parent material (Figure C.14). However, in general, the dial. and filtrate fractions displayed considerably higher fluorescence quantum yields (Figures C.17B–C and C.18) than the corresponding retent. fractions (or nonpurified functionalized samples), illustrating that highly fluorescent, molecular by-products do indeed form during surface functionalization of FCDs with amine passivating agents. Thus, even top-down syntheses of FCDs require careful purification, particularly postfunctionalization with molecular capping agents.

Effects of Purification on Quenchometric Applications and Cell Viability Studies

The lack of proven and widely adopted purification protocols to isolate FCDs free of fluorescent contaminants leads to misconceptions about their photophysical properties and will undoubtedly propagate errors and misinterpretations during their use in applications that rely on their fluorescent nature (*e.g.*, sensors, bioimaging agents). As a first step toward examining such a possibility, the quenchability of as-synth. and dialyzed fractions (*i.e.*, retent., dial.) of CA–U (Figure 4.5) and CA–EDA (Figure C.19) derived samples were evaluated using the transition metal ions Cu^{2+}, Fe^{3+}, and Hg^{2+}. To provide a basis for direct head-to-head comparison, samples were diluted to an absorbance of 0.9 ± 0.3 at 375 nm, the excitation wavelength employed in the fluorescence quenching studies. For the three metal ions tested, the retent. fractions proved to be more strongly quenched than the nonpurified samples or the corresponding dial. fractions, which were quenched to similar

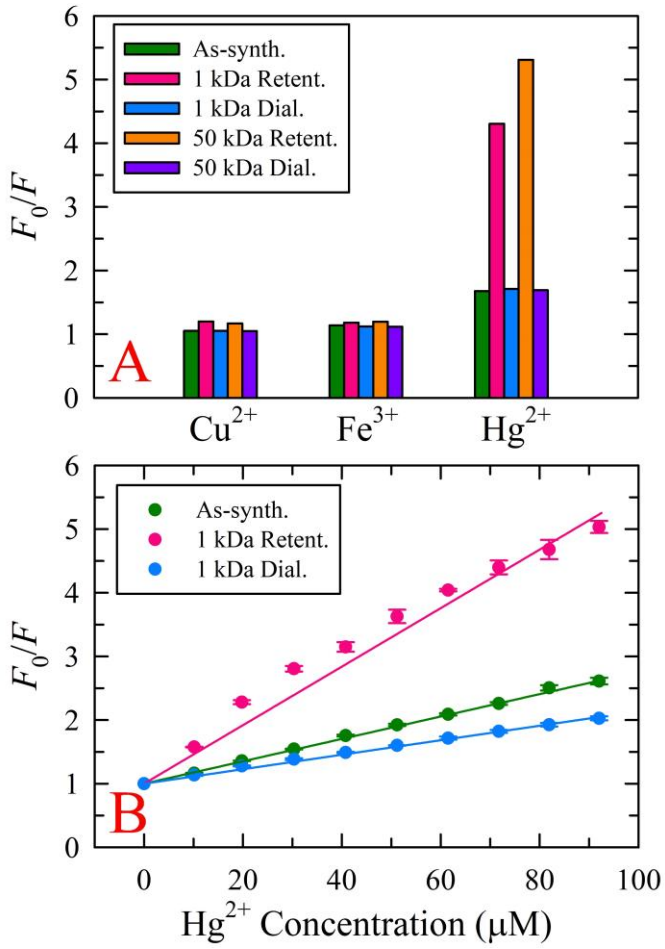

Figure 4.5 (A) Metal ion quenching studies conducted on the microwave-treated CA–U as-synth. sample and the corresponding retent. and dial. fractions. For the metal ions tested (Cu^{2+}, Fe^{3+}, or Hg^{2+}), the retent. fractions were quenched more strongly by 100 μM Hg^{2+} than their as-synth. or dial. counterparts, while the quenching in the presence of 100 μM Cu^{2+} or Fe^{3+} was essentially identical for all three fractions. (B) Stern-Volmer plots of Hg^{2+} titrations of CA–U-derived FCDs. These results reveal that improper purification can clearly impact the performance of the investigated material, in this case masking the analytical responsivity of the FCDs (the limit of detection for Hg^{2+} is 2–3 times better for the retent. fraction compared with the dial.). For all metal ion quenching studies, the concentration of the FCD fractions was "normalized" by adopting the same absorbance (~0.1) at the excitation wavelength (375 nm) employed in the fluorescence spectra acquisitions.

extents. Although the differences in quenching behavior between the retent. and dial. fractions were marginal for Cu^{2+} and Fe^{3+}, the retent. fraction was conspicuously more responsive to Hg^{2+} compared to the dial. fraction. To further explore this behavior, Hg^{2+} quenching titrations were conducted on an as-synth. CA–U sample alongside the retent. and dial. fractions resulting from dialysis using a 1 kDa MWCO membrane. Figure 4.5B provides representative Stern–Volmer plots of Hg^{2+} quenching of the CA–U fluorescence, where F_0 and F represent the fluorescence intensities in the absence and presence of Hg^{2+}, respectively. The limits of detection (LOD) were estimated from these data using the 3σ convention. For similar absorbances, the estimated LODs for as-synth., retent., and dial. CA–U fractions were 607 nM, 229 nM, and 1.53 μM, respectively. This outcome demonstrates that the presence of molecular by-products can mask the true response of the FCDs, restricting their analytical potential. A larger implication of this result is that many previous works may need to be revisited with more meticulous purification to validate or refute the original findings.

Recently, Vinci *et al*. demonstrated that a nonpurified FCD sample generated from the oxidation of graphite nanofibers was substantially more toxic than the individual fractions obtained from dialysis and HPLC fractionation,[109] an indication that sample complexity can influence functional properties. In this light, the cytotoxicities of as-synth. CA–U-derived FCDs and their dialysis fractions (*i.e.*, retent., dial.) were evaluated using three different cell lines: mice embryonic fibroblasts (MEFs; Figure C.20), human breast cancer cells (T-47D; Figure C.21), and HeLa cells (Figure C.22). Contrary to the results reported by Vinci *et al*., regardless of the cell line studied or the membrane MWCO employed for dialysis, no clear trends emerged when comparing the toxicities for as-synth. material with

that of the retent. and dial. fractions. At this point, the relative cytotoxicities of nanocarbons compared with those of the organic by-products resulting from various synthetic routes remains an open question. In-depth cellular toxicity studies on chromatographically fractionated FCD samples are needed to truly understand the origin of any observed cytotoxicity and to show cellular compatibility.

Improper Interpretation of Luminescent Characteristics due to Inner Filter Effects

Another fallacy cultivated in the literature entails the improper collection and interpretation of FCD fluorescence emission. In some instances, FCDs have been claimed to display red emission due to the appearance of the sample under illumination. In many of these cases, the red color is in fact a visual artifact arising from illumination of a concentrated solution already brick red in color. This is illustrated in Figures C.23 and C.24 for CA–U- and Arg-derived FCD samples. Comparing the emission spectra for the as-synth. Arg-derived FCDs with results for 10- and 100-fold diluted samples (Figure C.24), the emission is more redshifted for the undiluted dispersion. This phenomenon, which arises from the re-absorption of blue-edge photons in highly absorbing solutions, is well-known. In this case, we note that although this secondary inner filter effect causes redshifted emission due to attenuation of the blue edge, the emission color remains in the blue under UV excitation. Clearly, the ruddy appearance of the undiluted Arg-derived FCD sample belies the true emission color. Figure C.24D provides a comparison of the emission maximum *vs* excitation wavelength for the various dilutions of Arg-derived FCDs, further highlighting this distortion, revealing the apparent insensitivity to excitation wavelength from 300 to 500 nm, an artifact of self-absorption. Although this distortion at high optical densities has been documented in the literature,[110] it has escaped the attention of many researchers.

Conclusions

The primary conclusion drawn from this study is that adequate purification of fluorescent carbon dots, while frequently neglected, is absolutely critical to acquiring meaningful results, especially for bottom-up chemical synthesis involving molecular precursors (*e.g.*, citric acid, food wastes). In fact, rigorous purification and fractionation is not needed solely to properly characterize the performance of carbon dots but also to answer questions on the hotly debated origin of their luminescence. Currently, purification practices have been frequently inadequate, with the majority of studies utilizing insufficient methods (*i.e.*, centrifugation, filtration), performing dialysis with inappropriate (*e.g.*, too low) molecular weight cut-offs, or performing no separation step of any kind. Consequently, numerous previous findings may be called into question and require careful revisitation. Certainly, fluorescence-based applications (*e.g.*, heavy metal detection, cellular imaging) will be heavily impacted by the unaccounted presence of organic molecular fluorophores.

While some researchers have employed membrane-based fractionation as a means for successfully size separating carbon dots,[102, 111] the majority of these examples involve the fractionation of graphitic dots generated from top-down approaches (*e.g.*, electrochemical etching of graphite electrodes). This is noteworthy because top-down formation of carbon dots appears to be associated with fewer molecular by-products. In contrast, we provide clear and abundant evidence that in nonpurified samples produced by bottom-up syntheses, carbon dot emission is dominated by fluorescence from small molecular weight organic fluorophores. Worse, even when performing dialysis with a membrane molecular weight cut-off of 50 kDa, the complete removal of fluorescent organic by-products putatively formed alongside the carbon dots is not guaranteed. As pointed out by Gong *et al.*,[112] as-

synthesized carbon dots are complex, multicomponent systems, suggesting that dialysis, despite its convenience, may not be a satisfactory mode of purification in some instances. Chromatographic techniques likely represent the most analytically sound means for fractionating these complex mixtures,[40, 109, 112-123] illustrated by the extensive HPLC fractionation studies conducted by the Colón[109, 114-115] and Choi[112, 118-122] groups, although these currently constitute less than 10% of the reported purification protocols for carbon dots. One hallmark of such fractionation is, intuitively, a reduction in sample complexity. Indeed, individual fractions generally possess optical properties distinct from the starting mixture, such as excitation wavelength-independent emission.[109, 112] What is needed now is a scalable, analytically sound, and vetted separation method that can arrive at high-purity, single-component carbon dot samples in practical quantities (beyond laboratory scale). This remains an unmet challenge; however, if the field of carbon dot research is to continue unabated, it is a challenge that must be answered.

Acknowledgements

This work was supported by the Mizzou Advantage funding program at the University of Missouri.

References

1. Baker, S. N.; Baker, G. A., Luminescent Carbon Nanodots: Emergent Nanolights. *Angew. Chem. Int. Ed.* **2010**, *49*, 6726–6744.
2. Ding, C.; Zhu, A.; Tian, Y., Functional Surface Engineering of C-dots for Fluorescent Biosensing and In Vivo Bioimaging. *Acc. Chem. Res.* **2013**, *47*, 20–30.
3. Li, H.; Kang, Z.; Liu, Y.; Lee, S.-T., Carbon Nanodots: Synthesis, Properties and Applications. *J. Mater. Chem.* **2012**, *22*, 24230–24253.

4. Li, L.; Wu, G.; Yang, G.; Peng, J.; Zhao, J.; Zhu, J.-J., Focusing on Luminescent Graphene Quantum Dots: Current Status and Future Perspectives. *Nanoscale* **2013**, *5*, 4015–4039.

5. Shen, J.; Zhu, Y.; Yang, X.; Li, C., Graphene Quantum Dots: Emergent Nanolights for Bioimaging, Sensors, Catalysis and Photovoltaic Devices. *Chem. Commun.* **2012**, *48*, 3686–3699.

6. Wang, J.; Xin, X.; Lin, Z., Cu_2ZnSnS_4 Nanocrystals and Graphene Quantum Dots for Photovoltaics. *Nanoscale* **2011**, *3*, 3040–3048.

7. Zhang, Z.; Zhang, J.; Chen, N.; Qu, L., Graphene Quantum Dots: An Emerging Material for Energy-related Applications and Beyond. *Energy Environ. Sci.* **2012**, *5*, 8869–8890.

8. Zheng, X. T.; Ananthanarayanan, A.; Luo, K. Q.; Chen, P., Glowing Graphene Quantum Dots and Carbon Dots: Properties, Syntheses, and Biological Applications. *Small* **2015**, *11*, 1620–1636.

9. Essner, J. B.; Laber, C. H.; Baker, G. A., Carbon Dot Reduced Bimetallic Nanoparticles: Size and Surface Plasmon Resonance Tunability for Enhanced Catalytic Applications. *J. Mater. Chem. A* **2015**, *3*, 16354–16360.

10. Bourlinos, A. B.; Stassinopoulos, A.; Anglos, D.; Zboril, R.; Karakassides, M.; Giannelis, E. P., Surface Functionalized Carbogenic Quantum Dots. *Small* **2008**, *4*, 455–458.

11. Bourlinos, A. B.; Stassinopoulos, A.; Anglos, D.; Zboril, R.; Georgakilas, V.; Giannelis, E. P., Photoluminescent Carbogenic Dots. *Chem. Mater.* **2008**, *20*, 4539–4541.

12. Krysmann, M. J.; Kelarakis, A.; Dallas, P.; Giannelis, E. P., Formation Mechanism of Carbogenic Nanoparticles with Dual Photoluminescence Emission. *J. Am. Chem. Soc.* **2011**, *134*, 747–750.

13. Qu, S.; Wang, X.; Lu, Q.; Liu, X.; Wang, L., A Biocompatible Fluorescent Ink based on Water-soluble Luminescent Carbon Nanodots. *Angew. Chem. Int. Ed.* **2012**, *51*, 12215–12218.

14. Wang, L.; Zhu, S.-J.; Wang, H.-Y.; Qu, S.-N.; Zhang, Y.-L.; Zhang, J.-H.; Chen, Q.-D.; Xu, H.-L.; Han, W.; Yang, B.; Sun, H.-B., Common Origin of Green Luminescence in Carbon Nanodots and Graphene Quantum Dots. *ACS Nano* **2014**, *8*, 2541–2547.

15. Laber, C. H.; Essner, J. B.; Scott, T. A.; Polo-Parada, L.; Baker, G. A., Domestic Pressure Cooker as Inexpensive Hydrothermal Vessel: Demonstrated Utility for Eco-friendly Synthesis of Non-toxic Carbon Dots. *Nano-Struct. Nano-Objects* **2016**, *6*, 52–58.

16. Choi, Y.; Ryu, G. H.; Min, S. H.; Lee, B. R.; Song, M. H.; Lee, Z.; Kim, B.-S., Interface-controlled Synthesis of Heterodimeric Silver–Carbon Nanoparticles Derived from Polysaccharides. *ACS Nano* **2014**, *8*, 11377–11385.

17. Yang, Y.; Cui, J.; Zheng, M.; Hu, C.; Tan, S.; Xiao, Y.; Yang, Q.; Liu, Y., One-step Synthesis of Amino-functionalized Fluorescent Carbon Nanoparticles by Hydrothermal Carbonization of Chitosan. *Chem. Commun.* **2012**, *48*, 380–382.

18. Chowdhury, D.; Gogoi, N.; Majumdar, G., Fluorescent Carbon Dots Obtained from Chitosan Gel. *RSC Adv.* **2012**, *2*, 12156–12159.

19. Shen, L.-M.; Chen, M.-L.; Hu, L.-L.; Chen, X.-W.; Wang, J.-H., Growth and Stabilization of Silver Nanoparticles on Carbon Dots and Sensing Application. *Langmuir* **2013**, *29*, 16135–16140.

20. Shen, L.-M.; Chen, Q.; Sun, Z.-Y.; Chen, X.-W.; Wang, J.-H., Assay of Biothiols by Regulating the Growth of Silver Nanoparticles with C-dots as Reducing Agent. *Anal. Chem.* **2014**, *86*, 5002–5008.

21. Yang, Z.-C.; Wang, M.; Yong, A. M.; Wong, S. Y.; Zhang, X.-H.; Tan, H.; Chang, A. Y.; Li, X.; Wang, J., Intrinsically Fluorescent Carbon Dots with Tunable Emission Derived from Hydrothermal Treatment of Glucose in the Presence of Monopotassium Phosphate. *Chem. Commun.* **2011**, *47*, 11615–11617.

22. Tang, L.; Ji, R.; Cao, X.; Lin, J.; Jiang, H.; Li, X.; Teng, K. S.; Luk, C. M.; Zeng, S.; Hao, J.; Lau, S. P., Deep Ultraviolet Photoluminescence of Water-soluble Self-passivated Graphene Quantum Dots. *ACS Nano* **2012**, *6*, 5102–5110.

23. Mewada, A.; Pandey, S.; Shinde, S.; Mishra, N.; Oza, G.; Thakur, M.; Sharon, M.; Sharon, M., Green Synthesis of Biocompatible Carbon Dots using Aqueous Extract of *Trapa bispinosa* Peel. *Mater. Sci. Eng. C* **2013**, *33*, 2914–2917.

24. Lu, W.; Qin, X.; Liu, S.; Chang, G.; Zhang, Y.; Luo, Y.; Asiri, A. M.; Al-Youbi, A. O.; Sun, X., Economical, Green Synthesis of Fluorescent Carbon Nanoparticles and their use as Probes for Sensitive and Selective Detection of Mercury(II) Ions. *Anal. Chem.* **2012**, *84*, 5351–5357.

25. Prasannan, A.; Imae, T., One-pot Synthesis of Fluorescent Carbon Dots from Orange Waste Peels. *Ind. Eng. Chem. Res.* **2013**, *52*, 15673–15678.

26. Vikneswaran, R.; Ramesh, S.; Yahya, R., Green Synthesized Carbon Nanodots as a Fluorescent Probe for Selective and Sensitive Detection of Iron(III) Ions. *Mater. Lett.* **2014**, *136*, 179–182.

27. Zhou, J.; Sheng, Z.; Han, H.; Zou, M.; Li, C., Facile Synthesis of Fluorescent Carbon Dots using Watermelon Peel as a Carbon Source. *Mater. Lett.* **2012**, *66*, 222–224.

28. Lu, W.; Qin, X.; Asiri, A.; Al-Youbi, A.; Sun, X., Green Synthesis of Carbon Nanodots as an Effective Fluorescent Probe for Sensitive and Selective Detection of Mercury(II) Ions. *J. Nanopart. Res.* **2012**, *15*, 1344.

29. Krysmann, M. J.; Kelarakis, A.; Giannelis, E. P., Photoluminescent Carbogenic Nanoparticles Directly Derived from Crude Biomass. *Green Chem.* **2012**, *14*, 3141–3145.

30. Briscoe, J.; Marinovic, A.; Sevilla, M.; Dunn, S.; Titirici, M., Biomass-derived Carbon Quantum Dot Sensitizers for Solid-state Nanostructured Solar Cells. *Angew. Chem. Int. Ed.* **2015**, *54*, 4463–4468.

31. Liu, S.; Tian, J.; Wang, L.; Zhang, Y.; Qin, X.; Luo, Y.; Asiri, A. M.; Al-Youbi, A. O.; Sun, X., Hydrothermal Treatment of Grass: A Low-cost, Green Route to Nitrogen-doped, Carbon-rich, Photoluminescent Polymer Nanodots as an Effective Fluorescent Sensing Platform for Label-Free Detection of Cu(II) Ions. *Adv. Mater.* **2012**, *24*, 2037–2041.

32. Qin, X.; Lu, W.; Asiri, A. M.; Al-Youbi, A. O.; Sun, X., Green, Low-cost Synthesis of Photoluminescent Carbon Dots by Hydrothermal Treatment of Willow Bark and their Application as an Effective Photocatalyst for Fabricating Au Nanoparticles-reduced Graphene Oxide Nanocomposites for Glucose Detection. *Catal. Sci. Techol.* **2013**, *3*, 1027–1035.

33. Sun, D.; Ban, R.; Zhang, P.-H.; Wu, G.-H.; Zhang, J.-R.; Zhu, J.-J., Hair Fiber as a Precursor for Synthesizing of Sulfur- and Nitrogen-co-doped Carbon Dots with Tunable Luminescence Properties. *Carbon* **2013**, *64*, 424–434.

34. Wang, J.; Peng, F.; Lu, Y.; Zhong, Y.; Wang, S.; Xu, M.; Ji, X.; Su, Y.; Liao, L.; He, Y., Large-scale Green Synthesis of Fluorescent Carbon Nanodots and their use in Optics Applications. *Adv. Opt. Mater.* **2015**, *3*, 103–111.

35. Liu, S.-S.; Wang, C.-F.; Li, C.-X.; Wang, J.; Mao, L.-H.; Chen, S., Hair-derived Carbon Dots Toward Versatile Multidimensional Fluorescent Materials. *J. Mater. Chem. C* **2014**, *2*, 6477–6483.

36. Essner, J. B.; Laber, C. H.; Ravula, S.; Polo-Parada, L.; Baker, G. A., Pee-dots: Biocompatible Fluorescent Carbon Dots Derived from the Upcycling of Urine. *Green Chem.* **2016**, *18*, 243–250.

37. D'Angelis do E. S. Barbosa, C.; Corrêa, J. R.; Medeiros, G. A.; Barreto, G.; Magalhães, K. G.; de Oliveira, A. L.; Spencer, J.; Rodrigues, M. O.; Neto, B. A. D., Carbon Dots (C-dots) from Cow Manure with Impressive Subcellular Selectivity Tuned by Simple Chemical Modification. *Chem. Eur. J.* **2015**, *21*, 5055–5060.

38. Cayuela, A.; Soriano, M. L.; Carrillo-Carrion, C.; Valcarcel, M., Semiconductor and Carbon-based Fluorescent Nanodots: The Need for Consistency. *Chem. Commun.* **2016**, *52*, 1311–1326.

39. Qi, B.-P.; Bao, L.; Zhang, Z.-L.; Pang, D.-W., Electrochemical Methods to Study Photoluminescent Carbon Nanodots: Preparation, Photoluminescence Mechanism and Sensing. *ACS Appl. Mater. Interfaces* **2016**, *8*, 28372–28382.

40. Hu, Q.; Meng, X.; Chan, W., An Investigation on the Chemical Structure of Nitrogen and Sulfur Codoped Carbon Nanoparticles by Ultra-performance Liquid Chromatography-tandem Mass Spectrometry. *Anal. Bioanal. Chem.* **2016**, *408*, 5347–5357.

41. Demchenko, A. P.; Dekaliuk, M. O., The Origin of Emissive States of Carbon Nanoparticles Derived from Ensemble-averaged and Single-molecular Studies. *Nanoscale* **2016**, *8*, 14057–14069.

42. Sarswat, P. K.; Free, M. L., Light Emitting Diodes based on Carbon Dots Derived from Food, Beverage, and Combustion Wastes. *Phys. Chem. Chem. Phys.* **2015**, *17*, 27642–27652.

43. Zhu, S.; Zhao, X.; Song, Y.; Lu, S.; Yang, B., Beyond Bottom-up Carbon Nanodots: Citric-acid Derived Organic Molecules. *Nano Today* **2016**, *11*, 128–132.

44. Song, Y.; Zhu, S.; Zhang, S.; Fu, Y.; Wang, L.; Zhao, X.; Yang, B., Investigation from Chemical Structure to Photoluminescent Mechanism: A Type of Carbon Dots from the Pyrolysis of Citric Acid and an Amine. *J. Mater. Chem. C* **2015**, *3*, 5976–5984.

45. Schneider, J.; Reckmeier, C. J.; Xiong, Y.; von Seckendorff, M.; Susha, A. S.; Kasák, P.; Rogach, A. L., Molecular Fluorescence in Citric Acid-based Carbon Dots. *J. Phys. Chem. C* **2017**, *121*, 2014–2022.

46. Shi, L.; Yang, J. H.; Zeng, H. B.; Chen, Y. M.; Yang, S. C.; Wu, C.; Zeng, H.; Yoshihito, O.; Zhang, Q., Carbon Dots with High Fluorescence Quantum Yield: The Fluorescence Originates from Organic Fluorophores. *Nanoscale* **2016**, *8*, 14374–14378.

47. He, L.; Wang, T.; An, J.; Li, X.; Zhang, L.; Li, L.; Li, G.; Wu, X.; Su, Z.; Wang, C., Carbon Nanodots@Zeolitic Imidazolate Framework-8 Nanoparticles for Simultaneous pH-responsive Drug Delivery and Fluorescence Imaging. *CrystEngComm* **2014**, *16*, 3259–3263.

48. Karthik, S.; Saha, B.; Ghosh, S. K.; Pradeep Singh, N. D., Photoresponsive Quinoline Tethered Fluorescent Carbon Dots for Regulated Anticancer Drug Delivery. *Chem. Commun.* **2013**, *49*, 10471–10473.

49. Niu, Q.; Gao, K.; Lin, Z.; Wu, W., Amine-capped Carbon Dots as a Nanosensor for Sensitive and Selective Detection of Picric Acid in Aqueous Solution via Electrostatic Interaction. *Anal. Methods* **2013**, *5*, 6228–6233.

50. Strauss, V.; Margraf, J. T.; Dolle, C.; Butz, B.; Nacken, T. J.; Walter, J.; Bauer, W.; Peukert, W.; Spiecker, E.; Clark, T.; Guldi, D. M., Carbon Nanodots: Toward a

Comprehensive Understanding of their Photoluminescence. *J. Am. Chem. Soc.* **2014**, *136*, 17308–17316.

51. Qu, S.; Chen, H.; Zheng, X.; Cao, J.; Liu, X., Ratiometric Fluorescent Nanosensor based on Water Soluble Carbon Nanodots with Multiple Sensing Capacities. *Nanoscale* **2013**, *5*, 5514–5518.

52. Chen, Y.-C.; Nien, C.-Y.; Albert, K.; Wen, C.-C.; Hsieh, Y.-Z.; Hsu, H.-Y., Pseudo-multicolor Carbon Dots Emission and the Dilution-induced Reversible Fluorescence Shift. *RSC Adv.* **2016**, *6*, 44024–44028.

53. Pei, S.; Zhang, J.; Gao, M.; Wu, D.; Yang, Y.; Liu, R., A Facile Hydrothermal Approach Towards Photoluminescent Carbon Dots from Amino Acids. *J. Colloid Interface Sci.* **2015**, *439*, 129–133.

54. Zhu, S.; Meng, Q.; Wang, L.; Zhang, J.; Song, Y.; Jin, H.; Zhang, K.; Sun, H.; Wang, H.; Yang, B., Highly Photoluminescent Carbon Dots for Multicolor Patterning, Sensors, and Bioimaging. *Angew. Chem. Int. Ed.* **2013**, *52*, 3953–3957.

55. Bian, J.; Huang, C.; Wang, L.; Hung, T.; Daoud, W. A.; Zhang, R., Carbon Dot Loading and TiO_2 Nanorod Length Dependence of Photoelectrochemical Properties in Carbon Dot/TiO_2 Nanorod Array Nanocomposites. *ACS Appl. Mater. Interfaces* **2014**, *6*, 4883–4890.

56. Cui, X.; Zhu, L.; Wu, J.; Hou, Y.; Wang, P.; Wang, Z.; Yang, M., A Fluorescent Biosensor based on Carbon Dots-labeled Oligodeoxyribonucleotide and Graphene Oxide for Mercury (II) Detection. *Biosens. Bioelectron.* **2015**, *63*, 506–512.

57. Song, Y.; Zhu, S.; Xiang, S.; Zhao, X.; Zhang, J.; Zhang, H.; Fu, Y.; Yang, B., Investigation into the Fluorescence Quenching Behaviors and Applications of Carbon Dots. *Nanoscale* **2014**, *6*, 4676–4682.

58. Do, S.; Kwon, W.; Rhee, S.-W., Soft-template Synthesis of Nitrogen-doped Carbon Nanodots: Tunable Visible-light Photoluminescence and Phosphor-based Light-emitting Diodes. *J. Mater. Chem. C* **2014**, *2*, 4221–4226.

59. Li, H.; He, X.; Kang, Z.; Huang, H.; Liu, Y.; Liu, J.; Lian, S.; Tsang, C. H. A.; Yang, X.; Lee, S.-T., Water-soluble Fluorescent Carbon Quantum Dots and Photocatalyst Design. *Angew. Chem. Int. Ed.* **2010**, *49*, 4430–4434.

60. Zhang, H.; Huang, H.; Ming, H.; Li, H.; Zhang, L.; Liu, Y.; Kang, Z., Carbon Quantum Dots/Ag_3PO_4 Complex Photocatalysts with Enhanced Photocatalytic Activity and Stability under Visible Light. *J. Mater. Chem.* **2012**, *22*, 10501–10506.

61. Xuelian, Y.; Rongji, L.; Guangjin, Z.; Hongbin, C., Carbon Quantum Dots as Novel Sensitizers for Photoelectrochemical Solar Hydrogen Generation and their Size-dependent Effect. *Nanotechnology* **2013**, *24*, 335401.

62. Zhu, A.; Qu, Q.; Shao, X.; Kong, B.; Tian, Y., Carbon-dot-based Dual-emission Nanohybrid Produces a Ratiometric Fluorescent Sensor for In Vivo Imaging of Cellular Copper Ions. *Angew. Chem. Int. Ed.* **2012**, *51*, 7185–7189.

63. Kong, B.; Zhu, A.; Ding, C.; Zhao, X.; Li, B.; Tian, Y., Carbon Dot-based Inorganic–Organic Nanosystem for Two-photon Imaging and Biosensing of pH Variation in Living Cells and Tissues. *Adv. Mater.* **2012**, *24*, 5844–5848.

64. Tang, J.; Kong, B.; Wu, H.; Xu, M.; Wang, Y.; Wang, Y.; Zhao, D.; Zheng, G., Carbon Nanodots Featuring Efficient FRET for Real-time Monitoring of Drug Delivery and Two-photon Imaging. *Adv. Mater.* **2013**, *25*, 6569–6574.

65. Li, H.; Liu, R.; Lian, S.; Liu, Y.; Huang, H.; Kang, Z., Near-infrared Light Controlled Photocatalytic Activity of Carbon Quantum Dots for Highly Selective Oxidation Reaction. *Nanoscale* **2013**, *5*, 3289–3297.

66. Sun, Y.-P.; Zhou, B.; Lin, Y.; Wang, W.; Fernando, K. A. S.; Pathak, P.; Meziani, M. J.; Harruff, B. A.; Wang, X.; Wang, H.; Luo, P. G.; Yang, H.; Kose, M. E.; Chen, B.; Veca, L. M.; Xie, S.-Y., Quantum-sized Carbon Dots for Bright and Colorful Photoluminescence. *J. Am. Chem. Soc.* **2006**, *128*, 7756–7757.

67. Liu, X.; Liu, H.-J.; Cheng, F.; Chen, Y., Preparation and Characterization of Multi Stimuli-responsive Photoluminescent Nanocomposites of Graphene Quantum Dots with Hyperbranched Polyethylenimine Derivatives. *Nanoscale* **2014**, *6*, 7453–7460.

68. Cao, L.; Wang, X.; Meziani, M. J.; Lu, F.; Wang, H.; Luo, P. G.; Lin, Y.; Harruff, B. A.; Veca, L. M.; Murray, D.; Xie, S.-Y.; Sun, Y.-P., Carbon Dots for Multiphoton Bioimaging. *J. Am. Chem. Soc.* **2007**, *129*, 11318–11319.

69. Zhang, Y.; Goncalves, H.; Esteves da Silva, J. C. G.; Geddes, C. D., Metal-enhanced Photoluminescence from Carbon Nanodots. *Chem. Commun.* **2011**, *47*, 5313–5315.

70. Turkevich, J.; Stevenson, P. C.; Hillier, J., A Study of the Nucleation and Growth Processes in the Synthesis of Colloidal Gold. *Discuss. Faraday Soc.* **1951**, *11*, 55–75.

71. Grasseschi, D.; Ando, R. A.; Toma, H. E.; Zamarion, V. M., Unraveling the Nature of Turkevich Gold Nanoparticles: The Unexpected Role of the Dicarboxyketone Species. *RSC Adv.* **2015**, *5*, 5716–5724.

72. Wuithschick, M.; Birnbaum, A.; Witte, S.; Sztucki, M.; Vainio, U.; Pinna, N.; Rademann, K.; Emmerling, F.; Kraehnert, R.; Polte, J., Turkevich in New Robes: Key Questions Answered for the Most Common Gold Nanoparticle Synthesis. *ACS Nano* **2015**, *9*, 7052–7071.

73. Kimling, J.; Maier, M.; Okenve, B.; Kotaidis, V.; Ballot, H.; Plech, A., Turkevich Method for Gold Nanoparticle Synthesis Revisited. *J. Phys. Chem. B* **2006**, *110*, 15700–15707.

74. Schulz, F.; Homolka, T.; Bastús, N. G.; Puntes, V.; Weller, H.; Vossmeyer, T., Little Adjustments Significantly Improve the Turkevich Synthesis of Gold Nanoparticles. *Langmuir* **2014**, *30*, 10779–10784.

75. Deraedt, C.; Salmon, L.; Gatard, S.; Ciganda, R.; Hernandez, R.; Ruiz, J.; Astruc, D., Sodium Borohydride Stabilizes Very Active Gold Nanoparticle Catalysts. *Chem. Commun.* **2014**, *50*, 14194–14196.

76. Lakowicz, J. R., *Principles of Fluorescence Spectroscopy*. 3rd ed.; Springer: 2006.

77. Jones, G.; Jackson, W. R.; Choi, C. Y.; Bergmark, W. R., Solvent Effects on Emission Yield and Lifetime for Coumarin Laser Dyes. Requirements for a Rotatory Decay Mechanism. *J. Phys. Chem.* **1985**, *89*, 294–300.

78. Porrès, L.; Holland, A.; Pålsson, L.-O.; Monkman, A.; Kemp, C.; Beeby, A., Absolute Measurements of Photoluminescence Quantum Yields of Solutions using an Integrating Sphere. *J. Fluoresc.* **2006**, *16*, 267–273.

79. Magde, D.; Rojas, G. E.; Seybold, P. G., Solvent Dependence of the Fluorescence Lifetimes of Xanthene Dyes. *Photochem. Photobiol.* **1999**, *70*, 737–744.

80. Skehan, P.; Storeng, R.; Scudiero, D.; Monks, A.; McMahon, J.; Vistica, D.; Warren, J. T.; Bokesch, H.; Kenney, S.; Boyd, M. R., New Colorimetric Cytotoxicity Assay for Anticancer-drug Screening. *J. Natl. Cancer Inst.* **1990**, *82*, 1107–1112.

81. Rubinstein, L. V.; Shoemaker, R. H.; Paull, K. D.; Simon, R. M.; Tosini, S.; Skehan, P.; Scudiero, D. A.; Monks, A.; Boyd, M. R., Comparison of In Vitro Anticancer-drug-screening Data Generated with a Tetrazolium Assay versus a Protein Assay against a Diverse Panel of Human Tumor Cell Lines. *J. Natl. Cancer Inst.* **1990**, *82*, 1113–1117.

82. Pop, E.; Varshney, V.; Roy, A. K., Thermal Properties of Graphene: Fundamentals and Applications. *MRS Bull.* **2012**, *37*, 1273–1281.

83. Xu, X.; Ray, R.; Gu, Y.; Ploehn, H. J.; Gearheart, L.; Raker, K.; Scrivens, W. A., Electrophoretic Analysis and Purification of Fluorescent Single-walled Carbon Nanotube Fragments. *J. Am. Chem. Soc.* **2004**, *126*, 12736–12737.

84. Essner, J. B.; Kist, J. A.; Polo-Parada, L.; Baker, G. A., Artifacts and Errors Associated with the Ubiquitous Presence of Fluorescent Impurities in Carbon Nanodots. *Chem. Mater.* **2018**, *30*, 1878–1887.

85. Buffo, R. A.; Cardelli-Freire, C., Coffee Favour: An Overview. *Flavour Fragr. J.* **2004**, *19*, 99–104.

86. Schenker, S.; Heinemann, C.; Huber, M.; Pompizzi, R.; Perren, R.; Escher, R., Impact of Roasting Conditions on the Formation of Aroma Compounds in Coffee Beans. *J. Food Sci.* **2002**, *67*, 60–66.

87. Esquivel, P.; Jiménez, V. M., Functional Properties of Coffee and Coffee By-products. *Food Res. Int.* **2012**, *46*, 488–495.

88. Samaras, T. S.; Camburn, P. A.; Chandra, S. X.; Gordon, M. H.; Ames, J. M., Antioxidant Properties of Kilned and Roasted Malts. *J. Agr. Food Chem.* **2005**, *53*, 8068–8074.

89. Carvalho, D. O.; Correia, E.; Lopes, L.; Guido, L. F., Further Insights into the role of Melanoidins on the Antioxidant Potential of Barley Malt. *Food Chem.* **2014**, *160*, 127–133.

90. Carvalho, D. O.; Øgendal, L. H.; Andersen, M. L.; Guido, L. F., High Molecular Weight Compounds Generated by Roasting Barley Malt are Pro-oxidants in Metal-catalyzed Oxidations. *Eur. Food Res. Technol.* **2016**, *242*, 1545–1553.

91. Yahya, H.; Linforth, R. S. T.; Cook, D. J., Flavour Generation During Commercial Barley and Malt Roasting Operations: A Time Course Study. *Food Chem.* **2014**, *145*, 378–387.

92. Carvalho, D. O.; Gonçalves, L. M.; Guido, L. F., Overall Antioxidant Properties of Malt and how they are Influenced by the Individual Constituents of Barley and the Malting Process. *Compr. Rev. Food Sci. Food Saf.* **2016**, *15*, 927–943.

93. Yang, J.; Zhang, Y.; Gautam, S.; Liu, L.; Dey, J.; Chen, W.; Mason, R. P.; Serrano, C. A.; Schug, K. A.; Tang, L., Development of Aliphatic Biodegradable Photoluminescent Polymers. *Proc. Natl. Acad. Sci. U.S.A* **2009**, *106*, 10086–10091.

94. Kim, J. P.; Xie, Z.; Creer, M. H.; Liu, Z.; Yang, J., Citrate-based Fluorescent Materials for Low-cost Chloride Sensing in the Diagnosis of Cystic Fibrosis. *Chem. Sci.* **2017**, *8*, 550–558.

95. Xie, Z.; Zhang, Y.; Liu, L.; Weng, H.; Mason, R. P.; Tang, L.; Nguyen, K. T.; Hsieh, J.-T.; Yang, J., Development of Intrinsically Photoluminescent and Photostable Polylactones. *Adv. Mater.* **2014**, *26*, 4491–4496.

96. Wang, H.-X.; Yang, Z.; Liu, Z.-G.; Wan, J.-Y.; Xiao, J.; Zhang, H.-L., Facile Preparation of Bright-fluorescent Soft Materials from Small Organic Molecules. *Chem. Eur. J.* **2016**, *22*, 8096–8104.

97. Kasprzyk, W.; Bednarz, S.; Zmudzki, P.; Galica, M.; Bogdal, D., Novel Efficient Fluorophores Synthesized from Citric Acid. *RSC Adv.* **2015**, *5*, 34795–34799.

98. Repligen Corporation, Relative Pore Size Chart. https://www.repligen.com/resources/knowledge-base/references/mabselectsure-1 (accessed March 20, 2021).

99. Liu, Y.; Li, S.; Li, K.; Zheng, Y.; Zhang, M.; Cai, C.; Yu, C.; Zhou, Y.; Yan, D., A Srikaya-like Light-harvesting Antenna based on Graphene Quantum Dots and Porphyrin Unimolecular Micelles. *Chem. Commun.* **2016**, *52*, 9394–9397.

100. Ryu, S.; Lee, K.; Hong, S. H.; Lee, H., Facile Method to Sort Graphene Quantum Dots by Size through Ammonium Sulfate Addition. *RSC Adv.* **2014**, *4*, 56848–56852.

101. Rajendran, R.; Sohila, S.; Muralidharan, R.; Muthamizhchelvan, C.; Ponnusamy, S., One-Pot Microwave Synthesis of Fluorescent Carbogenic Nanoparticles from Triton X-100 for Cell Imaging. *Eur. J. Inorg. Chem.* **2014**, *2014*, 392–396.

102. Kim, S.; Hwang, S. W.; Kim, M.-K.; Shin, D. Y.; Shin, D. H.; Kim, C. O.; Yang, S. B.; Park, J. H.; Hwang, E.; Choi, S.-H.; Ko, G.; Sim, S.; Sone, C.; Choi, H. J.; Bae, S.; Hong, B. H., Anomalous Behaviors of Visible Luminescence from Graphene Quantum Dots: Interplay between Size and Shape. *ACS Nano* **2012**, *6*, 8203–8208.

103. Khan, S.; Sharma, A.; Ghoshal, S.; Jain, S.; Hazra, M. K.; Nandi, C. K., Small Molecular Organic Nanocrystals Resemble Carbon Nanodots in terms of their Properties. *Chem. Sci.* **2018**, *9*, 175–180.

104. Kozawa, D.; Miyauchi, Y.; Mouri, S.; Matsuda, K., Exploring the Origin of Blue and Ultraviolet Fluorescence in Graphene Oxide. *J. Phys. Chem. Lett.* **2013**, *4*, 2035–2040.

105. Galande, C.; Mohite, A. D.; Naumov, A. V.; Gao, W.; Ci, L.; Ajayan, A.; Gao, H.; Srivastava, A.; Weisman, R. B.; Ajayan, P. M., Quasi-Molecular Fluorescence from Graphene Oxide. *Sci. Rep.* **2011**, *1*, 85.

106. Dekaliuk, M. O.; Viagin, O.; Malyukin, Y. V.; Demchenko, A. P., Fluorescent Carbon Nanomaterials: "Quantum Dots" or Nanoclusters? *Phys. Chem. Chem. Phys.* **2014**, *16*, 16075–16084.

107. Yang, C.; Zhu, S.; Li, Z.; Li, Z.; Chen, C.; Sun, L.; Tang, W.; Liu, R.; Sun, Y.; Yu, M., Nitrogen-doped Carbon Dots with Excitation-independent Long-wavelength Emission Produced by Room-temperature Reaction. *Chem. Commun.* **2016**, *52*, 11912–11914.

108. Repligen Corporation, Frequently Asked Questions | Lab Dialysis. https://www.repligen.com/technologies/dialysis/FAQ-dialysis (accessed March 20, 2021).

109. Vinci, J. C.; Ferrer, I. M.; Seedhouse, S. J.; Bourdon, A. K.; Reynard, J. M.; Foster, B. A.; Bright, F. V.; Colón, L. A., Hidden Properties of Carbon Dots Revealed after HPLC Fractionation. *J. Phys. Chem. Lett.* **2013**, *4*, 239–243.

110. Khan, S.; Gupta, A.; Verma, N. C.; Nandi, C. K., Time-resolved Emission Reveals Ensemble of Emissive States as the Origin of Multicolor Fluorescence in Carbon Dots. *Nano Lett.* **2015**, *15*, 8300–8305.

111. Zhao, Q.-L.; Zhang, Z.-L.; Huang, B.-H.; Peng, J.; Zhang, M.; Pang, D.-W., Facile Preparation of Low Cytotoxicity Fluorescent Carbon Nanocrystals by Electrooxidation of Graphite. *Chem. Commun.* **2008**, 5116–5118.

112. Gong, X.; Chin Paau, M.; Hu, Q.; Shuang, S.; Dong, C.; Choi, M. M. F., UHPLC Combined with Mass Spectrometric Study of As-synthesized Carbon Dots Samples. *Talanta* **2016**, *146*, 340–350.

113. Fuyuno, N.; Kozawa, D.; Miyauchi, Y.; Mouri, S.; Kitaura, R.; Shinohara, H.; Yasuda, T.; Komatsu, N.; Matsuda, K., Drastic Change in Photoluminescence Properties of Graphene Quantum Dots by Chromatographic Separation. *Adv. Opt. Mater.* **2014**, *2*, 983–989.

114. Vinci, J. C.; Colon, L. A., Fractionation of Carbon-based Nanomaterials by Anion-exchange HPLC. *Anal. Chem.* **2011**, *84*, 1178–1183.

115. Baker, J. S.; Colón, L. A., Influence of Buffer Composition on the Capillary Electrophoretic Separation of Carbon Nanoparticles. *J. Chromatogr. A* **2009**, *1216*, 9048–9054.

116. Ding, H.; Yu, S.-B.; Wei, J.-S.; Xiong, H.-M., Full-color Light-emitting Carbon Dots with a Surface-state-controlled Luminescence Mechanism. *ACS Nano* **2016**, *10*, 484–491.

117. Liu, H.; Ye, T.; Mao, C., Fluorescent Carbon Nanoparticles Derived from Candle Soot. *Angew. Chem. Int. Ed.* **2007**, *46*, 6473–6475.

118. Gong, X.; Hu, Q.; Chin Paau, M.; Zhang, Y.; Zhang, L.; Shuang, S.; Dong, C.; Choi, M. M. F., High-performance Liquid Chromatographic and Mass Spectrometric Analysis of Fluorescent Carbon Nanodots. *Talanta* **2014**, *129*, 529–538.

119. Hu, Q.; Paau, M. C.; Choi, M. M. F.; Zhang, Y.; Gong, X.; Zhang, L.; Liu, Y.; Yao, J., Better Understanding of Carbon Nanoparticles via High-performance Liquid Chromatography-Fluorescence Detection and Mass Spectrometry. *Electrophoresis* **2014**, *35*, 2454–2462.

120. Gong, X.; Hu, Q.; Paau, M. C.; Zhang, Y.; Shuang, S.; Dong, C.; Choi, M. M. F., Red-green-blue Fluorescent Hollow Carbon Nanoparticles Isolated from Chromatographic Fractions for Cellular Imaging. *Nanoscale* **2014**, *6*, 8162–8170.

121. Hu, Q.; Paau, M. C.; Zhang, Y.; Gong, X.; Zhang, L.; Lu, D.; Liu, Y.; Liu, Q.; Yao, J.; Choi, M. M. F., Green Synthesis of Fluorescent Nitrogen/Sulfur-doped Carbon Dots and Investigation of their Properties by HPLC Coupled with Mass Spectrometry. *RSC Adv.* **2014**, *4*, 18065–18073.

122. Hu, Q.; Paau, M. C.; Zhang, Y.; Chan, W.; Gong, X.; Zhang, L.; Choi, M. M. F., Capillary Electrophoretic Study of Amine/Carboxylic Acid-functionalized Carbon Nanodots. *J. Chromatogr. A* **2013**, *1304*, 234–240.

123. Wei, J.; Qiu, J., Unveil the Fluorescence of Carbon Quantum Dots. *Adv. Eng. Mater.* **2015**, *17*, 138–142.

Chapter 5: Reaction By-products Strike Again: Effects of Membrane Dialysis on the Performance of Carbon-Nanodot-Sensitized Mesoporous-TiO_2-based Photovoltaic Devices†

†The material contained within this chapter (*e.g.*, figures, data, analysis) is derived from a manuscript to be submitted to a yet-to-be-determined, peer-reviewed journal. Upon acceptance, the information contained herein should be appropriately cited with the proper copyright holder.

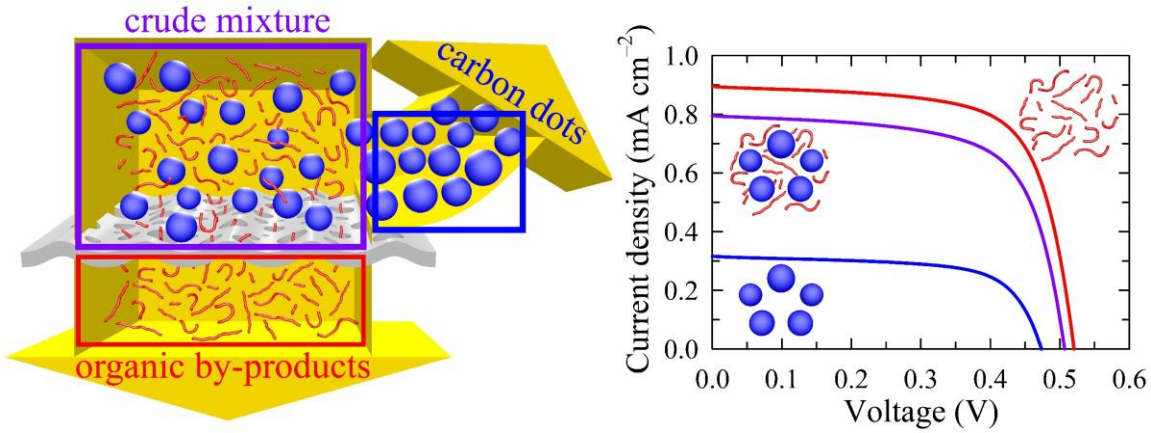

Scheme 5.1 Graphical abstract highlighting the impact that molecular by-products generated in FCD syntheses have on photosensitizer applications, particularly when employed in photovoltaics.

Abstract

Fluorescent carbon dots have attracted widespread interest owing to their unique properties, particularly their superlative optical characteristics, however, in recent years, evidence has emerged suggesting some of these fluorescent features originate from molecular by-products, not the nanocarbons. In this work, a series of bottom-up carbon dot syntheses were conducted and the as-synthesized samples were fractionated with membrane dialysis to yield two additional fractions; the dialysate fraction containing reaction by-products and the retentate fraction containing the desired nanocarbons. These fractions were then employed as photosensitizers in mesoporous-TiO_2-based photovoltaic devices to explore the effects purification has on light-harvesting applications. Our results unequivocally show that reaction by-products ubiquitously generated photocurrent and, thus, contributed to the observed performance for devices employing the nonpurified, as-synthesized fraction. Furthermore, in one precursor system, the molecular by-products were responsible for the majority of the photocurrent and device performance, while in another system, the performance of the nanocarbon-containing retentate fraction was markedly higher than the performance of its parent as-synthesized sample. These results draw further attention to and clearly highlight the dire need for a uniformly implemented tactical change in carbon dot syntheses from purification-free to rigorous fractionation protocols.

Introduction

Fluorescent carbon dots (FCDs), which constitute the newest addition to the nanoscale carbon family, have been the focus of intensive research in recent years due to their purportedly unique and useful optical features[1-3], as well as preferential properties over

other quantum dot (QD) systems (*e.g.*, CdS).[4-6] This subclass of the nanoscale carbon family encompasses many classifications of fluorescent nanocarbons (*e.g.*, carbon (nano)dots, carbon QDs, graphene QDs), with the literature suggesting that these materials can be produced through a myriad of top-down or bottom-up approaches, where the appropriate thermal treatment of virtually any carbon-containing precursor professedly results in FCDs. For example, FCDs have been reported to originate from citrates,[7-13] saccharides (*e.g.*, glucose, chitosan),[14-16] biomass,[17-21] and even human urine.[22] Due to their facile preparation and putatively promising characteristics, research on FCDs saw an exponential explosion in published works, however, the unbridled zeal and precipitous publication rate organically produced several uncritical, unsubstantiated, and detrimental claims and misconceptions entering the literature record. As has been previously pointed out, in many instances, revisiting prior work with more scientific rigor is warranted, in particular, employing proper characterization, consistent nomenclature, and, most of all, meticulous purification,[23-24] however, such practices have yet to see widespread implementation.

While FCDs are reported to possess intriguing photophysical properties, the exact origin of these materials' fluorescence remains elusive, which is, in large part, due to the lack of consistent and methodical purification, where ineffective and uncorroborated means are frequently employed, or worse, missing altogether. Historically, the emission characteristics observed from these materials have been attributed to variations in physical and chemical properties such as nanocarbon core size, extent of conjugation, surface functionality/defects, or heteroatom (*e.g.*, O, N, S) doping,[25-28] although, in recent years several researchers have alluded to the need for the reduction of sample complexity via

efficient and consistent separation procedures to illuminate the true origin of FCD fluorescence.[29-34] Exacerbating the issue is the mounting evidence that the fluorescence associated with FCDs originates significantly from molecular/oligomeric by-products that are generated alongside the nanoscale carbons,[10, 23, 35-39] where the properties of molecular by-product aggregates resemble the reported characteristics of FCDs,[40-42] making a unified purification approach all the more pressing.[24] Indeed, a variety of citric acid (CA) derived molecular emitters,[40, 43-50] such as 2-pyridone derivatives, have been identified, by-products originating from the direct thermal degradation of CA[40] or from CA reacted with a range of N- or S-containing, heteroatom dopants.[40, 44-50] Furthermore, works not attempting FCD formation synthesized these exact (or structurally related) molecular fluorophores through the reaction of CA with similar N- or S-containing precursors.[51-55]

Although FCDs are commonly employed in fluorescence-based applications, their other reported photophysical and electronic properties such as high molar absorptivity and tunable visible light absorption (typically via N-/S-doping), as well as redox, donor/acceptor, and charge transfer capabilities, have resulted in significant interest in exploiting these properties in energy applications,[56] in particular, in a wide range of photovoltaic (PV) architectures.[57-58] Specifically, these materials are of keen interest as the sole or co-light harvester in sensitized (typically, metal-oxide-based) PV cells due to their intriguing optical properties, appropriate band alignments, and ability to inject charges into the semiconductor (*e.g.*, TiO_2).[14, 20-21, 59-77] Since this area was last comprehensively reviewed,[58, 78] additional works have emerged employing FCDs as the sole sensitizer[15-16, 18-19, 79-84] or in tandem with a dye,[17-18, 80, 85] where the highest reported power conversion efficiencies (η) employing FCDs as the sole sensitizer were between ~0.8 and 0.9%.[67, 83-84]

Specifically, Wang *et al*. reported a maximum η of 0.79% employing N-doped CDs (thermally derived from citric acid and ammonia) as the sensitizer in devices with an architecture of FTO/mesoporous TiO_2/TiO_2 scattering layer/gel electrolyte/Pt, where the observed performance was dependent on the precursor mass ratio.[67] Carolan and co-workers reported a comparable η of 0.80% employing N-doped CQDs generated via the application of a direct current, atmospheric-pressure microplasma to an aqueous solution of citric acid and ethylenediamine, where the CQDs were utilized as the photoactive layer in solid-state devices with an architecture of ITO/compact TiO_2/CQDs/Au.[83] Zhang *et al*. further pushed the η to 0.87% by hydrothermally treating citric acid and ethylenediamine in the presence of a TiO_2 film and employing the CQD-sensitized photoanodes in devices with an architecture of FTO/mesoporous TiO_2/CQDs/S^{2-}:S_x^{2-}/Cu_2S/brass.[84] Unfortunately, many of the FCD works focused on energy-based applications, particularly sensitizer-centered PV explorations, fell victim to the unsubstantiated but perpetuated notion that filtration and centrifugation are sufficient modes of purification, begging the question, are the FCDs themselves or their reaction by-products responsible for the PV action observed in photosensitizer-driven applications?

As an extension to our previous work, in which we unequivocally demonstrated the importance of adequate purification to generate meaningful, error-free results, particularly with regards to luminescent characterizations of FCDs,[23] herein, we present our findings on the effects that extensive purification with dialysis membranes has on the performance metrics of PV devices employing molecularly derived FCD fractions as the sole semiconductor sensitizer. The results disseminated here draw further attention to this detrimental purification issue, demonstrating that reaction by-products impact the observed

performance in PV devices based on "FCD"-sensitized mesoporous TiO_2 nanoparticle films. Four representative FCD synthetic protocols were explored, where two of the employed protocols have been reported to result in FCDs that function as photosensitizers,[15, 67] while the other two protocols derive from a common microwave approach[13, 23] and a solvothermal synthesis reported to generate dual blue- and red-emitting FCDs.[86] Specifically, the sample precursors consisted of citric acid and NH_4OH, L-arginine, citric acid and urea, and glutathione in formamide, which are abbreviated as CA–NH_4OH, Arg, CA–U, and GSH–F, respectively, throughout the remainder of the text.

Experimental

Materials and Reagents

Anhydrous citric acid (791725, ≥99.5%), urea (U5378, ≥98%), ammonium hydroxide (221228, 28.0–30.0% NH_3 basis), L-glutathione reduced (G4251, ≥98.0%), formamide (F9037, ≥99.5%), and titanium tetrachloride (208566, 99.9%) were purchased from Sigma-Aldrich (St. Louis, MO). L-arginine (BP2505500, ≥99%, free base), acetone (A949SK, ≥99.5%), isopropanol (A416, ≥99.5%), hydrochloric acid (A144S-212, 36.5–38.0%), sulfuric acid (A300S-212, 95.0–98.0 w/w%), anthracite coal (S26610), and syringe filters (09-719C, 0.20 µm pore size) were acquired from Fisher Scientific (Pittsburg, PA). Ethanol (2716, 200 proof) was procured from Decon Labs, Inc., (King of Prussia, PA) and regenerated cellulose dialysis membranes with molecular weight cut-offs (MWCOs) of 15 and 50 kDa (Spectra/Por® 7, 132124 and 132130, respectively) were acquired from Repligen® (formerly Spectrum Labs®, Rancho Dominguez, CA). All chemicals were used as received. Ultrapure Millipore water polished to a resistivity of 18.2 MΩ·cm was employed for all aqueous solutions and substrate rinsing. The specific materials used for

the fabrication of PV devices and their sources are provided in the "PV Device Preparation and Assembly" subsection below.

Fluorescent Carbon Dot Syntheses and Purification

Thermal Treatment of Citric Acid in Ammonium Hydroxide

N-doped FCD samples were generated following a reported protocol in which the obtained material had been employed as a photosensitizer in mesoporous TiO_2-based devices.[67] Specifically, 4 g of citric acid (CA) and 1 g of ammonium hydroxide (NH_4OH) were dissolved in 10 mL of water. The mixture was transferred to a porcelain crucible and then thermally treated at 200 °C for 3 h in a programmable oven. Upon natural cooling, the resultant carbogenic product was dispersed with 20–25 mL of acetone and the crucible was rinsed consecutively with 10- and 5-mL aliquots of acetone to collect as much product as possible; the three fractions were combined, totaling approximately 40 mL of sample. The synthesis was replicated 9–11 times to give a total of 10–12 individual syntheses per sample batch, which were all homogenized before proceeding. Note, substantial sedimentation was observed in the samples shortly after redispersion, therefore, once the samples were homogenized, the entire volume (400–480 mL) was left undisturbed for 15–30 min. The acetone-dispersed supernatant was carefully decanted into 50 mL falcon tubes and centrifuged at 9k rpm for 15 min, after which the supernatant was again carefully decanted and all sediment stemming from the reaction was discarded. Although the sediment did not disperse well in acetone and, thus, was not explored in this work, we note that it appeared to disperse fairly well in water so the sediment material may not consist solely of large carbon structures. After centrifugation, typically 50 mL of the supernatant, with an average concentration of 35 mg mL^{-1}, was retained for studies of the as-synthesized

(as-synth.) fraction while the remaining solution volume was concentrated via rotary evaporation (25 °C, <100 mbar) to a volume of 50 mL for purification with dialysis. Initially, samples were dialyzed against water, however, as our studies progressed, substantial irreproducibility in performance was observed, which arose from apparent water-induced irreversible aggregation, as directed studies later confirmed (Figure D.17). Attempts were made to dialyze the samples against acetone, however, the solvent proved too harsh on the cellulose membranes, leading to severe membrane leakage and even complete membrane failure (*i.e.*, catastrophic rupturing). We found that a mixed solvent system of 50:50 vol% acetone:ethanol (EtOH) worked well as the acetone content kept the material dispersed while the presence of EtOH alleviated the issues previously encountered with 100% acetone. Therefore, the concentrated supernatant fraction (40–50 mL) was dialyzed against 2 L of a 50:50 vol% acetone:EtOH mixture with a 50 kDa MWCO membrane and the exchange solvent was refreshed daily for one week. The material permeating the membrane into the exchange solvent over the first 2–3 days of dialysis was collected, concentrated, and, eventually, dried via rotary evaporation (50 °C, <100 mbar). Once all the solvent was visibly removed, the sample was rotovaped under the same conditions for 3 h to ensure adequate removal of all EtOH and the dried material was redispersed in 50 mL of acetone to yield the dialysate (dial.) fraction. Upon completion of dialysis, the material retained within the membrane was collected and treated in a similar fashion to the dial. fraction to yield the retentate (retent.) fraction. Fraction concentrations were assessed by adding 1 mL of solution to premassed scintillation vials, driving off the solvent at ~65 °C, drying the material at ~80 °C for 24–48 h, and re-massing the vials to determine the material quantity delivered in 1 mL. All concentration assessments were

conducted in triplicate and vials were massed multiple times throughout the drying period, stopping the drying once the mass values were consistent with the previous assessment. The parent solutions of the three fractions were diluted to 5, 10, or 30 mg mL^{-1} in 100% acetone or 50:50 vol% acetone:EtOH for sensitization of TiO_2 films. Due to the poor yield of this reaction (~1% or less), the highest concentration of retentate that could be obtained that still yielded a workable volume was 5 mg mL^{-1}. Note, irreversible sedimentation was observed in as-synth. solutions of concentrations higher than 30 mg mL^{-1}, as well as the 5 mg mL^{-1} retent. solutions.

Solvothermal Treatments of Arginine and Glutathione-Formamide

Two reported solvothermal approaches using distinct precursors were explored: (i) L-arginine (Arg) and (ii) L-glutathione (GSH) in formamide (F). The product resulting from the former approach has been reported as a photosensitizer in mesoporous TiO_2-based devices[15] while the product from the latter approach is reported to exhibit strong absorbance and fluorescence in the visible region, particularly two distinct peaks at red wavelengths,[86] features that were verified in-house (Figure D.1).

(i) The Arg-derived samples were prepared by dispersing 0.35 g L-arginine in 10 mL of EtOH via brief (<5 min) bath sonication and transferring the dispersion to a 23 mL Teflon-lined stainless-steel autoclave for a 6 h solvothermal treatment at 200 °C in a programmable oven. After treatment, a vibrant orange solution was obtained, which was carefully poured out and the Teflon sleeve was rinsed with a 5-mL aliquot of EtOH, combining the rinse with the orange solution. The synthesis was replicated at least nine additional times and the resulting orange solutions were homogenized to generate one sample batch. The homogenized products were placed in 50 mL Falcon tubes and

centrifuged at 9k rpm for 15 min, although, in all syntheses conducted, little to no sediment was obtained upon centrifugation. Regardless, the solutions were carefully decanted out to leave any potential sediment behind. The solutions were then homogenized again and, typically, 50 mL of this homogenized solution, with an average concentration of ~18 mg mL^{-1}, was retained for studies of the as-synth. fraction, with approximately half of this volume being passed through a 0.20 μm pore size syringe filter to generate a filtered as-synth. fraction (denoted as "as-synth. filt."). The remaining solution volume was concentrated via rotary evaporation (50 °C, <100 mbar) to a volume of 40 mL for purification with dialysis. Similar to the CA–NH_4OH samples, initial studies showed that the Arg-derived samples may also be negatively impacted by water (data not shown) as only a few mg of retentate were obtained even when dialyzing with a 15 kDa MWCO membrane, therefore, the samples explored in this work were dialyzed against absolute EtOH. Specifically, the concentrated samples (40–50 mL) were dialyzed against 2 L of EtOH with a 50 kDa MWCO membrane and the exchange solvent was refreshed daily for one week. Due to the low concentrations this precursor system yields, the material permeating the membrane into the exchange solvent was collected and concentrated via rotary evaporation (50 °C, <100 mbar) for the entire dialysis period, although by the fourth to fifth day, very little material appeared to still be permeating the membrane. Upon completion of dialysis, the final round of solvent was combined with the previously concentrated fractions and again concentrated via rotary evaporation (50 °C, <100 mbar) to 50 mL to yield the dial. fraction. The parent solutions of the as-synth., as-synth. filt., and dial. fractions were diluted to 10 mg mL^{-1} in EtOH for sensitization of TiO_2 films. Additionally, the original

40 mL of sample placed on dialysis was collected from the membrane and concentrated via rotary evaporation (50 °C, <100 mbar) to 10–15 mL to yield the 10 mg mL^{-1} retent. fraction employed for sensitization of TiO_2 films. Solution concentrations were assessed in a similar fashion to the CA–NH_4OH samples. Note, irreversible sedimentation, in the form of a light orange to tan powder, was observed in all fractions days after synthesis with some electroless deposition occurring when stored in plastic Falcon tubes.

Furthermore, the generation of a disc- or bean-shaped, dark red to brown solid was consistently observed in the bottom of the Teflon sleeve after solvothermal treatment. The formation of this insoluble material was attributed to the significant quantity of sedimented, solid Arg in the sleeve prior to synthesis, as the Arg concentration employed in the synthesis (35 mg mL^{-1}) is well beyond the solubility limit of Arg in EtOH. The solid product was only sparingly soluble to insoluble in most conventional solvents, specifically, water, methanol, EtOH, isopropanol, acetone, acetonitrile, dichloromethane, dimethylformamide, dimethylsulfoxide (DMSO), tetrahydrofuran, chloroform, toluene, and hexane, with higher apparent solubilities in more polar solvents. The solid pellets appeared most soluble in DMSO, yielding a concentration of ~8 mg mL^{-1}. TiO_2 films were sensitized in this solution and PV characterizations were conducted, however, the performance was comparable to that of the as-synth. fraction (Table D.1), therefore, the solid pellets were not explored any further. Lastly, although different concentrations of the Arg fractions were not extensively explored, a 30 mg mL^{-1} as-synth. solution was tested and the increase in concentration led to an increase in V_{OC} to over 0.6 V (Table D.1), therefore, based on the observed results for

the 10 mg mL^{-1} fractions, a purified retent. fraction of higher concentration may yield further improvements in performance, if the photocurrent also increases.

(ii) The GSH–F-derived samples were prepared by dissolving approximately 100 mg of L-glutathione in 10 mL of formamide and solvothermally treating this solution for 4 h at 180 °C in a 23 mL Teflon-lined stainless-steel autoclave placed in a programmable oven. After treatment and natural cooling, the viscous, greenish-black samples were collected and the sleeves were rinsed with two 5-mL aliquots of water, combining the rinses with the parent sample. The synthesis was replicated at least nine additional times and the resulting solutions were homogenized to generate one sample batch. The homogenized products were placed in 50 mL Falcon tubes and centrifuged at 9k rpm for 15 min and the supernatants were decanted into a single flask to homogenize again. Then 40–50 mL of this homogenized solution was placed on dialysis against 1.5–2 L of water with a 50 kDa MWCO membrane and the exchange solvent was refreshed daily for one week. The remaining solution volume was set aside for as-synth. studies. The material permeating the membrane into the exchange solvent over the first 2–3 days of dialysis was collected and concentrated via rotary evaporation (50 °C, <100 mbar). Upon completion of dialysis, the material retained within the membrane was collected and the solution was lyophilized to obtain a solid powder. Due to the difficult-to-remove formamide content in the as-synth. and dial. fractions of this sample system, solid powders could not be obtained for these fractions, therefore, the solutions were rotovaped (50 °C, <100 mbar) for >3 h so that the samples were dispersed in essentially 100% formamide and then the solutions were diluted 2-fold with water. These 50:50 vol% formamide:water solutions of the as-synth. and dial. fractions were used as is for

sensitization of TiO_2 while a 10 mg mL^{-1} aqueous solution of the retent. fraction was prepared for sensitization. Note, irreversible sedimentation, in the form of a green to black powder, was observed in all fractions days after synthesis and extensive electroless deposition of green to black colored thin films occurred regardless if the solutions were stored in plastic Falcon tubes or glass scintillation vials.

Domestic Microwave Treatment of Citric Acid and Urea

Following a common and widely reported protocol,[13, 87-92] FCDs were synthesized from citric acid (CA) and urea (U) in a 1:3 CA:U molar ratio using a 900 W Frigidaire domestic microwave oven. Specifically, 6 g of CA and 6 g of U were dissolved in 20 mL of water in a round bottom flask stabilized in a beaker and the solution was treated in the microwave on the default power setting (100% power) for 5 min, forming a charred, porous product. The resultant carbonaceous material was dissolved in 50 mL of water and the round bottom flask was rinsed with two additional 50 mL aliquots of water to ensure adequate removal of all the product, homogenizing these three fractions. The homogenized solution was placed in 50 mL Falcon tubes, centrifuged at 9k rpm for 15 min, and the supernatants were decanted into a single flask to homogenize again. Then 40–50 mL of this homogenized solution was placed on dialysis against 1.5–2 L of water with a 50 kDa MWCO membrane and the exchange solvent was refreshed daily for one week. The remaining solution volume was set aside for as-synth. studies or additional dialysis. The material permeating the membrane into the exchange solvent over the first 24 h of dialysis was collected and concentrated via rotary evaporation (50 °C, <100 mbar) to yield the dial. fraction. Upon completion of dialysis, the material retained within the membrane was collected and this solution, as well as the as-synth. and dial. fractions, were lyophilized to obtain solid

powders. Then 10 mg mL^{-1} aqueous solutions of these fractions were prepared for sensitization of TiO_2. Note, minor irreversible sedimentation was observed in all fractions 1–2 weeks after synthesis.

Acid Oxidation of Coal to GQDs

Coal-derived graphene quantum dots (GQDs) were generated following a reported protocol.[93] Specifically, anthracite coal was first coarsely crushed with a hammer followed by fine pulverization with a plastic, handheld "ball mill". Then, 325 mg of the pulverized coal was suspended in a mixture of concentrated sulfuric (60 mL) and nitric (20 mL) acids. The suspension was bath sonicated for 2 h and then heated for 24 h at 100 °C under reflux and stirring in an improvised sand bath consisting of an anodized aluminum, round cake pan (Fat Daddio's®) filled with copper-coated airgun BBs (0.177 caliber; Crosman® Copperhead®). Temperature control was achieved to within 2 °C using a digital stirring hotplate (Super-Nuova™; Thermo Scientific™) connected to a J-type thermocouple immersed in the BBs while stirring (250 rpm) was provided by a PTFE-coated, magnetic stir bar placed within the round-bottom flask. After the 24 h refluxing period, the solution was allowed to naturally cool and the product was slowly poured over ~12 large ice cubes (~200 mL of solid ice). The reaction flask was rinsed multiple times with water and the rinses (totaling 100 mL) were combined with the above solution. NaOH pellets were slowly and carefully added to the product solution until the pH was near 7. The neutralized solution was gravimetrically filtered (Fisherbrand™ filter paper, 09-801C, P5, medium porosity), however, due to the high salt concentration, salt crystallization occurred immediately upon pouring into the filter paper. Therefore, multiple pieces of filter paper were used and copious amounts of water was passed through the filter paper to ensure that nearly all the

sample had been filtered, which resulted in over 1.5 L of solution. Thus, the sample was concentrated via rotary evaporation (50 °C, <100 mbar) to decrease the volume to <0.5 L and then 40–50 mL fractions of the sample were dialyzed for a week against 1.5 L of water using a 50 kDa MWCO membrane, refreshing the exchange solvent daily. Due to the large volume, dialysis of the entire sample was conducted over a period of weeks to obtain a workable volume of a reasonably concentrated solution. Once a few hundred mL of the retent. fraction were collected, the solution was concentrated via rotary evaporation (50 °C, <100 mbar) to <40 mL and the sample was lyophilized to obtain a solid powder. Then 10 mg mL^{-1} aqueous solutions of the purified GQDs were prepared for 24 h sensitization of TiO_2.

Photovoltaic Device Preparation and Assembly

TEC™ 7 fluorine-doped tin oxide (FTO) coated glass was sourced from Pilkington Glass (Toledo, OH). The large glass sheets (12” x 12”) were cut down to electrode size (1” x 0.670” or ~25 mm x 17 mm) with a laboratory glass cutting table (GC0101) procured from MSE Supplies (Tucson, AZ). The cut glass was then cleaned by sequentially sonicating the substrates for 60 min in a dilute solution of Alconox® detergent (0.5 wt%), an ethanolic solution of 0.1 M HCl, isopropanol, and acetone. After cleaning with detergent and ethanolic HCl, the glass was thoroughly rinsed with water before proceeding and after sonication in acetone the substrates were dried upright at 50–70 °C. The substrates were then placed in a 40 mM aqueous $TiCl_4$ solution for 40 min at 70 °C (FTO side up), after which the treated substrates were rinsed with water and EtOH and dried upright at 50–70 °C. Transparent titania (TiO_2) paste, sourced from GreatCell Energy® (MS002010) or Sigma-Aldrich (791547), was applied to the FTO side of the glass via a Doctor blade

approach using precut vinyl masks (~100 μm thick) to define the film area. The adhesive-backed, removable masks were cut from a 12" x 48" roll of black Cricut® Premium Vinyl™ - Removable using Cricut Explore Air™ 2 or Cricut Maker® machines with each individual mask possessing outer dimensions of 1" x 0.620" (or ~25 mm x 15.8 mm) and a 1 cm^2 (1 cm x 1 cm) centered window. After carefully removing the masks, the films were allowed to relax at room temperature in the dark for 24 h and were then dried in a programmable oven at 125 °C and 200 °C for 24 and 4 h, respectively. Lastly, the dried films were sintered in a muffle furnace at 525 °C for 1 h using a ramp rate of 1 °C min^{-1}. After the 1 h sintering period, the furnace was shut off and allowed to cool naturally with the films inside. The TiO_2 films were then sensitized for 2–24 h in the FCD fractions depending on the exact sample and study being conducted. Specifically, the CA-derived fractions (*i.e.*, CA–NH_4OH, CA–U) were sensitized for 2 h, the Arg fractions for 12 h, and the GSH–F fractions for 24 h. These sensitization times were chosen based on reported times in the literature[15, 67] as well as the results of 24 h uptake studies (Figures D.2–D.5). Pt counter electrodes were prepared on precleaned FTO-coated glass by masking off a trough with 2 layers of Scotch™ brand tape and applying Pt paste (PT-1, 006210, GreatCell Energy® or 791512, Sigma-Aldrich) via the Doctor blade technique. After carefully removing the tape, the films were dried at 70–100 °C for 24 h and then fired at 450 °C for 1 h in a muffle furnace. Devices were then assembled by sandwiching a non-melted DuPont™ Surlyn® 60 μm spacer (Meltonix 1170-60; sourced from Solaronix, Aubonne, Switzerland) between a FCD-sensitized TiO_2 photoanode and a Pt counter electrode. Prior to clamping the device shut with 1" binder clips, electrolyte containing the I^-/I_3^- redox couple (Iodolyte AN-50 from Solaronix) was injected in between the electrodes. The external areas of the devices

were carefully wiped down with an EtOH-soaked Kimwipe™ to remove any residual electrolyte and potential light scattering contaminants.

Sensitized TiO_2 Film Characterizations

Absorbance spectra of bare and sensitized TiO_2 films were collected on an Aligent® Cary® 60 UV-vis spectrophotometer from 200 to 1100 nm prior to device assembly. Photographs of all sensitized films were also collected. For the temporal (*i.e.*, 2, 4, 6, 8, 12, 24 h) uptake studies, films were placed in the sensitizer solutions for 2 h and, upon removal, rinsed with the appropriate solvent (CA–NH_4OH: acetone; Arg: EtOH; CA–U and GSH–F: water) and dried under ambient conditions. UV-vis spectra were then collected and the films were placed back in the sensitizer solutions for another 2 h to yield 4 h of total sensitization time. This process was repeated for additional 2, 2, 4, and 12 h intervals such that the total sensitization time was 6, 8, 12, and 24 h, respectively. The temporal uptake studies for each fraction were conducted in triplicate and the absorbance spectra for each time interval were averaged prior to further analysis. Since many of the fractions for the different precursor systems did not display distinct absorbance peaks and, within each precursor system, the fractions often had markedly different absorbance spectra, single peak (or wavelength) tracking was not possible for a proper comparison of the uptake rate. Therefore, the area of the absorbance spectra was calculated (typically between 400 and 800 nm) and the natural logarithm of the ratio of the sensitized film absorbance area at time, t (A_t), to its respective bare TiO_2 absorbance area (A_0) was calculated and plotted as $\ln(A_t/A_0)$ *vs* sensitization time.

Photovoltaic Device Characterizations

Solar irradiation (1 sun or 100 mW cm^{-2}) was simulated with a Newport® Oriel® LCS-100™ solar simulator (94011A-ES) equipped with a Newport® AM1.5G air mass filter (81088A-LCS) and calibrated with a certified Newport® Oriel® silicon reference cell and meter (91150V). Current-voltage data were collected with a Keithley 2400 SourceMeter™ and Oriel® I-V Test Station software under reverse-bias from –0.20 to 0.75 V at 0.08 V s^{-1} with a 0.5 s presweep delay and 30 ms dwell time per voltage increment. Select metrics, specifically, efficiency (η), short-circuit current density (J_{SC}), open-circuit voltage (V_{OC}), and fill factor (FF), for all characterized devices are provided in Table D.1. Monochromatic light for external quantum efficiency (EQE) measurements was generated with a 300 W Xe arc lamp whose collimated irradiation was directed through 280 or 550 nm longpass filters prior to wavelength selection with a Newport® CS 130 dual grating monochromator using only "grating 2" (blaze: 500, grating lines: 1200). The power density at each wavelength (*i.e.*, 300–800 nm every 10 nm) was measured with a Newport® power meter (1936-R) equipped with a UV silicon detector (918D-UV-OD3R). For the collection of the power density readings, the monochromator and power meter were simultaneously controlled with Newport's TracQ™ Basic software. The wavelength-dependent J_{SC} values were measured with the Keithley 2400 SourceMeter™ controlled by the Oriel® I-V Test Station software collecting 10–30 J_{SC} values at each wavelength while holding the voltage at 0 V with a 0.5 s premeasurement delay and 1 s dwell time per data point. The collected J_{SC} values for each wavelength were averaged and the resulting photocurrent was used in the following equation to calculate the EQE at each tested wavelength (λ_x), where P_{in} is the measured power density at each of these wavelengths.

$$EQE\ @\ \lambda_x(\%) = \frac{J_{SC}\ @\ \lambda_x\ (\mu A\ cm^{-2})}{P_{in}\ @\ \lambda_x(\mu W\ cm^{-2})} \times \frac{1240}{\lambda_x\ (nm)} \times 100$$

CA–NH_4OH Dialysate-spiked Retentate Studies

For the CA–NH_4OH dial. spiking of retent. solutions, 1 or 5 mg mL^{-1} acetone-dispersed CA–NH_4OH retent. solutions were prepared and the solution volume was reduced by half via rotary evaporation (25 °C, <100 mbar). An appropriate volume of 10 mg mL^{-1} acetone-dispersed CA–NH_4OH dial. solution was then added such that the final dial. concentration would be 1 mg mL^{-1} upon diluting the sample back to its starting volume with acetone. TiO_2 films were sensitized in this solution for 2 h and characterized in a similar fashion to all other films described herein. This process was repeated to yield final dial. concentrations of 2.5, 5, 10, or 30 mg mL^{-1} in the 1 or 5 mg mL^{-1} retent. solutions. Note, to yield spiked dial. concentrations of 10 and 30 mg mL^{-1}, dial. stock solutions of 60 mg mL^{-1} or higher were employed. Ethanolic solutions of the 30 mg mL^{-1} dial.-spiked 1 or 5 mg mL^{-1} retent. samples were also prepared and studied. These solutions were generated by reducing the volume of the aforementioned solutions by half via rotary evaporation (25 °C, <100 mbar) and replacing the removed acetone with EtOH to yield samples dispersed in 50:50 vol% acetone:EtOH.

Mass Spectrometric Analyses

For the mass spectrometric analyses, 5 mg mL^{-1} aqueous stocks of the CA–NH_4OH and CA–U as-synth. fractions and their precursors (note, the CA–NH_4OH precursor only contained neat CA) were prepared and the solutions were appropriately diluted for analysis. Mass spectrometry (MS) was performed using an Applied Biosystems Mariner™ orthogonal time-of-flight (TOF) instrument operated under positive ion mode, employing

an electrospray ionization (ESI) source for sample introduction. Spectra were typically acquired and averaged over a 30 s interval having a constant total ion count. The instrument was mass calibrated externally using a series of CsI adducts between 126 and 1166 *m/z*. MS data was processed using the AB Sciex Data Explorer® software.

Results and Discussion

Spectroscopic Studies of FCD Fraction Uptake by TiO_2

For all precursor systems, the as-synthesized, unfractionated samples (denoted as as-synth.) were subjected to extensive purification via membrane dialysis using a 50 kDa MWCO cellulose membrane (see the "Fluorescent Carbon Dot Syntheses" subsection under the "Experimental" section above for specific details) to obtain a purified FCD-containing fraction (*i.e.*, retentate or retent.) and a fraction consisting of reaction by-products (*i.e.*, dialysate or dial.). The three fractions (*i.e.*, as-synth., retent., dial.) were then employed as sensitizers in TiO_2-based photoelectrochemical solar cells to assess the impact of reaction by-products on device performance. Sensitized films were characterized with UV-vis spectroscopy, and, while the goal of this work was not to explore the optimization of thoroughly purified FCD samples, the temporal sensitization (2, 4, 6, 8, 12, and 24 h) of the TiO_2 films with all sample fractions was monitored to assess the optimal sensitization times and probe for any fraction-dependent rates of sensitizer uptake (Figures D.2–D.5). While the apparent uptake rates varied between certain fractions within each respective system, these absorption differences between the adsorbed sensitizers likely arose from markedly different extinction coefficients for the various constituents. Regardless, the fractions within a single system appeared to reach maximal sensitization in comparable time frames, therefore, based on this data, as well as reported sensitization times,[15, 67] TiO_2

films were sensitized with the CA–NH_4OH, Arg, CA–U, and GSH–F fractions for 2, 12, 2, and 24 h, respectively. Devices with the architecture FTO/TiO_2/FCD fractions/I^-:I_3^-/Pt were then assembled and characterized with *J-V* curve and external quantum efficiency (EQE) measurements (see the "Photovoltaic Device Preparation and Assembly" and "Photovoltaic Device Characterizations" subsections in the "Experimental" section above for details).

PV Characterizations of TiO_2 Films Sensitized in CA–NH_4OH Fractions

Of the four precursor systems studied in this work, particular emphasis was placed on thoroughly exploring the fractions generated from the thermal treatment of citric acid dissolved in a dilute aqueous ammonia solution (*i.e.*, CA–NH_4OH) due to preliminary, screening studies indicating that the reaction by-products contributed significantly to the observed photocurrent (>50%) and, therefore, the overall device performance of the nonpurified, as-synth. fraction; however, the samples for these initial studies were dialyzed against water, which, as we will show, negatively impacted the observed results for the dial. fraction, leading to erroneous conclusions about the photocurrent origin. Indeed, in-depth studies of FCD sensitizer solutions (5 mg mL^{-1} in acetone), where the dial. and retent. fractions were obtained from dialysis against a 50:50 vol% mixture of acetone:ethanol, show that the by-product species that permeate the membrane (*i.e.*, dial. fraction) are the undeniable origin of the observed performance for the unfractionated, parent sample, while the FCD-containing fraction (*i.e.*, retent.) produced substantially lower PV action, marginally increasing the performance above that of unsensitized, bare TiO_2 (Figure 5.1). Specifically, devices containing films sensitized with the as-synth., dial., and retent. fractions presented with short-circuit current densities (J_{SC}), open-circuit voltages (V_{OC}),

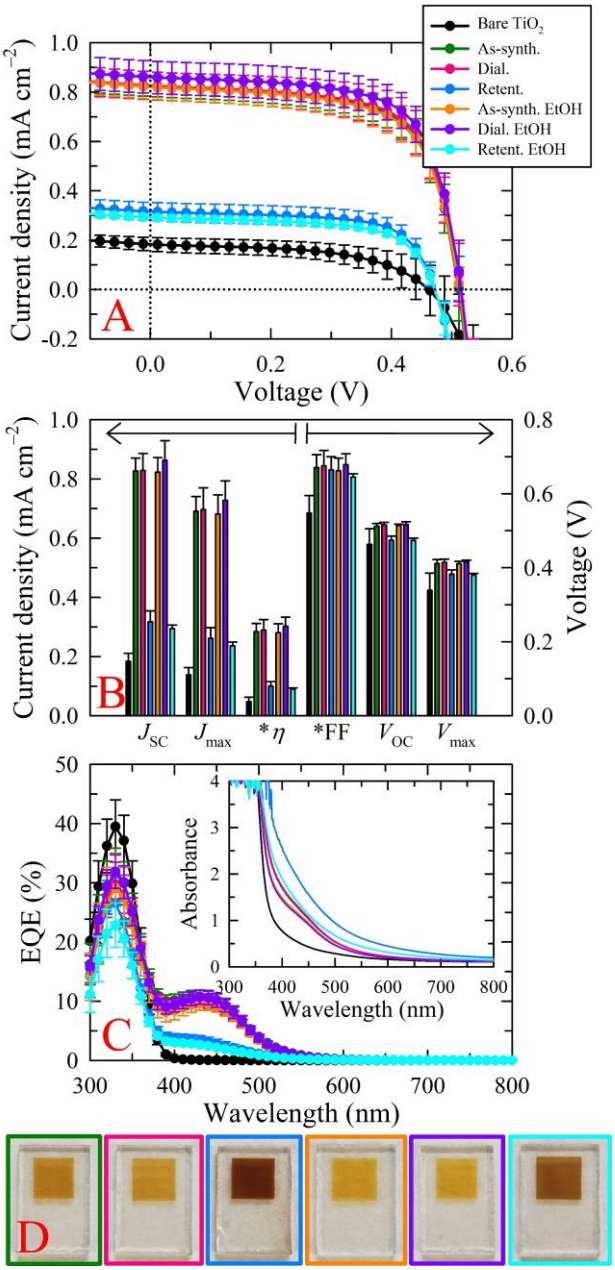

Figure 5.1 (A) Average *J*-*V* curves (with corresponding standard deviations) of illuminated devices employing TiO_2 films sensitized in 5 mg mL^{-1} CA–NH_4OH-derived fractions dispersed in 100% acetone or 50:50 vol% acetone:ethanol (denoted by "EtOH"). (B) Average device metrics. *Note, efficiency (η) is reported in percent and FF is a unitless parameter but both values are on the same scale as the left and right y-axes, respectively. (C) Average EQE and UV-vis absorbance (inset) spectra. (D) Photographs of representative films used in the devices. The performance of bare TiO_2 (black curves) is provided in all plots for comparison.

and fill factors (FF) of 0.827 ± 0.043 mA cm^{-2}, 0.512 ± 0.007 V, and 67.05 ± 3.50%, 0.828 ± 0.058 mA cm^{-2}, 0.516 ± 0.007 V, and 67.50 ± 4.19%, and 0.317 ± 0.037 mA cm^{-2}, 0.474 ± 0.011 V, and 66.44 ± 3.54%, respectively, which yielded average power conversion efficiencies (η) of $0.28_4 \pm 0.02_7$%, $0.28_9 \pm 0.03_6$%, and $0.10_0 \pm 0.01_5$% (Figure 5.1B). Note, bare TiO_2 produced values of 0.184 ± 0.027 mA cm^{-2}, 0.463 ± 0.042 V, and 54.75 ± 4.73%, leading to an η of $0.04_8 \pm 0.01_5$%.

While the as-synth. and dial. fractions produced comparable increases in photovoltages relative to bare TiO_2, an improvement not observed for the retent. fraction, the main source of the prominent performance deviation between the dial. and retent. fractions is the stark difference in photocurrent, the origin of which was elucidated with EQE measurements (Figure 5.1C). All three fractions displayed increased photon-to-electron conversion (relative to bare TiO_2) from 360 to 600 nm, however, the as-synth. and dial. fractions, showing comparable EQE to one another, as expected, presented distinct EQE peaks ranging from 9 to 12% at 430 nm, whereas the retent. fraction produced a less discernable peak, presenting more like a pseudo-shoulder, with a statistically significant drop in EQE to 1–3.5% and a shift in the peak maximum to 410 nm (Figure D.6A). Additionally, all three fractions negatively impacted the photon-to-electron conversion originating from the TiO_2 film (λ = 300–375 nm) and, on average, the extent of the EQE reduction increased as such: as-synth. < dial. < retent. Interestingly, UV-vis spectra (and photographs) of the sensitized films revealed that the as-synth. and dial. fractions possessed nearly identical optical absorption while the retent. fraction was markedly darker and had stronger absorbance (Figures 5.1C–D and D.6B), presumably, due to the presence of nanoscale carbons, which are reported to possess high absorption coefficients.[94-95] The striking

similarity between films sensitized with the as-synth. and dial. fractions and the pronounced difference between these fractions and films sensitized with the retent. fraction undoubtedly originates from the predominance of by-product production over nanoscale carbon generation within this reaction system. Indeed, crude calculations of retent. yield for this synthetic approach revealed that nanocarbon production was near or less than 1% meaning that a 5 mg mL^{-1} as-synth. fraction roughly consisted of 4.95 mg mL^{-1} dial. species and 0.05 mg mL^{-1} retent. species, hence, why the observed properties of as-synth.- and dial.-sensitized films and their corresponding device metrics are nearly identical. In fact, it was this poor yield that dictated the concentration employed for these studies since 5 mg mL^{-1} was the highest concentration of retent. that we could reasonably obtain while still retaining a utilizable solution volume. Although the retent. fraction displayed potentially beneficial UV-vis optical properties for PV applications, clearly the nanocarbons stemming from this precursor system are inefficient sensitizers due to weak photon-to-electron conversion that could stem from poor band alignment, weak photoelectron injection, or the promotion of parasitic back reactions, whereas the dial. fraction consists of by-product species that are largely responsible for the induced photocurrent and can be more effectively utilized as sensitizers due to improved photon-to-electron conversion despite weaker absorptivity.

Interestingly, we found that when the TiO_2 films were sensitized in as-synth. and dial. solutions with a solvent composition of 50:50 vol% acetone:ethanol (denoted by "EtOH" in all relevant plots), the photoactive species appeared to "selectively" sensitize, evidenced by the comparable performance to films sensitized in 100% acetone despite having slightly lower absorbance between 375 and 600 nm, which was visualized in the film color

changing from orange/light brown to yellow/orange. Note, while we state selective sensitization, since the exact chemical compositions of the by-product species contained in the as-synth. and dial. fractions are unknown, we cannot conclude that the sensitized species producing the yellow/orange film color are all photoactive and contribute to the generated photocurrent. Although, the more prominent shoulder observed near 450 nm in the UV-vis spectra of films sensitized in the presence of EtOH correlates quite well with the EQE spectral profiles, implying that the species responsible for this absorption feature may be the source of the photocurrent. This "selective" effect was more pronounced for films sensitized in 10 and 30 mg mL^{-1} solutions of the as-synth. and dial. fractions as shown in Figures D.7 and D.8, which clearly demonstrate that the photocurrent originates from certain by-product species generated in route to the desired FCDs. Additionally, sensitization in the presence of EtOH resulted in more distinct EQE peaks due to lower photon-to-current conversion between 390 and 410 nm, an effect that was most prominent at higher concentrations, particularly for the dial. fraction. Therefore, at lower concentrations, the observed photocurrent for acetone-dispersed fractions originates almost solely from by-product species due to the small nanocarbon content, whereas, at higher concentrations, specifically, 30 mg mL^{-1}, the increase in EQE between 390 and 410 nm can be attributed, in part, to photocurrent contributions from the nanocarbons since this wavelength range coincides with the highest EQE values for the retent. fraction. However, these results also clearly indicate that the dial. fraction consists of multiple species that contribute to the photocurrent to varying degrees (or not at all), evidenced by the differing film optical properties stemming from the two sensitizer-solvent systems and the slight increase in EQE between 390 and 410 nm, relative to the max, for films sensitized in 100%

acetone. Direct comparisons of the results for the 5, 10, and 30 mg mL^{-1} as-synth. and dial. fractions are provided in Figure D.9. Although films sensitized in 100% acetone showed clear concentration-dependent sensitizer uptake, the resulting PV performance was essentially independent of concentration or employed solvent system, except for films sensitized in the ethanolic dial. fraction, which showed a uniform increase in average photocurrent as concentration increased.

PV Characterizations of TiO_2 Sensitized in CA–NH_4OH Dial.-spiked Retent. Fractions

Further undisputable evidence that the observed PV metrics for the as-synth. fraction, specifically, the photocurrent, predominately arise from reaction by-products, and not nanoscale carbons, is provided through the statistically significant performance changes observed for films sensitized with varying concentrations (0, 1, 2.5, 5, 10, or 30 mg mL^{-1}) of dial.-spiked 5 or 1 mg mL^{-1} retent. solutions (Figures 2, D.10, and D.11). The specifics of solution preparation for these studies are detailed in the "CA–NH_4OH Dialysate-spiked Retentate Studies" subsection under the "Experimental" section above. For both retent. concentrations explored, spiking in increasing quantities of dial. fraction to yield the listed concentrations led to continual increases in photocurrent and photovoltage, despite minimal changes to film optical properties for dial. concentrations lower than 30 mg mL^{-1}, except for films sensitized in the 5:1 mg mL^{-1} retent.:dial. solution, which oddly led to a slight decrease in performance relative to neat 5 mg mL^{-1} retent. Additionally, upon increasing the dial. concentration from 10 to 30 mg mL^{-1}, the performance remained static (5 mg mL^{-1} retent.) or decreased (1 mg mL^{-1} retent.); however, when the solvent system was 50:50 vol% acetone:EtOH instead of 100% acetone, the performance of films sensitized in the 5 or 1 mg mL^{-1} retent. solutions containing 30 mg mL^{-1} dial. increased

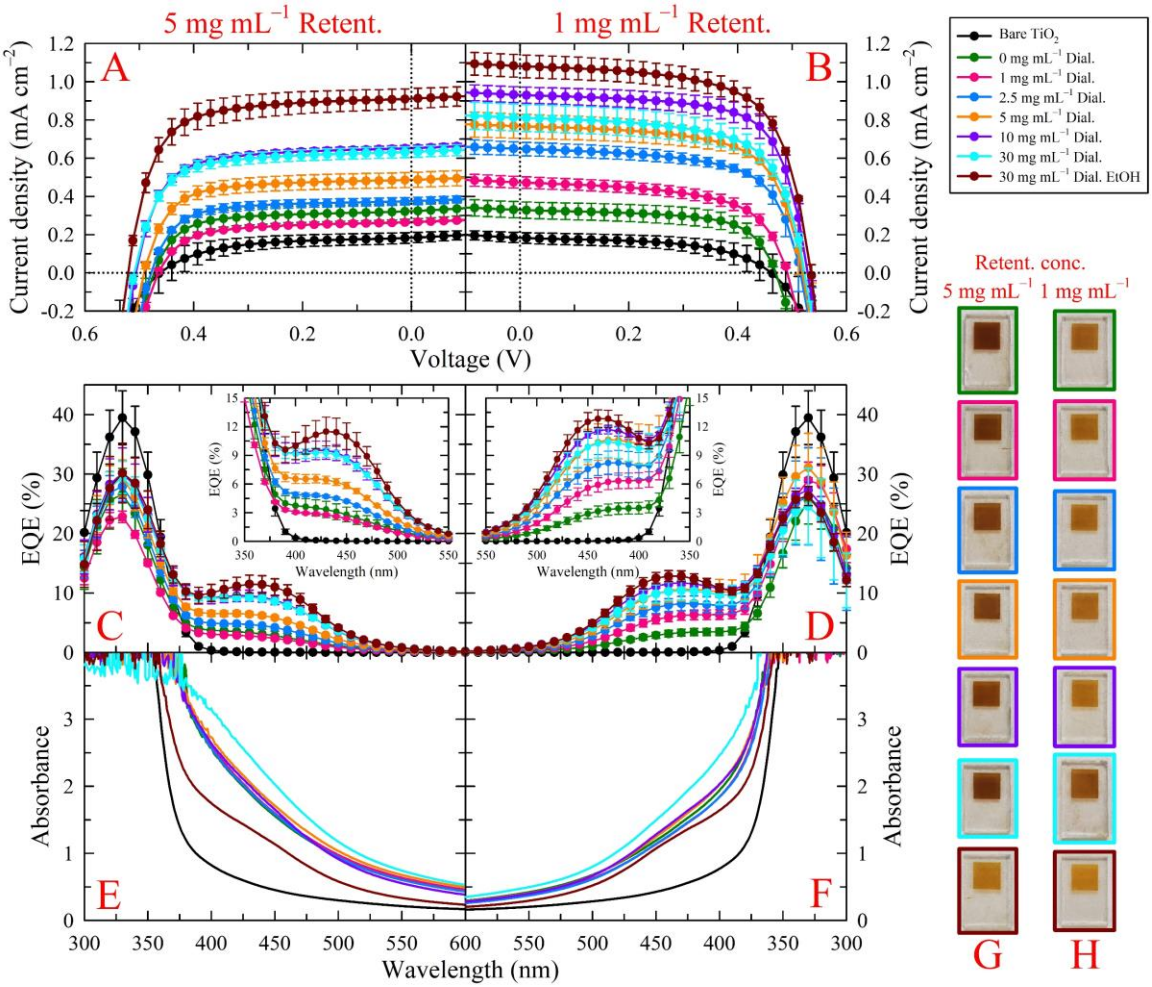

Figure 5.2 (A–B) Average *J*-*V* curves (with corresponding standard deviations) of illuminated devices employing TiO_2 films sensitized in dial.-spiked (A) 5 mg mL^{-1} or (B) 1 mg mL^{-1} CA–NH_4OH retent. fractions dispersed in 100% acetone or 50:50 vol% acetone:ethanol (denoted by "EtOH"). Appropriate quantities of dial. fraction were spiked in the retent. solutions to yield concentrations of 1, 2.5, 5, 10, or 30 mg mL^{-1}. (C–F) Average EQE and absorbance spectra for the dial.-spiked (C and E) 5 mg mL^{-1} or (D and F) 1 mg mL^{-1} CA–NH_4OH retent. fraction with magnified versions of the EQE spectra provided as insets in panels C and D. (G–H) Photographs of representative films sensitized with dial.-spiked (G) 5 mg mL^{-1} or (H) 1 mg mL^{-1} CA–NH_4OH retent. fractions. The performance of bare TiO_2 (black curves) is provided in all plots for comparison.

markedly. In fact, the highest performances obtained across all studies performed on the CA–NH_4OH-derived samples were for films sensitized in the ethanolic 1:30 mg mL^{-1}

retent.:dial. solution. The exact origins of this noteworthy increase are unclear since films sensitized in the ethanolic solution of neat 30 mg mL^{-1} dial. yielded slightly lower photocurrent and performance. However, given that the concentrations of the dial. and retent. fractions were not optimized, as such studies were beyond the scope of this work, it is possible that at the optimal ratio of nanocarbons and photocurrent-producing by-products, synergistic effects arise and yield performances higher that those obtained for the individual constituents, since FCDs have previously been employed as photoanode dopants to enhance the performance of sensitizer-based PVs.[57-58] Indeed, performance metric comparisons of the 10 mg mL^{-1} dial.-spiked retent. solutions to the 10 mg mL^{-1} as-synth. solution, which contains ~0.1 and nominally 10 mg mL^{-1} of the retent. and dial. species, respectively, reveal that this may indeed be the case (Figure D.12A). Although ratio-dependent synergistic effects between these species are evident, in general, increased concentrations of the species comprising both the dial. and retent. fractions, which translated to increased uptake, negatively impacted the performance, particularly for the latter fraction. This is clearly seen in head-to-head comparisons of the performances for the different dial. concentrations in the spiking studies, as decreasing the retent. concentration from 5 to 1 mg mL^{-1} led to markedly higher performances, even for the ethanolic sensitizer solutions. Therefore, at higher concentrations of retent. species, the apparent "selectivity" previously observed in the presence of EtOH may begin to fail and marginal nanocarbon uptake occurs, which could explain why films sensitized in an ethanolic solution of 1:30 mg mL^{-1} retent.:dial. yielded the highest performance (Figure D.12B–C); possible synergistic effects arose due to optimal uptake of nanocarbons and photocurrent-producing species.

Effects of 24 h Sensitization in CA–NH_4OH Fractions on PV Performance

The negative impact on performance imparted by increased sensitizer uptake was further revealed by 24 h sensitization studies (Figures D.13–D.15); in all conditions explored, the PV performance decreased regardless of concentration, solvent system, or fraction. Note, due to the observed trends for the as-synth. fraction 24 h uptake, extensive studies of 24 h dial. uptake were not conducted and, due to the unchanged performance upon increasing the neat retent. concentration from 1 to 5 mg mL^{-1}, PV characterizations on 24 h retent. uptake were not explored. While increased uptake of species that negatively impact performance could explain the drop in performance for longer sensitization times, TiO_2-induced degradation of photoactive species cannot be ruled out even though films were sensitized under dark conditions.

Aging and Water-exposure Effects on PV Performance of As-synth. CA–NH_4OH Samples

Additionally, slight aging effects were observed for 30 mg mL^{-1} as-synth. fractions that were 1–4 weeks old (Figure D.16), however, no noteworthy trends emerged after the initial performance decrease that occurred roughly 1 week after synthesis. Although degradation of the photoactive species as the origin of this decrease cannot be ruled out, the same decrease was not observed for films sensitized in ethanolic solutions or at any other concentrations, therefore, the decrease in performance may originate from the degradation of a non-photoactive species of low concentration to a compound that negatively impacts performance. Moreover, as previously mentioned, our initial studies revealed that exposure to water appeared to negatively impact the photoactive species, presumably through irreversible aggregation. To verify this, studies were conducted in which as-synth. samples were intentionally exposed to water and dried via two different means (details can be found

in Appendix D), redispersing the solid in acetone. As shown in Figure D.17, exposure to water clearly produced a negative impact on the photoactive species present in the sample but the negative effects appear to depend on the contact time with water and are potentially exacerbated by elevated temperatures.

PV Characterizations of TiO_2 Films Sensitized in Arg-derived Fractions

Contrary to the trends observed for CA–NH_4OH samples, purification of Arg produced the opposite effect. That is, instead of the photocurrent arising from species within the dial. fraction and the retent. performance being the lowest of the three fractions, for Arg, upon fractionating away reaction by-products, device performance improved markedly (Figure 5.3). Four different fractions were generated and tested for the Arg-derived samples: as-synth., an as-synth. fraction filtered with a 0.20 μm pore size syringe filter (denoted as "as-synth. filt."), dial., and retent. The performance of films sensitized with the as-synth. and as-synth. filt. fractions were almost identical, indicating that syringe filtration had minimal effects on the sample, despite material clearly being deposited in the filter, although, the photocurrent for the filtered fraction was statistically lower so removal of certain species may have marginally impacted current production. Regardless, the photocurrent for both fractions falls within the range generated by bare TiO_2 so the species within these fractions are clearly ineffective sensitizers, however, a statistically significant increase in photovoltage was observed for both fractions. The dial. fraction, on the other hand, did not show this same increase in photovoltage and also yielded the lightest colored films, lowest average photocurrent, and lowest EQE. Conversely, the retent. fraction, showing the darkest films of all fractions and most intense absorbance, produced a massive increase in photocurrent and slight improvement to FF while retaining the higher photovoltage, all of

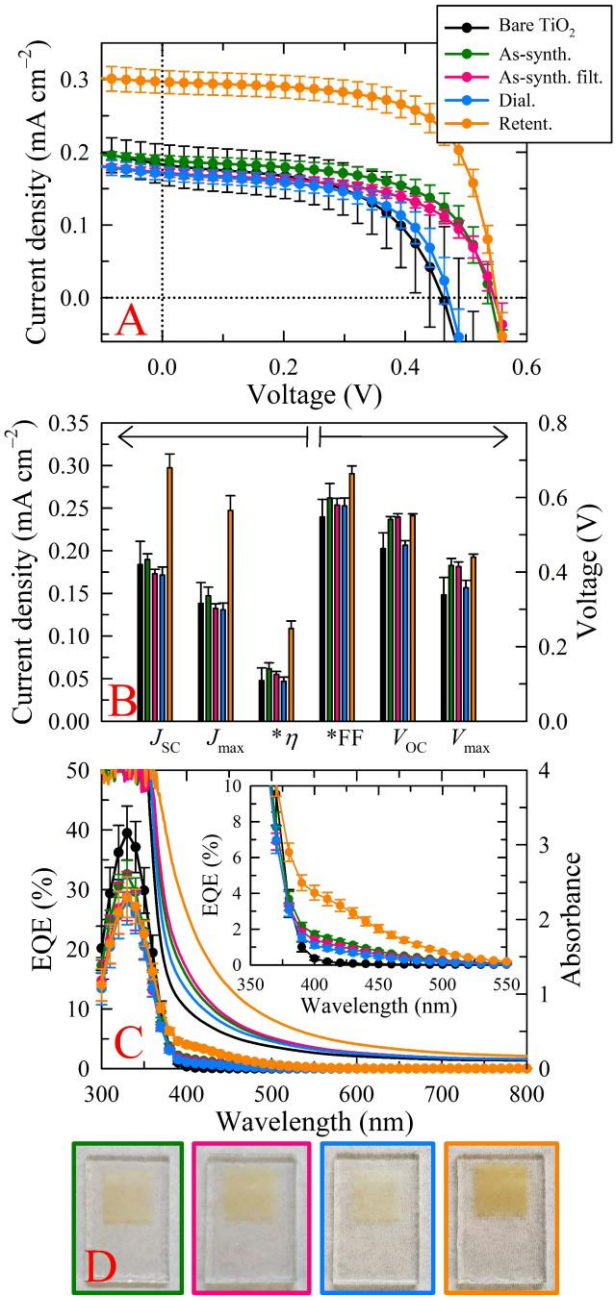

Figure 5.3 (A) Average *J-V* curves (with corresponding standard deviations) of illuminated devices employing TiO_2 films sensitized in 10 mg mL^{-1} Arg-derived fractions dispersed in EtOH. (B) Average device metrics. *Note, efficiency (η) is reported in percent and FF is a unitless parameter but both values are on the same scale as the left and right y-axes, respectively. (C) Average EQE and UV-vis absorbance spectra with a magnified version of the EQE spectra provided as an inset. (D) Photographs of representative films used in the devices. The performance of bare TiO_2 (black curves) is provided in all plots for comparison.

which led to nearly a doubling in device efficiency. Specifically, devices containing films sensitized with the as-synth., as-synth. filt., dial., and retent. fractions presented with short-circuit current densities (J_{SC}), open-circuit voltages (V_{OC}), and fill factors (FF) of 0.190 ± 0.007 mA cm^{-2}, 0.541 ± 0.008 V, and 59.86 ± 3.88%, 0.173 ± 0.005 mA cm^{-2}, 0.547 ± 0.009 V, and 57.99 ± 1.80%, 0.171 ± 0.009 mA cm^{-2}, 0.472 ± 0.012 V, and 57.76 ± 2.11%, and 0.297 ± 0.016 mA cm^{-2}, 0.551 ± 0.005 V, and 66.36 ± 2.09%, respectively, which yielded average η of $0.06_2 \pm 0.00_7$%, $0.05_5 \pm 0.00_3$%, $0.04_7 \pm 0.00_5$%, and $0.10_9 \pm 0.00_9$% (Figure 5.3B). Again, bare TiO_2 produced values of 0.184 ± 0.027 mA cm^{-2}, 0.463 ± 0.042 V, and 54.75 ± 4.73%, leading to $\eta = 0.04_8 \pm 0.01_5$%. Thus, syringe filtration, following centrifugation, is not a sufficient purification protocol for removing reaction by-products, consistent with the (fluorescence) conclusions we previously arrived at.[23] Akin to the CA–NH_4OH samples, all four fractions negatively impacted the EQE of TiO_2 (λ = 300–375 nm) but presented with increased EQE over TiO_2 from 375 to 550 nm, effects that yielded similar photocurrents for the first three fractions to that of bare TiO_2 while the retent. fraction produced a large enough EQE in this range to increase the J_{SC} by approximately 0.1 mA cm^{-2}. Additionally, the EQE for the retent. fraction showed marked increases on the bathochromic side of the curve, harvesting more UV photons over the other fractions (Figure D.18). These results clearly show that the photovoltage improvements stem from the putative nanocarbons in the retent. fractions and these species can generate appreciable photocurrent over bare TiO_2, however, when the reaction by-products are not removed, these species negatively impact the performance, possibly through parasitic charge scavenging. Although, given the prevalence of the dial. species in the as-synth. fraction (approximately 70:30 dial.:retent. by mass) and the fact that the optical properties of the

as-synth. sensitized films are closer to those of the dial. over the retent., the poor observed performances for the as-synth. fractions likely arise from competitive adsorption between the dial. and retent. species, with the former dominating uptake and adsorption sites due to its higher concentration, severely restricting nanocarbon adsorption. We also note that, similar to the CA–NH_4OH system, dialyzing Arg against water negatively impacted the sample but, in this case, the retent. fraction; less than 5 mg of product was obtained when dialyzing against water with 15 or 50 kDa membranes. Therefore, regardless of the purification mode employed (*e.g.*, dialysis, liquid chromatography), care must be taken when choosing the solvent system since the negative impacts of water, such as irreversible aggregation, were not always immediately detectable by the naked eye and only became apparent upon conducting careful UV-vis (both in solution and on film) and *J*-*V* measurements.

PV Characterizations of TiO_2 Films Sensitized in CA–U- and GSH–F-derived Fractions

Purification of the other two precursor systems explored in this work (*i.e.*, CA–U, GSH–F) did not result in such drastic performance differences between the fractions, with most of the performances minimally deviating from that of bare TiO_2. Although, the results clearly demonstrate the role purification plays on the proper reporting of PV action arising from nanoscale FCD sensitizers since by-product species in the dial. fractions impacted the observed performance and generated photocurrent at incident wavelengths of 375–550 nm (Figures D.19–D.20). Additionally, essentially all fractions stemming from both precursor systems severely impacted the EQE attributed to TiO_2, decreasing and shifting the EQE maximum for TiO_2 from approximately 40% at 340 nm to approximately 20% (on average) at 330 nm. Furthermore, apparent aging effects were observed in every fraction for both

precursor systems, presumably due to sample degradation (Figures D.19–D.21). Since the previous two systems (*i.e.*, CA–NH_4OH, Arg) were negatively impacted by water, it is possible that these latter two systems were affected as well, however, such explorations were beyond the scope of this work.

Interestingly, the GSH–F as-synth. and retent. fractions featured two minor peaks in the UV-vis spectra centered near 645 and 690 nm that yielded stark differences in film color (brown *vs* vibrant green) and distinguishable photon-to-electron conversion at red wavelengths (Figure D.20). Specifically, the as-synth. fraction produced a distinct peak at 650 nm with an EQE of 0.15%, whereas, upon purification, the EQE at 650 nm for the retent. fraction promisingly jumped up to 0.25% with the EQE between 620 and 720 nm also showing an increase relative to the as-synth. fraction, a trend that correlates well with the observed changes in absorbance upon fractionation. Conversely, the dial. fraction displayed little to no peak between 620 and 720 nm with a maximum EQE of 0.05% occurring at 650 nm. Although extremely low, the minor peak appearing at 650 nm in the EQE spectrum of the GSH–F retent. fraction is highly encouraging, as with a more fundamental understanding of the exact origin of these absorbance features (*i.e.*, originating from FCDs or quasi-molecular species), the chemical composition and resulting photophysics of this FCD system could be better tailored to simultaneously increase the absorbance in the red end of the visible spectrum and improve the photon-to-electron conversion to yield more efficient FCD sensitizers. As a step towards this, samples were generated at a higher carbonization temperature (200 *vs* 180 °C) to assess the influence on overall PV performance and, in particular, any deviations in the photophysics of the species giving rise to the peaks between 600 and 800 nm (via UV-vis and EQE). A

more detailed analysis is provided in Appendix D but, briefly, increasing the reaction temperature led to a decrease in all PV metrics for all three fractions, however, only a marginal drop in photocurrent occurred while the V_{OC} and FF experienced marked reductions, resulting in negative deviations away from the performance of bare TiO_2 (Figure D.22). Most notably, the distinct UV-vis and EQE peaks observed for the as-synth. and retent. fractions between 600 and 750 nm almost completely disappeared and a further reduction in the EQE attributed to TiO_2 occurred, indicating that the higher carbonization temperature negatively affected the species responsible for the observed PV action, in particular, the photocurrent, and especially the photon-to-current conversion at redder wavelengths. We postulate that the higher reaction temperature led to the degradation of quasi-molecular moieties tethered to the nanocarbons via increased carbonization, species that are responsible for the distinct green coloration and, in part, a fraction of the photocurrent, particularly at redder wavelengths. Thus, it stands to reason that the increased reaction temperature reduced the molecular and sp^3 characteristics of the materials, resulting in higher sp^2 content (*i.e.*, higher degree of carbonization), a well-known occurrence in FCD syntheses,[10, 35] that apparently leads to poorer PV performance for the device architecture employed herein. Further detailed analyses of the CA–U and GSH–F results can be found in Appendix D.

PV Characterizations of TiO_2 Films Sensitized in Coal-derived GQDs

In a similar vein, all FCD-containing retent. fractions performed poorly, producing power conversion efficiencies of ~0.1% or lower, loosely implying that thoroughly purified nanoscale carbons may not function as sufficient sensitizer replacements to the higher performing, albeit more toxic semiconductor QDs. Further evidence of this notion is

provided via characterizations of devices sensitized with extensively purified coal-derived GQDs,[93] a subset of the FCD family with more well-defined, graphitic nanostructures (*i.e.*, highly carbonized). In line with the molecularly derived, FCD-containing retent. fractions, these GQD sensitizers produced adverse effects on PV performance relative to bare TiO_2, however, the deleterious consequences were even more drastic, plummeting device efficiency to essentially 0% (Figure D.23). The origin of this negligible power conversion was from a reduction in all PV metrics; specifically, the V_{OC} and FF decreased by over half and one third, respectively, while the J_{SC} dropped nearly 10-fold (relative to bare TiO_2). Despite the immense uptake of the GQDs, as evidenced by the deep brown color of the films and their corresponding UV-vis spectra, EQE measurements revealed that the source of the marked reduction in photocurrent was a lowering in photon-to-electron conversion to below 10% across all wavelengths, even at the wavelengths that the GQD sensitizers absorb strongly, such that the EQE was well below that observed for bare TiO_2. Furthermore, akin to other systems studied herein, the GQDs produced a large 20 nm shift in the EQE attributed to TiO_2 implying modification of the semiconductor band properties, which could account for the substantially lower photovoltage. Given these results, we speculate that the photocurrent observed in the molecularly derived, FCD-containing retent. fractions arises, at least in part, from quasi-molecular moieties tethered to the FCD surface, while the nanocarbon core mostly functions as a conduit for delivering photogenerated charge carriers to the semiconductor but, in some instances, negatively impacts the semiconductor scaffold to such an extent that these adverse effects outweigh the desired photosensitizer charge generation.

Mass Spectrometric Analyses of CA-based FCD Systems

As previously mentioned, bottom-up FCD syntheses are known to generate a variety of molecular by-products, [10, 23, 35-39] especially those employing CA as the carbon source,[40, 43-50] therefore, ESI-TOF mass spectrometry was conducted (in positive ion mode) on select as-synth. fractions to identify potential molecular species that could be responsible for the observed PV action, namely, the photocurrent. Specifically, the CA-derived as-synth. fractions, as well as neat CA and CA–U precursor solutions, were analyzed since the reactions, although differing in synthetic approach, share similar precursors (that is, CA and ammonia; in the CA–U system the latter is generated in situ from the breakdown of U) but yield products exhibiting drastically different PV performances. Thus, direct comparisons between the mass spectra were made to identify molecular species that could be responsible for the substantially larger photocurrent observed in the CA–NH_4OH system over CA–U, as well as potential species (other than nanocarbons) that negatively impacted the performance of the CA–U as-synth. and dial. fractions. The spectra of the precursor solutions, shown in Figure D.24, displayed numerous peaks attributable to various sodiated adducts of CA or U, including mono- or dibasic species of the former, labeled as NaCA or Na_2CA, respectively. Specifically, the peaks at a *m/z* of 215, 237, 407, 429, and 643 were assigned to $[CA+Na]^+$ (or $[NaCA+H]^+$), $[NaCA+Na]^+$ (or $[Na_2CA+H]^+$), $[2CA+Na]^+$, $[2Na_2CA+H]^+$, and $[3Na_2CA+H]^+$, respectively, while the peak at a *m/z* of 143 was attributed to $[2U+Na]^+$. Upon reaction, essentially all of the peaks ascribed to the employed precursors vanished (Figure D.25) indicating complete degradation of the N-dopants and carbon source, CA, processes that are quite complex for the latter. Indeed, CA is known to go through multistep and multi-pathway degradation processes leading to a host of

carboxylic acid by-products through various dehydration and decarboxylation steps.[96-97] Specifically, one of the primary thermal decomposition pathways for CA involves two dehydration steps to produce the *cis*- and *trans*-isomers of aconitic acid and then their corresponding anhydride versions, followed by a decarboxylation step to yield itaconic acid and citraconic acid anhydrides. These anhydrides can then be hydrolyzed to form itaconic and citraconic acids. Additionally, CA can go through an immediate decarboxylation step yielding 3-hydroxyglutaric acid.[96] Although CA was reacted in the presence of potential N-dopants in this work, some of these decomposition products were still observed, where the exact carboxylic acid formed was dependent on the reaction. Specifically, the thermal reaction of CA and NH_4OH appeared to result in more complete decomposition as itaconic and citraconic acids (abbreviated ICA) were the main decomposition species observed (*m/z* = 132) with very little aconitic acid (AA) detected (*m/z* = 175), whereas, for CA–U, aconitic acid was the main decomposition product observed with little to no itaconic and citraconic acids detected. Interestingly, aconitic acid was also observed in the CA–U precursor solution. Since all these species are colorless solids in their virgin forms, it is highly improbable that they are responsible for the observed photocurrent, however, since they all possess carboxyl groups, they could be impacting the photovoltaic performance through modification of TiO_2; whether they impart positive or negative effects is unclear.

Since the CA-based precursor systems explored in this work employed potential N-dopants in the reactions, the presence of N-containing molecular by-products was highly anticipated. Indeed, the reaction of CA with ammonia-generating compounds (*e.g.*, NH_4OH, U) has been reported to result in various 2-pryidone derivatives such as citrazinic

acid (CzA)[45, 98] and 4-hydroxy-1*H*-pyrrolo[3,4-*c*]pyridine-1,3,6(2*H*,5*H*)-trione (HPPT);[45] however, the production of these species did not appear to occur, an observation that could be due to the employed reaction conditions since the reported generation of these by-products arose from lower reaction temperatures (<160 °C *vs* 200 °C) and higher N-dopant:CA mole ratios (≥3:1 *vs* ≤3:1). Furthermore, the reported peak absorbance of these by-products[45] does not coincide with the observed absorbance for sensitized films; that is, the reported peak absorbance (350–400 nm) is blueshifted relative to the sensitized species (450 nm). Additionally, HPPT does not possess carboxyl moieties that would allow it to strongly chemisorb to the TiO_2 film. While the photocurrent does not appear to arise from CzA or HPPT, the reaction of CA with hexamethylenetetramine, which yields ammonia upon decomposition, has been proposed to generate CzA derivatives functionalized in the three and five positions.[44] Therefore, under the appropriate conditions, the generation of 3,5-derivatized CzA species in the reaction of CA with NH_4OH or U cannot be discounted. Indeed, a peak was observed at *m/z* of 186 in both systems which could be attributed to an aminated derivative of CzA, such as 2,6-dihydroxy-3,5-diaminopyridine-4-carboxylic acid (HAPCA). Furthermore, a peak was observed at *m/z* of 142 in both precursor systems that could correspond to a decarboxylated version of the proposed CzA derivative, HAPCA. Since CzA absorbs UV to blue wavelengths, this feature may be retained upon derivatization, with a possible redshift in peak absorbance, as long as the aromaticity is not lost. Thus, this species could be responsible for the observed photocurrent. However, since a peak at *m/z* of 186 is observed in both systems, as well as the precursor solutions, we suspect that this peak arises from tributylammonium (tba), a species originating from tetrabutylammonium (TBA), which is an ever-present contaminant in the ESI source used

as an internal lock mass for yielding high mass accuracies. Therefore, we suspect that the observed photocurrent in the CA–NH_4OH as-synth. and dial. fractions does not originate from any known or proposed CzA-derived species. Since further functionalization of CzA to HPPT produces redshifted absorbance peaks, namely a shift from 350 to 400 nm, it is plausible that a more extensively derivatized form of CzA (possibly in the 1, 3, or 5 positions) was produced, a species that absorbs around 450 nm, possesses aromaticity, and still contains a carboxyl headgroup, all of which would be minimum requirements to yield the observed sensitization and PV performance. Indeed, CzA derivatives functionalized with various uret species (*e.g.*, urea, biuret) have been proposed,[99] however, these postulated species were not observed either.

Although appreciable photocurrent production was only observed in the CA–NH_4OH as-synth. and dial. fractions, it is possible that the species responsible for the photocurrent is present in both the CA-derived samples, however, in the case of CA–U, a different by-product species, distinct to this system, is negatively impacting photocurrent production. Indeed, both systems displayed similar (major) peaks at *m/z* of 142, 184, 258, 307, and 413 while prominent, seemingly system-specific, peaks were observed at *m/z* of 279, 308, 330, 336, 352, and 379 and 277, 291, 383, 468, and 493 for CA–U and CA–NH_4OH, respectively. Note, the listed peaks may still appear in the other system, however, for any shared peaks designated as system-specific, the peak intensities in one system are extremely low relative to the other. Despite the prominence of the above peaks within their respective systems, essentially all of these peaks were also identifiable in the spectra of the precursor solutions, indicating that the species giving rise to these *m/z* values were not from reaction by-product formation. Thus, given the lack of evidence for the existence of a

molecular by-product that could be responsible for the generated photocurrent, the sensitized species responsible for the observed performance in the CA–NH_4OH as-synth. and dial. fractions could be a large, poorly carbonized polymeric species possessing a molecular weight between 2 and 50 kDa such that its presence was not observed in the probed *m/z* range but its size (*i.e.*, hydrodynamic radius) was small enough that the species could still permeate the dialysis membrane. That said, the lack of current evidence for the formation of molecular by-products does not preclude their existence since the resultant positive ion mass spectra do not necessarily represent every species constituting the analyzed fractions. Therefore, further analyses are warranted to elucidate the exact origin, whether molecular or polymeric, of the produced photocurrent. Regardless, the results clearly indicate that the species responsible for the majority of the observed performance in the CA–NH_4OH system, specifically, the photocurrent, is not a nanocarbon.

While the results obtained herein imply that FCDs may not hold the perpetuated promise as greener, inexpensive sensitizer replacements, further studies are necessary to better understand the exact origin of why these purified nanocarbons negatively impact PV performance such as poor band alignment or weak/slow photogenerated charge-carrier injection into the semiconductor. Additionally, as FCDs are reported to possess both donor and acceptor properties, for the investigated systems, the nanoscale carbons could be behaving as electron sinks accepting but retaining more electrons than they donate. Furthermore, the FCDs could be strong electron donors toward triiodide reduction, promoting parasitic back reactions that substantially reduce the photocurrent produced. Regardless, before such studies exploring the exact origins of the observed effects on PV devices, particularly sensitizer-driven architectures, are undertaken, analytically rigorous

purification of the FCD parent samples and subsequent systematic characterization of the fundamental chemical, physical, and photophysical properties of the nanocarbon-containing fractions must be conducted to provide a better context for why these materials behave as they do when employed in PV devices, namely, as sensitizers. Moreover, every fraction in all four precursor systems displayed some form of instability such as water-induced irreversible aggregation or sample degradation and, in fact, every fraction displayed solution instabilities with sedimentation or electroless deposition occurring within days to weeks after synthesis, regardless of the storage container (*i.e.*, glass, plastic) utilized, thus, these sample instabilities must also be addressed.

Conclusions

In conclusion, we have attempted to draw further attention to the improper and insufficient purification of FCDs, particularly those derived from molecular precursors, through the exploration of membrane-separated fractions to better understand how these nanocarbons, as photosensitizers, contribute to and affect PV performance in mesoporous TiO_2-based solar cells, a common area of FCD application that has yet to implement analytically rigorous purification protocols. This detrimental issue, that is still unsettlingly common, has hindered the field in elucidating these nanocarbons true properties, particularly, the origin of their reported photoluminescence. The results disseminated herein further illuminate how the lack of sufficient purification is impeding the field in arriving at a fundamental understanding of these nanocarbons' inherent properties, particularly in relation to their photophysical and photoelectric properties, revealing that scrupulous purification is necessary to properly report the source of the observed PV action and the devices' corresponding performance metrics. Specifically, in some precursor systems, the

observed PV action may not originate from the nanocarbons themselves but from molecular by-products generated alongside the nanocarbons, as was apparent for CA–NH_4OH, or from quasi-molecular functional groups on the FCD core, as the results for GSH–F may indicate. Conversely, in other instances, such as the Arg system, proper fractionation may lead to even higher PV performance than that observed for nonpurified samples due to reaction by-products negatively impacting performance and masking the true potential of the nanocarbon sensitizers. Additionally, in all systems except Arg, substantial uptake of the various sensitizing species was observed resulting in dark, strongly absorbing films yet devices containing these films produced very little photocurrent implying that some of the chromophoric species, whether molecular or nanocarbon, do not contribute meaningfully to photocurrent production. Therefore, remedial studies employing analytically rigorous purification should be undertaken to reassess previously reported properties, particularly those that are highly relevant to PV applications such as band gap, band alignment, donor/acceptor capabilities, charge injection, and heteroatom doping.

Acknowledgements

The authors acknowledge the University of Missouri for supporting this work through the Mizzou Advantage funding program. The authors also graciously thank Mark W. Lee for assistance with the mass spectrometric analyses and Ian C. Siercks for aiding in the completion of this work.

References

1. Baker, S. N.; Baker, G. A., Luminescent Carbon Nanodots: Emergent Nanolights. *Angew. Chem. Int. Ed.* **2010**, *49*, 6726–6744.

2. Zheng, X. T.; Ananthanarayanan, A.; Luo, K. Q.; Chen, P., Glowing Graphene Quantum Dots and Carbon Dots: Properties, Syntheses, and Biological Applications. *Small* **2015**, *11*, 1620–1636.

3. Gao, J.; Zhu, M.; Huang, H.; Liu, Y.; Kang, Z., Advances, Challenges and Promises of Carbon Dots. *Inorg. Chem. Front.* **2017**, *4*, 1963–1986.

4. Anwar, S.; Ding, H.; Xu, M.; Hu, X.; Li, Z.; Wang, J.; Liu, L.; Jiang, L.; Wang, D.; Dong, C.; Yan, M.; Wang, Q.; Bi, H., Recent Advances in Synthesis, Optical Properties, and Biomedical Applications of Carbon Dots. *ACS Appl. Bio Mater.* **2019**, *2*, 2317–2338.

5. Du, J.; Xu, N.; Fan, J.; Sun, W.; Peng, X., Carbon Dots for In Vivo Bioimaging and Theranostics. *Small* **2019**, *15*, 1805087.

6. Ding, C.; Zhu, A.; Tian, Y., Functional Surface Engineering of C-dots for Fluorescent Biosensing and In Vivo Bioimaging. *Acc. Chem. Res.* **2013**, *47*, 20–30.

7. Essner, J. B.; Laber, C. H.; Baker, G. A., Carbon Dot Reduced Bimetallic Nanoparticles: Size and Surface Plasmon Resonance Tunability for Enhanced Catalytic Applications. *J. Mater. Chem. A* **2015**, *3*, 16354–16360.

8. Bourlinos, A. B.; Stassinopoulos, A.; Anglos, D.; Zboril, R.; Karakassides, M.; Giannelis, E. P., Surface Functionalized Carbogenic Quantum Dots. *Small* **2008**, *4*, 455–458.

9. Bourlinos, A. B.; Stassinopoulos, A.; Anglos, D.; Zboril, R.; Georgakilas, V.; Giannelis, E. P., Photoluminescent Carbogenic Dots. *Chem. Mater.* **2008**, *20*, 4539–4541.

10. Krysmann, M. J.; Kelarakis, A.; Dallas, P.; Giannelis, E. P., Formation Mechanism of Carbogenic Nanoparticles with Dual Photoluminescence Emission. *J. Am. Chem. Soc.* **2011**, *134*, 747–750.

11. Laber, C. H.; Essner, J. B.; Scott, T. A.; Polo-Parada, L.; Baker, G. A., Domestic Pressure Cooker as Inexpensive Hydrothermal Vessel: Demonstrated Utility for Eco-friendly Synthesis of Non-toxic Carbon Dots. *Nano-Struct. Nano-Objects* **2016**, *6*, 52–58.

12. Essner, J. B.; McCay, R. N.; Smith Ii, C. J.; Cobb, S. M.; Laber, C. H.; Baker, G. A., A Switchable Peroxidase Mimic Derived from the Reversible Co-assembly of Cytochrome *c* and Carbon Dots. *J. Mater. Chem. B* **2016**, *4*, 2163–2170.

13. Qu, S.; Wang, X.; Lu, Q.; Liu, X.; Wang, L., A Biocompatible Fluorescent Ink based on Water-soluble Luminescent Carbon Nanodots. *Angew. Chem. Int. Ed.* **2012**, *51*, 12215–12218.

14. Briscoe, J.; Marinovic, A.; Sevilla, M.; Dunn, S.; Titirici, M., Biomass-derived Carbon Quantum Dot Sensitizers for Solid-state Nanostructured Solar Cells. *Angew. Chem. Int. Ed.* **2015**, *54*, 4463–4468.

15. Marinovic, A.; Kiat, L. S.; Dunn, S.; Titirici, M.-M.; Briscoe, J., Carbon-nanodot Solar Cells from Renewable Precursors. *ChemSusChem* **2017**, *10*, 1004–1013.

16. Sta. Ana, J. C.; Camacho, D. H., Influence of Precursor Size in the Hydrothermal Synthesis of Cellulose-based Carbon Nanodots and its Application Towards Solar Cell Sensitization. *Mater. Chem. Phys.* **2019**, *228*, 187–193.

17. Dou, D.; Duan, J.; Zhao, Y.; He, B.; Tang, Q., Cubic Carbon Quantum Dots for Light-harvesters in Mesoscopic Solar Cells. *Electrochim. Acta* **2018**, *275*, 275–280.

18. Liu, L.; Yu, X.; Yi, Z.; Chi, F.; Wang, H.; Yuan, Y.; Li, D.; Xu, K.; Zhang, X., High Efficiency Solar Cells Tailored using Biomass-converted Graded Carbon Quantum Dots. *Nanoscale* **2019**, *11*, 15083–15090.

19. Meng, Y.; Zhang, Y.; Sun, W.; Wang, M.; He, B.; Chen, H.; Tang, Q., Biomass Converted Carbon Quantum Dots for All-weather Solar Cells. *Electrochim. Acta* **2017**, *257*, 259–266.

20. Yang, J.; Tang, Q.; Meng, Q.; Zhang, Z.; Li, J.; He, B.; Yang, P., Photoelectric Conversion Beyond Sunny Days: All-weather Carbon Quantum Dot Solar Cells. *J. Mater. Chem. A* **2017**, 2143–2150.

21. Zhang, H.; Wang, Y.; Liu, P.; Li, Y.; Yang, H. G.; An, T.; Wong, P.-K.; Wang, D.; Tang, Z.; Zhao, H., A Fluorescent Quenching Performance Enhancing Principle for Carbon Nanodot-sensitized Aqueous Solar Cells. *Nano Energy* **2015**, *13*, 124–130.

22. Essner, J. B.; Laber, C. H.; Ravula, S.; Polo-Parada, L.; Baker, G. A., Pee-dots: Biocompatible Fluorescent Carbon Dots Derived from the Upcycling of Urine. *Green Chem.* **2016**, *18*, 243–250.

23. Essner, J. B.; Kist, J. A.; Polo-Parada, L.; Baker, G. A., Artifacts and Errors Associated with the Ubiquitous Presence of Fluorescent Impurities in Carbon Nanodots. *Chem. Mater.* **2018**, *30*, 1878–1887.

24. Chen, C.-Y.; Tsai, Y.-H.; Chang, C.-W., Evaluation of the Dialysis Time Required for Carbon Dots by HPLC and the Properties of Carbon Dots after HPLC Fractionation. *New J. Chem.* **2019**, *43*, 6153–6159.

25. Barman, M. K.; Patra, A., Current Status and Prospects on Chemical Structure Driven Photoluminescence Behaviour of Carbon Dots. *J. Photochem. Photobio. C* **2018**, *37*, 1–22.

26. Yan, F.; Sun, Z.; Zhang, H.; Sun, X.; Jiang, Y.; Bai, Z., The Fluorescence Mechanism of Carbon Dots, and Methods for Tuning their Emission Color: A Review. *Microchim. Acta* **2019**, *186*, 583.

27. Liu, M. L.; Chen, B. B.; Li, C. M.; Huang, C. Z., Carbon Dots: Synthesis, Formation Mechanism, Fluorescence Origin and Sensing Applications. *Green Chem.* **2019**, *21*, 449–471.

28. Mintz, K. J.; Zhou, Y.; Leblanc, R. M., Recent Development of Carbon Quantum Dots Regarding their Optical Properties, Photoluminescence Mechanism, and Core Structure. *Nanoscale* **2019**, *11*, 4634–4652.

29. Vinci, J. C.; Colon, L. A., Fractionation of Carbon-based Nanomaterials by Anion-exchange HPLC. *Anal. Chem.* **2011**, *84*, 1178–1183.

30. Vinci, J. C.; Ferrer, I. M.; Seedhouse, S. J.; Bourdon, A. K.; Reynard, J. M.; Foster, B. A.; Bright, F. V.; Colón, L. A., Hidden Properties of Carbon Dots Revealed after HPLC Fractionation. *J. Phys. Chem. Lett.* **2013**, *4*, 239–243.

31. Qi, B.-P.; Bao, L.; Zhang, Z.-L.; Pang, D.-W., Electrochemical Methods to Study Photoluminescent Carbon Nanodots: Preparation, Photoluminescence Mechanism and Sensing. *ACS Appl. Mater. Interfaces* **2016**, *8*, 28372–28382.

32. Hu, Q.; Meng, X.; Chan, W., An Investigation on the Chemical Structure of Nitrogen and Sulfur Codoped Carbon Nanoparticles by Ultra-performance Liquid Chromatography-tandem Mass Spectrometry. *Anal. Bioanal. Chem.* **2016**, *408*, 5347–5357.

33. Gong, X.; Chin Paau, M.; Hu, Q.; Shuang, S.; Dong, C.; Choi, M. M. F., UHPLC Combined with Mass Spectrometric Study of As-synthesized Carbon Dots Samples. *Talanta* **2016**, *146*, 340–350.

34. Gong, X.; Hu, Q.; Chin Paau, M.; Zhang, Y.; Zhang, L.; Shuang, S.; Dong, C.; Choi, M. M. F., High-performance Liquid Chromatographic and Mass Spectrometric Analysis of Fluorescent Carbon Nanodots. *Talanta* **2014**, *129*, 529–538.

35. Zhu, S.; Zhao, X.; Song, Y.; Lu, S.; Yang, B., Beyond Bottom-up Carbon Nanodots: Citric-acid Derived Organic Molecules. *Nano Today* **2016**, *11*, 128–132.

36. Ehrat, F.; Bhattacharyya, S.; Schneider, J.; Löf, A.; Wyrwich, R.; Rogach, A. L.; Stolarczyk, J. K.; Urban, A. S.; Feldmann, J., Tracking the Source of Carbon Dot Photoluminescence: Aromatic Domains versus Molecular Fluorophores. *Nano Lett.* **2017**, *17*, 7710–7716.

37. Righetto, M.; Privitera, A.; Fortunati, I.; Mosconi, D.; Zerbetto, M.; Curri, M. L.; Corricelli, M.; Moretto, A.; Agnoli, S.; Franco, L.; Bozio, R.; Ferrante, C., Spectroscopic Insights into Carbon Dot Systems. *J. Phys. Chem. Lett.* **2017**, *8*, 2236–2242.

38. Hsu, Y.-F.; Chen, Y.-H.; Chang, C.-W., The Spectral Heterogeneity and Size Distribution of the Carbon Dots Derived from Time-resolved Fluorescence Studies. *Phys. Chem. Chem. Phys.* **2016**, *18*, 30086–30092.

39. Obadiya, T.; Uppala, H.; Sidebottom, D., Fluorescent Carbon Particles Formed from Concentrated Glucose Solutions. *MRS Adv.* **2019**, *4*, 67–72.

40. Khan, S.; Sharma, A.; Ghoshal, S.; Jain, S.; Hazra, M. K.; Nandi, C. K., Small Molecular Organic Nanocrystals Resemble Carbon Nanodots in terms of their Properties. *Chem. Sci.* **2018**, *9*, 175–180.

41. Reckmeier, C. J.; Schneider, J.; Xiong, Y.; Häusler, J.; Kasák, P.; Schnick, W.; Rogach, A. L., Aggregated Molecular Fluorophores in the Ammonothermal Synthesis of Carbon Dots. *Chem. Mater.* **2017**, *29*, 10352–10361.

42. Gude, V.; Das, A.; Chatterjee, T.; Mandal, P. K., Molecular Origin of Photoluminescence of Carbon Dots: Aggregation-induced Orange-red Emission. *Phys. Chem. Chem. Phys.* **2016**, *18*, 28274–28280.

43. Xiong, Y.; Schneider, J.; Ushakova, E. V.; Rogach, A. L., Influence of Molecular Fluorophores on the Research Field of Chemically Synthesized Carbon Dots. *Nano Today* **2018**, *23*, 124–139.

44. Schneider, J.; Reckmeier, C. J.; Xiong, Y.; von Seckendorff, M.; Susha, A. S.; Kasák, P.; Rogach, A. L., Molecular Fluorescence in Citric Acid-based Carbon Dots. *J. Phys. Chem. C* **2017**, *121*, 2014–2022.

45. Kasprzyk, W.; Świergosz, T.; Bednarz, S.; Walas, K.; Bashmakova, N. V.; Bogdał, D., Luminescence Phenomena of Carbon Dots Derived from Citric Acid and Urea – A Molecular Insight. *Nanoscale* **2018**, *10*, 13889–13894.

46. Das, A.; Gude, V.; Roy, D.; Chatterjee, T.; De, C. K.; Mandal, P. K., On the Molecular Origin of Photoluminescence of Nonblinking Carbon Dot. *J. Phys. Chem. C* **2017**, *121*, 9634–9641.

47. Song, Y.; Zhu, S.; Zhang, S.; Fu, Y.; Wang, L.; Zhao, X.; Yang, B., Investigation from Chemical Structure to Photoluminescent Mechanism: A Type of Carbon Dots from the Pyrolysis of Citric Acid and an Amine. *J. Mater. Chem. C* **2015**, *3*, 5976–5984.

48. Liu, X.; Li, H.-B.; Shi, L.; Meng, X.; Wang, Y.; Chen, X.; Xu, H.; Zhang, W.; Fang, X.; Ding, T., Structure and Photoluminescence Evolution of Nanodots during Pyrolysis of Citric Acid: From Molecular Nanoclusters to Carbogenic Nanoparticles. *J. Mater. Chem. C* **2017**, *5*, 10302–10312.

49. Shi, L.; Yang, J. H.; Zeng, H. B.; Chen, Y. M.; Yang, S. C.; Wu, C.; Zeng, H.; Yoshihito, O.; Zhang, Q., Carbon Dots with High Fluorescence Quantum Yield: The Fluorescence Originates from Organic Fluorophores. *Nanoscale* **2016**, *8*, 14374–14378.

50. Zhang, J.; Yang, L.; Yuan, Y.; Jiang, J.; Yu, S.-H., One-pot Gram-scale Synthesis of Nitrogen and Sulfur Embedded Organic Dots with Distinctive Fluorescence Behaviors in Free and Aggregated States. *Chem. Mater*. **2016**, *28*, 4367–4374.

51. Kasprzyk, W.; Bednarz, S.; Bogdał, D., Luminescence Phenomena of Biodegradable Photoluminescent Poly(diol citrates). *Chem. Commun.* **2013**, *49*, 6445–6447.

52. Kasprzyk, W.; Bednarz, S.; Zmudzki, P.; Galica, M.; Bogdal, D., Novel Efficient Fluorophores Synthesized from Citric Acid. *RSC Adv.* **2015**, *5*, 34795–34799.

53. Kim, J. P.; Xie, Z.; Creer, M. H.; Liu, Z.; Yang, J., Citrate-based Fluorescent Materials for Low-cost Chloride Sensing in the Diagnosis of Cystic Fibrosis. *Chem. Sci.* **2017**, *8*, 550–558.

54. Wang, H.-X.; Yang, Z.; Liu, Z.-G.; Wan, J.-Y.; Xiao, J.; Zhang, H.-L., Facile Preparation of Bright-fluorescent Soft Materials from Small Organic Molecules. *Chem. Eur. J.* **2016**, *22*, 8096–8104.

55. Kokorina, A. A.; Bakal, A. A.; Sapelkin, A. V.; Sukhorukov, G. B.; Goryacheva, I. Y., High Luminescent Fluorophore Synthesized at Atmospheric Pressure from Citric Acid and Ethylenediamine, International Symposium on Optics and Biophotonics VI: Saratov Fall Meeting 2018. *SPIE* **2019**, Vol. 11067.

56. Hu, C.; Li, M.; Qiu, J.; Sun, Y.-P., Design and Fabrication of Carbon Dots for Energy Conversion and Storage. *Chem. Soc. Rev.* **2019**, *48*, 2315–2337.

57. Paulo, S.; Palomares, E.; Martinez-Ferrero, E., Graphene and Carbon Quantum Dot-based Materials in Photovoltaic Devices: From Synthesis to Applications. *Nanomaterials* **2016**, *6*, 157.

58. Essner, J. B.; Baker, G. A., The Emerging Roles of Carbon Dots in Solar Photovoltaics: A Critical Review. *Environ. Sci.: Nano* **2017**, *4*, 1216–1263.

59. Yan, X.; Cui, X.; Li, B.; Li, L.-s., Large, Solution-Processable Graphene Quantum Dots as Light Absorbers for Photovoltaics. *Nano Lett.* **2010**, *10*, 1869–1873.

60. Yan, X.; Li, B.; Li, L.-s., Colloidal Graphene Quantum Dots with Well-defined Structures. *Acc. Chem. Res.* **2012**, *46*, 2254–2262.

61. Mirtchev, P.; Henderson, E. J.; Soheilnia, N.; Yip, C. M.; Ozin, G. A., Solution Phase Synthesis of Carbon Quantum Dots as Sensitizers for Nanocrystalline TiO_2 Solar Cells. *J. Mater. Chem.* **2012**, *22*, 1265–1269.

62. Wang, C.; Wu, X.; Li, X.; Wang, W.; Wang, L.; Gu, M.; Li, Q., Upconversion Fluorescent Carbon Nanodots Enriched with Nitrogen for Light Harvesting. *J. Mater. Chem.* **2012**, *22*, 15522–15525.

63. Sun, M.; Ma, X.; Chen, X.; Sun, Y.; Cui, X.; Lin, Y., A Nanocomposite of Carbon Quantum Dots and TiO_2 Nanotube Arrays: Enhancing Photoelectrochemical and Photocatalytic Properties. *RSC Adv.* **2014**, *4*, 1120–1127.

64. Chen, L.; Wei, J.; Zhang, C.; Du, Z.; Li, H.; Zou, W., Synthesis of a Carbon Quantum Dots Functionalized Carbon Nanotubes Nanocomposite and its Application as a Solar Cell Active Material. *RSC Adv.* **2014**, *4*, 51084–51088.

65. Sun, M.; Qu, S.; Ji, W.; Jing, P.; Li, D.; Qin, L.; Cao, J.; Zhang, H.; Zhao, J.; Shen, D., Towards Efficient Photoinduced Charge Separation in Carbon Nanodots and TiO_2 Composites in the Visible Region. *Phys. Chem. Chem. Phys.* **2015**, *17*, 7966–7971.

66. Margraf, J. T.; Lodermeyer, F.; Strauss, V.; Haines, P.; Walter, J.; Peukert, W.; Costa, R. D.; Clark, T.; Guldi, D. M., Using Carbon Nanodots as Inexpensive and Environmentally Friendly Sensitizers in Mesoscopic Solar Cells. *Nanoscale Horiz.* **2016**, *1*, 220–226.

67. Wang, H.; Sun, P.; Cong, S.; Wu, J.; Gao, L.; Wang, Y.; Dai, X.; Yi, Q.; Zou, G., Nitrogen-doped Carbon Dots for "Green" Quantum Dot Solar Cells. *Nanoscale Res. Lett.* **2016**, *11*, 27.

68. Fang, X.; Li, M.; Guo, K.; Li, J.; Pan, M.; Bai, L.; Luoshan, M.; Zhao, X., Graphene Quantum Dots Optimization of Dye-sensitized Solar Cells. *Electrochim. Acta* **2014**, *137*, 634–638.

69. Mihalache, I.; Radoi, A.; Mihaila, M.; Munteanu, C.; Marin, A.; Danila, M.; Kusko, M.; Kusko, C., Charge and Energy Transfer Interplay in Hybrid Sensitized Solar Cells Mediated by Graphene Quantum Dots. *Electrochim. Acta* **2015**, *153*, 306–315.

70. Majumder, T.; Mondal, S. P., Advantages of Nitrogen-doped Graphene Quantum Dots as a Green Sensitizer with ZnO Nanorod based Photoanodes for Solar Energy Conversion. *J. Electroanal. Chem.* **2016**, *769*, 48–52.

71. Majumder, T.; Debnath, K.; Dhar, S.; Hmar, J. J. L.; Mondal, S. P., Nitrogen-doped Graphene Quantum Dot-decorated ZnO Nanorods for Improved Electrochemical Solar Energy Conversion. *Energy Technol.* **2016**, *4*, 950–958.

72. Salam, Z.; Vijayakumar, E.; Subramania, A.; Sivasankar, N.; Mallick, S., Graphene Quantum Dots Decorated Electrospun TiO_2 Nanofibers as an Effective Photoanode for Dye Sensitized Solar Cells. *Sol. Energy Mater. Sol. Cells* **2015**, *143*, 250–259.

73. Bian, J.; Huang, C.; Wang, L.; Hung, T.; Daoud, W. A.; Zhang, R., Carbon Dot Loading and TiO_2 Nanorod Length Dependence of Photoelectrochemical Properties in Carbon Dot/TiO_2 Nanorod Array Nanocomposites. *ACS Appl. Mater. Interfaces* **2014**, *6*, 4883–4890.

74. Wang, X.; Ling, D.; Wang, Y.; Long, H.; Sun, Y.; Shi, Y.; Chen, Y.; Jing, Y.; Sun, Y.; Dai, Y., N-doped Graphene Quantum Dots-functionalized Titanium Dioxide

Nanofibers and their Highly Efficient Photocurrent Response. *J. Mater. Res.* **2014**, *29*, 1408–1416.

75. Zhang, Y.-Q.; Ma, D.-K.; Zhang, Y.-G.; Chen, W.; Huang, S.-M., N-doped Carbon Quantum Dots for TiO_2-based Photocatalysts and Dye-sensitized Solar Cells. *Nano Energy* **2013**, *2*, 545–552.

76. Ma, Z.; Zhang, Y.-L.; Wang, L.; Ming, H.; Li, H.; Zhang, X.; Wang, F.; Liu, Y.; Kang, Z.; Lee, S.-T., Bioinspired Photoelectric Conversion System based on Carbon-quantum-dot-doped Dye–Semiconductor Complex. *ACS Appl. Mater. Interfaces* **2013**, *5*, 5080–5084.

77. Dutta, M.; Sarkar, S.; Ghosh, T.; Basak, D., ZnO/Graphene Quantum Dot Solid-state Solar Cell. *J. Phys. Chem. C* **2012**, *116*, 20127–20131.

78. Gao, N.; Huang, L.; Li, T.; Song, J.; Hu, H.; Liu, Y.; Ramakrishna, S., Application of Carbon Dots in Dye-sensitized Solar Cells: A Review. *J. Appl. Polym. Sci.* **2020**, *137*, 48443.

79. Majumder, T.; Dhar, S.; Chakraborty, P.; Debnath, K.; Mondal, S. P., S, N Co-doped Graphene Quantum Dots Decorated C-doped ZnO Nanotaper Photoanodes for Solar Cells Applications. *Nano* **2019**, *14*, 1950012.

80. Ghann, W.; Sharma, V.; Kang, H.; Karim, F.; Richards, B.; Mobin, S. M.; Uddin, J.; Rahman, M. M.; Hossain, F.; Kabir, H.; Uddin, N., The Synthesis and Characterization of Carbon Dots and their Application in Dye Sensitized Solar Cell. *Int. J. Hydrog. Energy* **2019**, *44*, 14580–14587.

81. Shen, K.; Luo, G.; Liu, J.; Zheng, J.; Xu, C., Highly Transparent Photoelectrochromic Device based on Carbon Quantum Dots Sensitized Photoanode. *Sol. Energy Mater. Sol. Cells* **2019**, *193*, 372–378.

82. Chava, R. K.; Im, Y.; Kang, M., Nitrogen Doped Carbon Quantum Dots as a Green Luminescent Sensitizer to Functionalize ZnO Nanoparticles for Enhanced Photovoltaic Conversion Devices. *Mater. Res. Bull.* **2017**, *94*, 399–407.

83. Carolan, D.; Rocks, C.; Padmanaban, D. B.; Maguire, P.; Svrcek, V.; Mariotti, D., Environmentally Friendly Nitrogen-doped Carbon Quantum Dots for Next Generation Solar Cells. *Sustain. Energy Fuels* **2017**, *1*, 1611–1619.

84. Zhang, Q.; Zhang, G.; Sun, X.; Yin, K.; Li, H., Improving the Power Conversion Efficiency of Carbon Quantum Dot-sensitized Solar Cells by Growing the Dots on a TiO_2 Photoanode In Situ. *Nanomaterials* **2017**, *7*, 130.

85. Sehgal, P.; Narula, A. K., Enhanced Performance of Porphyrin Sensitized Solar Cell based on Graphene Quantum Dots Decorated Photoanodes. *Opt. Mater.* **2018**, *79*, 435–445.

86. Wang, Y.; Lao, S.; Ding, W.; Zhang, Z.; Liu, S., A Novel Ratiometric Fluorescent Probe for Detection of Iron Ions and Zinc Ions based on Dual-emission Carbon Dots. *Sens. Actuators B Chem.* **2019**, *284*, 186–192.

87. He, L.; Wang, T.; An, J.; Li, X.; Zhang, L.; Li, L.; Li, G.; Wu, X.; Su, Z.; Wang, C., Carbon Nanodots@Zeolitic Imidazolate Framework-8 Nanoparticles for Simultaneous pH-responsive Drug Delivery and Fluorescence Imaging. *CrystEngComm* **2014**, *16*, 3259–3263.

88. Karthik, S.; Saha, B.; Ghosh, S. K.; Pradeep Singh, N. D., Photoresponsive Quinoline Tethered Fluorescent Carbon Dots for Regulated Anticancer Drug Delivery. *Chem. Commun.* **2013**, *49*, 10471–10473.

89. Niu, Q.; Gao, K.; Lin, Z.; Wu, W., Amine-capped Carbon Dots as a Nanosensor for Sensitive and Selective Detection of Picric Acid in Aqueous Solution via Electrostatic Interaction. *Anal. Methods* **2013**, *5*, 6228–6233.

90. Strauss, V.; Margraf, J. T.; Dolle, C.; Butz, B.; Nacken, T. J.; Walter, J.; Bauer, W.; Peukert, W.; Spiecker, E.; Clark, T.; Guldi, D. M., Carbon Nanodots: Toward a Comprehensive Understanding of their Photoluminescence. *J. Am. Chem. Soc.* **2014**, *136*, 17308–17316.

91. Wang, L.; Zhu, S.-J.; Wang, H.-Y.; Qu, S.-N.; Zhang, Y.-L.; Zhang, J.-H.; Chen, Q.-D.; Xu, H.-L.; Han, W.; Yang, B.; Sun, H.-B., Common Origin of Green Luminescence in Carbon Nanodots and Graphene Quantum Dots. *ACS Nano* **2014**, *8*, 2541–2547.

92. Qu, S.; Chen, H.; Zheng, X.; Cao, J.; Liu, X., Ratiometric Fluorescent Nanosensor based on Water Soluble Carbon Nanodots with Multiple Sensing Capacities. *Nanoscale* **2013**, *5*, 5514–5518.

93. Ye, R.; Xiang, C.; Lin, J.; Peng, Z.; Huang, K.; Yan, Z.; Cook, N. P.; Samuel, E. L. G.; Hwang, C.-C.; Ruan, G.; Ceriotti, G.; Raji, A.-R. O.; Martí, A. A.; Tour, J. M., Coal as an Abundant Source of Graphene Quantum Dots. *Nat. Commun.* **2013**, *4*, 2943.

94. Martindale, B. C. M.; Hutton, G. A. M.; Caputo, C. A.; Prantl, S.; Godin, R.; Durrant, J. R.; Reisner, E., Enhancing Light Absorption and Charge Transfer Efficiency in Carbon Dots through Graphitization and Core Nitrogen Doping. *Angew. Chem. Int. Ed.* **2017**, *56*, 6459–6463.

95. Yan, X.; Cui, X.; Li, L.-s., Synthesis of Large, Stable Colloidal Graphene Quantum Dots with Tunable Size. *J. Am. Chem. Soc.* **2010**, *132*, 5944–5945.

96. Fischer, J. W.; Merwin, L. H.; Nissan, R. A., NMR Investigation of the Thermolysis of Citric Acid. *Appl. Spectrosc.* **1995**, *49*, 120–126.

97. Wyrzykowski, D.; Hebanowska, E.; Nowak-Wiczk, G.; Makowski, M.; Chmurzyński, L., Thermal Behaviour of Citric Acid and Isomeric Aconitic Acids. *J. Therm. Anal. Calorim.* **2011**, *104*, 731–735.

98. Sell, W. J.; Easterfield, T. H., LXXIII.—Studies on Citrazinic Acid. Part I. *J. Chem. Soc., Trans.* **1893**, *63*, 1035–1051.

99. Wang, T.; Wang, A.; Wang, R.; Liu, Z.; Sun, Y.; Shan, G.; Chen, Y.; Liu, Y., Carbon Dots with Molecular Fluorescence and their Application as a "Turn-off" Fluorescent Probe for Ferricyanide Detection. *Sci. Rep.* **2019**, *9*, 10723.

Chapter 6: Conclusions

In conclusion, FCDs constitute an emerging class of highly intriguing carbon-based nanomaterial that possess a host of promising properties such as chemical inertness, high thermal stability, compositional tunability, and, most notably, exceptional luminescent characteristics that have been reported to be dependent on size, graphitic content (that is, size and quantity of sp^2 islands), or core/surface composition. Additionally, these green nanocarbons can be synthesized through several different approaches, deriving from a myriad of (sustainable) carbon precursors, such as low-value wastes, including human urine, often resulting in heteroatom-doped FCDs whose absorbance and luminescent properties are bathochromically shifted relative to undoped nanocarbons. Furthermore, these carbonaceous nanomaterials' donor/acceptor capabilities afford noteworthy exploitations in a variety of applications such as surface enhanced Raman spectroscopy and (noble) metal nanoparticle formation. Regarding the latter, FCDs can act as dual reducing and capping agents in the synthesis of both mono- and bimetallic nanoparticles, resulting in FCD/MNP composites whose optical properties (*i.e.*, surface plasmon resonance) can be experimentally tuned through systematic variation of the FCD:metal and metal:metal ratios. Due to the ability to sustainably synthesize these green nanocarbons from heteroatom-containing carbon precursors, yielding improved optical properties, and the ability to generate FCD/MNP composites with tunable plasmon resonances, these materials hold enticing prospects for exploitation in PV applications, namely, as inexpensive, non-toxic sensitizer alternatives and plasmonic performance enhancers, respectively. Furthermore, coupling the alluring properties of heteroatom-doped FCDs

with those of FCD/MNP composites could result in further improvements to PV device performance metrics, affording cheaper and more efficient solar energy harvesting.

Undoubtedly the biggest hurdles in achieving these realizations though are the mysterious mechanism of FCD formation and how altering the precursor chemistry influences these formation pathways. Stemming from these issues is the exact origin of FCDs' purportedly distinguishing characteristics from their nanocarbon relatives; that is, their excitation wavelength-dependent emission, the genesis of which continues to elude the field. Historically, the source of these intriguing luminescent properties has been attributed to carbon core size and compositional variation. However, in recent years, mounting evidence has surfaced demonstrating that the intense blue luminescence, and corresponding high fluorescence quantum yields, originates not from the FCDs but from molecular by-products produced during the carbonization, a severe oversight emanating from the naïve concept that these materials are the exclusive product generated, negating any need for postsynthetic purification. Indeed, unequivocal evidence to the contrary has been provided herein, demonstrating that this notion is assuredly not the case; adequate purification of these materials is absolutely necessary prior to detailed characterization and implementation in applied technologies. The unsettling and recurring trend of insufficient separation of reaction by-products from the target nanocarbons currently plaguing the FCD field is undoubtedly hindering maturation of the area, particularly, with respects to illuminating the exact origin of their purported luminescence, and, worse, has led to a number of misconceptions entering the publication record. Furthermore, this widespread lack of mandatory purification not only influences the observed optical properties but the presence of molecular by-products drastically affects the characteristics and performance

of common applications for these materials, namely, quenchometric-based detection and sensitizers in PV devices.

Chapter 7: Future Outlooks

Looking to the future, given the relentless fervor and intense velocity of research that has led to thousands of published FCD works in recent years with a disconcerting percentage ignorantly performing inadequate purification (based on the representative sampling provided in Chapter 4), the field needs to temporarily restrain and then redirect this zeal toward reassessing the employed fractionation practices (or lack thereof) in order to uncover the true nature of these nanocarbons' properties. For instance, until the exact compositions of these carbonaceous cocktails are deconvoluted, the precise formation mechanisms and origin of FCDs' properties, namely, the genesis of their luminescence, will continue to evade the field. To address this need, a proposed path forward is outlined below.

First, the comprehensive implementation of an analytically rigorous and thoroughly scrutinized separation technique that yields high-purity, single-component FCD samples is of utmost importance since as-synthesized FCDs are complex, multicomponent systems whose constituents and, therefore, chemical compositions, vary widely depending on the precursor(s) employed. While membrane-based separations, such as dialysis, offer an unrivaled convenience for purifying FCD samples, due to as-synthesized FCDs' multifarious nature and the separation restrictions inherent to these membranes (that is, only select molecular weight cut-offs, and, therefore, membrane pore sizes are commercially available), these techniques may not be a satisfactory mode of purification in some instances. Thus, the prime candidate for analytically sound fractionation of these intricate mixtures is chromatographic techniques since a hallmark of these methodologies is naturally a reduction in sample complexity, however, these approaches have only been

championed by select groups and currently constitute less than 10% of all reported purification protocols. Therefore, adequate purification needs to be implemented immediately for all future FCD studies, in which, at minimum, the FCD samples are initially fractionated with careful and thorough membrane-based purification to begin to isolate and understand the properties of specific size regimes, followed by chromatographic separations to further deconvolute the still diverse composition of these membrane-restricted size regimes. In the ideal scenario, chromatographic separations would become the benchmark mode of purification, however, given the, often, costly nature of and lack of easy access to these high-end fractionation techniques, rigorous membrane separations and characterizations of the resulting fractions would lay the foundation for groups well-equipped to undertake sophisticated chromatographic separations of these prefractionated size regimes.

Once a purification standard is meticulously vetted and unanimously put into practice, revisiting previous works concerning the inherent properties of FCDs is necessary to verify the authenticity of these preceding claims, particularly, the luminescent nature of these materials. As the complexity of these samples is deconvoluted and a new, correct understanding of their inherent properties is established, then (and only then) can the field begin to truly exploit these materials. At this point, however, additional remedial studies will be warranted to reassess the performance of the pure FCDs in the many applications that they have previously been employed in, especially those reliant on the luminescent properties. While the continual rampant lack of adequate purification in the FCD field is disheartening, as future research begins to uncover the exact nature of these nanocarbons

and their true properties, their previously hypothesized potentials may finally come to fruition.

Appendix A: Supporting Figures for Chapter 2

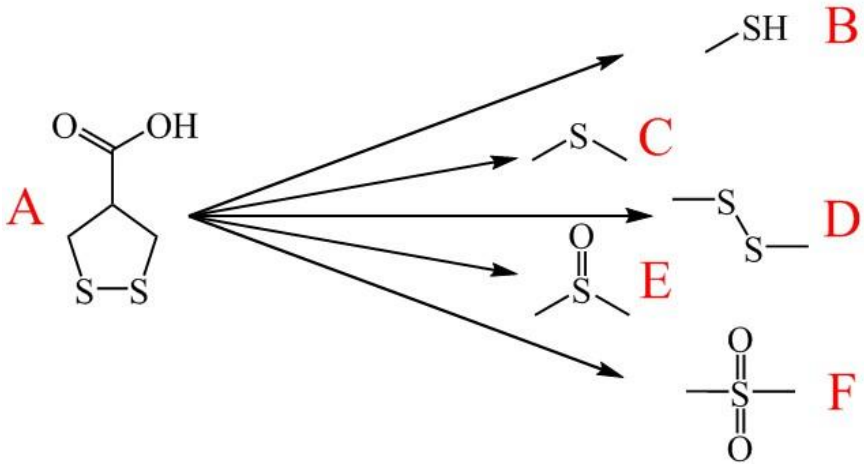

Figure A.1 Key suspected products of the metabolic breakdown of (A) asparagusic acid: (B) methanethiol, (C) dimethyl sulfide, (D) dimethyl disulfide, (E) dimethyl sulfoxide, and (F) dimethyl sulfone.

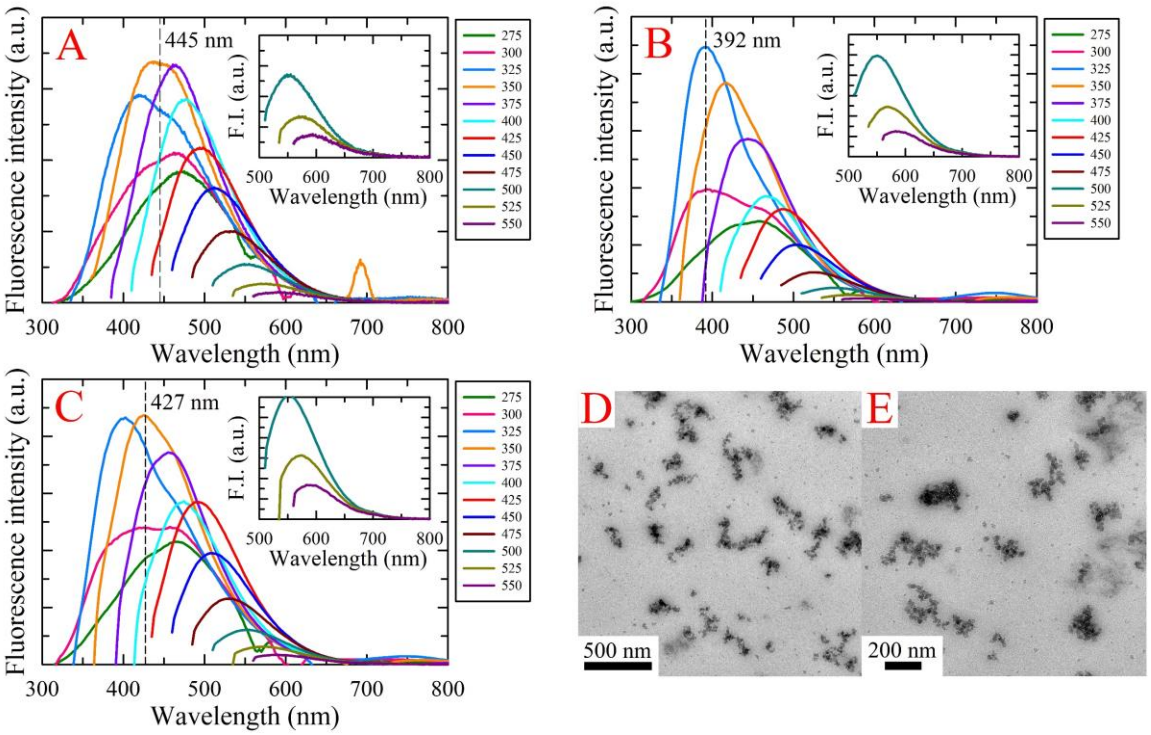

Figure A.2 (A) An extended pyrolysis time (24 h) of urine collected during the donor's unmodified diet phase generated a redshift in peak emission relative to the emission arising from a 12 h thermal treatment of the same urine (panel B). Specifically, the peak emission for the latter occurred at 392 nm under 325 nm excitation while the peak emission shifted to 445 under 350 nm excitation after an additional 12 h of pyrolysis. (C) The CPDs displayed a slight redshift in emission over the UPDs (12 h) but did not show as large of a redshift as the APDs (Figure 2.2A) or the UPDs from the 24 h pyrolysis. This loosely implies that a longer treatment time of the dietary-doped urine samples could lead to an even further redshift in emission. (D–E) TEM imaging analysis of the UPDs (24 h) confirmed that small, presumably carbonaceous, nanocrystals were still generated when a longer pyrolysis time was employed. Note, the abbreviation "F.I." used in the inset plots of panels A–C stands for fluorescence intensity.

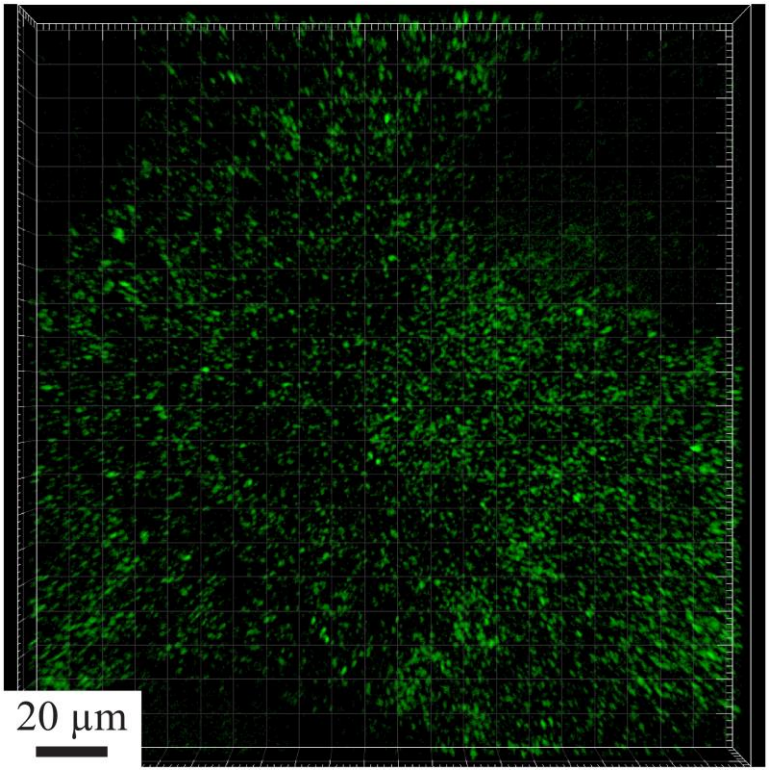

Figure A.3 Confocal fluorescence micrograph of APD-labelled BT-474 (human mammary gland, ductal carcinoma) cells adhered to a 96-well plate.

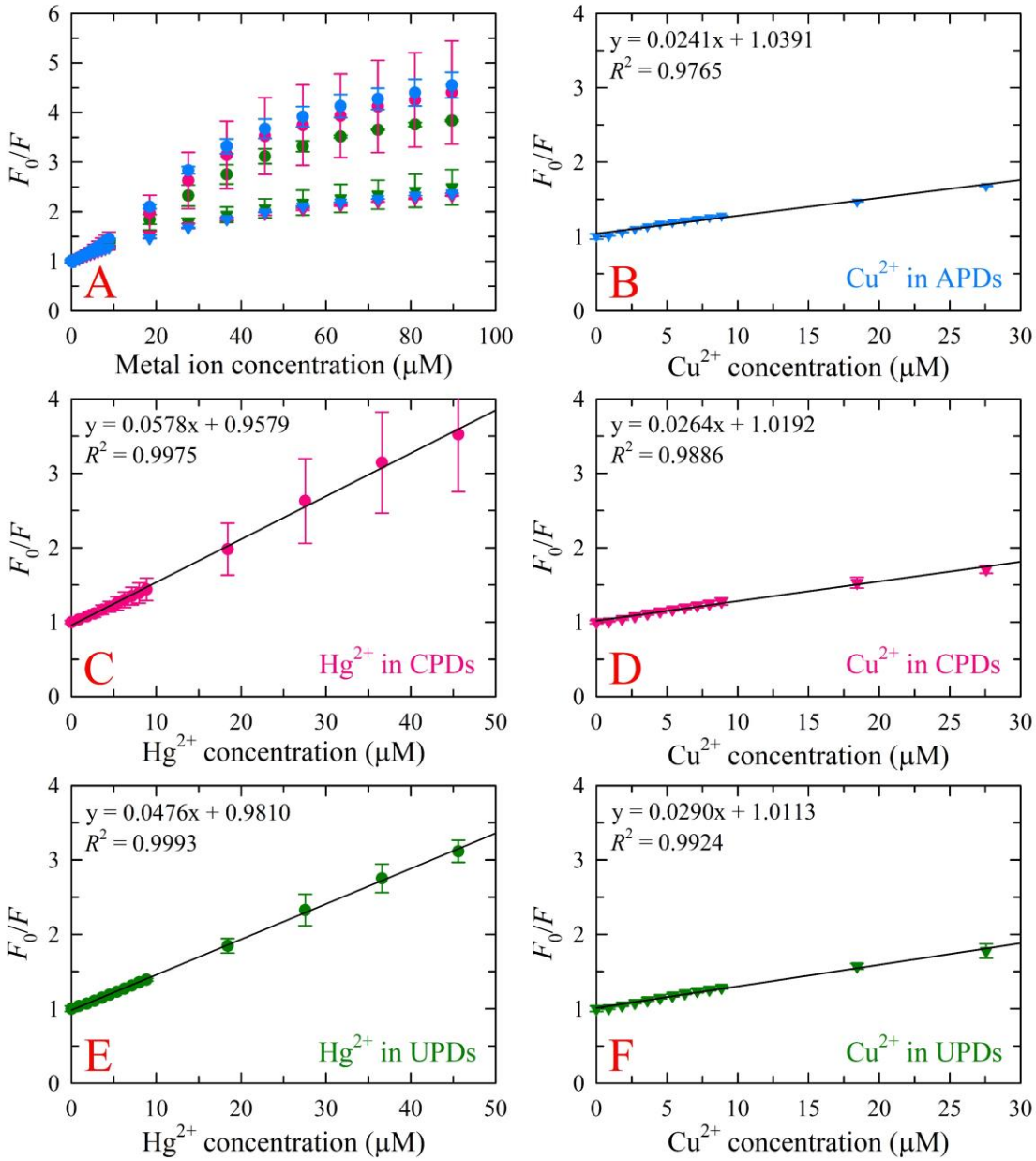

Figure A.4 (A) Quenching curves for UPDs (green), CPDs (magenta), and APDs (cyan) in the presence of Hg^{2+} (circles) and Cu^{2+} (triangles). Both metal ions showed fluorescence quenching with Hg^{2+} displaying stronger quenching over Cu^{2+}. Each respective metal quenched all three samples in a similar manner. (B–F) Quenching curves used for the determination of quenching constants and limit of detection (LOD) calculations. The color and shape schemes employed in panel A were kept consistent for all panels (*i.e.*, B–F). Note, the quenching curve used for the LOD calculation of APD quenching in the presence of Hg^{2+} is provided as panel B of Figure 2.6.

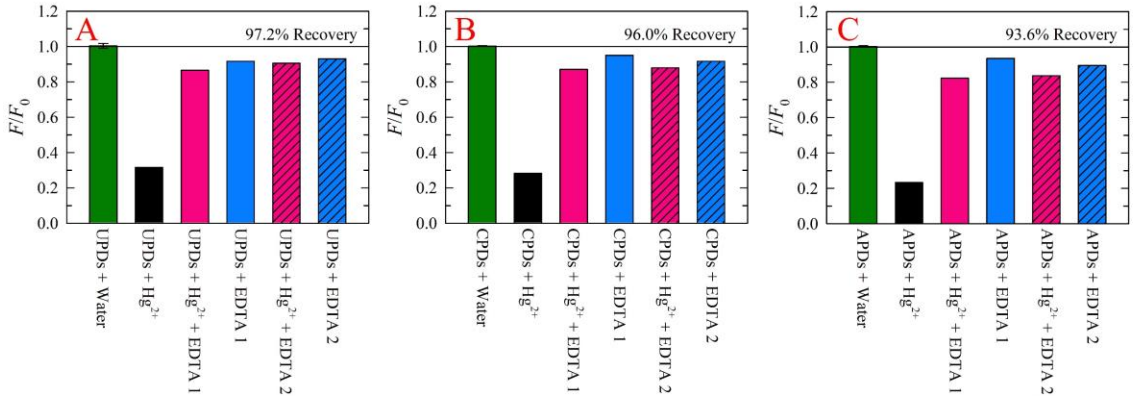

Figure A.5 PD fluorescence signal recovery using EDTA to preferentially chelate Hg^{2+}, restoring the previously quenched fluorescent site to >90% of the original signal. Specifically, the (A) UPDs, (B) CPDs, and (C) APDs displayed 97.2%, 96.0%, and 93.6% recovery, respectively.

Appendix B: Supporting Figures for Chapter 3

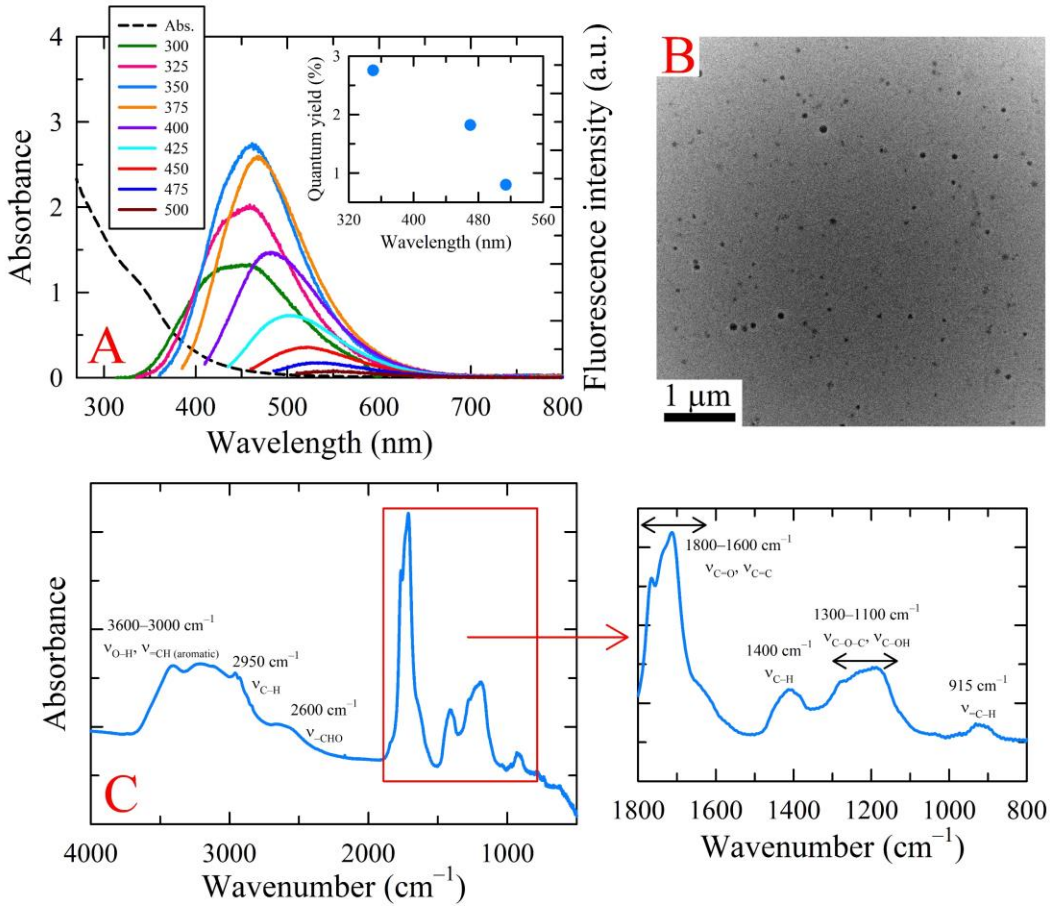

Figure B.1 (A) Photophysical properties of the CA-derived FCDs employed in this work. Akin to other reported FCDs, these carbon dots displayed excitation wavelength-dependent emission and quantum yields (panel A inset). (B) Representative TEM micrograph of the CA-derived sample indicating that, presumably carbonaceous, nanodots, 30–60 nm (up to 100 nm) in size were produced. (C) FTIR spectrum of the CA-derived FCDs revealing that the nanocarbons possessed alcohol, carboxyl, epoxy, ester, and ether surface functionalities, moieties that account for the FCDs' high aqueous solubility. The FTIR peaks were assigned as such: stretching vibrations of O–H ($\nu_{O–H}$, 3600–3000 cm^{-1}), stretching vibrations of C=O ($\nu_{C=O}$, 1800–1600 cm^{-1}), skeletal vibrations of aromatic groups ($\nu_{C=C}$, 1800–1600 cm^{-1}), stretching vibrations of C–O moieties ($\nu_{C–O–C}$ and $\nu_{C–OH}$, 1300–1000 cm^{-1}), and aliphatic carbon stretches ($\nu_{C–H}$ and $\nu_{=C–H}$, 2900, 1400, and 915 cm^{-1}). The outset panel to the right of panel C is an expanded plot of the area within the red box shown in panel C.

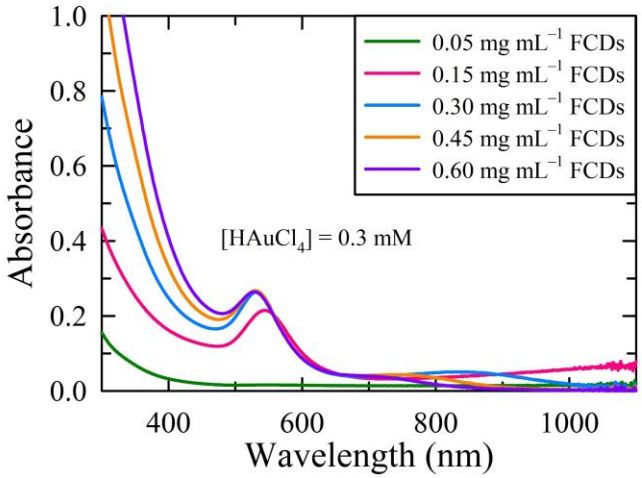

Figure B.2 UV-vis spectra of the resultant Au@FCD NP solutions when the concentration of Au salt was held constant at 0.3 mM and the FCD concentration was increased from 0.05 to 0.60 mg mL^{-1}. As the FCD concentration increased up to 0.30 mg mL^{-1}, the Au NP SPR appeared and hypsochromically shifted. For the three highest concentrations of FCDs, the Au NP SPR remained relatively constant in intensity and peak position.

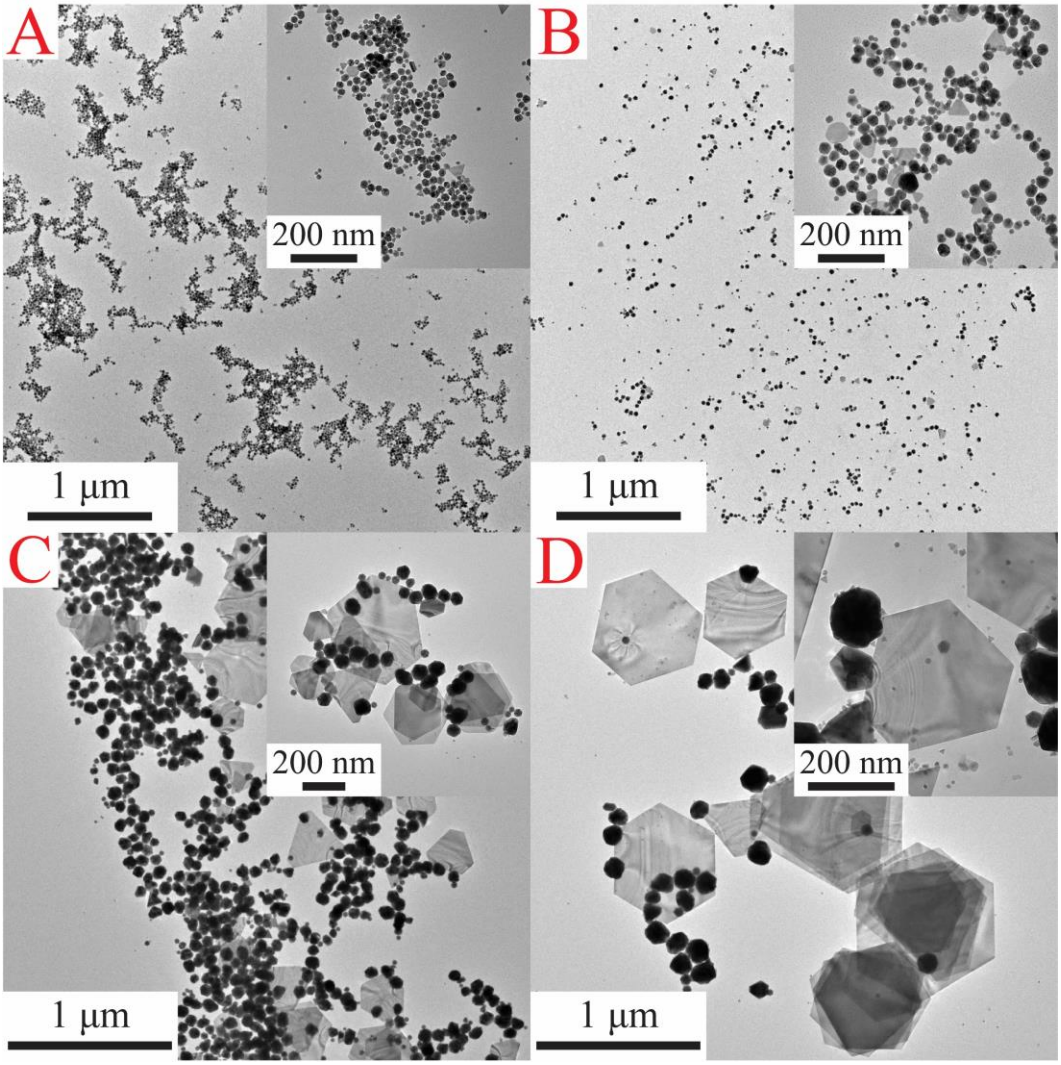

Figure B.3 Representative TEM micrographs of the resultant Au@FCD NPs when the FCD concentration was held at 0.3 mg mL^{-1} and the Au concentration was (A) 0.20 mM, (B) 0.35 mM, (C) 0.45 mM, or (D) 0.60 mM. Such FCD:Au ratios resulted in average quasi-spherical particle sizes of (A) 17.8 ± 6.4, (B) 26.7 ± 10.0, (C) 47.8 ± 20.7, and (D) 96.7 ± 29.9 nm, respectively. For the higher Au:FCD ratios, large hexagonal and trigonal Au plates formed with average particle sizes of 266.7 ± 99.3 and 528.8 ± 214.3 nm for Au concentrations of 0.45 and 0.60 mM, respectively. The higher Au:FCD ratios also produced much smaller quasi-spherical particles in the 5–20 nm regime as evidenced by the insets of panels C and D but these particles were less concentrated than the larger quasi-spherical particles and platelets.

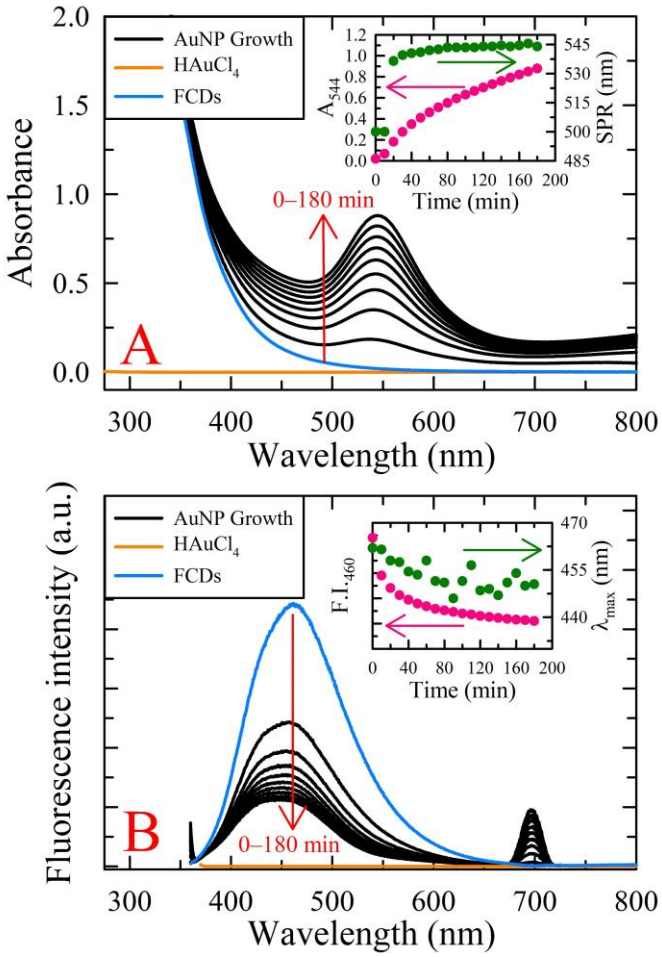

Figure B.4 (A) Time-dependent UV-vis spectra of the room temperature Au reduction (0.3 mg mL^{-1} FCDs:0.35 mM $HAuCl_4$) showing that the reduction was near completion after 3 h. (B) Time-dependent fluorescence spectra (λ_{ex} = 350 nm) of the room temperature Au reduction (0.3 mg mL^{-1} FCDs:0.35 mM $HAuCl_4$). After the reduction, the Au@FCD NPs still retained approximately 25% of the original FCD fluorescence. Since $HAuCl_4$ did not show any absorbance or fluorescence features within the wavelength range of interest, the increase in absorbance and decrease in fluorescence intensity was solely attributed to the growth of Au NPs.

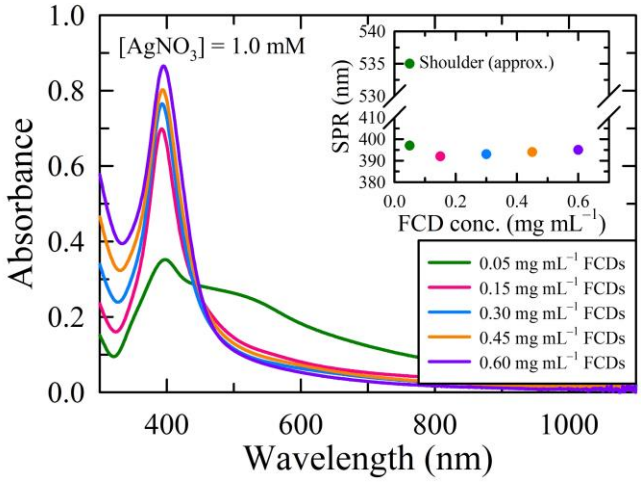

Figure B.5 UV-vis spectra of the resultant Ag@FCD NP solutions when the concentration of Ag salt was held constant at 1.0 mM and the FCD concentration was increased from 0.05 to 0.60 mg mL^{-1}. In general, as the FCD concentration increased, the Ag NP SPR displayed a slight bathochromic shift. Interestingly, at the lowest concentration of FCDs (0.05 mg mL^{-1}), a broad shoulder centered at approximately 535 nm appeared in addition to the SPR peak at 396 nm, a feature that is indicative of larger Ag nanostructures with high polydispersity.

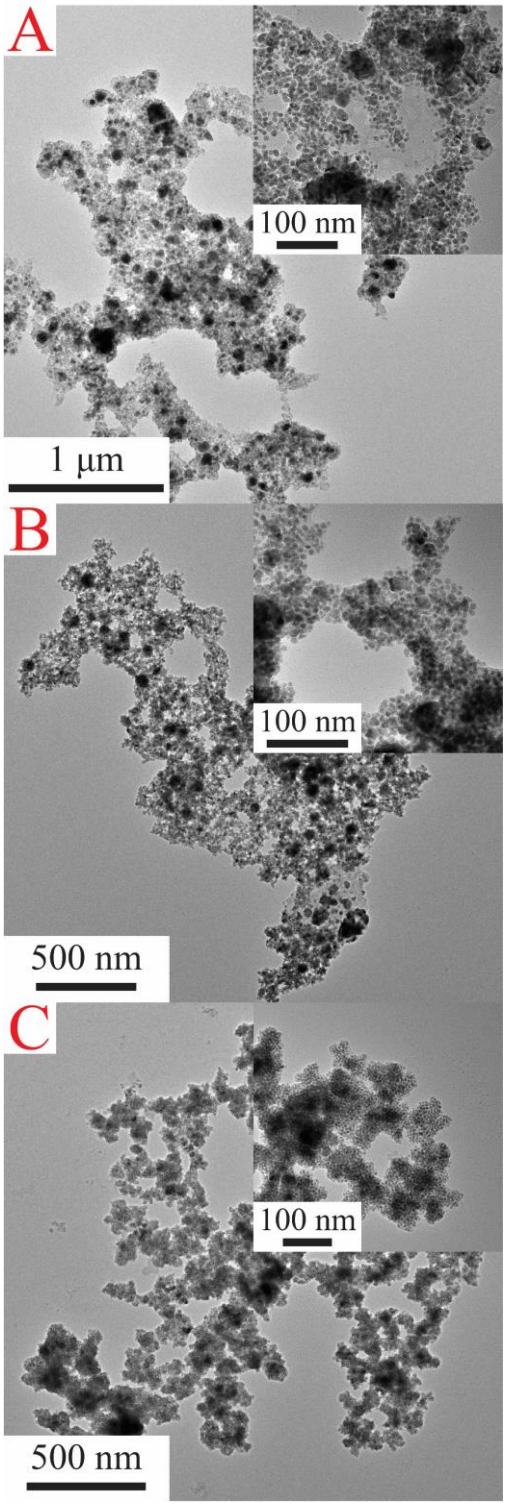

Figure B.6 Representative TEM micrographs of the resultant quasi-spherical Ag@FCD NPs when the FCD concentration was held at 0.3 mg mL^{-1} and the Ag concentration was (A) 0.30 mM, (B) 1.00 mM, or (C) 3.00 mM. Such FCD:Ag ratios resulted in average particle sizes of (A) 11.1 ± 9.9, (B) 6.9 ± 3.4, and (C) 6.0 ± 4.0 nm, respectively.

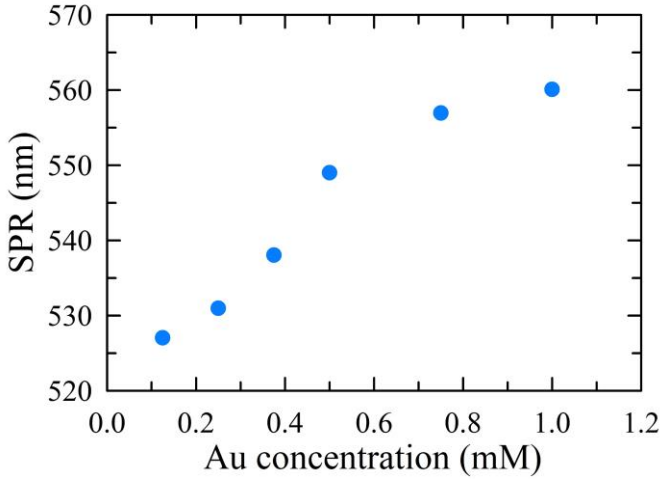

Figure B.7 Resultant Au@FCD NP SPR as a function of the Au concentration within samples synthesized at 100 °C. Similar to the room temperature reductions of Au salt using FCDs, the 100 °C reductions resulted in a bathochromic shift of the SPR with increasing Au concentration, a transition indicative of the formation of larger Au NPs and further highlighting the degree of SPR tunability, even when using elevated temperatures.

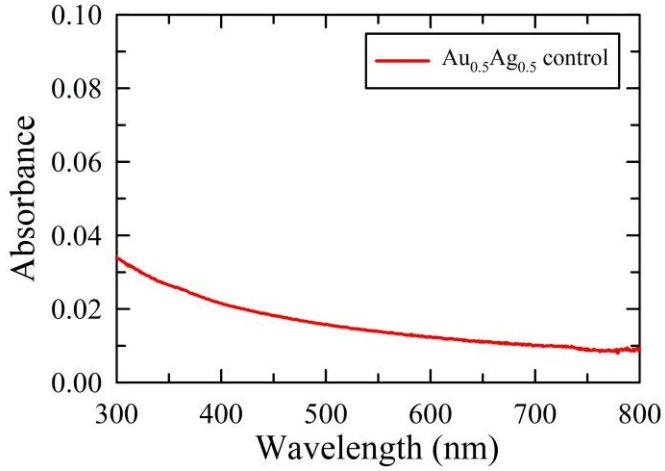

Figure B.8 UV-vis spectrum of a control sample that was heated at 100 °C in the presence of 50:50 mol% Au:Ag but in the absence of FCDs. The lack of a discernable SPR peak provides further evidence that the CA-derived FCDs act as reducing agents towards Au_xAg_{1-x} NP formation.

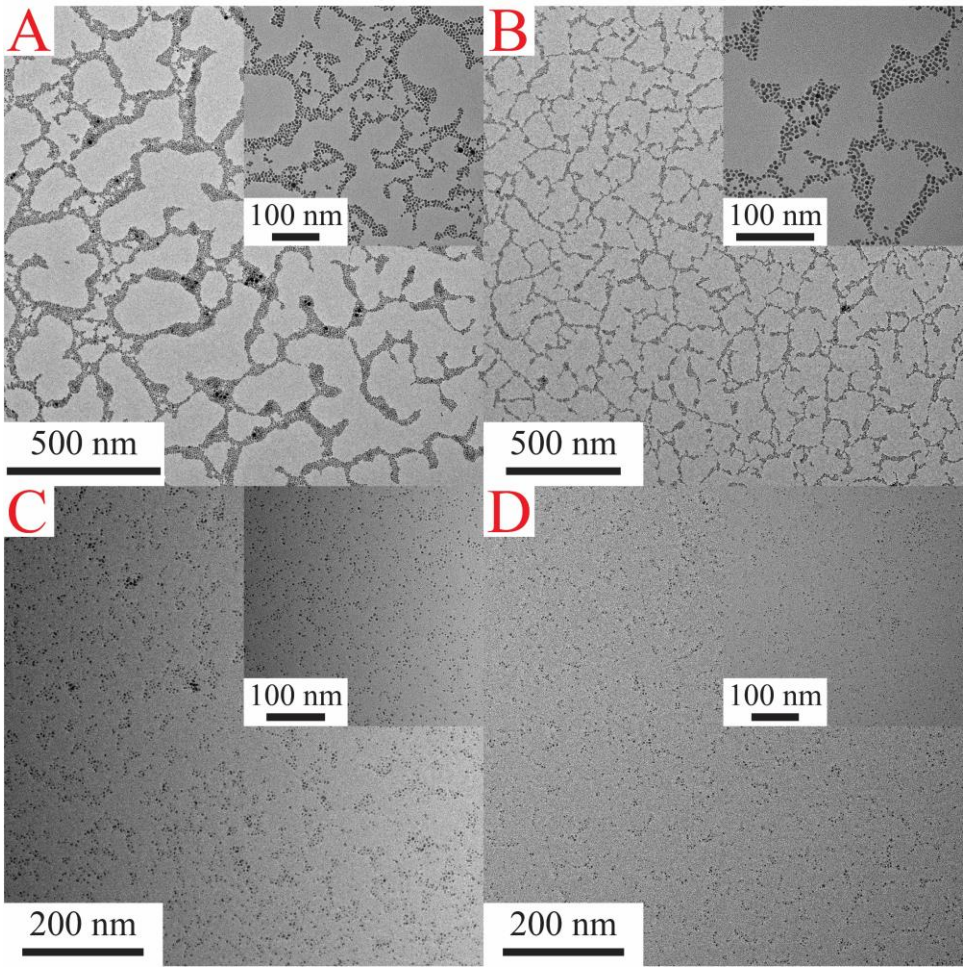

Figure B.9 Representative TEM micrographs of the (A) $Au_{0.9}Ag_{0.1}$@FCD, (B) $Au_{0.7}Ag_{0.3}$@FCD, (C) $Au_{0.3}Ag_{0.7}$@FCD, and (D) $Au_{0.1}Ag_{0.9}$@FCD BMNPs. Interestingly, the size of the Au_xAg_{1-x} NPs decreased slightly with increasing Ag content. Specifically, size analyses of the imaged BMNPs yielded average particle sizes of 4.1 ± 1.4, 3.4 ± 0.9, 2.4 ± 0.8, and 1.9 ± 0.7 nm for the $Au_{0.9}Ag_{0.1}$@FCD, $Au_{0.7}Ag_{0.3}$@FCD, $Au_{0.3}Ag_{0.7}$@FCD, and $Au_{0.1}Ag_{0.9}$@FCD BMNPs, respectively.

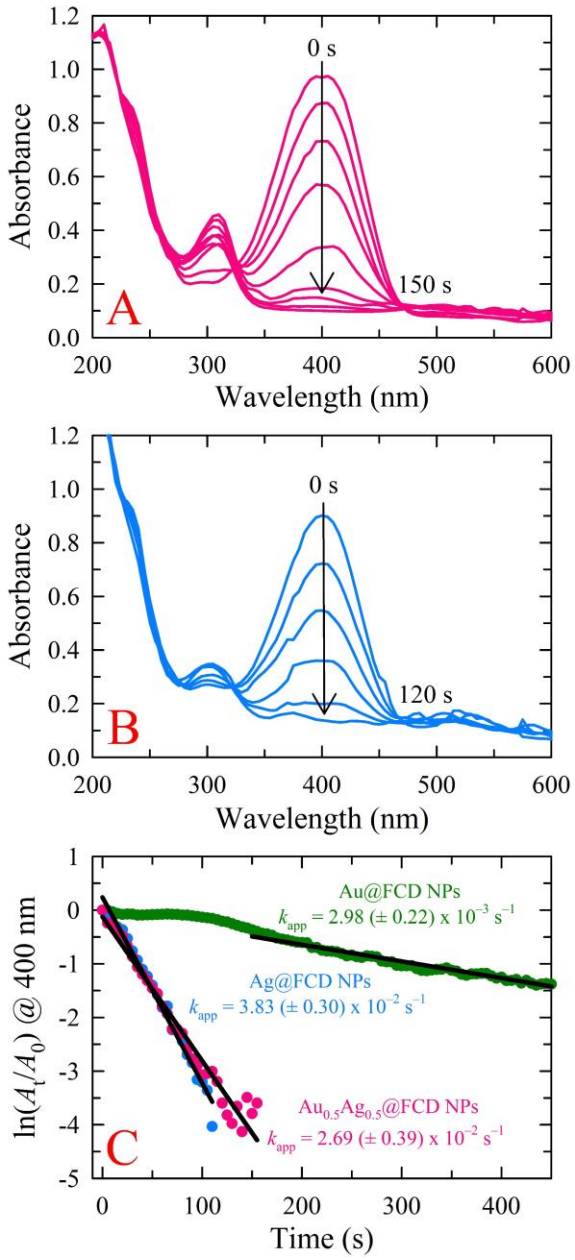

Figure B.10 (A–B) Time-dependent UV-vis absorption spectra of the $NaBH_4$-assisted reduction of 4-NP catalyzed by (A) $Au_{0.5}Ag_{0.5}$@FCD NPs and (B) Ag@FCD NPs. (C) Plots of $\ln(A_t/A_0)$ of 4-NP absorbance at 400 nm *vs* time for various aged MNP@FCD catalysts.

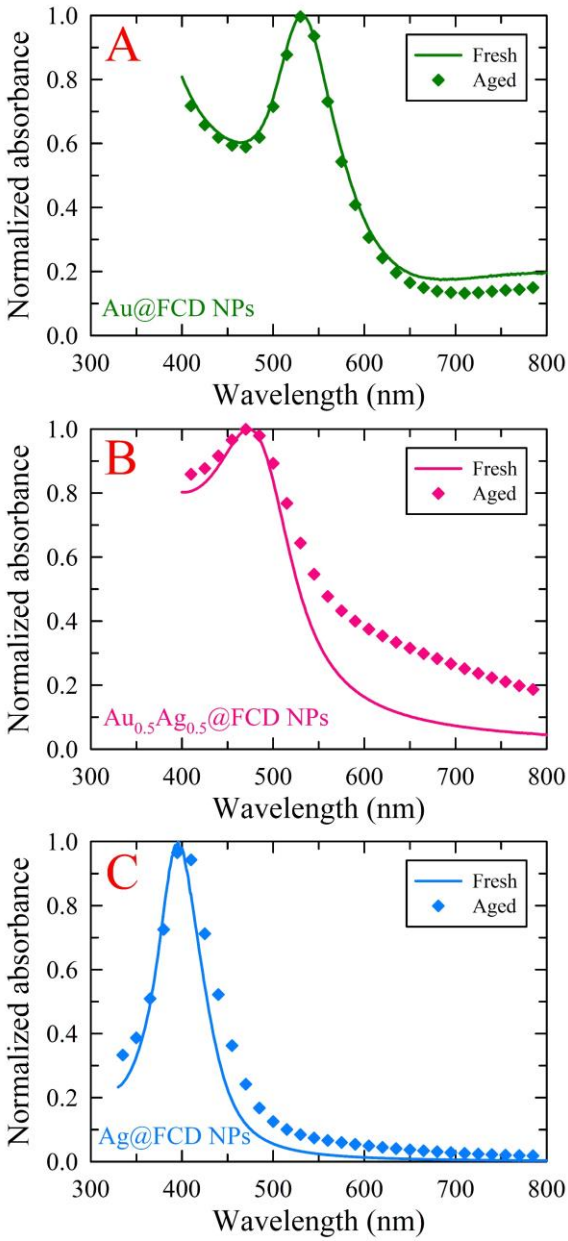

Figure B.11 Normalized UV-vis absorption spectra of freshly prepared and aged (for 5 months in a lab drawer) MNP@FCD NPs highlighting the stability of the (A) Au@FCD, (B) $Au_{0.5}Ag_{0.5}$@FCD, and (C) Ag@FCD NPs. Comparison of the spectral profiles for fresh samples to those arising from their aged counterparts reveals that the Au@FCD NPs remained essentially unchanged after storing for 5 months while the aged $Au_{0.5}Ag_{0.5}$@FCD and Ag@FCD NPs displayed increased absorbance at longer wavelengths, features that likely stem from marginal particle aggregation.

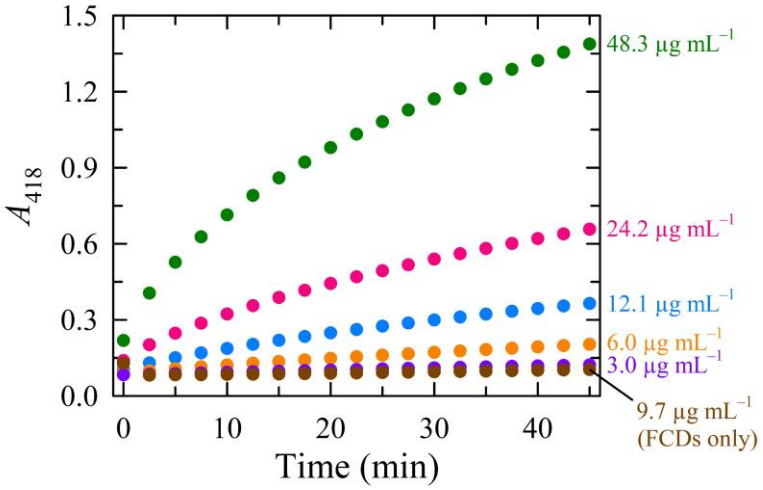

Figure B.12 Concentration-dependent, peroxidase-mimicking activity of the Au@FCD NPs assessed by temporally monitoring absorbance changes of ABTS (0.805 mM) at 418 nm in the presence of 5.4 mM H_2O_2 and 3.0–48.3 μg mL^{-1} Au@FCD NPs. Note, the reported concentrations indicate the quantity of FCDs present in the Au@FCD aliquot added; the concentration of Au (in μM) within each Au@FCD sample is half the value of the corresponding FCD concentration (*e.g.*, the 24.2 μg mL^{-1} FCD sample contains 12.1 μM Au). Results of a control experiment using a 9.7 μg mL^{-1} solution of neat FCDs (*i.e.*, metal-free) are also provided (brown circles). While no activity was observed on this timescale for the "naked", metal-free FCDs, the Au@FCD NPs clearly showed higher activity with increasing nanocatalyst concentration.

Appendix C: Supporting Figures for Chapter 4

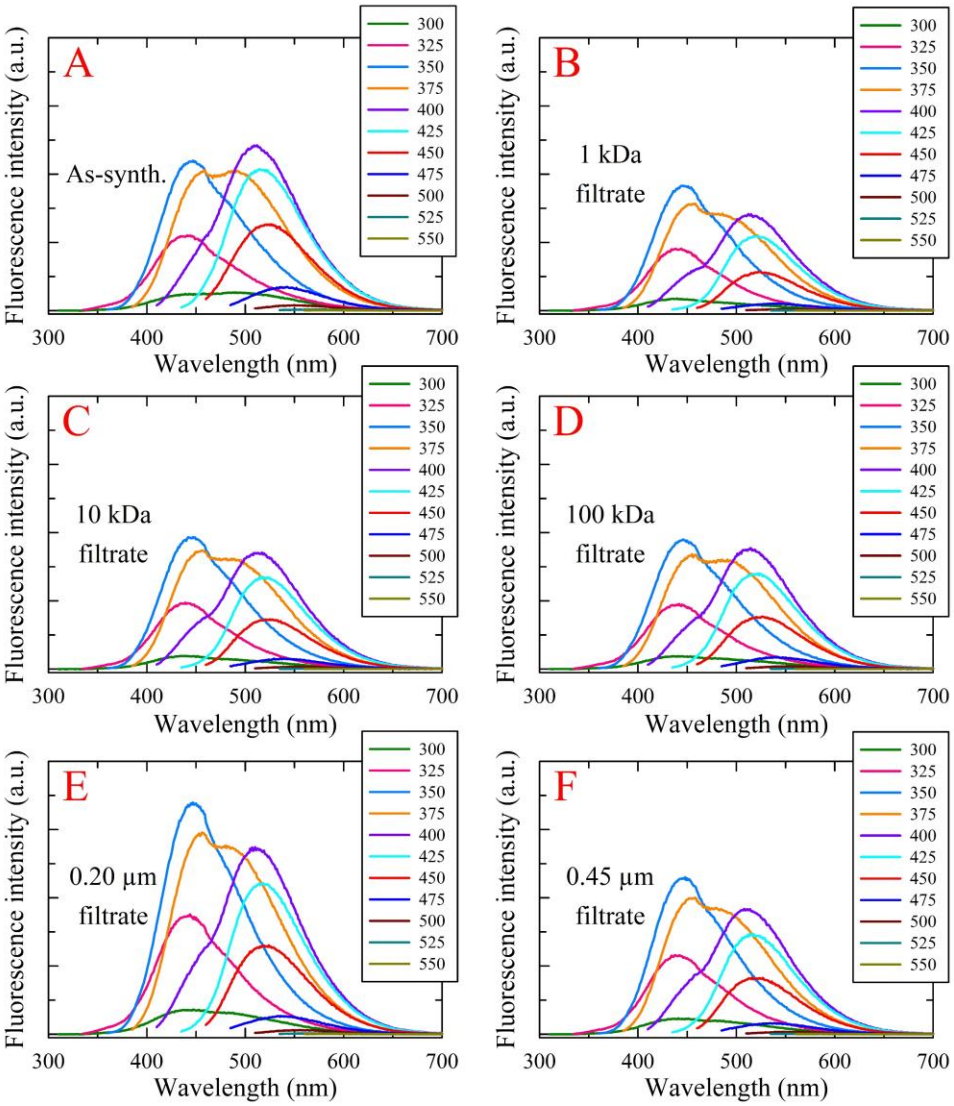

Figure C.1 Excitation wavelength-dependent emission of the microwave-generated, CA–U-derived (A) as-synth. sample and its filtrate fractions after ultrafiltration with (B) 1 kDa, (C) 10 kDa, or (D) 100 kDa MWCO membranes or bulk filtration with syringe filters of (E) 0.20 µm or (F) 0.45 µm pore size. The excitation wavelength-dependent emission profiles of all filtrate fractions were essentially identical to those of the as-synthesized sample indicating that the small organic material (<1 kDa) that traverses the membrane is associated with the majority of the observed fluorescence. Further, these results highlight that the common practice of purifying solely with a syringe filter is entirely inadequate.

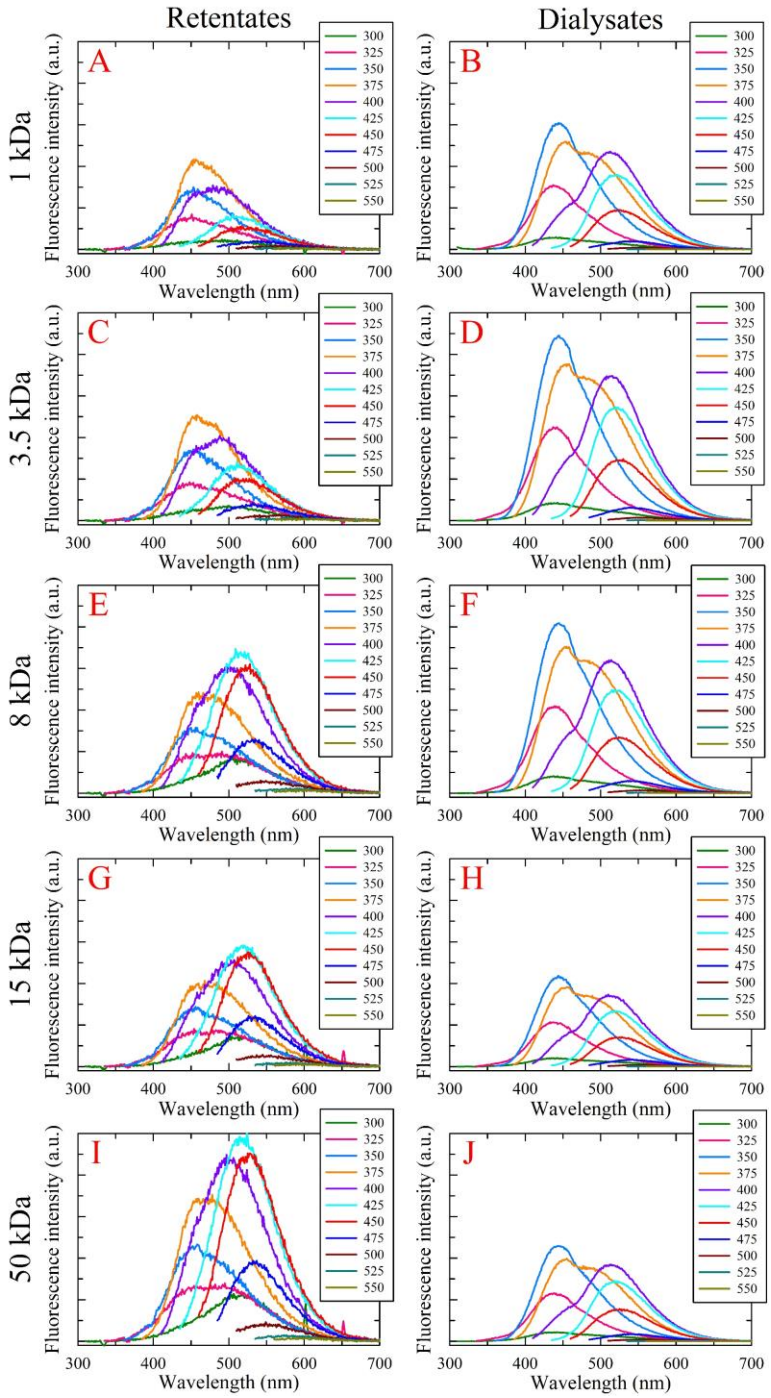

Figure C.2 Excitation wavelength-dependent emission of dialysis fractions stemming from membrane purification (MWCOs of 1, 3.5, 8, 15, and 50 kDa) of the CA–U-derived, microwave-generated sample, specifically the (A, C, E, G, and I) retent. and (B, D, F, H, and J) dial. fractions. Within each respective category (*i.e.*, retent., dial.), the fractions displayed similar spectral characteristics to one another regardless of the membrane MWCO employed; however, the emission profiles in cross-category comparisons were

markedly different, alluding to the existence of at least two distinct populations of fluorophores. Even further, when the emission was collected on fractions “normalized” to similar absorbance values in the near-UV region, the retent. fractions presented drastically lower emission intensities compared to the dial. fractions. That is, the y-axis maxima of the retent. emission plots are an order of magnitude lower than the maxima used for the plots of the dial. emission; the data were plotted as such to better show the spectral features of the retent. fractions. These results indicate that the retent. fractions, which should contain the desired FCDs (if present), are not nearly as fluorescent as once thought and that the majority of the fluorescence arises from small molecular species (<1 kDa) that permeate the membrane.

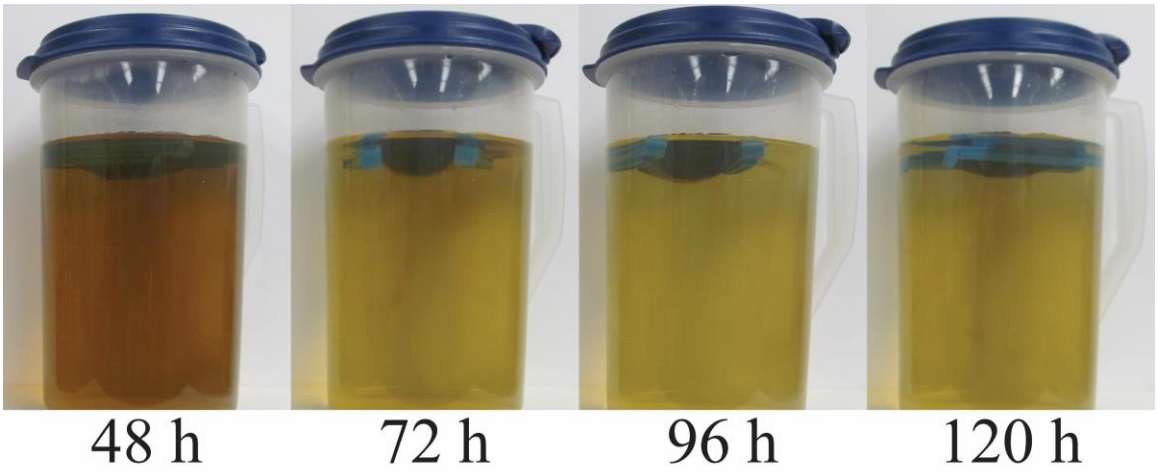

Figure C.3 Sequence of photographs showing the progress of dialysis for a microwave-generated, CA–U-derived sample after 48, 72, 96, and 120 h of dialysis. The images were collected immediately before replenishing the exchange solvent (*i.e.*, ultrapure water). These results highlight the sheer quantity of small molecular material (<1 kDa) that continues to permeate the membrane even after four additional 24 h dialysis periods against fresh exchange solvent.

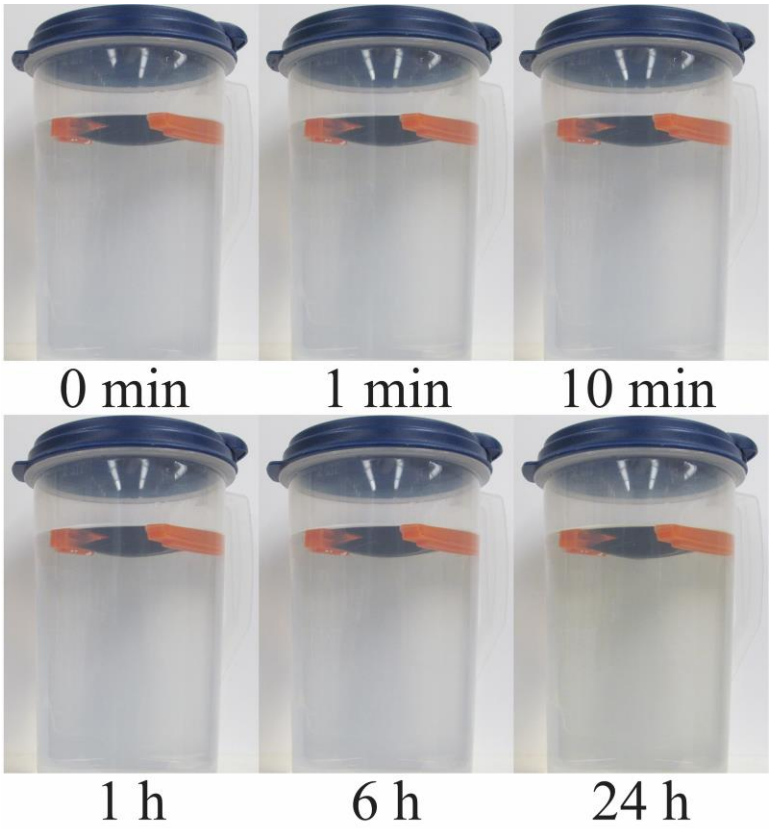

Figure C.4 Sequence of photographs showing the dialysis progression of a 1 kDa CA–U retent. fraction dialyzed with a 50 kDa MWCO membrane. That is, the retent. fraction employed in this study was a microwave-generated, CA–U-derived parent (as-synth.) sample that had previously been extensively dialyzed with a 1 kDa MWCO membrane. These images further highlight that the resulting product consists of two size-disparate species: one less than 1 kDa (*e.g.*, molecular/polymeric material) and the other greater than 50 kDa (*e.g.*, FCDs).

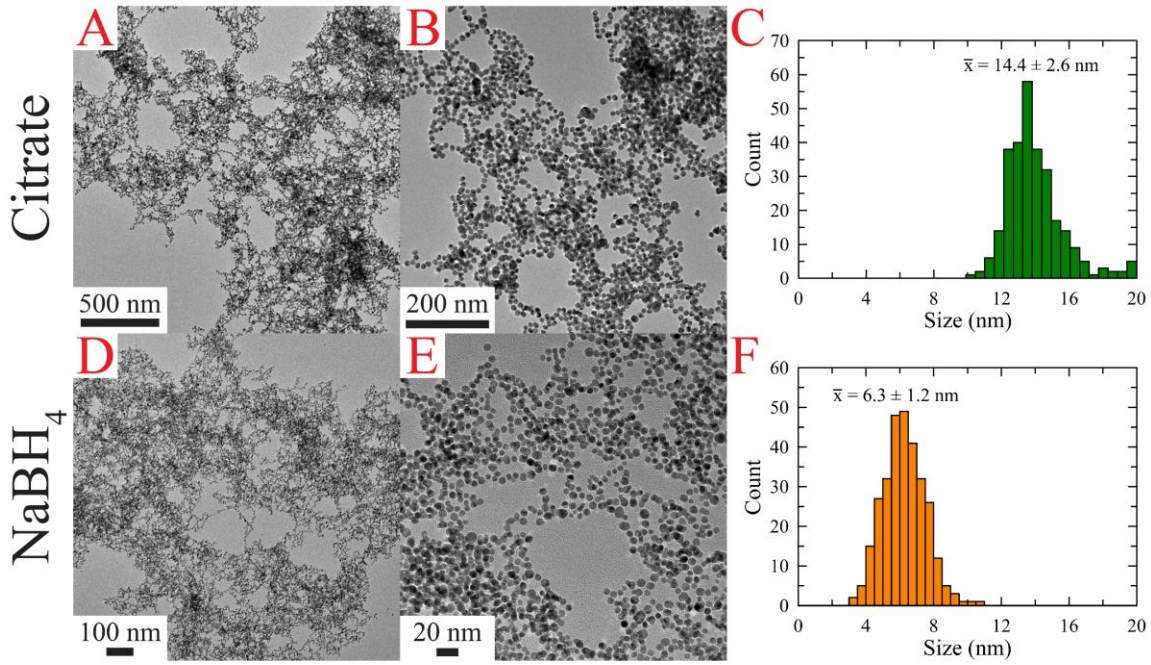

Figure C.5 Representative TEM micrographs of (A–B) citrate- and (D–E) $NaBH_4$-stabilized Au NPs. Corresponding histograms from the size analysis of the citrate- and $NaBH_4$-stabilized Au NPs are shown in panels C and F, respectively. The Au NPs were employed as a convenient means to clarify nanoscale membrane permeability for a given MWCO.

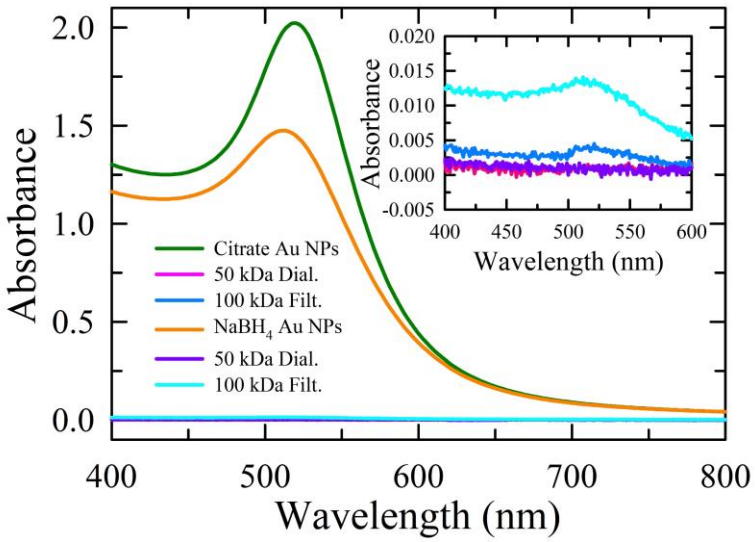

Figure C.6 UV-vis spectra of the dialysate (dial.) and ultrafiltration (filt.) fractions of the 14 nm citrate-stabilized and 6 nm $NaBH_4$-stabilized Au NPs compared to their parent (nonpurified) solutions. These benchmark experiments reveal that neither Au NP samples permeate the 50 kDa dialysis membrane, whereas minute quantities of both Au NP sizes pass through the 100 kDa ultrafiltration membrane, with the larger citrate-stabilized Au NPs mobilizing to a lesser extent. The inset panel is a magnified plot of the spectra for the dialysate and filtrate fractions to better highlight these revelations.

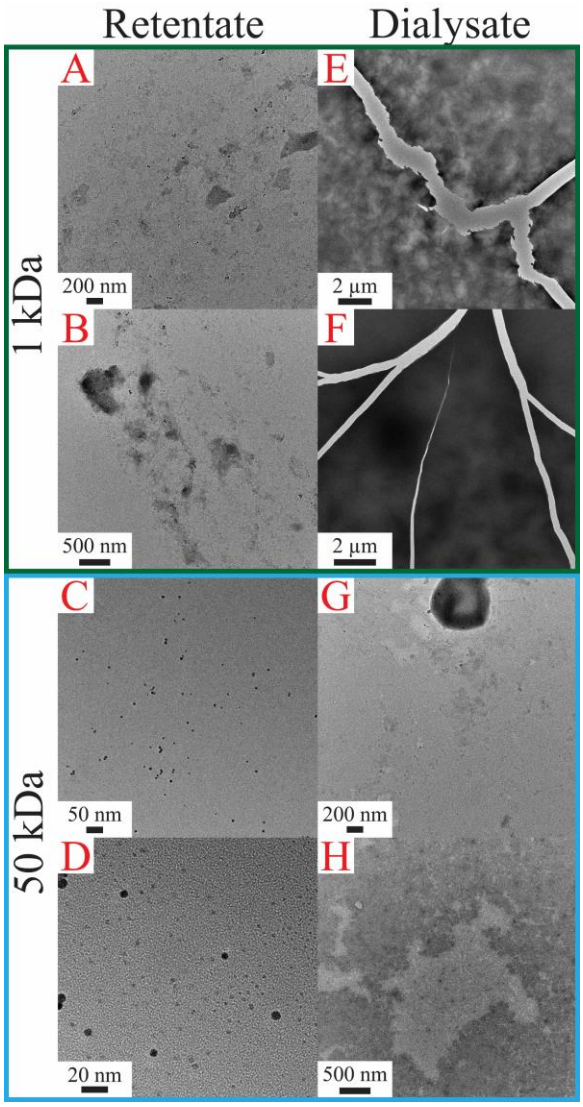

Figure C.7 Representative TEM micrographs of the (A, B, E, and F) 1 kDa and (C, D, G, and H) 50 kDa MWCO retent. (panels A–D) and dial. (panels E–H) fractions from dialysis of the microwave-generated, CA–U-derived material. Some FCDs were visible in the 1 kDa MWCO retent. fraction but proved difficult to image due to the large quantity of film-forming, molecular by-products still present. Contrarily, FCDs were more prominent in the 50 kDa retent. fraction and were more easily imaged due to fewer (or no) by-product impurities still contaminating the fraction. However, some apparent FCDs were visible in the 50 kDa MWCO dial. fraction indicating that, in general, dialysis may be less than ideal due to the difficulty in segregating the target FCDs from molecular (oligo- or polymeric) by-products, a scenario worsened by the potential for small, organic fluorophores to form supramolecular aggregates that resemble FCDs under TEM imaging.

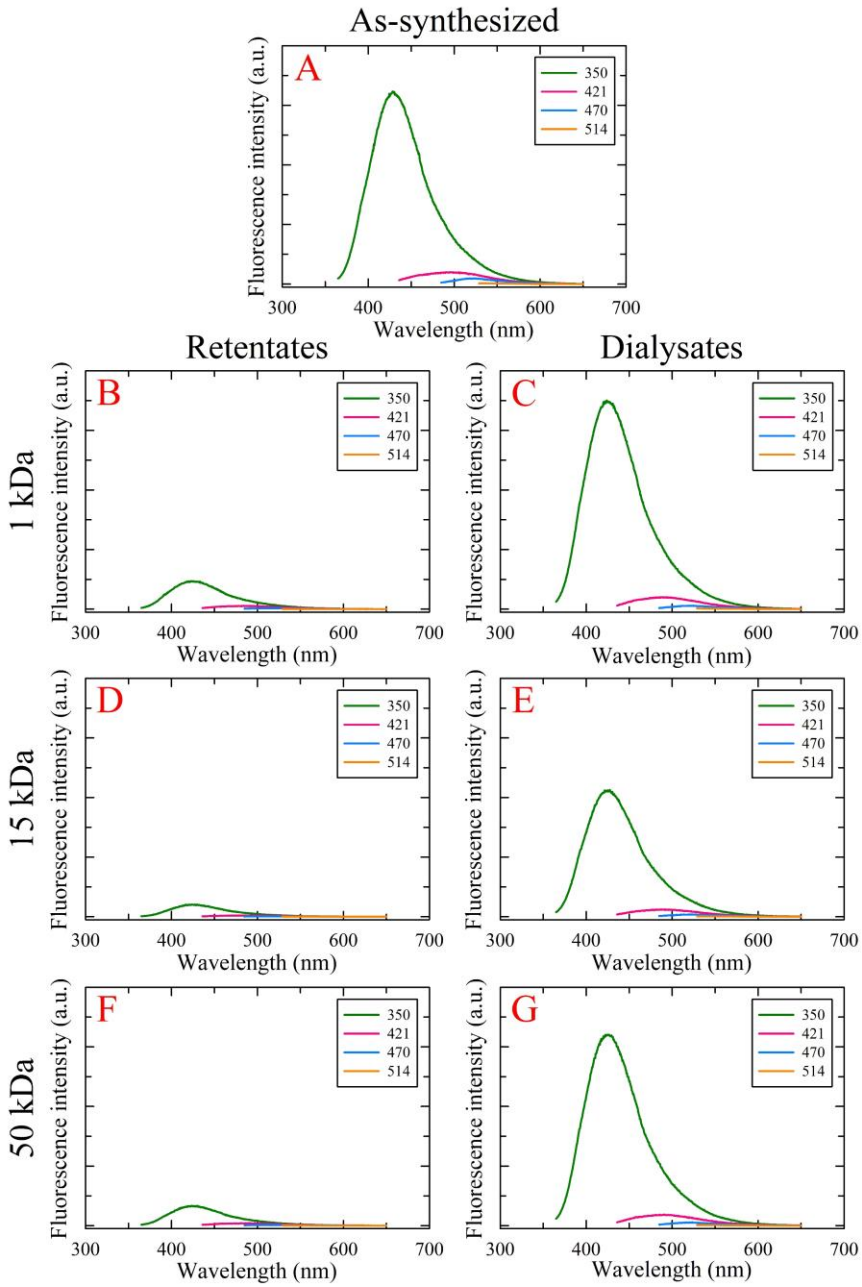

Figure C.8 Excitation wavelength-dependent emission of the hydrothermally treated, Arg-derived (A) as-synth. sample and its corresponding (B, D, and F) retent. and (C, E, and G) dial. fractions arising from the membrane MWCO-dependent dialysis study. All fractions had similar spectral characteristics to one another; however, the emission of the retent. fractions was drastically lower despite all fractions possessing similar absorbance values in the near-UV region. These results, in combination with the fluorescence quantum yield data (Figure C.10), further iterate that the majority of the photoluminescence arises from small molecular species (<1 kDa) and not FCDs.

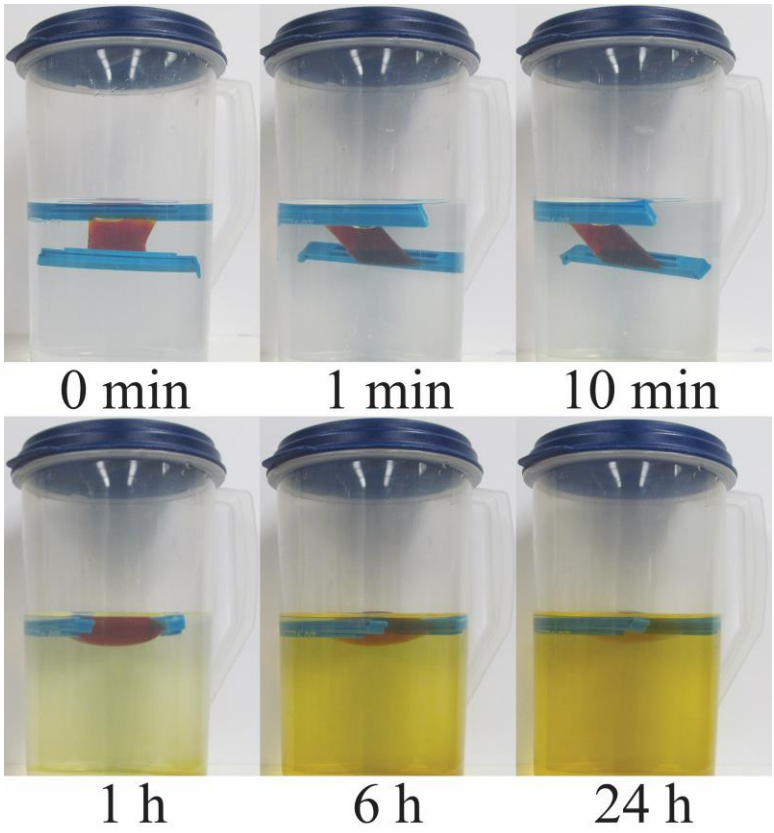

Figure C.9 Sequence of photographs showing the dialysis progression of a hydrothermally treated, Arg-derived sample dialyzed with a 1 kDa MWCO membrane. The continued mobilization of material through the membrane out to 24 h further highlights that a single dialysis treatment of <24 h is wholly insufficient to fully fractionate the target FCDs from small molecular by-products.

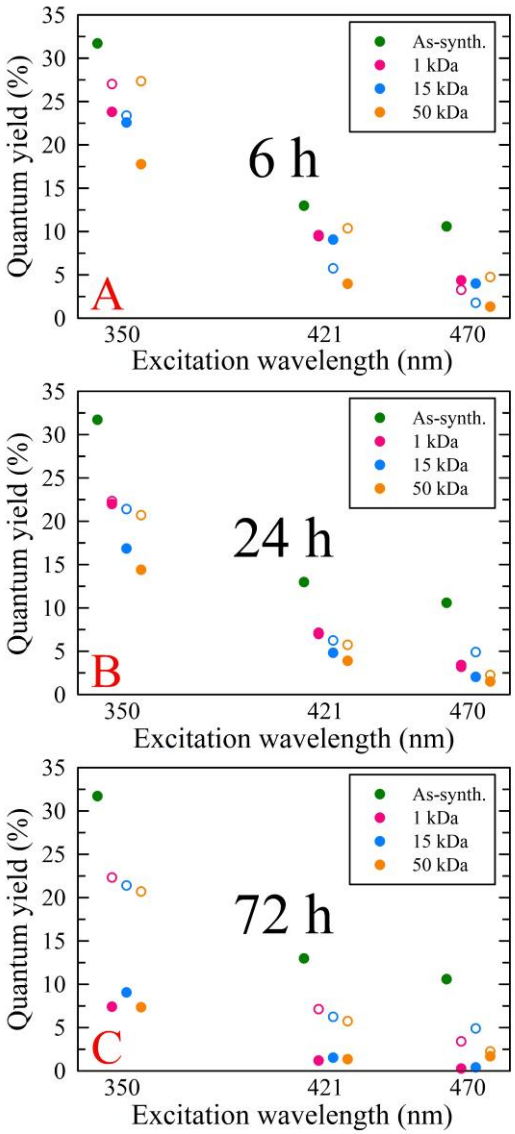

Figure C.10 Wavelength-dependent fluorescence quantum yields of hydrothermally synthesized, Arg-derived as-synth. samples and their corresponding retent. (closed circles) and dial. (open circles) fractions after dialysis for (A) 6 h and (B) 24 h with 1, 15, or 50 kDa MWCO membranes. Panel C compares the measured fluorescence quantum yields of the 24 h dial. fractions to those determined for retent. fractions after an additional 48 h of dialysis (72 h in total with the exchange solvent replenished every 24 h). The results clearly show that 6 h of dialysis is insufficient, as evidenced by the quantum yields of the retent. fractions continually decreasing with longer dialysis periods, trends that further support the notion that the majority of the observed fluorescence of the as-synth. sample originates from material constituting the dial. fraction (*i.e.*, by-products).

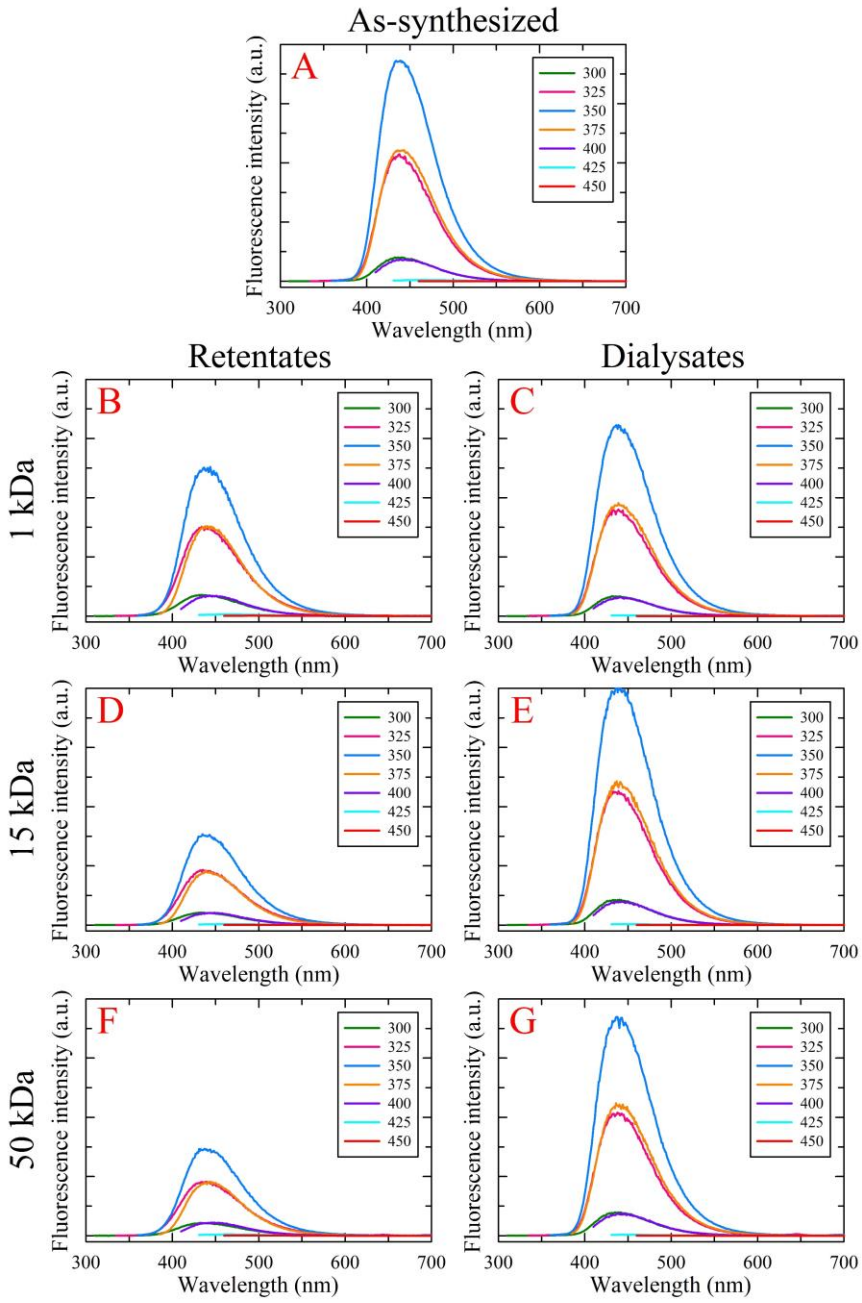

Figure C.11 Excitation wavelength-independent emission of hydrothermally treated, CA–EDA-derived (A) as-synth. samples and their corresponding (B, D, and F) retent. and (C, E, and G) dial. fractions from the membrane MWCO-dependent dialysis study. All fractions had similar spectral characteristics to one another although the emission of the retent. fractions was drastically lower even for samples with comparable absorbance values. These trends are consistent with the other systems explored in this work and, again, allude to small molecular species (<1 kDa) accounting for the majority of observed emission.

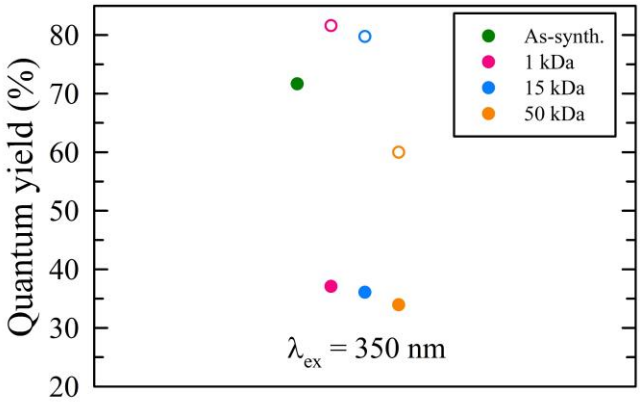

Figure C.12 Fluorescence quantum yields of a hydrothermally synthesized, nonpurified CA–EDA-derived sample (*i.e.*, as-synth.) and its corresponding 72 h retent. (closed circles) and 24 h dial. fractions (open circles). The results are consistent with all other dialysis studies and clearly show that the retent. fractions consist of less photoluminescent species, whereas the majority of the fluorescence of the as-synth. sample originates from species comprising the dial. fractions. The excitation wavelength (λ_{ex}) employed for these quantum yield assessments was 350 nm for all fractions.

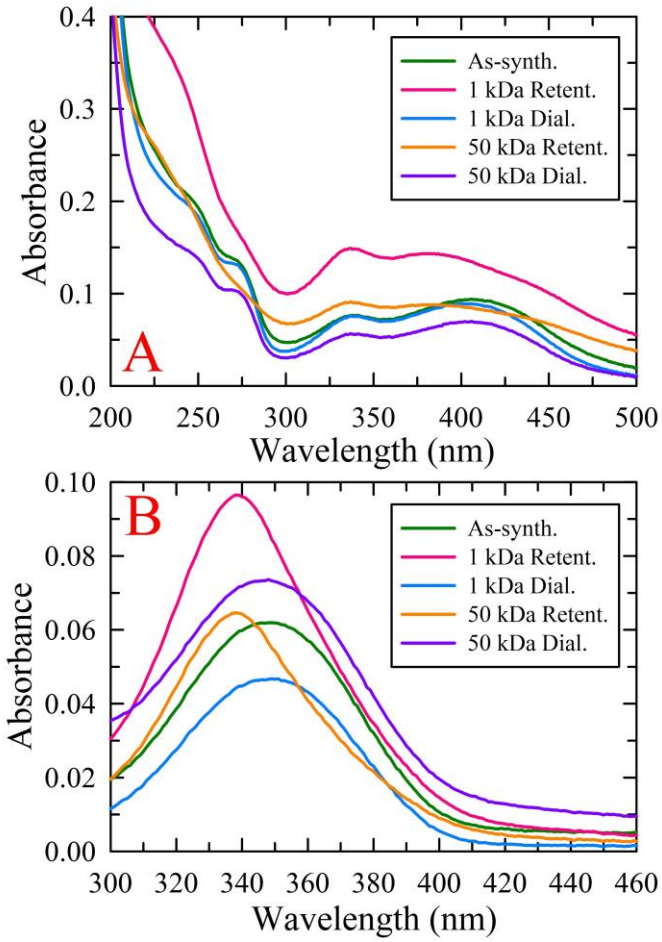

Figure C.13 UV-vis spectra of as-synth. samples from syntheses that employed (A) CA–U or (B) CA–EDA as precursors, as well as the spectra of their corresponding retent. and dial. fractions that were obtained after dialysis of the as-synth. samples with 1 or 50 kDa MWCO membranes. Stark spectral differences between the retent. and dial. fractions were evident, where the latter fractions displayed identical features to their corresponding as-synth. sample, indicating that the species constituting the dial. fractions dominate the observed spectral properties of their respective parent, as-synth. sample.

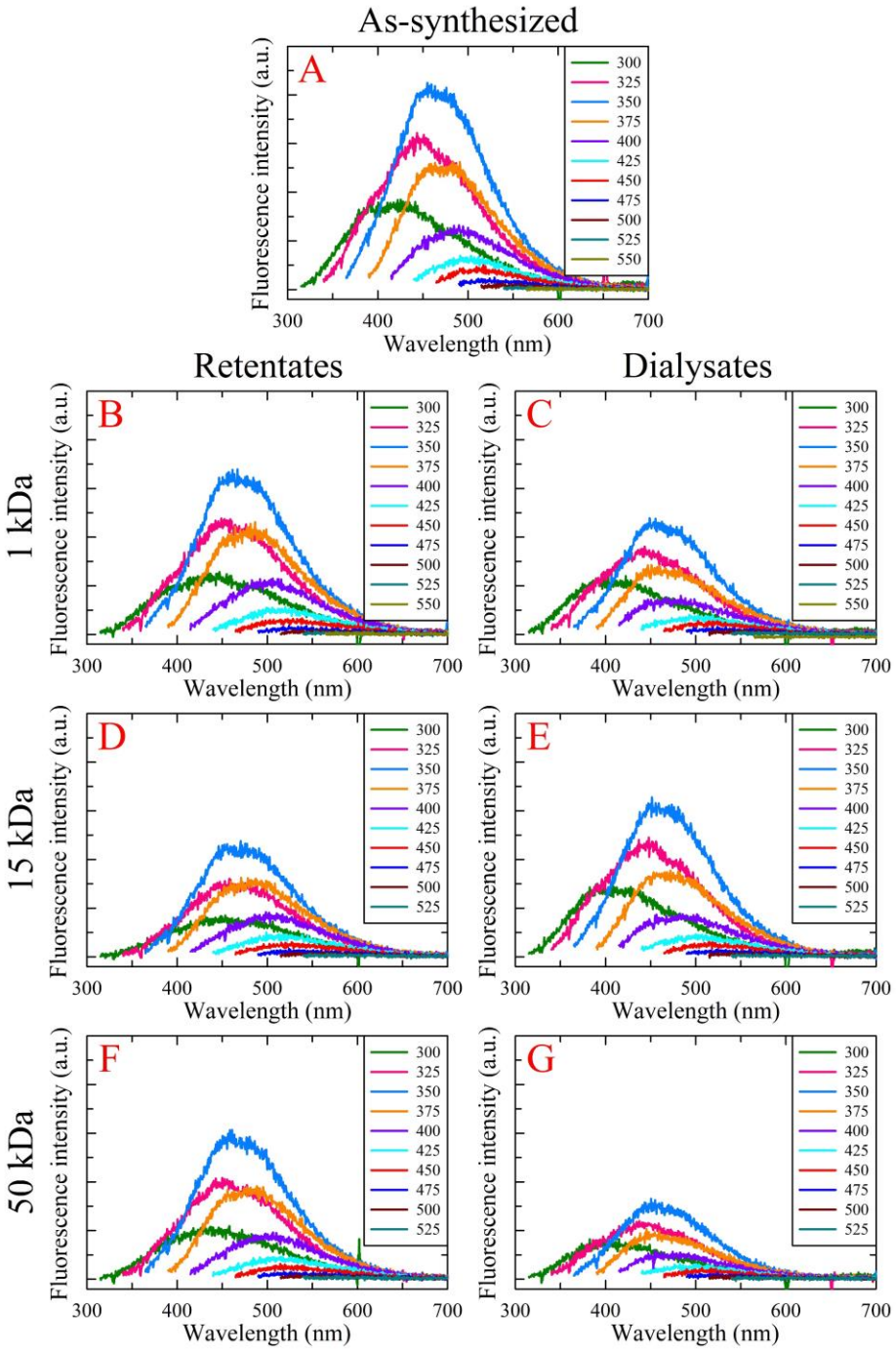

Figure C.14 Excitation wavelength-dependent emission of an electrochemically produced, graphite-derived (A) as-synth. sample and its corresponding (B, D, and F) retent. and (C, E, and G) dial. fractions obtained from a membrane MWCO-dependent (1, 15, and 50 kDa) dialysis study. While all fractions had similar spectral characteristics to one another, the results highlight that top-down approaches are not exempt from purification due to small photoluminescent by-products generated in situ during FCD synthesis.

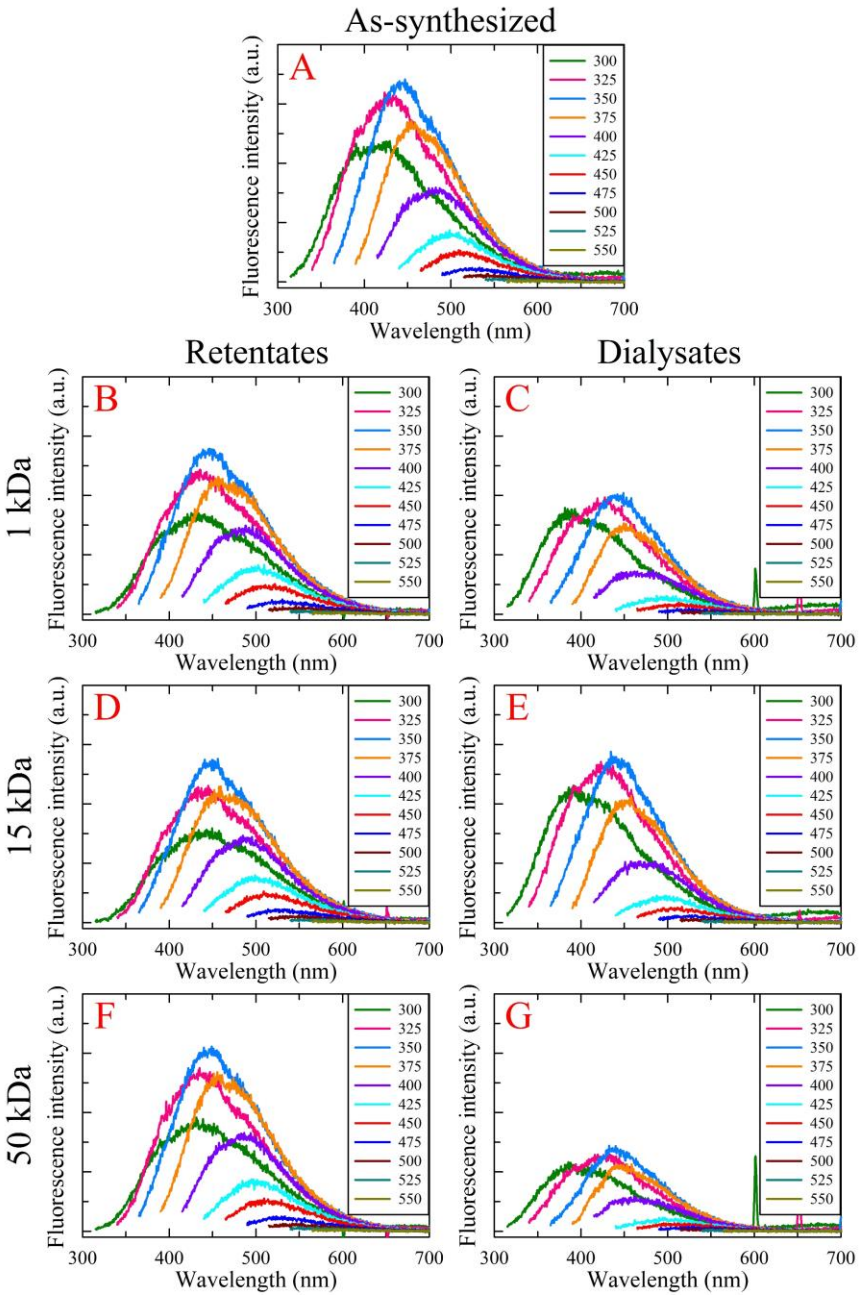

Figure C.15 Excitation wavelength-dependent emission of a (A) hydrothermally PEG-N-functionalized (1.5 kDa) sample and its corresponding (B, D, and F) retent. and (C, E, and G) dial. fractions obtained from a membrane MWCO-dependent (1, 15, and 50 kDa) dialysis study. These results highlight that the products from FCD functionalization reactions are not solely comprised of passivated FCDs but also contain small fluorescent molecular species (<1 kDa), thus indicating that postfunctionalization purification is an absolute necessity. Note, the parent sample employed in this study was electrochemically synthesized from graphite rods.

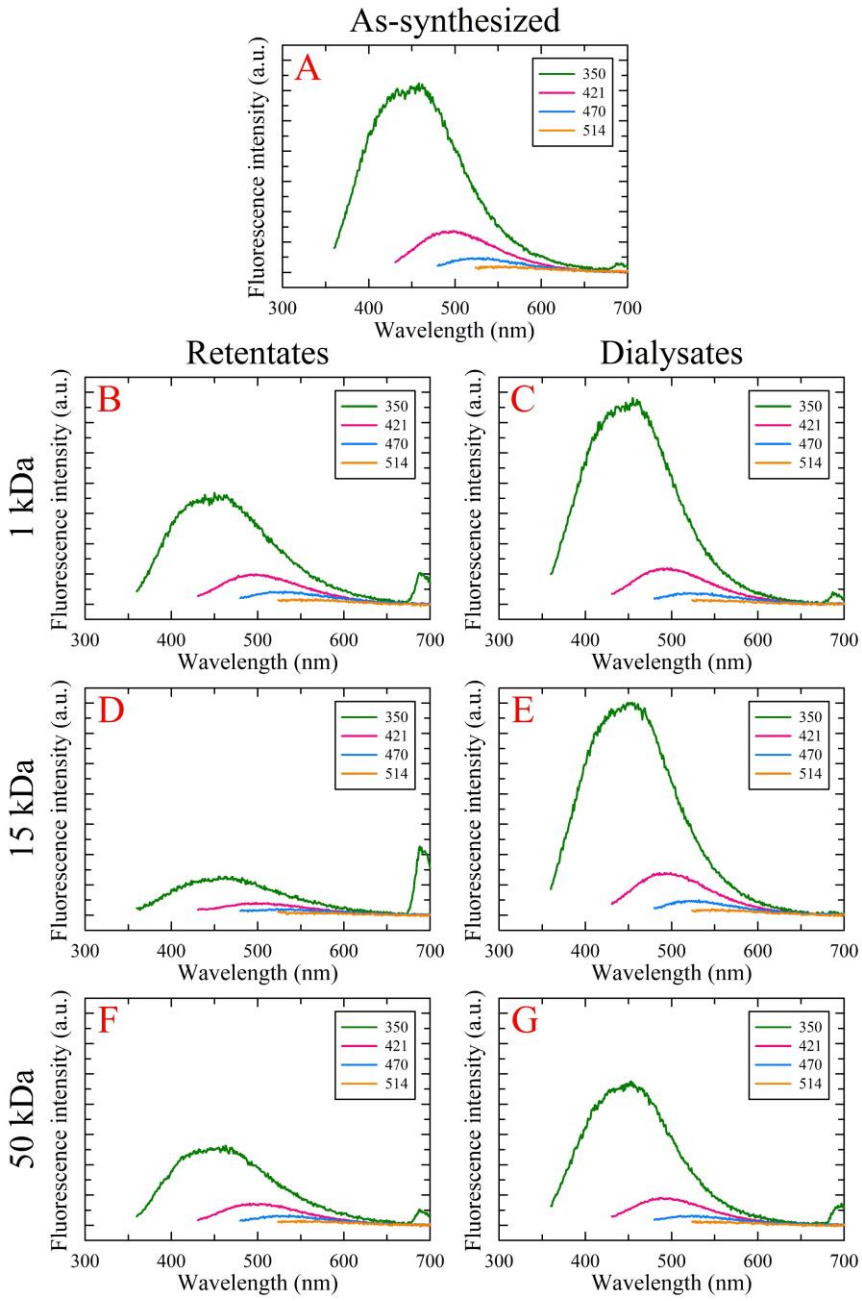

Figure C.16 Excitation wavelength-dependent emission of a (A) hydrothermally PEI-functionalized (1.2 kDa) sample and its corresponding (B, D, and F) retent. and (C, E, and G) dial. fractions obtained from a membrane MWCO-dependent (1, 15, and 50 kDa) dialysis study. Consistent with the fluorescence results obtained from the dialysis study of the PEG-N-functionalized sample, these results further reveal that postfunctionalization purification is essential to adequately separate the putatively functionalized FCDs from molecular (oligo- or polymeric) by-products. Note, the parent sample employed in this study was electrochemically synthesized from graphite rods.

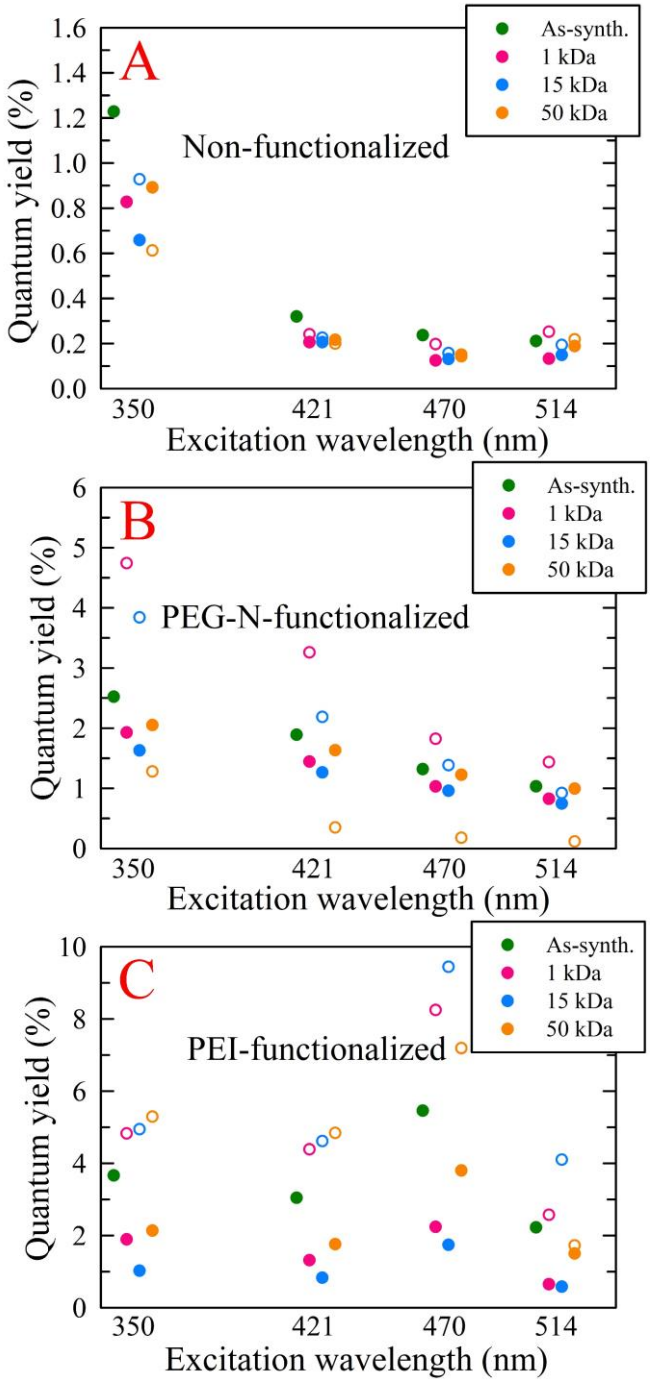

Figure C.17 Excitation wavelength-dependent fluorescence quantum yields assessed for the (A) electrochemically synthesized (non-functionalized), (B) PEG-N-functionalized (1.5 kDa), and (C) PEI-functionalized (1.2 kDa) materials, as well as their respective retent. (closed circles) and dial. (open circles) fractions. The resultant values highlight that even for top-down syntheses and their subsequent functionalization, adequate purification is a necessity after the initial synthesis as well as postfunctionalization.

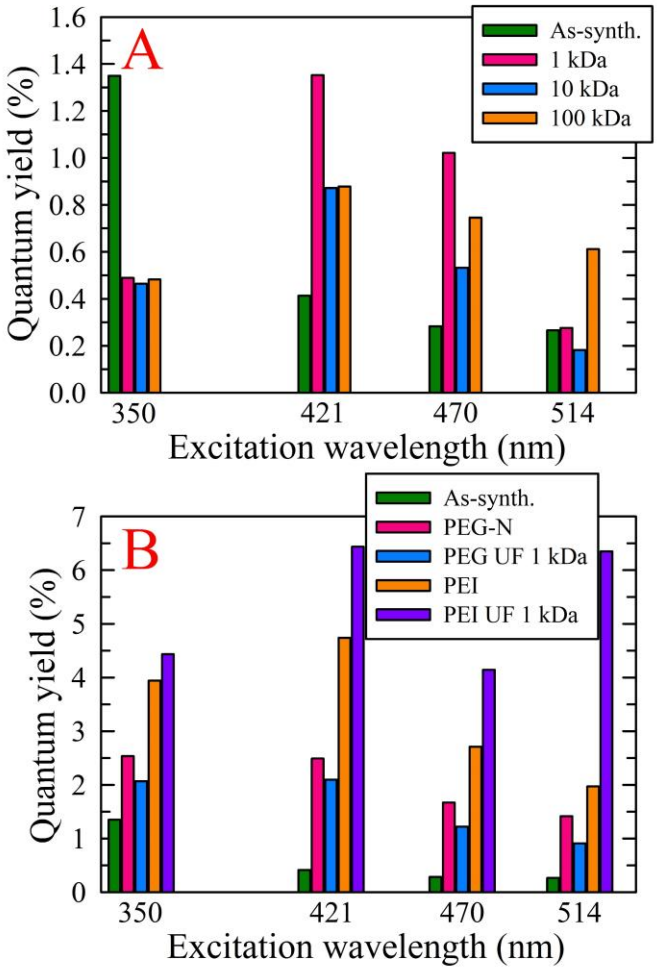

Figure C.18 (A) Excitation wavelength-dependent fluorescence quantum yields determined for an electrochemically synthesized (as-synth.) sample and its filtrate fractions obtained upon ultrafiltration (denoted by "UF") of the as-synth. sample with 1, 10, or 100 kDa MWCO membranes. The observed trends further highlight the need for adequate purification. (B) Excitation wavelength-dependent fluorescence quantum yields of the as-prepared PEG-N-functionalized (1.5 kDa) and PEI-functionalized (1.2 kDa) materials and their corresponding filtrate fractions after ultrafiltration with a 1 kDa MWCO membrane. The results clearly show that highly fluorescent by-products are indeed generated, necessitating fractionation from the target, functionalized FCDs. The excitation wavelength-dependent quantum yields of the electrochemically synthesized (as-synth.) parent sample are included in panel B for comparison.

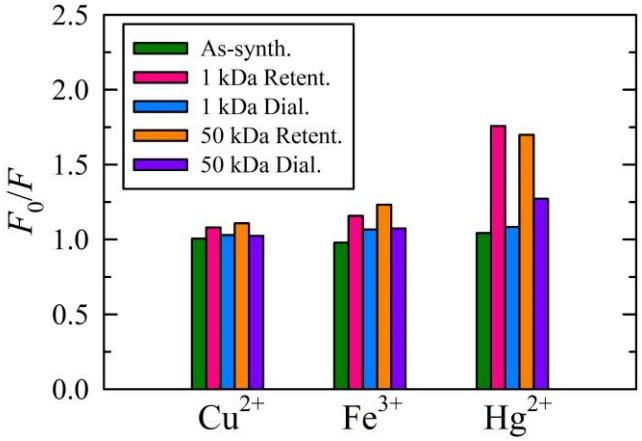

Figure C.19 Metal ion quenching studies of a hydrothermally treated, CA–EDA-derived as-synth. sample and its corresponding retent. and dial. fractions. In general, Cu^{2+} and Fe^{3+} induced little to no quenching for all fractions while Hg^{2+} quenched the emission of the retent. fraction more strongly than the as-synth. and dial. fractions. These results are consistent with the quenching studies of the microwave-generated CA–U-derived materials.

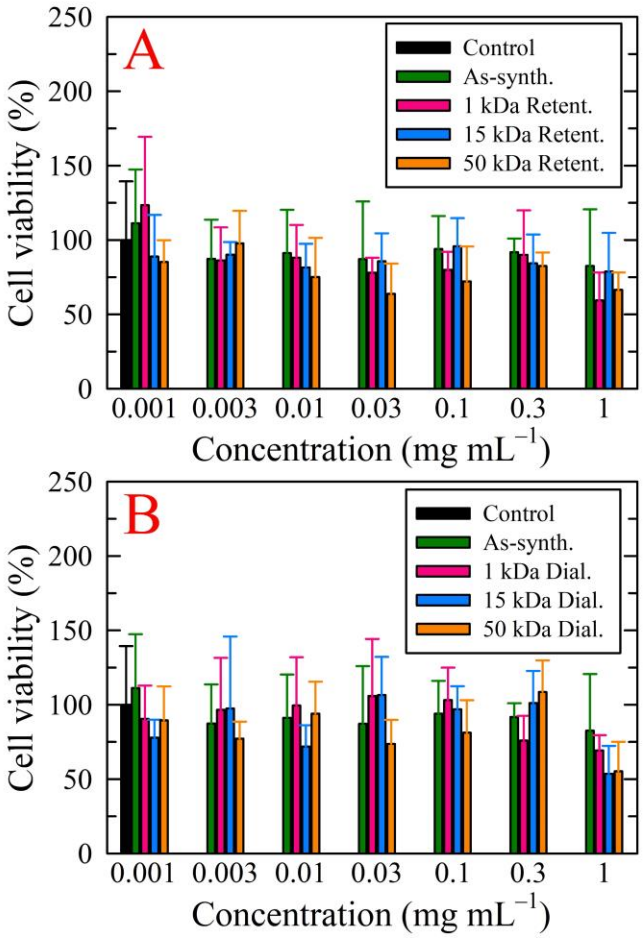

Figure C.20 Toxicity of microwave-generated, CA–U-derived (A) retent. and (B) dial. fractions toward mice embryonic fibroblasts. Although distinctive fraction- or membrane MWCO-dependent trends were not apparent for either fraction, minimal toxicity was observed for concentrations at or below 0.3 mg mL^{-1} while slight toxicities arose for concentrations of 1 mg mL^{-1}, regardless of the fraction. The toxicity of the as-synth., parent sample is provided in both panels for comparison.

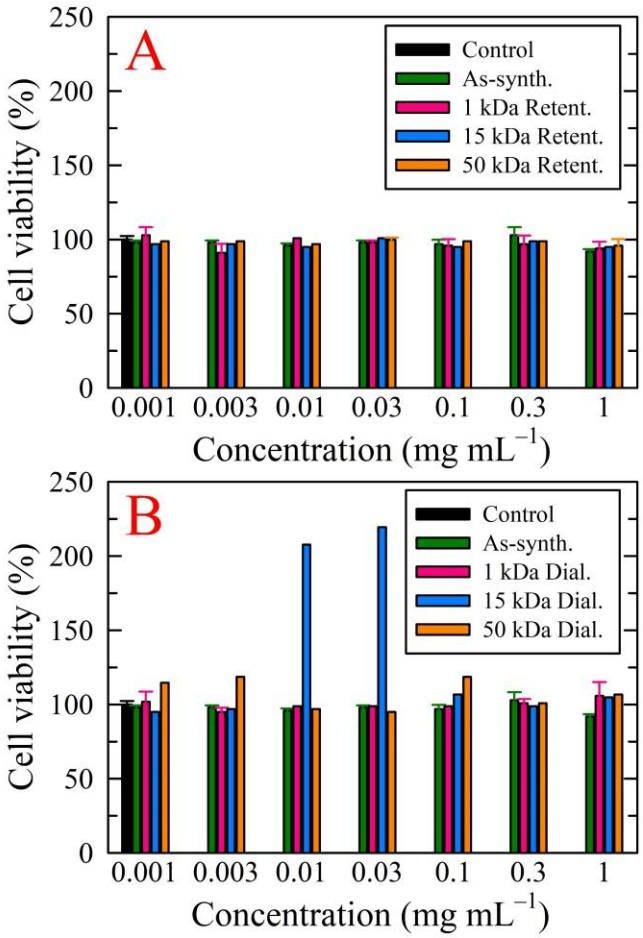

Figure C.21 Toxicity of microwave-generated, CA–U-derived (A) retent. and (B) dial. fractions toward human breast cancer cells (T-47D). Both retent. and dial. fractions for all membrane MWCOs studied had no toxic effects on this specific cell line. The toxicity of the as-synth., parent sample is provided in both panels for comparison.

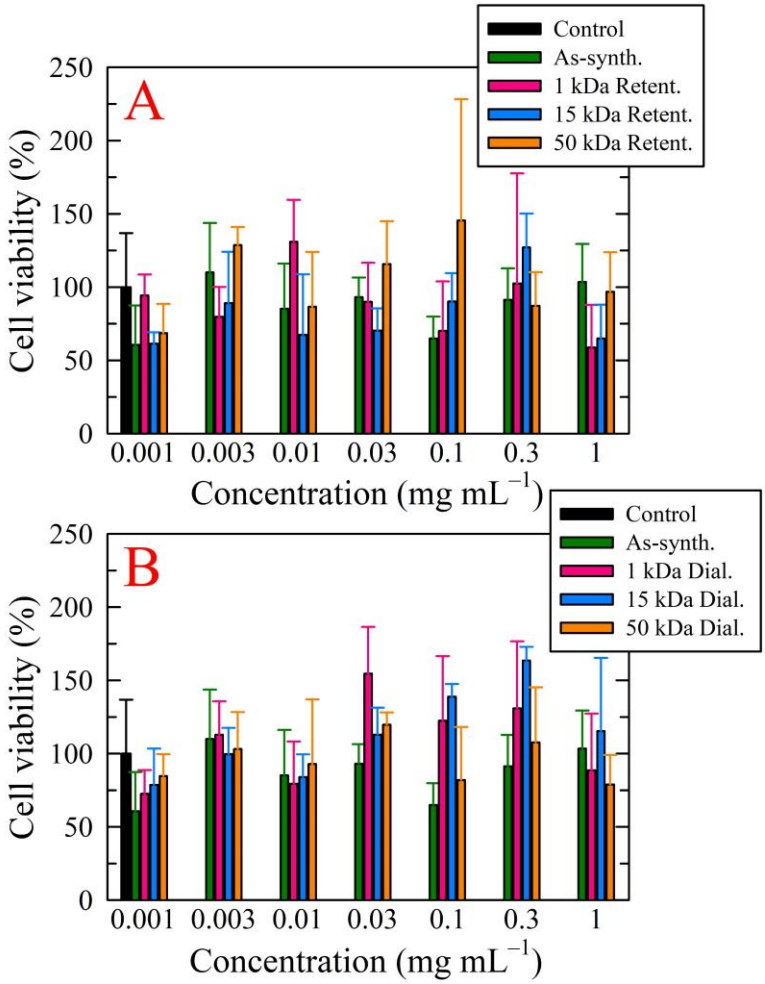

Figure C.22 Toxicity of microwave-generated, CA–U-derived (A) retent. and (B) dial. fractions towards HeLa cells. For this cell line, the fractions did not display any concentration-, membrane MWCO-, or fraction-dependent trends in toxicity. The toxicity of the as-synth., parent sample is provided in both panels for comparison.

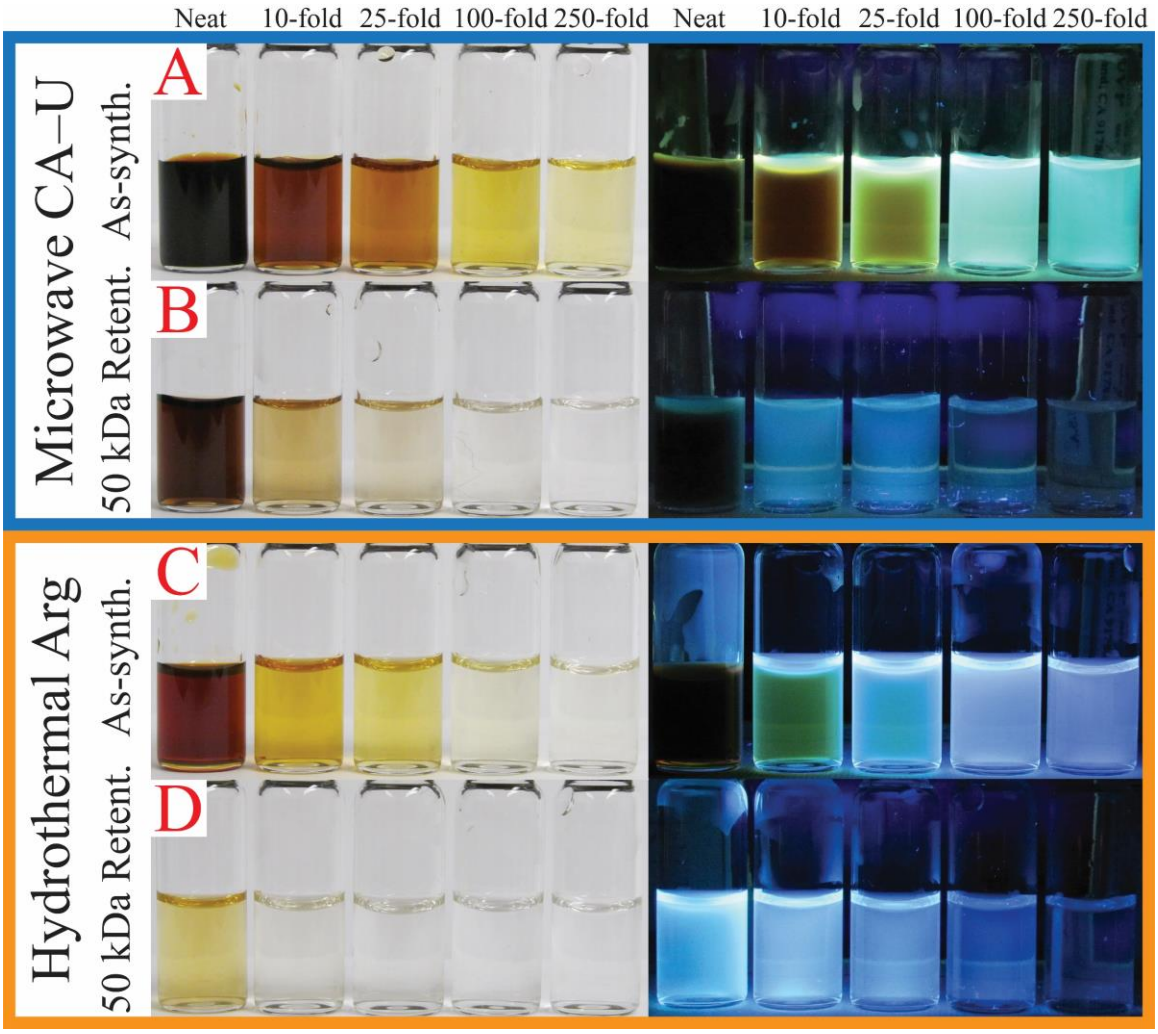

Figure C.23 Photographic comparison of (A and C) as-synth. samples to (B and D) 50 kDa retent. fractions for the (A–B) CA–U- and (C–D) Arg-derived materials under white light (left panels) and 354-nm UV light (right panels). This composite illustrates the misleading fluorescence results that arise when the samples are not properly diluted to a similar concentration (or absorbance value); that is, at higher concentrations, the samples will appear to fluoresce at longer (redder) wavelengths. However, this dubious observation is simply an artifact of the inner filter effect, arising from the (near complete) reabsorption of blue to green emission and the illumination of the already orange-, red-, or brown-colored solutions.

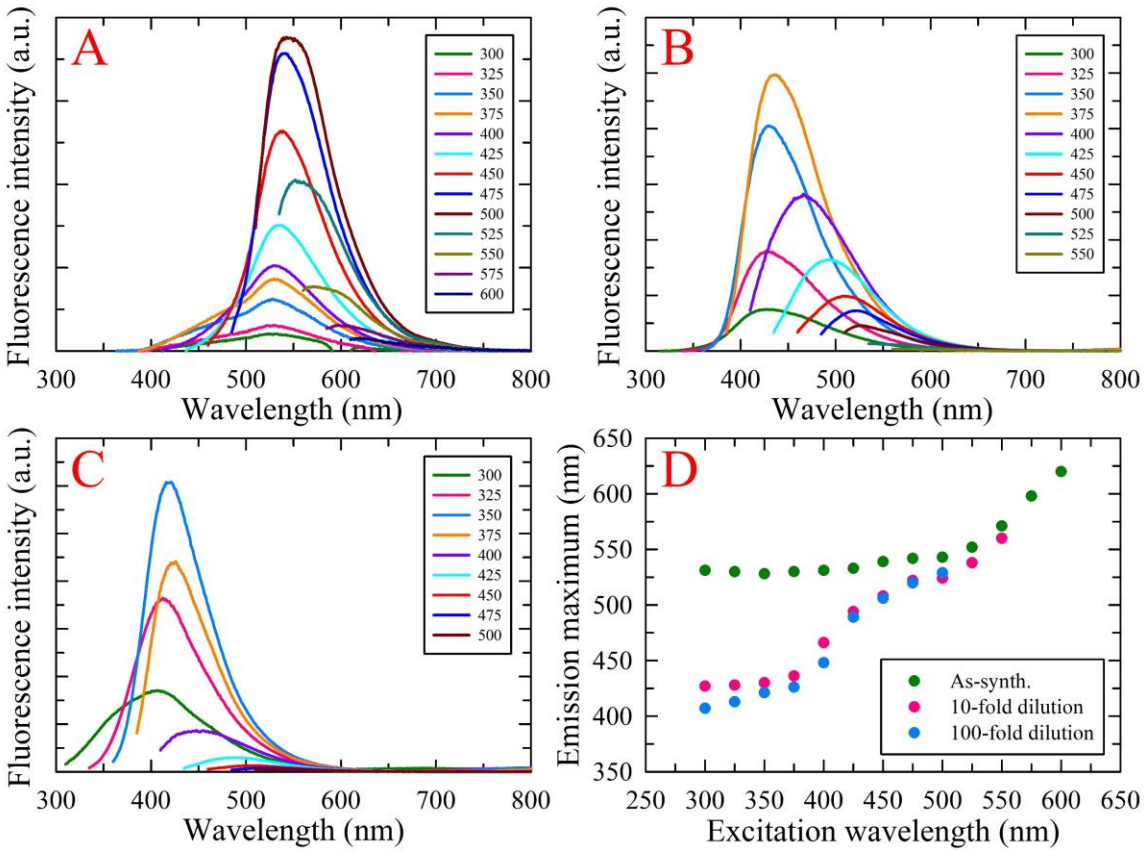

Figure C.24 Excitation wavelength-dependent emission spectra of a hydrothermally generated, Arg-derived (A) as-synth. sample as well as (B) 10-fold diluted and (C) 100-fold diluted solutions. The results appear to indicate that the fluorescence blueshifts as the sample is diluted, which might lead one to believe that the samples emit redder wavelengths with increasing concentration. However, this apparent bathochromic shift simply arises from inner filter effects that lead to attenuation of the intense blue edge and subsequently render the weakly emitting red edge the only emission visible. (D) Plotting the wavelength of maximum emission (extracted from panels A–C) as a function of the excitation wavelength further highlights the perceived but deceptive emission shift.

Appendix D: Supporting Figures and Analyses for Chapter 5

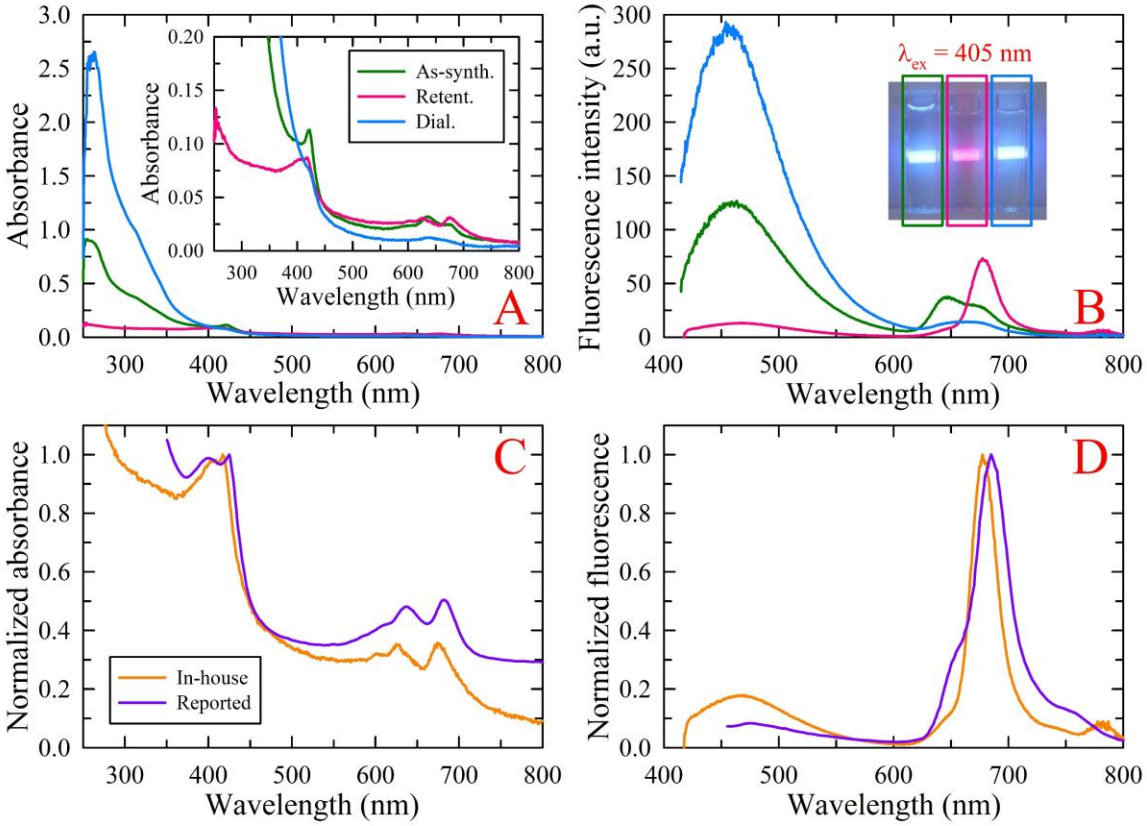

Figure D.1 (A) UV-vis and (B) fluorescence spectra of an as-synth. sample derived from GSH–F as well as its corresponding retent. and dial. fractions obtained after dialyzing with a 50 kDa MWCO membrane. The results further corroborate the need for adequate purification as the absorbance and emission profiles drastically change upon dialysis. Specifically, the as-synth. sample displays strong blue emission which decreased as the highly fluorescent by-products were removed leading to even stronger blue emission for the dial. fraction and the emergence of distinct red-emitting species (presumably FCDs) in the retent. fraction (see inset photograph). Normalized (C) absorbance and (D) fluorescence spectra of the retent. fractions compared to the results reported in the literature reveal the synthetic consistency of the published protocol. The data in panels C and D was reproduced with permission from reference 86 of Chapter 5. Copyright © 2019 Elsevier.

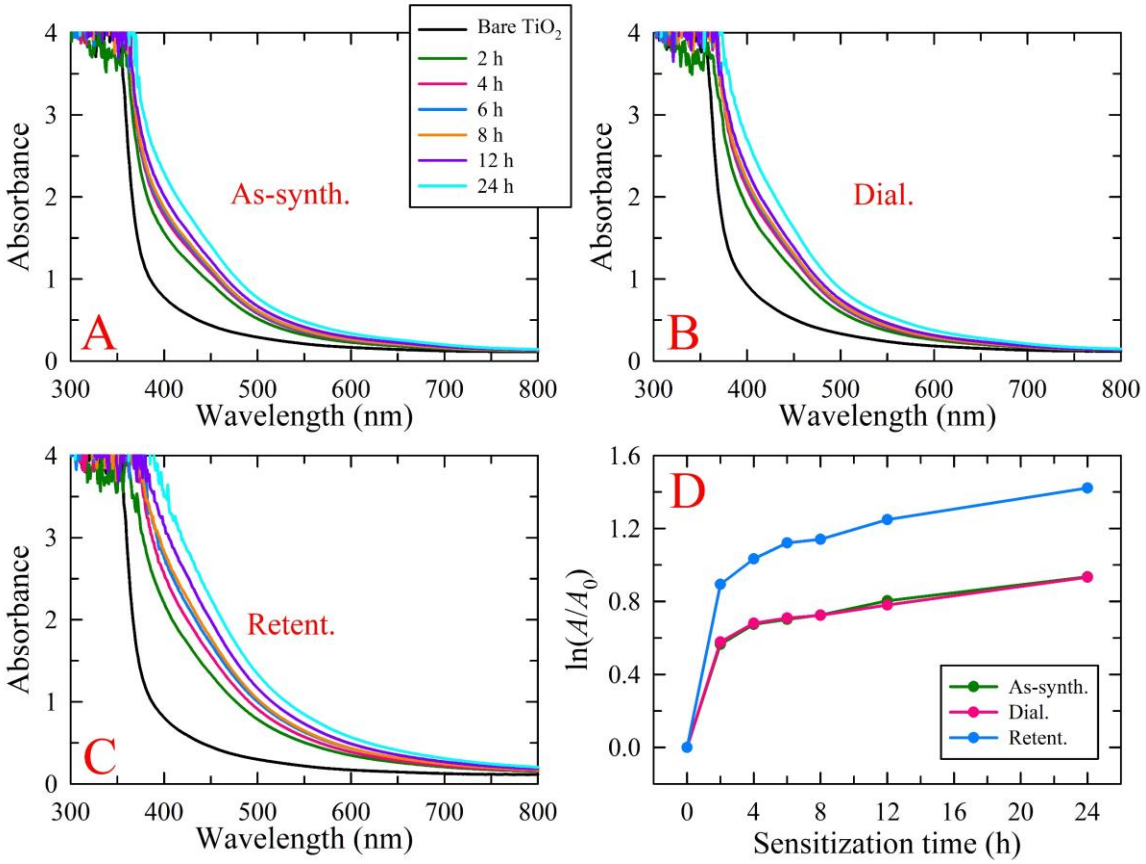

Figure D.2 Temporal uptake of 5 mg mL^{-1} CA–NH_4OH-derived (A) as-synth., (B) dial., and (C) retent. fractions (dispersed in acetone) by TiO_2 films, monitored with UV-vis spectroscopy. Panel D shows that the majority of uptake occurred within the first 2 h of sensitization with the retent. fraction showing higher apparent uptake, evidenced by more strongly absorbing films; however, this observation could arise from a larger extinction coefficient inherent to the adsorbed species. Additionally, continued but slowed uptake of the different fractions was observed after the initial, rapid adsorption during the first 2 h of sensitization. Given the spectral similarities between TiO_2 films sensitized with the as-synth. and dial. fractions, the species constituting the dial. fraction clearly account for the majority of the as-synth. product composition, materials that dominate adsorption and the resultant spectral features of the sensitized films.

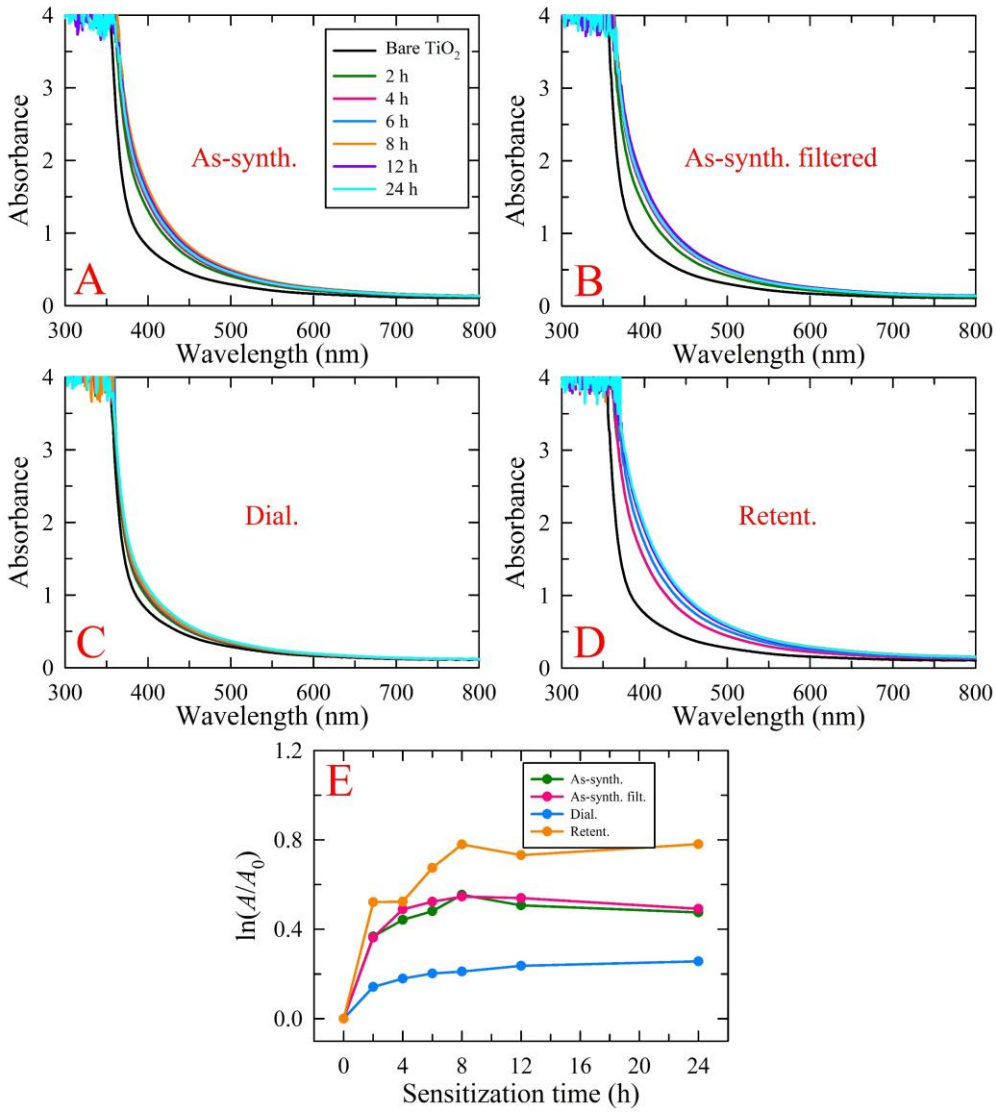

Figure D.3 Temporal uptake of 10 mg mL^{-1} Arg-derived (A) as-synth., (B) syringe-filtered as-synth. (as-synth. filt.), (C) dial., and (D) retent. fractions (dispersed in EtOH) by TiO_2 films, monitored with UV-vis spectroscopy. Panel E shows that over 50% of the sensitizer uptake occurred within the first 2 h of sensitization, however, appreciable uptake still occurred up to 12 h with minimal to no additional uptake occurring after 24 h of sensitization. In fact, the two as-synth. fractions showed a slight decrease from 12 to 24 h, indicating undesirable sensitizer desorption. These fractions, as well as the retent. fraction, also showed absorbance decreases from 8 to 12 h total sensitization time. The widely varying values of $\ln(A_t/A_0)$ for the studied fractions are attributed to drastically different extinction coefficients for the species comprising each fraction but could also arise from varying degrees of uptake.

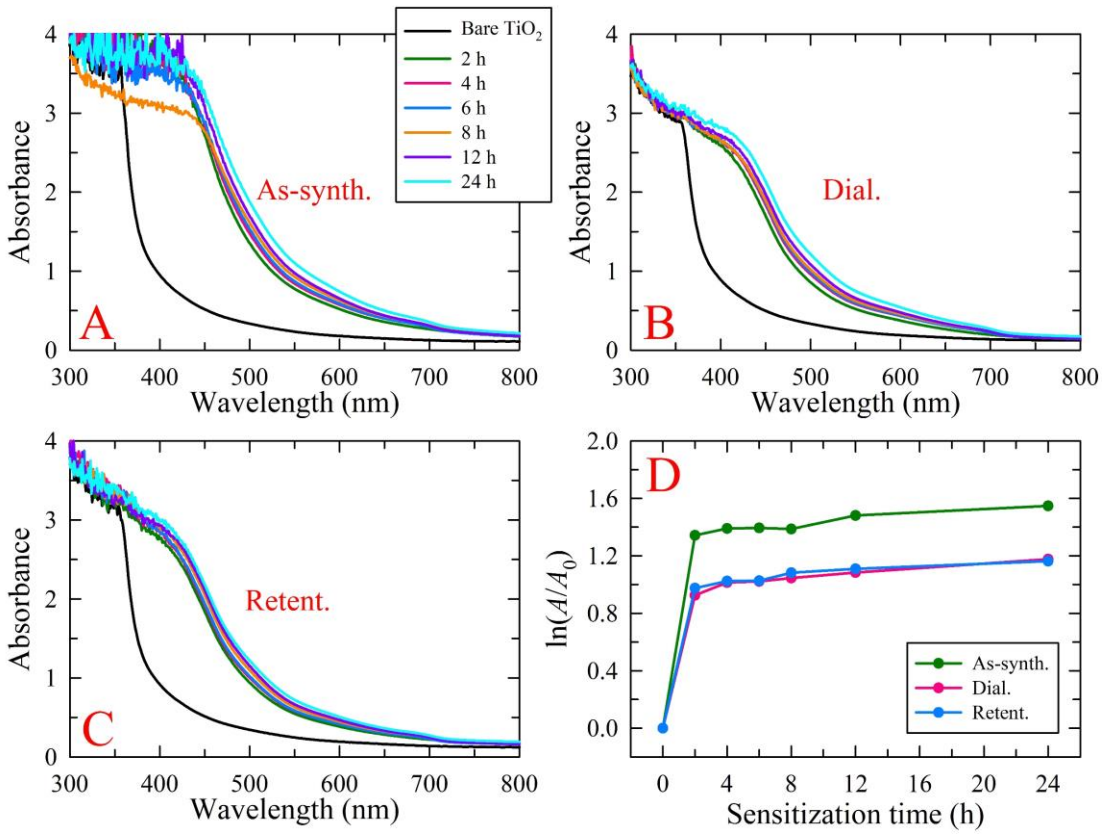

Figure D.4 Temporal uptake of aqueous 10 mg mL^{-1} CA–U-derived (A) as-synth., (B) dial., and (C) retent. fractions by TiO_2 films, monitored with UV-vis spectroscopy. Panel D shows that the majority of sensitizer uptake occurred within the first 2 h of sensitization with additional but minimal uptake occurring out to 24 h of total sensitization time. Interestingly, the dial. and retent. fractions showed almost identical uptake, both temporally and in terms of raw absorbance, while the as-synth. fraction showed a comparable trend in temporal uptake but yielded higher overall absorbance, the origin of which is currently unclear.

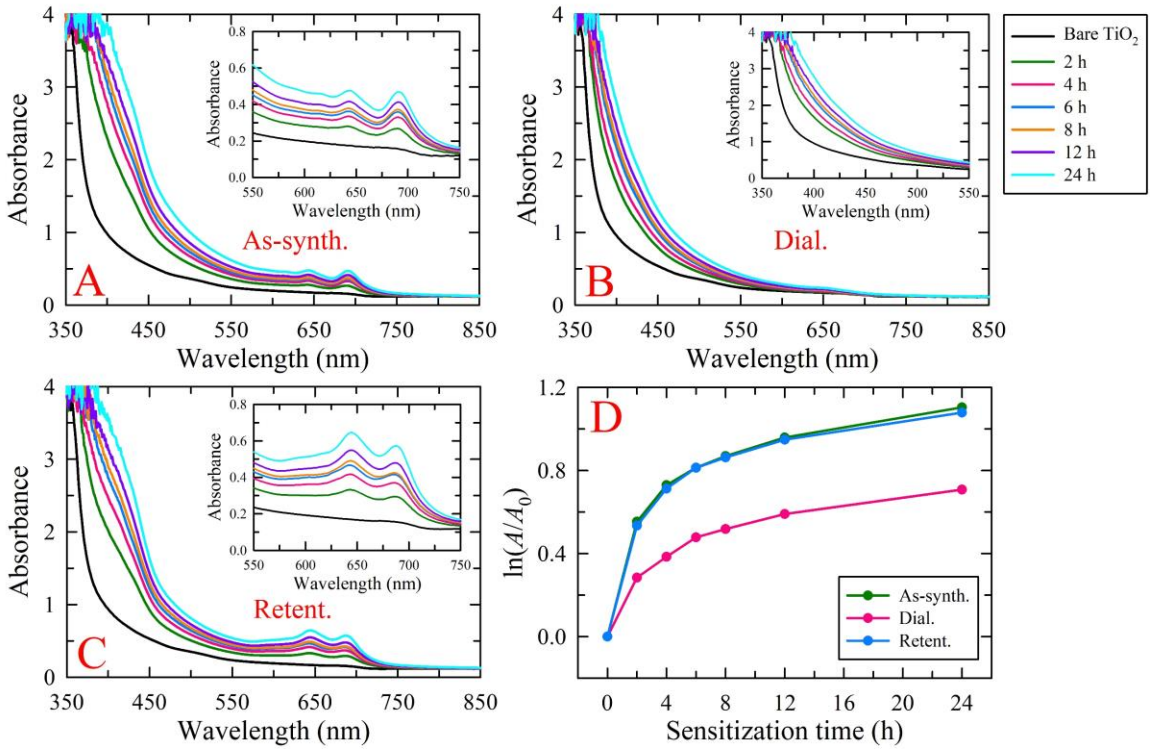

Figure D.5 Temporal uptake of GSH–F-derived (A) as-synth., (B) dial., and (C) retent. fractions by TiO_2 films, monitored with UV-vis spectroscopy. Note, the as-synth. and dial. fractions were dispersed in 50:50 vol% formamide:water at unknown concentrations while the retent. fraction was dispersed in 100% water at 10 mg mL^{-1}. Panel D shows that sensitizer uptake occurred rapidly within the first 4–6 h of sensitization and began to slow after 6 h but never fully levelled off, with sensitizing species still adsorbing out to 24 h of total sensitization time. Interestingly, the as-synth. and retent. uptakes were essentially identical despite the unknown concentration of the former, the different solvent systems employed, and the minor differences observed for the two fractions in their absorbance peaks between 600 and 750 nm. Additionally, substantially lower absorbance was observed for films sensitized in the dial. fraction, an occurrence that could stem from the concentration differences between the fractions since the concentration of the dial. fraction was not assessable due to residual formamide. However, given the stark differences in film color between the fractions (Figure D.20), the lower absorbance likely arises from markedly lower extinction coefficients for the species comprising the dial. fraction.

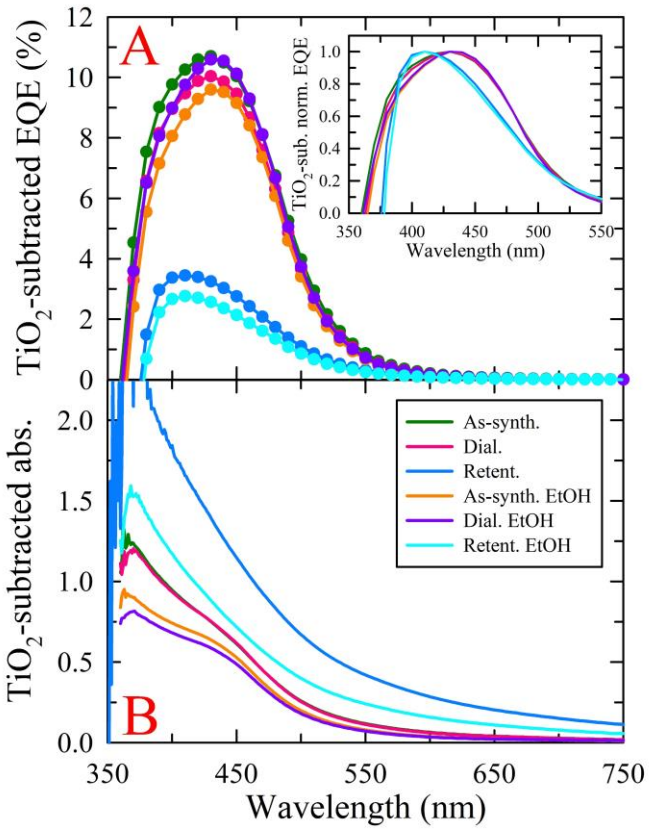

Figure D.6 TiO_2-subtracted (A) EQE and (B) absorbance (abs.) spectra of TiO_2 films that were sensitized in 5 mg mL^{-1} CA–NH_4OH-derived fractions in 100% acetone or 50:50 vol% acetone:ethanol (denoted by "EtOH"). The inset plot in panel A shows normalized (norm.) spectra for the TiO_2-subtracted (TiO_2-sub.) EQE spectra. Clearly, the photocurrent generated by species in the as-synth. fraction predominately originates from reaction by-products comprising the dial. fraction. Additionally, chromophoric but nonphotocurrent-generating, by-product species exist within the dial. fraction evidenced by lower absorbance for films sensitized in ethanolic solutions compared to those sensitized in 100% acetone yet the former films yielded comparable performance to the latter. Furthermore, the above results indicate that the photocurrent generated by the as-synth. and dial. fractions is likely produced by the species responsible for the shoulder observed at 450 nm in the absorbance spectra. Conversely, the retent. fractions generated substantially lower photocurrent despite having markedly higher absorbance. Moreover, the maximum EQE for the retent. fraction is hypsochromically shifted by 20 nm relative to the maxima observed for the as-synth. and dial. fractions.

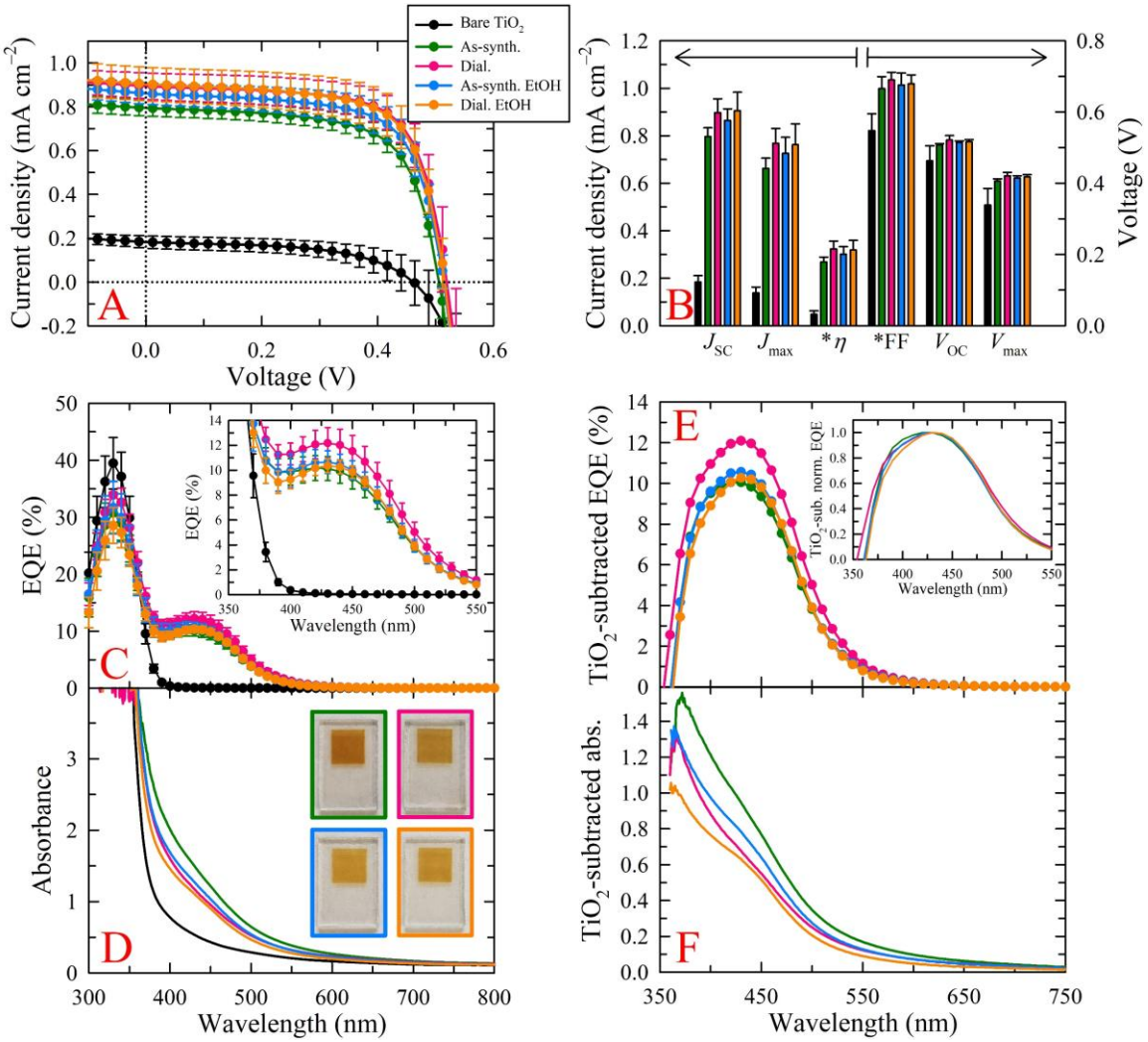

Figure D.7 (A) Average *J*-*V* curves (with corresponding standard deviations) of illuminated devices employing TiO_2 films that were sensitized in 10 mg mL^{-1} CA–NH_4OH-derived fractions dispersed in 100% acetone or 50:50 vol% acetone:ethanol (denoted by "EtOH"). (B) Average device metrics. *Note, efficiency (η) is reported in percent and FF is a unitless parameter but both values are on the same scale as the left and right y-axes, respectively. (C) Average EQE and (D) UV-vis absorbance spectra with their corresponding TiO_2-subtracted counterparts provided in panels E and F, respectively. A magnified plot of the EQE from 350 to 550 nm, photographs of representative films used in the devices, and a plot of normalized (norm.) spectra for the TiO_2-subtracted (TiO_2-sub.) EQE spectra are provided in the insets of panels C, D, and E, respectively. The conclusions drawn from the above results are similar to those arrived at for the 5 mg mL^{-1} fractions; that is, device performance, mainly the photocurrent, arises from reaction by-products,

specifically, species responsible for the absorbance shoulder at 450 nm and the yellow-orange color of the films. The performance of bare TiO_2 (black curves) is provided in all relevant plots for comparison.

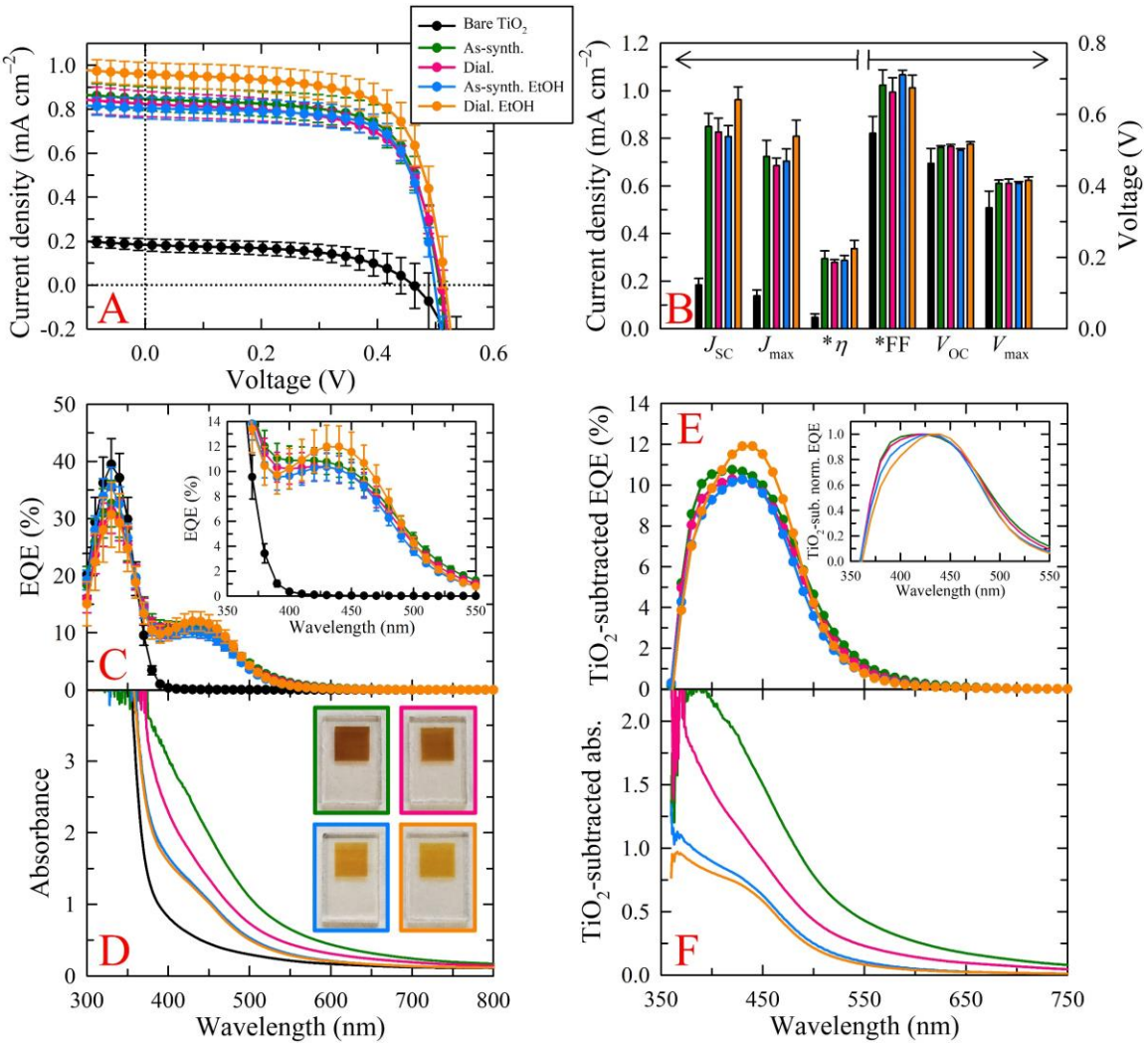

Figure D.8 (A) Average *J-V* curves (with corresponding standard deviations) of illuminated devices employing TiO_2 films that were sensitized in 30 mg mL^{-1} CA–NH_4OH-derived fractions dispersed in 100% acetone or 50:50 vol% acetone:ethanol (denoted by "EtOH"). (B) Average device metrics. *Note, efficiency (η) is reported in percent and FF is a unitless parameter but both values are on the same scale as the left and right y-axes, respectively. (C) Average EQE and (D) UV-vis absorbance spectra with their corresponding TiO_2-subtracted counterparts provided in panels E and F, respectively. A magnified plot of the EQE from 350 to 550 nm, photographs of representative films used in the devices, and a plot of normalized (norm.) spectra for the TiO_2-subtracted (TiO_2-sub.)

EQE spectra are provided in the insets of panels C, D, and E, respectively. The conclusions drawn from the above results are similar to those arrived at for the 5 and 10 mg mL^{-1} fractions; that is, device performance, mainly the photocurrent, arises from reaction by-products, specifically, species responsible for the absorbance shoulder at 450 nm and the yellow-orange color of the films. The performance of bare TiO_2 (black curves) is provided in all relevant plots for comparison.

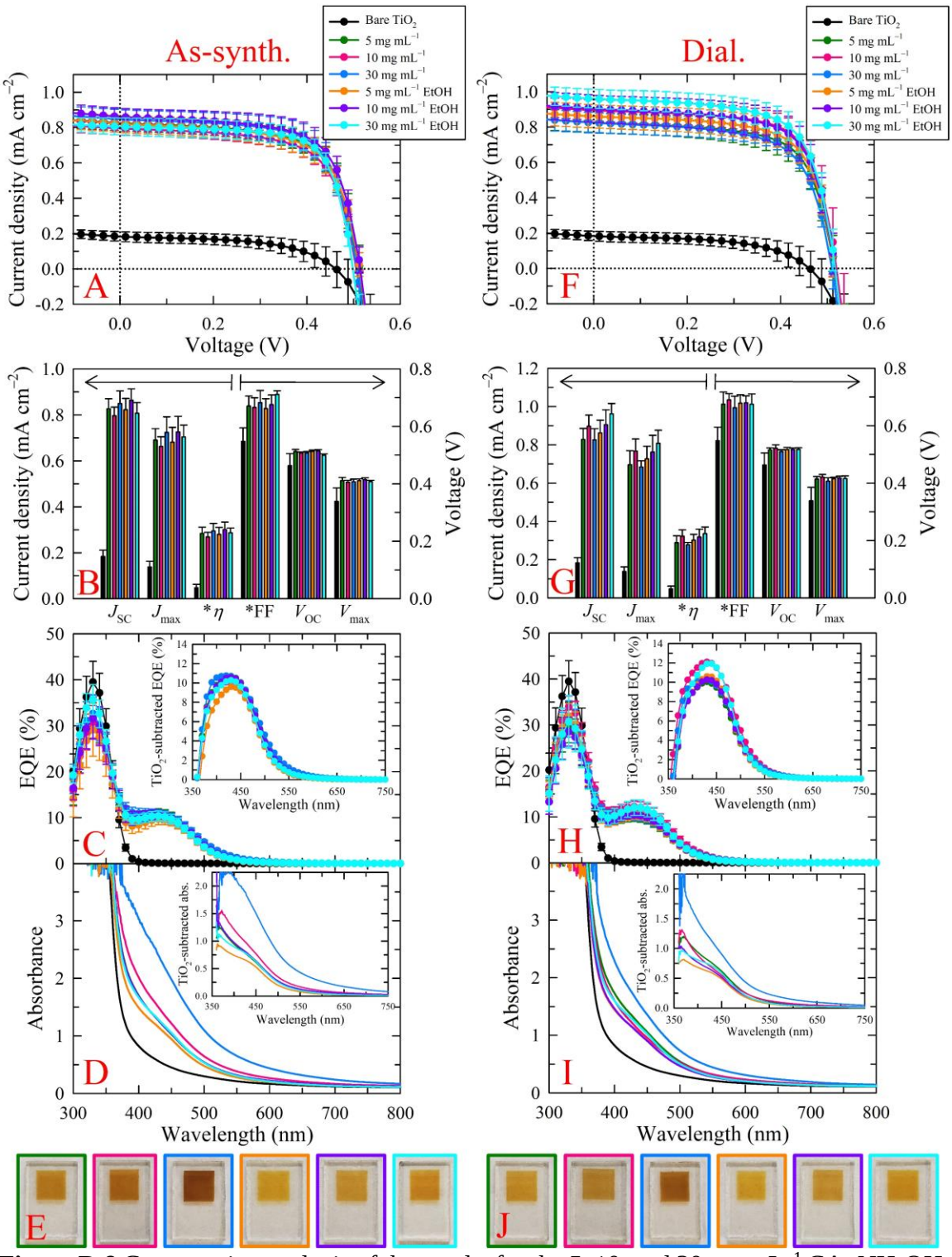

Figure D.9 Comparative analysis of the results for the 5, 10, and 30 mg mL^{-1} CA–NH_4OH-derived (A–E) as-synth. and (F–J) dial. fractions. (A and F) Average *J*-*V* curves (with corresponding standard deviations) of illuminated devices employing TiO_2 films that were sensitized in the above fractions ("EtOH" denotes samples dispersed in 50:50 vol%

acetone:ethanol). (B and G) Average device metrics. *Note, efficiency (η) is reported in percent and FF is a unitless parameter but both values are on the same scale as the left and right y-axes, respectively. (C and H) Average EQE and (D and I) UV-vis absorbance spectra with their corresponding TiO_2-subtracted counterparts provided as panel insets. (E and J) Photographs of representative films used in the devices. The performance of bare TiO_2 (black curves) is provided in all relevant plots for comparison.

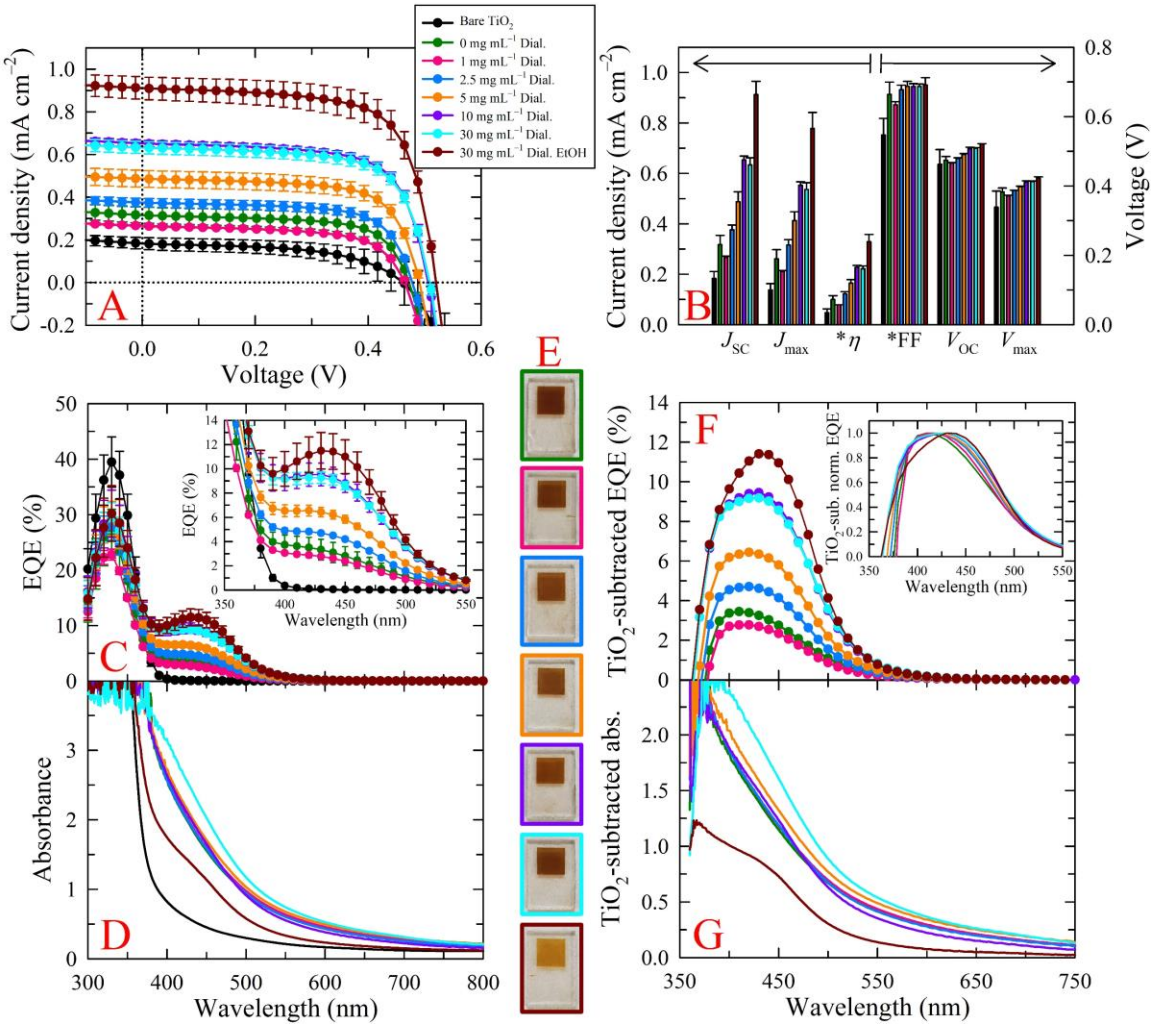

Figure D.10 (A) Average *J-V* curves (with corresponding standard deviations) of illuminated devices employing TiO_2 films that were sensitized in dial.-spiked, 5 mg mL^{-1} CA–NH_4OH-derived retent. solutions dispersed in 100% acetone or 50:50 vol% acetone:ethanol (denoted by "EtOH"). Appropriate quantities of the dial. fraction were spiked in 5 mg mL^{-1} retent. samples to yield 1, 2.5, 5, 10, or 30 mg mL^{-1} concentrations of the dial. species. (B) Average device metrics. *Note, efficiency (η) is reported in percent

and FF is a unitless parameter but both values are on the same scale as the left and right y-axes, respectively. (C) Average EQE and (D) absorbance spectra with their corresponding TiO_2-subtracted counterparts shown in panels F and G. (E) Photographs of representative films sensitized in the dial.-spiked, 5 mg mL^{-1} CA–NH_4OH retent. solutions. A magnified plot of the EQE from 350 to 550 nm and a plot of normalized (norm.) spectra for the TiO_2-subtracted (TiO_2-sub.) EQE spectra are provided in the insets of panels C and F, respectively. The performance of bare TiO_2 (black curves) is provided in all plots for comparison.

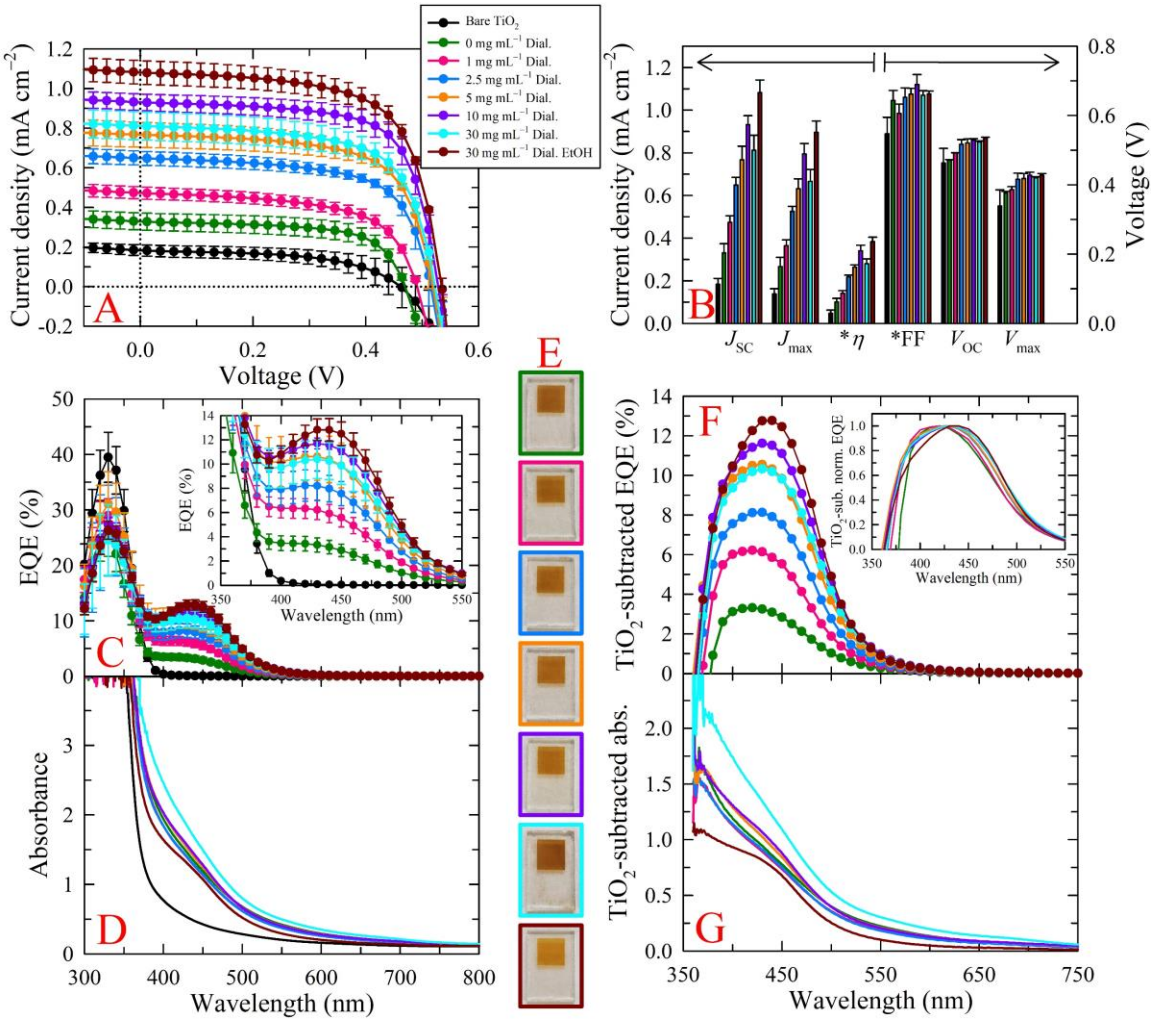

Figure D.11 (A) Average *J-V* curves (with corresponding standard deviations) of illuminated devices employing TiO_2 films that were sensitized in dial.-spiked, 1 mg mL^{-1} CA–NH_4OH-derived retent. solutions dispersed in 100% acetone or 50:50 vol% acetone:ethanol (denoted by "EtOH"). Appropriate quantities of the dial. fraction were

spiked in the 1 mg mL^{-1} retent. samples to yield 1, 2.5, 5, 10, or 30 mg mL^{-1} concentrations of the dial. species. (B) Average device metrics. *Note, efficiency (η) is reported in percent and FF is a unitless parameter but both values are on the same scale as the left and right y-axes, respectively. (C) Average EQE and (D) absorbance spectra with their corresponding TiO_2-subtracted counterparts shown in panels F and G. (E) Photographs of representative films sensitized in the dial.-spiked, 1 mg mL^{-1} CA–NH_4OH retent. solutions. A magnified plot of the EQE from 350 to 550 nm and a plot of normalized (norm.) spectra for the TiO_2-subtracted (TiO_2-sub.) EQE spectra are provided in the insets of panels C and F, respectively. The performance of bare TiO_2 (black curves) is provided in all plots for comparison.

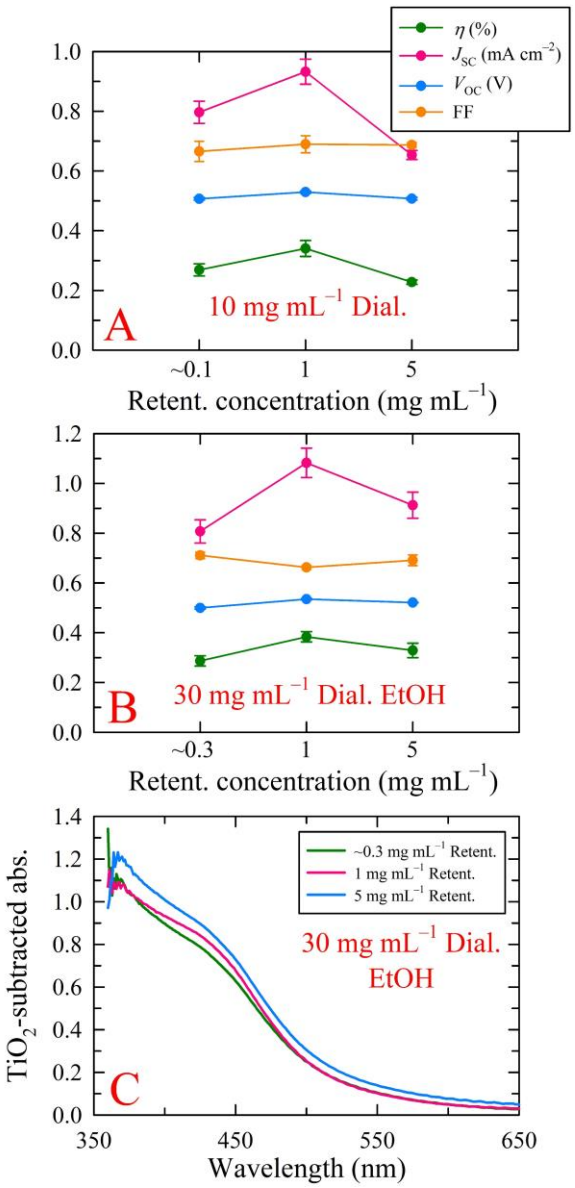

Figure D.12 Select comparisons of the results from the CA–NH_4OH dial. spiking studies. (A) Device metrics for TiO_2 films sensitized in 1 or 5 mg mL^{-1} retent. fractions spiked with 10 mg mL^{-1} dial. compared to films sensitized in a 10 mg mL^{-1} as-synth. fraction, which nominally contained 0.1 and 9.9 mg mL^{-1} retent. and dial. species, respectively. (B) Device metrics for TiO_2 films sensitized in 1 or 5 mg mL^{-1} retent. fractions spiked with dial. to a concentration of 30 mg mL^{-1} compared to films sensitized in ethanolic 30 mg mL^{-1} as-synth. fraction, which nominally contained 0.3 and 29.7 mg mL^{-1} retent. and dial. species, respectively. (C) Average UV-vis absorbance spectra for the films employed in the devices summarized in panel B. These results clearly show that synergistic effects between the dial. and retent. species exist, where an optimized nanocarbon content leads to improved device

performance, as widely reported in the literature. Furthermore, higher concentrations of the retent. fraction appear to diminish the apparent "selectivity" observed in ethanolic solutions, evidenced by increased film absorbance when sensitized in higher retent. content, even when in the presence of 50% ethanol (denoted by "EtOH").

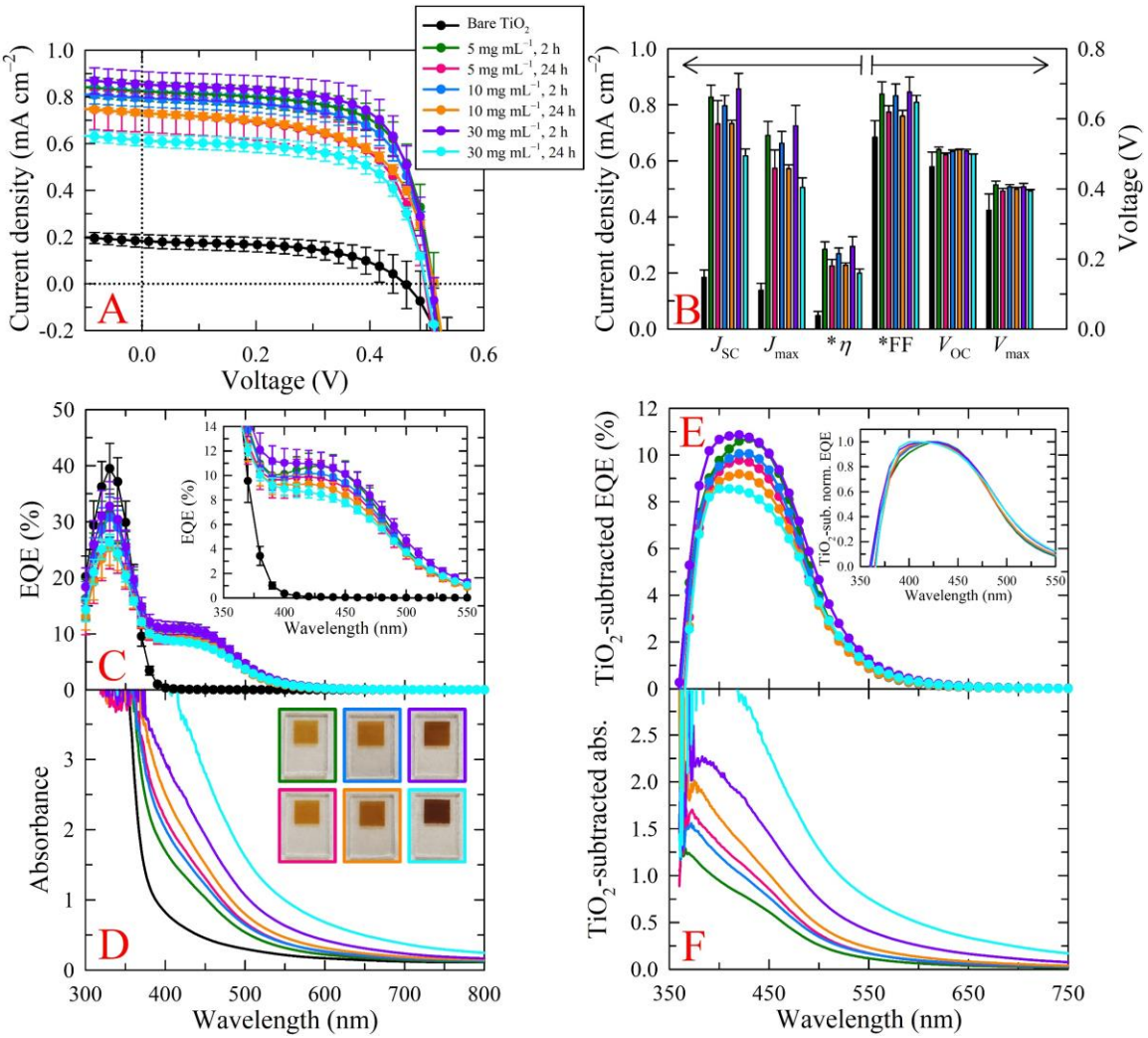

Figure D.13 Comparison of 2 h *vs* 24 h uptake for CA–NH_4OH-derived as-synth. fractions. (A) Average *J-V* curves (with corresponding standard deviations) of illuminated devices employing TiO_2 films that were sensitized in 5, 10, or 30 mg mL^{-1} CA–NH_4OH-derived as-synth. fractions dispersed in 100% acetone or 50:50 vol% acetone:ethanol (denoted by "EtOH"). (B) Average device metrics. *Note, efficiency (η) is reported in percent and FF is a unitless parameter but both values are on the same scale as the left and right y-axes, respectively. (C) Average EQE and (D) UV-vis absorbance spectra with their corresponding TiO_2-subtracted counterparts provided in panels E and F, respectively. A

magnified plot of the EQE from 350 to 550 nm, photographs of representative films used in the devices, and a plot of normalized (norm.) spectra for the TiO_2-subtracted (TiO_2-sub.) EQE spectra are provided in the insets of panels C, D, and E, respectively. The results clearly show that longer sensitization times negatively impacted device performance despite an increased uptake of chromophoric material, effects that were concentration dependent and, thus, most prominent for the 30 mg mL^{-1} as-synth. fraction. The performance of bare TiO_2 (black curves) is provided in all relevant plots for comparison.

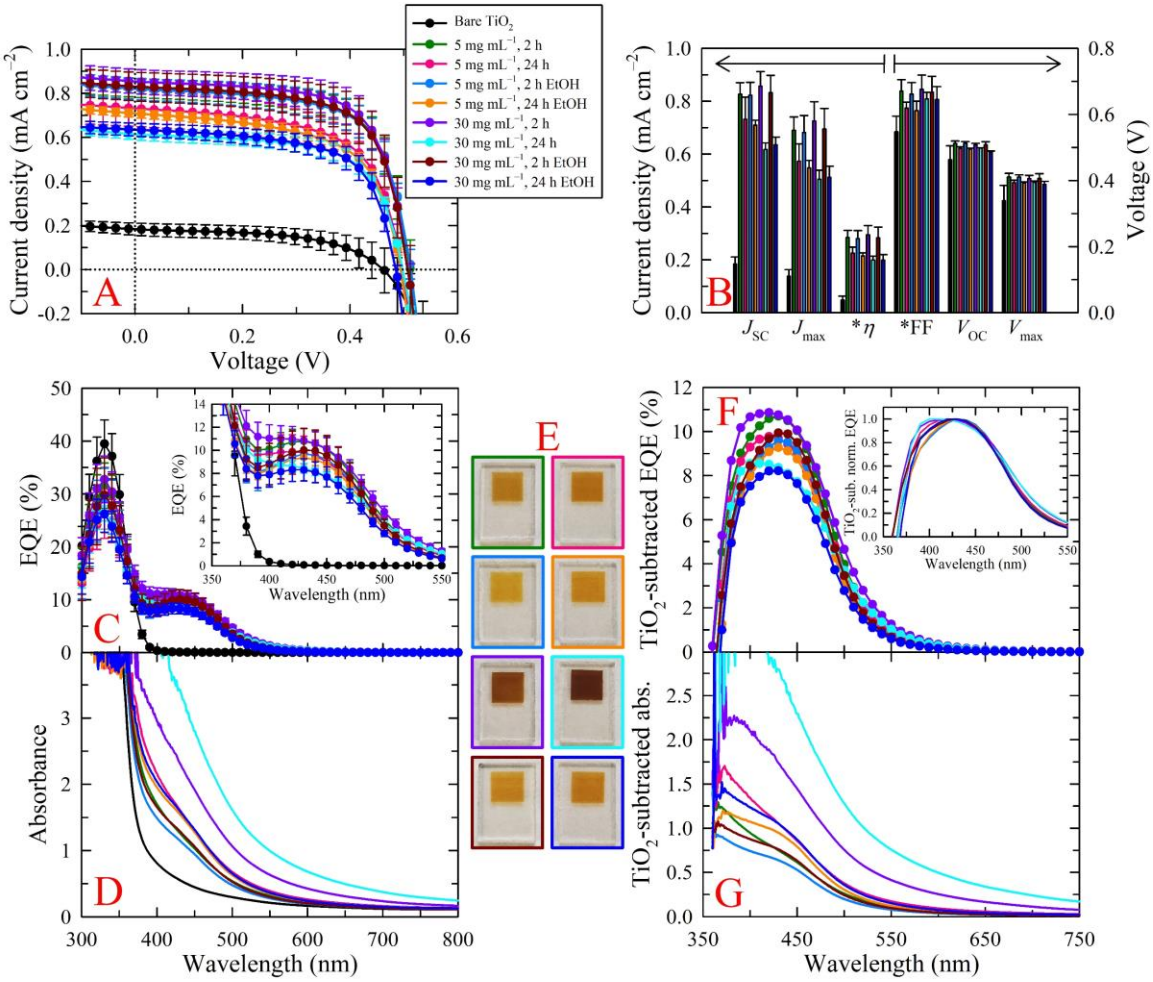

Figure D.14 Concentration-dependent comparison of 2 h *vs* 24 h uptake for CA–NH_4OH-derived as-synth. fractions. (A) Average *J-V* curves (with corresponding standard deviations) of illuminated devices employing TiO_2 films that were sensitized in 5 or 30 mg mL^{-1} CA–NH_4OH-derived as-synth. fractions dispersed in 100% acetone or 50:50 vol% acetone:ethanol (denoted by "EtOH"). (B) Average device metrics. *Note, efficiency (η) is reported in percent and FF is a unitless parameter but both values are on the same scale

as the left and right y-axes, respectively. (C) Average EQE and (D) absorbance spectra with their corresponding TiO_2-subtracted counterparts shown in panels F and G. (E) Photographs of representative films. A magnified plot of the EQE from 350 to 550 nm and a plot of normalized (norm.) spectra for the TiO_2-subtracted (TiO_2-sub.) EQE spectra are provided in the insets of panels C and F, respectively. The results clearly show that longer sensitization times led to diminished performance. Although, this observation is not solely a product of increased uptake, specifically, of nanocarbons, since 2 h sensitizations in 5 or 30 mg mL^{-1} as-synth. fractions yielded comparable performance to one another and 24 h sensitizations in ethanolic solutions produced similar decreases in performance as their 100% acetone counterparts. Therefore, the observed decreases in performance upon longer sensitizations may arise from TiO_2-induced degradation of the photoactive species. The performance of bare TiO_2 (black curves) is provided in all relevant plots for comparison.

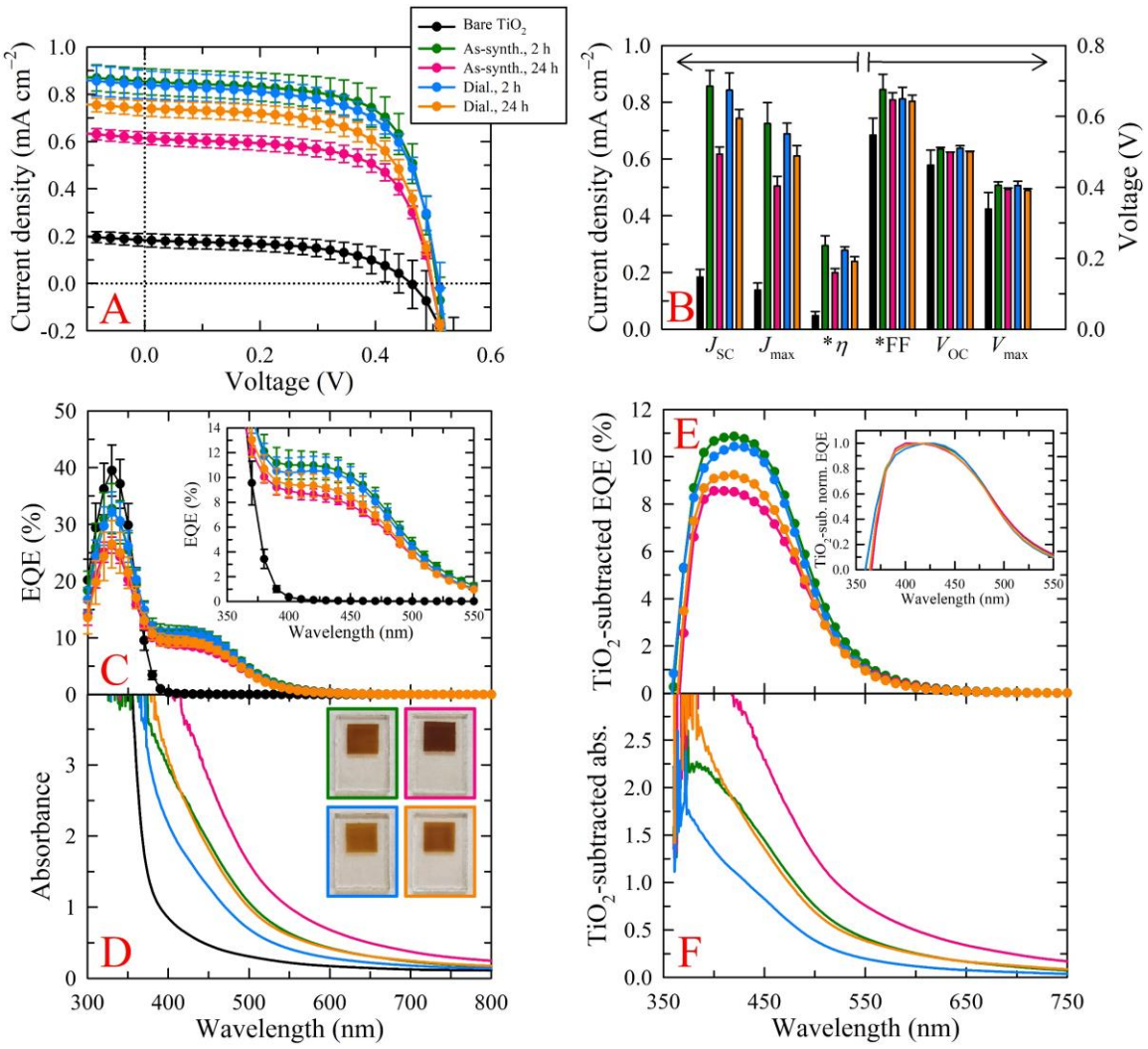

Figure D.15 Fraction-dependent comparison of 2 h *vs* 24 h uptake for CA–NH_4OH-derived samples. (A) Average *J-V* curves (with corresponding standard deviations) of illuminated devices employing TiO_2 films that were sensitized in 30 mg mL^{-1} CA–NH_4OH-derived as-synth. and dial. fractions dispersed in 100% acetone. (B) Average device metrics. *Note, efficiency (η) is reported in percent and FF is a unitless parameter but both values are on the same scale as the left and right y-axes, respectively. (C) Average EQE and (D) absorbance spectra with their corresponding TiO_2-subtracted counterparts shown in panels E and F. A magnified plot of the EQE from 350 to 550 nm, photographs of representative films used in the devices, and a plot of normalized (norm.) spectra for the TiO_2-subtracted (TiO_2-sub.) EQE spectra are provided in the insets of panels C, D, and E, respectively. Akin to the other 24 h sensitization studies, longer sensitization led to diminished performance for the 30 mg mL^{-1} as-synth. and dial. fractions, however, the decrease

observed in the latter was not nearly as prominent as that for the former, implying the nanocarbons may be playing a role in TiO_2-induced degradation of the photoactive species. The performance of bare TiO_2 (black curves) is provided in all relevant plots for comparison.

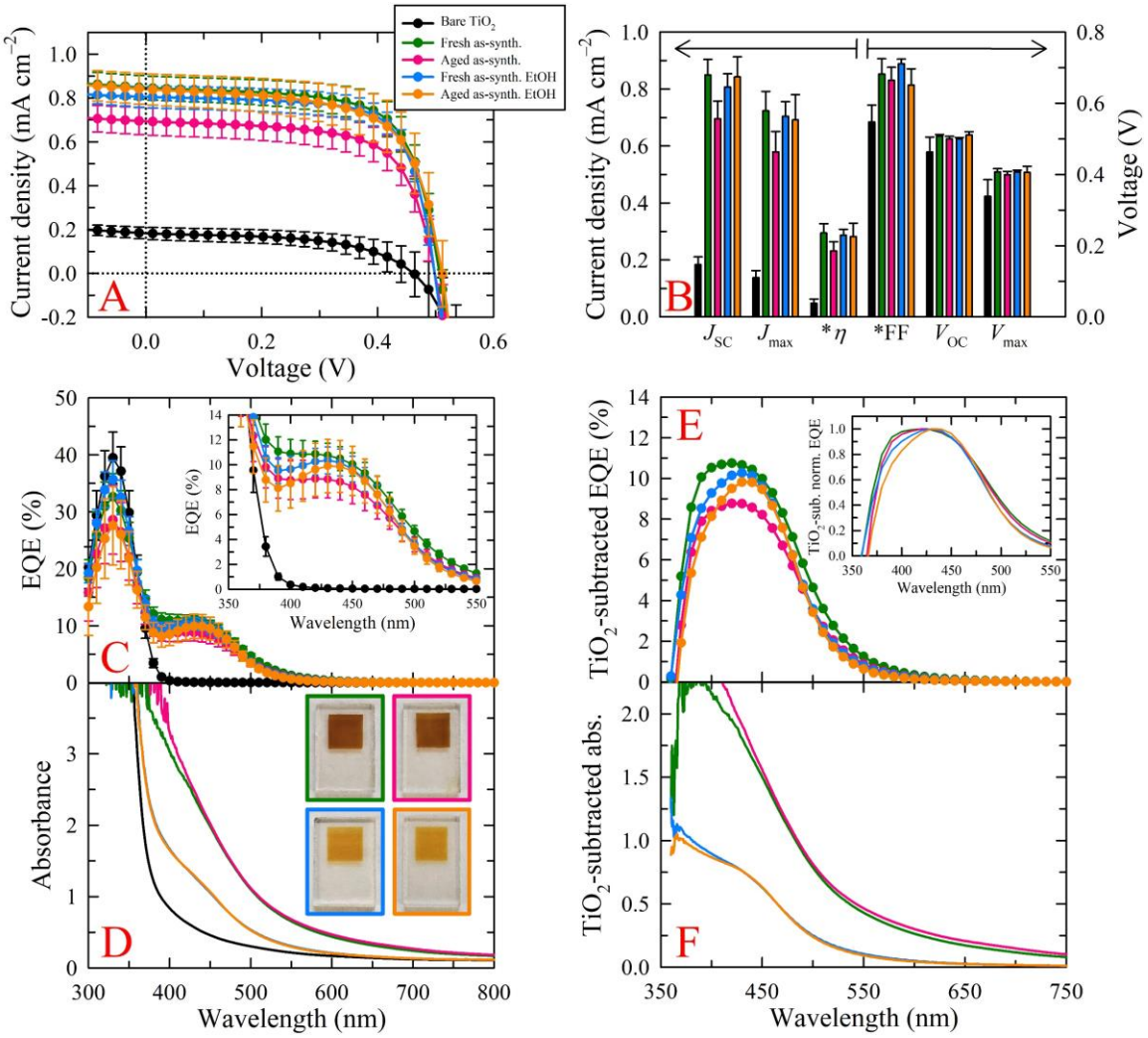

Figure D.16 Aging effects of CA–NH_4OH samples. (A) Average *J*-*V* curves (with corresponding standard deviations) of illuminated devices employing TiO_2 films that were sensitized in fresh or aged (>1 week old) 30 mg mL^{-1} CA–NH_4OH-derived as-synth. fractions dispersed in 100% acetone or 50:50 vol% acetone:ethanol (denoted by "EtOH"). (B) Average device metrics. *Note, efficiency (η) is reported in percent and FF is a unitless parameter but both values are on the same scale as the left and right y-axes, respectively. (C) Average EQE and (D) absorbance spectra with their corresponding TiO_2-subtracted counterparts shown in panels E and F. A magnified plot of the EQE from 350 to 550 nm,

photographs of representative films used in the devices, and a plot of normalized (norm.) spectra for the TiO_2-subtracted (TiO_2-sub.) EQE spectra are provided in the insets of panels C, D, and E, respectively. While not staggering, slight aging effects were observed in the 30 mg mL^{-1} as-synth. fractions. Although, when the same samples were sensitized in the presence of EtOH, the minor decrease in performance was not apparent. Such an observation implies the lower performance likely does not originate from degradation of the photoactive species but stems from the degradation of another species that is only present in a sufficient enough concentration to induce a negative impact in the 30 mg mL^{-1} as-synth. fraction, which could be the nanocarbons or an unidentified reaction by-product. The performance of bare TiO_2 (black curves) is provided in all relevant plots for comparison.

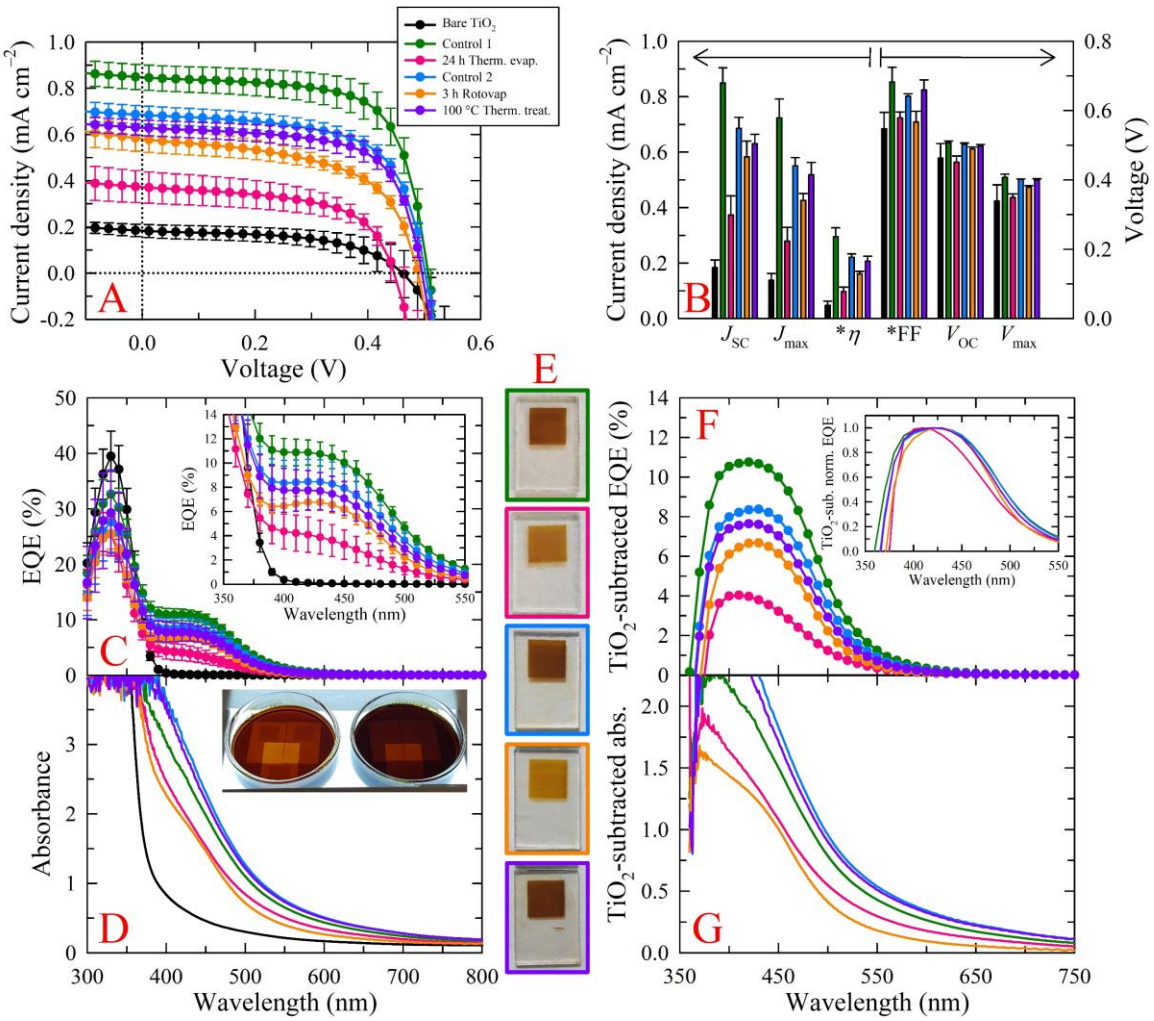

Figure D.17 Effects of water exposure on CA–NH_4OH samples. (A) Average *J-V* curves (with corresponding standard deviations) of illuminated devices employing TiO_2 films that were sensitized in 30 mg mL^{-1} CA–NH_4OH-derived as-synth. fractions dispersed in 100% acetone. (B) Average device metrics. *Note, efficiency (η) is reported in percent and FF is a unitless parameter but both values are on the same scale as the left and right y-axes, respectively. (C) Average EQE and (D) absorbance spectra with their corresponding TiO_2-subtracted counterparts shown in panels F and G. The inset in panel D illustrates the effects that water exposure (right) has on the acetone-dispersed solutions (left). (E) Photographs of representative films. A magnified plot of the EQE from 350 to 550 nm and a plot of normalized (norm.) spectra for the TiO_2-subtracted (TiO_2-sub.) EQE spectra are provided in the insets of panels C and F, respectively. The performance of bare TiO_2 (black curves) is provided in all relevant plots for comparison. The experimental details for these studies and an in-depth analysis of the results are provided below.

Experimental Details and Analysis of Water-exposure Effects on CA–NH_4OH Samples

The volume of 30 mg mL^{-1} acetone-dispersed as-synth. samples was reduced by half via rotary evaporation (25 °C, <100 mbar), after which the samples were reconstituted with ultrapure water to their original volume such that the solvent system consisted of 50:50 vol% acetone:water. The samples were then completely dried via thermal evaporation for 24 h at 75 °C ("24 h Therm. Evap.") or rotary evaporation (50 °C, <100 mbar) for 3 h ("3 h Rotovap") and reconstituted in 100% acetone. TiO_2 films were sensitized in these solutions for 2 h, as well as in appropriate control solutions. Additionally, a separate set of sensitized TiO_2 films was thermally treated at 100 °C for 15 min to rule out any thermal effects ("100 °C Therm. Treat."). Note, two separate controls were employed in these studies to account for any aging effects present, which are denoted as "Control 1" and "Control 2", since the latter two studies ("3 h Rotovap" and "100 °C Therm. Treat.") were conducted with an aged sample; the first control is paired with the thermally evaporated sample and the second control corresponds to the remaining two samples. Figure D.17 reveals that thermally treating the films had minimal impacts on device performance, relative to the corresponding control, showing just a slight decrease in photocurrent, whereas exposure to water and drying via rotary evaporation resulted in a larger decrease in photocurrent, as well as slight decreases in FF and photovoltage, leading to an appreciable drop in efficiency. On the other hand, exposure to water and thermally drying the sample yielded a substantial decrease in performance, relative to the sample's control, a drop that was by far greater than the other conditions tested, resulting in the lowest observed performance. Additionally, exposure to water not only negatively impacted the photocurrent but also produced significant detriments to the FF and photovoltage. These adverse effects imparted by water exposure are attributed to water-induced irreversible

aggregation, evidenced by the observed solution darkening (inset of Figure D.17D), which led to higher solution absorbance (not shown). Interestingly, although the water-exposed solutions were darker, sensitization in these solutions led to drastically lighter colored films. Furthermore, due to the slow nature of the thermal evaporation treatment, this sample remained in contact with water for a much longer period than the sample dried via rotary evaporation, implying that temporal effects play a role in the extent of aggregation. EQE measurements demonstrated that the drop in photocurrent upon exposure to water originated from a loss in photon-to-electron conversion across all wavelengths, particularly, the peak from 375 to 600 nm, which is associated with the photoactive species of these samples, results that clearly indicate that these specific photosensitizers are negatively impacted by water. Further evidence for this is observed in the UV-vis spectra of the sensitized films where the two samples exposed to water show a marked decrease in absorbance across all wavelengths relative to their controls. Although the photographs and results shown here are for an extreme case of intentional aggregation, they clearly demonstrate that regardless of the purification mode (*e.g.*, dialysis, liquid chromatography), care must be taken when choosing the solvent system as the water-induced aggregation was not always visible by the naked eye and only upon conducting careful UV-vis and *J*-*V* measurements was the discrepancy revealed.

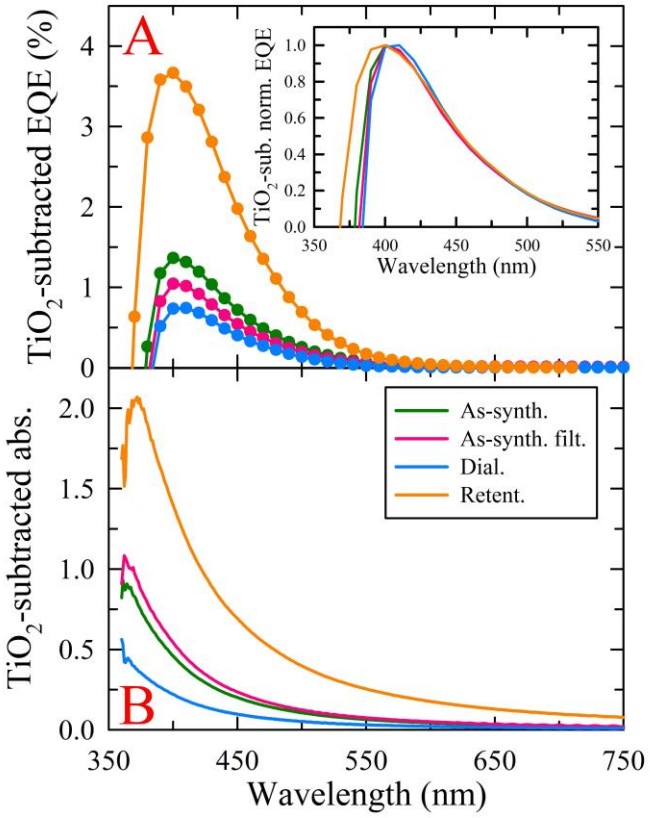

Figure D.18 TiO_2-subtracted (A) EQE and (B) absorbance (abs.) spectra for 10 mg mL^{-1} Arg fractions in EtOH. The inset plot in panel A shows normalized (norm.) spectra for the TiO_2-subtracted (TiO_2-sub.) EQE spectra. Clearly, photocurrent generation from the retent. fraction is negatively impacted by a species present in the dial. fraction since the photocurrent produced by the as-synth. fractions is only slightly higher than that created by the dial. fraction. Note, "as-synth. filt." represents the as-synth. sample that was passed through a 0.20 μm pore size syringe filter.

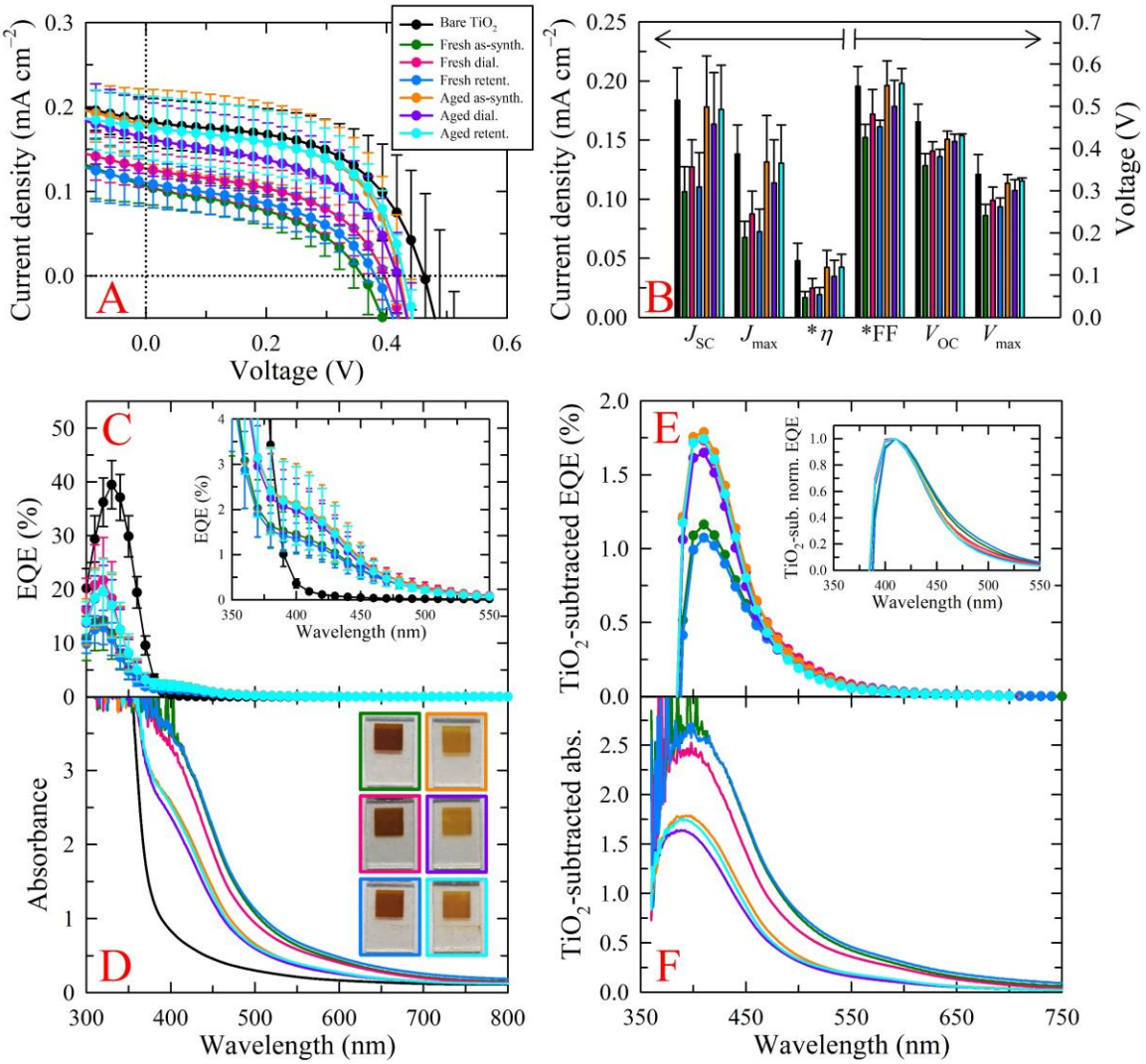

Figure D.19 Aging effects of CA–U-derived samples. (A) Average *J-V* curves (with corresponding standard deviations) of illuminated devices employing TiO_2 films that were sensitized in fresh or aged (>1 month old) 10 mg mL^{-1} CA–U-derived fractions dispersed in water. (B) Average device metrics. *Note, efficiency (η) is reported in percent and FF is a unitless parameter but both values are on the same scale as the left and right y-axes, respectively. (C) Average EQE and (D) absorbance spectra with their corresponding TiO_2-subtracted counterparts shown in panels E and F. A magnified plot of the EQE from 350 to 550 nm, photographs of representative films used in the devices, and a plot of normalized (norm.) spectra for the TiO_2-subtracted (TiO_2-sub.) EQE spectra are provided in the insets of panels C, D, and E, respectively. The performance of bare TiO_2 (black curves) is provided in all relevant plots for comparison. The experimental details for these studies and an in-depth analysis of the results are provided below.

Experimental Details and Analysis of Aging Effects on CA–U-derived Samples

Samples denoted as "fresh" were synthesized and characterized within a week of sample preparation, whereas samples denoted as "aged" were fresh samples dispersed in water and stored in the dark for at least one month. Fresh solutions of all three CA–U fractions negatively impacted the PV performance relative to bare TiO_2 with nearly a 2-fold reduction in photocurrent, a lowering of V_{OC} by ~0.1 V, and a >50% loss in FF at 330 nm (~40% down to <20%), leading to efficiencies that were nearly one third of the values observed for bare TiO_2 (Figure D.19). Despite the strong absorbance of all three fractions of the CA–U system, these sensitizers provided very little photon-to-electron conversion (<2%) between 375 and 800 nm, although, the EQE spectral profiles matched well with their corresponding absorbance profiles where the minor EQE shoulder between 390 and 500 nm arose from the strong shoulder across the same wavelength regime of the absorbance spectra. Additionally, these sensitizers had a drastic, negative impact on the EQE attributed to the bandgap of TiO_2, not only markedly decreasing the EQE but also hypsochromically shifting the entire EQE peak by 10 nm, possibly due to a band edge shift or alteration of the quasi-fermi level of TiO_2, which could account, in part, for the substantial drop in photovoltage. Interestingly, aged CA–U fractions led to "improved" PV metrics relative to fresh samples, presumably due to degradation of the species responsible for hindering the overall performance, where the lessening of performance hindrance originated from increased EQE across the wavelength range of 300–450 nm. This apparent degradation is further confirmed by the decrease in absorbance from the sensitized species and a clear color change (brown to tan) of the sensitized TiO_2 films. Interestingly, the fresh dial. fraction displayed the highest performance of the three fresh fractions while the aged dial. fraction showed the lowest performance of the three aged fractions implying that the

by-product species hinder the performance the least and degrade to a lesser extent than the retent. (presumably nanocarbon) species.

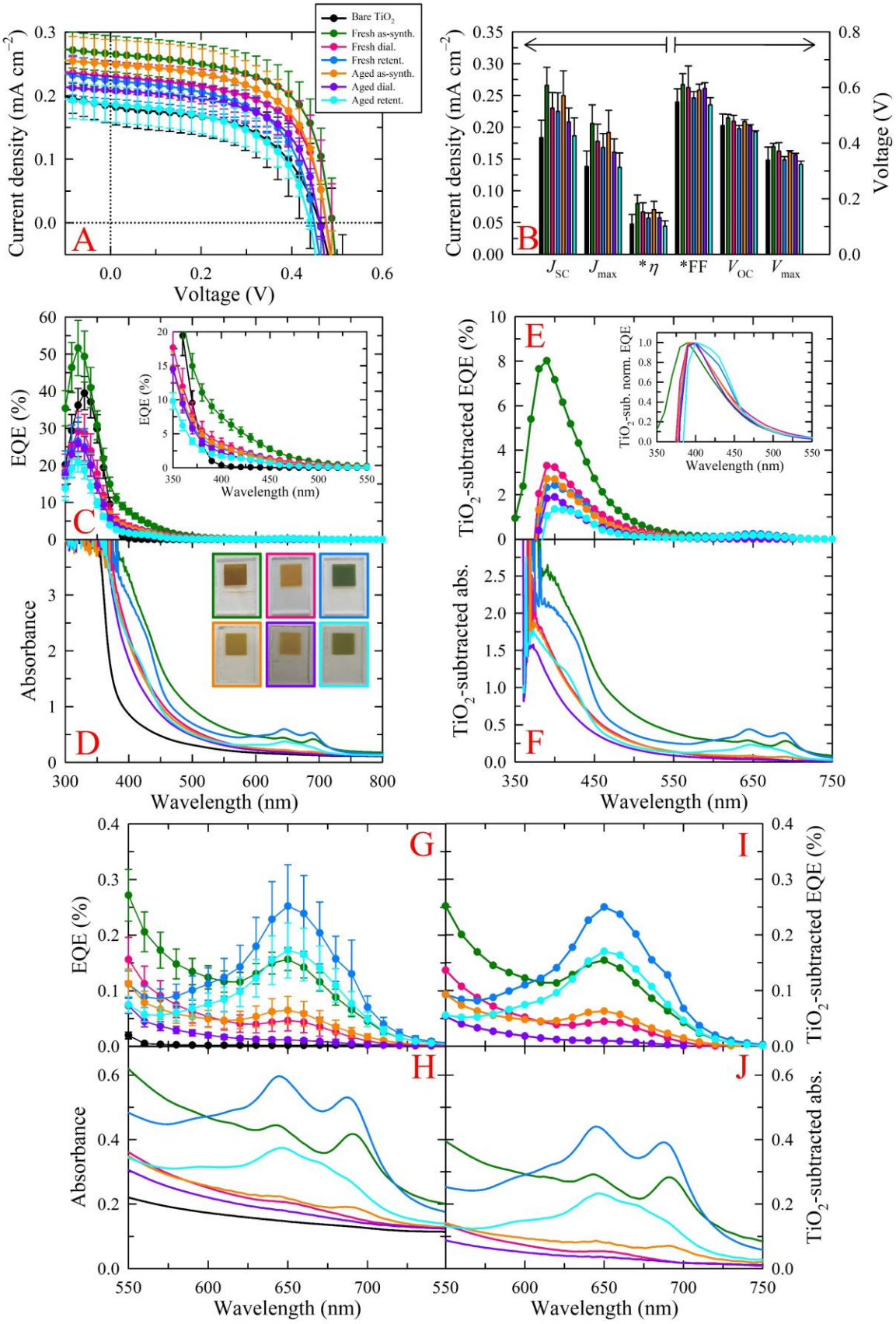
A
Current density (mA cm^{-2})
Voltage (V)
Bare TiO_2
Fresh as-synth.
Fresh dial.
Fresh retent.
Aged as-synth.
Aged dial.
Aged retent.
B
Current density (mA cm^{-2})
Voltage (V)
J_{SC}
J_{max}
*η
*FF
V_{OC}
V_{max}
C
EQE (%)
Wavelength (nm)
D
Absorbance
Wavelength (nm)
E
TiO_2-subtracted EQE (%)
TiO_2-sub. norm. EQE
Wavelength (nm)
F
TiO_2-subtracted abs.
Wavelength (nm)
G
EQE (%)
H
Absorbance
Wavelength (nm)
I
TiO_2-subtracted EQE (%)
J
TiO_2-subtracted abs.
Wavelength (nm)

Figure D.20 Aging effects of GSH–F-derived samples. (A) Average *J-V* curves (with corresponding standard deviations) of illuminated devices employing TiO_2 films that were sensitized in fresh or aged (>1 week old) solutions of the GSH–F-derived fractions. (B) Average device metrics. *Note, efficiency (η) is reported in percent and FF is a unitless parameter but both values are on the same scale as the left and right y-axes, respectively. (C) Average EQE and (D) absorbance spectra with their corresponding TiO_2-subtracted counterparts shown in panels E and F. A magnified plot of the EQE from 350 to 550 nm, photographs of representative films used in the devices, and a plot of normalized (norm.) TiO_2-subtracted (TiO_2-sub.) EQE spectra are provided in the insets of panels C, D, and E, respectively. Magnified plots of the EQE and absorbance from 550 to 750 nm are shown in panels G and H with their corresponding TiO_2-subtracted counterparts shown in panels I and J, respectively. The performance of bare TiO_2 (black curves) is provided in all relevant plots for comparison. The experimental details for these studies and an in-depth analysis of the results are provided below.

Experimental Details and Analysis of Aging Effects on GSH–F-derived Samples

Samples denoted as "fresh" were fractions that were characterized within a week of the individual fractions becoming available, whereas samples denoted as "aged" were fresh samples stored in the dark for at least one week after the fraction was ready. Specifically, fresh fractions were characterized no more than 10 days after synthesis, whereas all aged fractions were characterized at least 14 days after synthesis. All three fresh fractions produced slightly higher performance than that of bare TiO_2 with the average improvement decreasing in the following order as-synth. > dial. > retent. (Figure D.20). EQE measurements revealed that these sensitizers yield photon-to-electron conversion between 375 and 550 nm with the trend in increasing EQE correlating well with the trend in J_{SC}, however, the slight increase in photocurrent for the as-synth. fraction relative to the other two fractions does not track with the substantially higher EQE values observed for the as-synth. fraction, the origin of which is currently unclear. Additionally, the as-synth. fraction

produced higher EQE than bare TiO_2 between 300 and 375 nm while the dial. and retent. fractions negatively impacted the EQE attributed to TiO_2. The large discrepancy between the performance of the as-synth. fraction and that of the dial. and retent. fractions could stem from sample aging and degradation already taking affect since these fractions are not available for characterization until 3 and 7 days after synthesis, respectively, due to the slow processes inherent to dialysis purification. Furthermore, similar to the CA–U system, all three fractions produced a slight hypsochromic shift (~10 nm) in the EQE arising from TiO_2. Interestingly, the as-synth. and retent. fractions feature two minor peaks in the UV-vis spectra centered near 645 and 690 nm, which give rise to the distinct green color characteristic of this sample, particularly the retent. fraction. Indeed, upon purification of the as-synth. fraction, the solution color changed from dark brown/black with a slight green hue to a prominent dark black/green (*i.e.*, retent.), a difference that was most notable upon sensitization of the TiO_2 films, where the as-synth. fraction yielded dark brown films while the retent. fraction produced vibrant green films. Interestingly, the species responsible for these absorbance features yielded minor, albeit distinguishable, photon-to-electron conversion. That is, the UV-vis absorbance peak near 645 nm correlates fairly well with the EQE peak at 650 nm, however, since the UV-vis spectra display two peaks while the EQE spectra only show one, it is likely that both absorbance features contribute to the photocurrent to varying degrees such that the contributions converge into a single peak in the EQE. Although, a very minor shoulder was observed at 690 nm in the EQE spectra of the fresh retent. fraction, a feature that directly lines up with the absorbance observed at this same wavelength. Specifically, the as-synth. fraction produced a distinct peak at 650 nm with an EQE of 0.15%, whereas, upon purification, the EQE at 650 nm for the retent.

fraction promisingly jumped up to 0.25% with the EQE between 620 and 720 nm also showing an increase relative to the as-synth. fraction, a trend that correlates well with the observed changes in absorbance upon fractionation. Conversely, the dial. fraction displayed little to no peak between 620 and 720 nm with a maximum EQE of 0.05% arising at 650 nm.

Similar to the CA-derived systems (*i.e.*, CA–NH_4OH, CA–U), the GSH–F fractions displayed substantial temporal instability, especially the nanocarbon-containing retent. fraction. After an aging period of at least one week from the time the fractions became available, devices fabricated with films sensitized in these aged fractions produced slightly diminished average performance relative to their fresh counterparts, namely, the average V_{OC} and J_{SC} marginally decreased producing lower efficiencies. EQE measurements revealed that the decrease in photocurrent originated from a drop in photon-to-electron conversion across all wavelengths, indicating potential degradation of the sensitizing species. Further evidence of this degradation is in the observed color of the films and their corresponding UV-vis spectra. Both the as-synth. and retent. fractions showed marked decreases across their entire spectra, most notably, the shoulder around 425 nm for the retent. fraction nearly disappeared while the two peaks observed in their fresh counterparts at 645 and 690 nm became nearly indistinguishable for the aged as-synth. fraction and essentially merged into one peak for the retent. fraction, observations that correlate well with the diminished EQE.

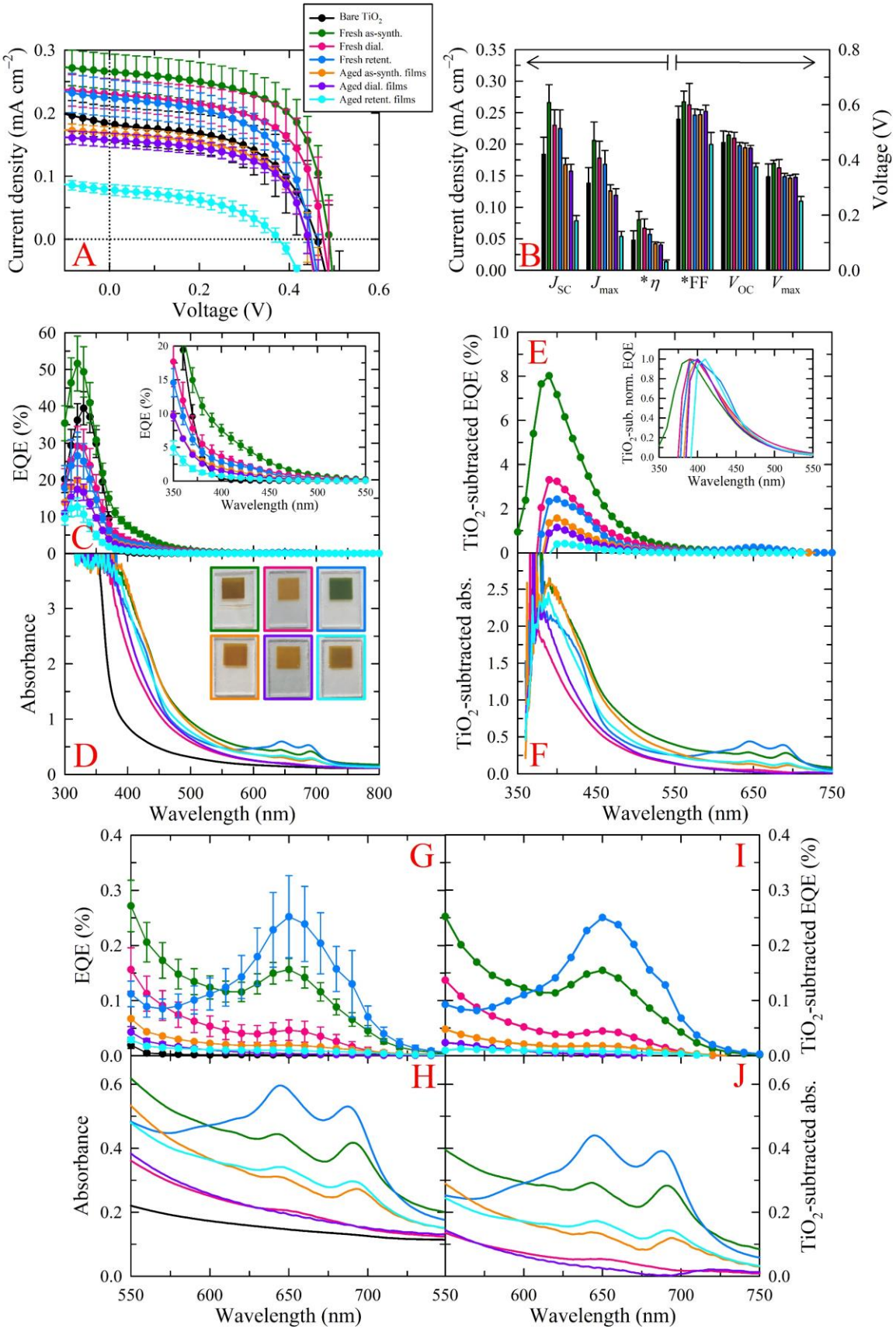
Bare TiO2
Fresh as-synth.
Fresh dial.
Fresh retent.
Aged as-synth. films
Aged dial. films
Aged retent. films
A
Current density (mA cm−2)
Voltage (V)
B
Current density (mA cm−2)
Voltage (V)
Jsc
Jmax
*η
*FF
Voc
Vmax
C
EQE (%)
Wavelength (nm)
D
Absorbance
Wavelength (nm)
E
TiO2-subtracted EQE (%)
TiO2-sub. norm. EQE
Wavelength (nm)
F
TiO2-subtracted abs.
Wavelength (nm)
G
EQE (%)
I
TiO2-subtracted EQE (%)
H
Absorbance
Wavelength (nm)
J
TiO2-subtracted abs.
Wavelength (nm)

Figure D.21 Effects of aging on GSH–F-sensitized TiO_2 films. (A) Average *J-V* curves (with corresponding standard deviations) of illuminated devices employing TiO_2 films that were sensitized in fresh or aged (>2 months old) films sensitized with the GSH–F-derived fractions. (B) Average device metrics. *Note, efficiency (η) is reported in percent and FF is a unitless parameter but both values are on the same scale as the left and right y-axes, respectively. (C) Average EQE and (D) absorbance spectra with their corresponding TiO_2-subtracted counterparts shown in panels E and F. A magnified plot of the EQE from 350 to 550 nm, photographs of representative films used in the devices, and a plot of normalized (norm.) spectra for the TiO_2-subtracted (TiO_2-sub.) EQE spectra are provided in the insets of panels C, D, and E, respectively. Magnified plots of the EQE and absorbance from 550 to 750 nm are shown in panels G and H with their corresponding TiO_2-subtracted counterparts shown in panels I and J, respectively. The performance of bare TiO_2 (black curves) is provided in all relevant plots for comparison. The experimental details for these studies and an in-depth analysis of the results are provided below.

Experimental Details and Analysis of Aging Effects on GSH–F-sensitized Films

Samples denoted as "fresh" were fractions that were characterized within a week of the fraction becoming available, whereas data denoted as "aged films" were films sensitized with fresh fractions and then intentionally aged for 2 months before characterization. An analysis of the results for the fresh data was provided in the discussion of Figure D.20, therefore, only the results for the aged films, relative to the fresh, will be discussed here. An even more drastic aging effect was observed for the fractions intentionally aged on film for 2 months (Figure D.21). The device metrics, and, thus, performance, for all three fractions decreased substantially relative to their fresh counterparts (and bare TiO_2) implying potential degradation of the photoactive species and indicating that the degraded form(s) of these species greatly hinder device photophysics, especially in the case of the retent. fraction. While all PV metrics were affected by this apparent degradation, the main contributing factor to the decrease in efficiency was a loss in photocurrent, the origin of

which was diminished photon-to-electron conversion across all wavelengths of interest (*i.e.*, 300–800 nm) as evidenced in the EQE spectra. Notably, the minor photon-to-electron conversion observed near 650 nm for the as-synth. and retent. fractions essentially disappeared, a reduction that corresponds well with the observed decrease in the UV-vis spectra, providing additional evidence for sample degradation. Given the apparent sample instability gleaned from the above results for both aging studies, we suspect that the prominent peaks in the UV-vis spectra at 645 and 690 nm, that produce the distinct green color of the retent. fraction and lead to the single EQE peak near 650 nm, originate from incompletely carbonized, N-/S-containing quasi-molecular species that are tethered to the nanocarbon but that are prone to oxidative degradation, a process which renders these species photo-inactive and, in fact, detrimental to PV performance.

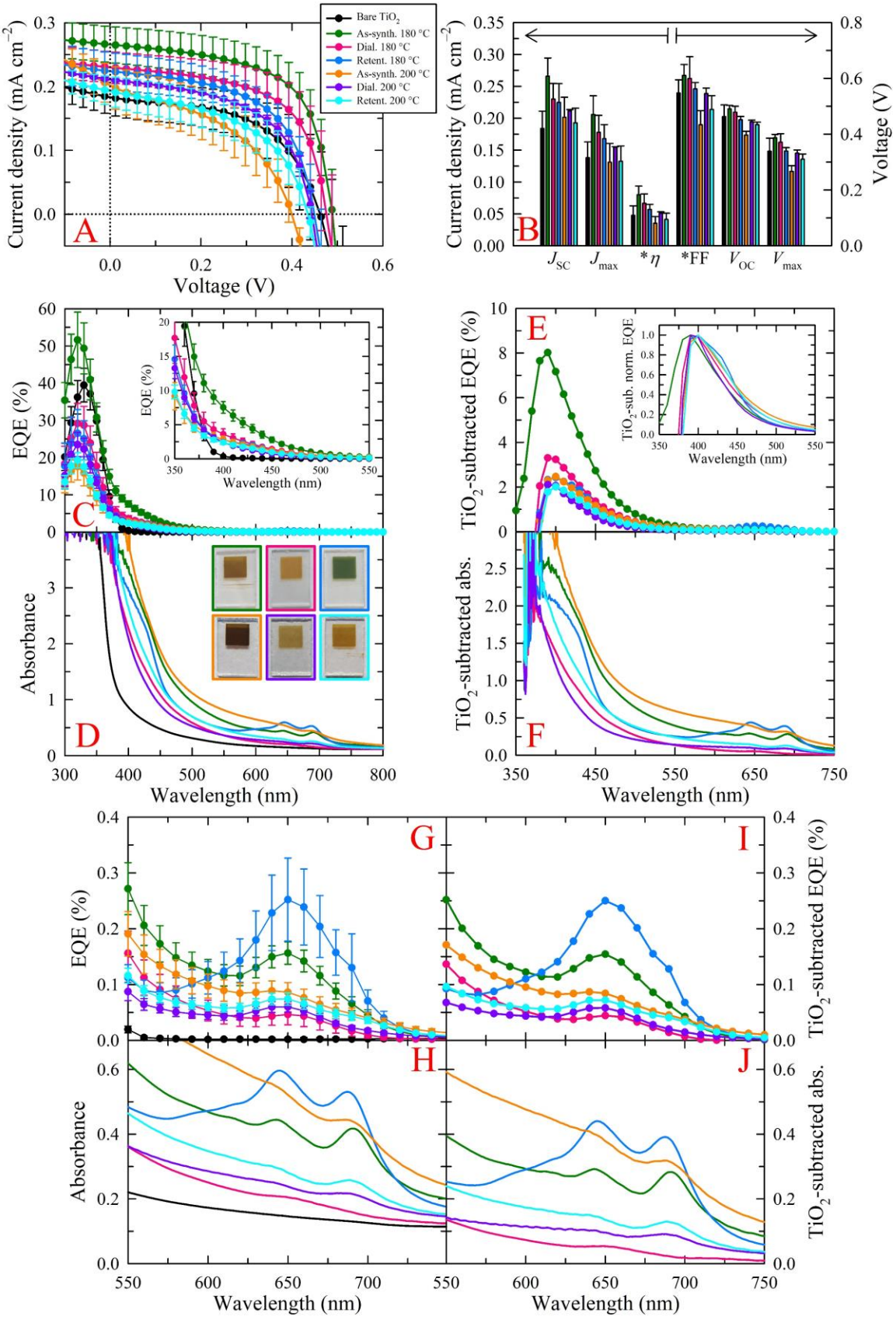
A
Current density (mA cm^{-2})
Voltage (V)
Bare TiO$_2$
As-synth. 180 °C
Dial. 180 °C
Retent. 180 °C
As-synth. 200 °C
Dial. 200 °C
Retent. 200 °C
B
Current density (mA cm^{-2})
Voltage (V)
J_{SC}
J_{max}
$*\eta$
*FF
V_{OC}
V_{max}
C
EQE (%)
Wavelength (nm)
D
Absorbance
Wavelength (nm)
E
TiO$_2$-subtracted EQE (%)
TiO$_2$-sub. norm. EQE
Wavelength (nm)
F
TiO$_2$-subtracted abs.
Wavelength (nm)
G
EQE (%)
I
TiO$_2$-subtracted EQE (%)
H
Absorbance
Wavelength (nm)
J
TiO$_2$-subtracted abs.
Wavelength (nm)

Figure D.22 Effects of synthesis temperature on GSH–F-derived fractions. (A) Average *J-V* curves (with corresponding standard deviations) of illuminated devices employing TiO_2 films that were sensitized in GSH–F-derived samples synthesized at either 180 or 200 °C. (B) Average device metrics. *Note, efficiency (η) is reported in percent and FF is a unitless parameter but both values are on the same scale as the left and right y-axes, respectively. (C) Average EQE and (D) absorbance spectra with their corresponding TiO_2-subtracted counterparts shown in panels E and F. A magnified plot of the EQE from 350 to 550 nm, photographs of representative films employed in the devices, and a plot of normalized (norm.) spectra for the TiO_2-subtracted (TiO_2-sub.) EQE spectra are provided in the insets of panels C, D, and E, respectively. Magnified plots of the EQE and absorbance from 550 to 750 nm are shown in panels G and H with their corresponding TiO_2-subtracted counterparts shown in panels I and J, respectively. The performance of bare TiO_2 (black curves) is provided in all relevant plots for comparison. The experimental details for these studies and an in-depth analysis of the results are provided below.

Experimental Details and Analysis of Synthetic Temperature on GSH–F-derived Samples

Although less than 0.5%, the minor EQE peak at 650 nm observed in the GSH–F-derived retent. fraction is promising, as with a more elementary understanding of these features, the nanocarbons could be better tailored to function as efficient photosensitizers. Towards this, samples were generated at a higher carbonization temperature (200 °C instead of 180 °C) to explore any deviations in the photophysics of the species giving rise to the UV-vis and EQE spectral features between 600 and 800 nm. Other than the higher synthetic temperature, the samples and fractions were prepared and treated in the exact same manner as the 180 °C samples (see the "Solvothermal Approaches" subsection under "Fluorescent Carbon Dot Syntheses" in the "Experimental" section of Chapter 5 for details). Contrary to the fractions generated at a lower temperature, the EQE spectra for these higher temperature fractions were relatively consistent across all wavelengths, however, the subtle trends in the average EQE near the TiO_2 bandgap, which account for the majority of the

photocurrent, line up closely with the trends observed in the average J_{SC}, specifically the dial. fraction showed the highest values. Although the as-synth. fraction showed the lowest EQE between 300 and 350 nm but the average J_{SC} was slightly higher than that of the retent. fraction, a crossover in EQE occurs around 375 nm where the as-synth. fraction produced marginally higher EQE than the retent. fraction, which could account for the slight increase in J_{SC}. While the EQE is quite low (<4%) in the wavelength range associated with sensitized species (>375 nm), the trends in average EQE correlate well with those observed in the UV-vis spectra; however, the marginal differences in the EQE are not mirrored in the UV-vis spectra, as large differences between the absorbance spectra were present, implying that some of the chromophoric species within these fractions likely do not contribute to photocurrent. Although the EQE spectra were relatively consistent across most wavelengths, statistically significant, albeit minor, differences in photon-to-current conversion did arise between 550 and 750 nm with the trends in EQE matching those observed in the UV-vis spectra; that is, the as-synth. fraction showed the highest absorbance and EQE followed by the retent. and dial. fractions. Interestingly, when compared to the lower temperature fractions, the peaks observed at 650 nm for the as-synth. and retent. fraction decreased markedly with the as-synth. fraction producing higher EQE between 575 and 750 nm. Specifically, the EQE at this wavelength decreased from 0.16 ± 0.02, 0.25 ± 0.07, and 0.05 ± 0.02% to 0.09 ± 0.02, 0.07 ± 0.01, and 0.06 ± 0.01% for the as-synth., retent., and dial. fractions, respectively. Furthermore, the EQE for these respective fractions also decreased at two select wavelengths (320 / 400 nm) from 51.62 ± 7.46 / 7.53 ± 0.87%, 26.54 ± 6.39 / 2.79 ± 0.46%, and 29.19 ± 5.39 / 3.60 ± 0.78% to 17.63 ± 3.64 / 2.83 ± 0.49%, 19.29 ± 2.04 / 2.37 ± 0.28%, and 23.51 ± 3.26 / 2.42 ± 0.30%. Thus,

the biggest effect of increasing the reaction temperature was on the EQE attributed to TiO_2, which indicates increased carbonization within the produced materials negatively impacts TiO_2's photon-to-electron conversion ability. Furthermore, the above results indicate that the higher carbonization temperature induced negative alterations to the species responsible for sensitizer-generated photocurrent, leading to diminished charge-carrier harvesting such as lower photon-to-current conversion at these redder wavelengths. We postulate that the higher reaction temperature led to the degradation of quasi-molecular moieties tethered to the nanocarbons via increased carbonization, species that are responsible for the distinct green coloration and, in part, a fraction of the photocurrent, in particular, at redder wavelengths, as evidenced by the absorbance peaks at 645 and 690 nm becoming less prominent and less distinguishable, in conjunction with the decrease in EQE in this wavelength range. Furthermore, the greater extent of carbonization brought about by a higher reaction temperature negatively impacted the other PV metrics, implying that, for this specific system, the generated nanocarbons do not function as efficient photosensitizers.

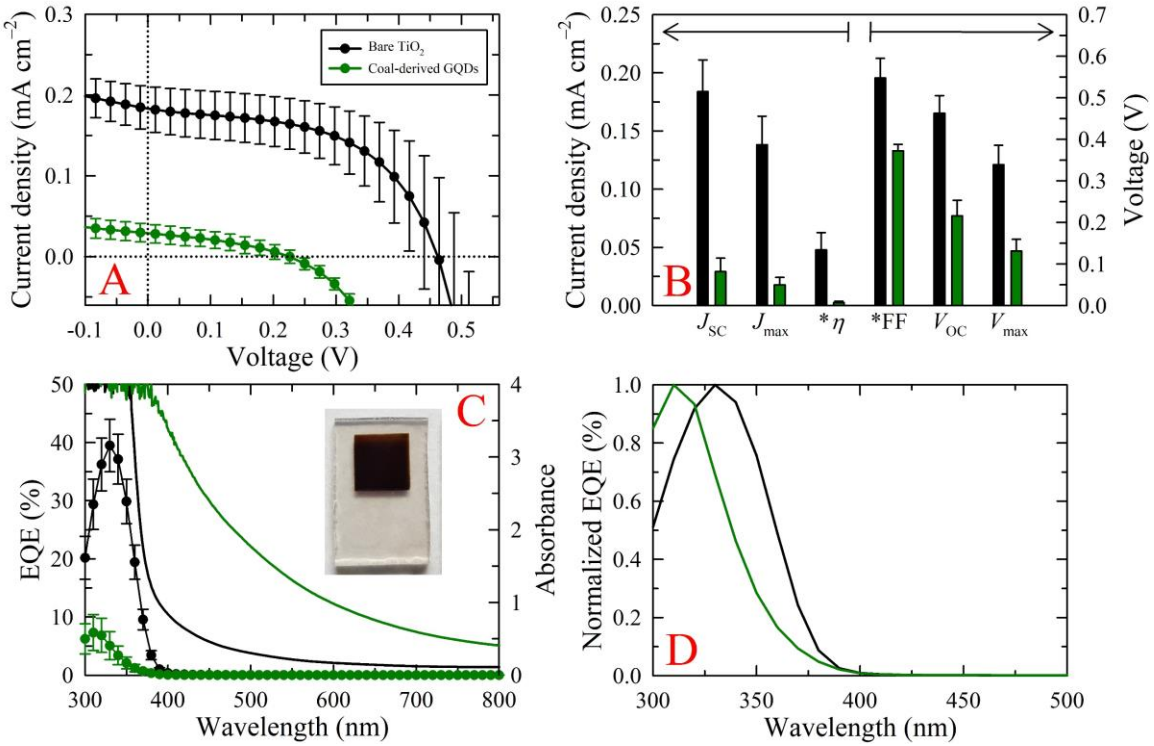

Figure D.23 Average *J-V* curves (with corresponding standard deviations) of devices employing TiO_2 films that were sensitized in an aqueous, 10 mg mL^{-1}, coal-derived retent. fraction that purportedly contains GQDs. (B) Average device metrics. *Note, efficiency (η) is reported in percent and FF is a unitless parameter but both values are on the same scale as the left and right y-axes, respectively. (C) Average EQE spectrum of the devices (left y-axis) and average absorbance spectrum of the films employed within (right y-axis). A representative photograph of the sensitized TiO_2 films is provided in the inset. (D) Plot of the normalized EQE spectra. The performance of bare TiO_2 (black curves) is provided in all relevant plots for comparison. Clearly, the highly graphitic nanocarbons negatively impacted PV action, decreasing the performance well below that of bare TiO_2 and generating near-zero power conversion efficiency, despite the intense uptake or high extinction coefficient of the material. Furthermore, the graphitic nanocarbons produced essentially no photocurrent and, in fact, substantially decreased the photocurrent arising from TiO_2 and hypsochromically shifted the EQE peak by 20 nm.

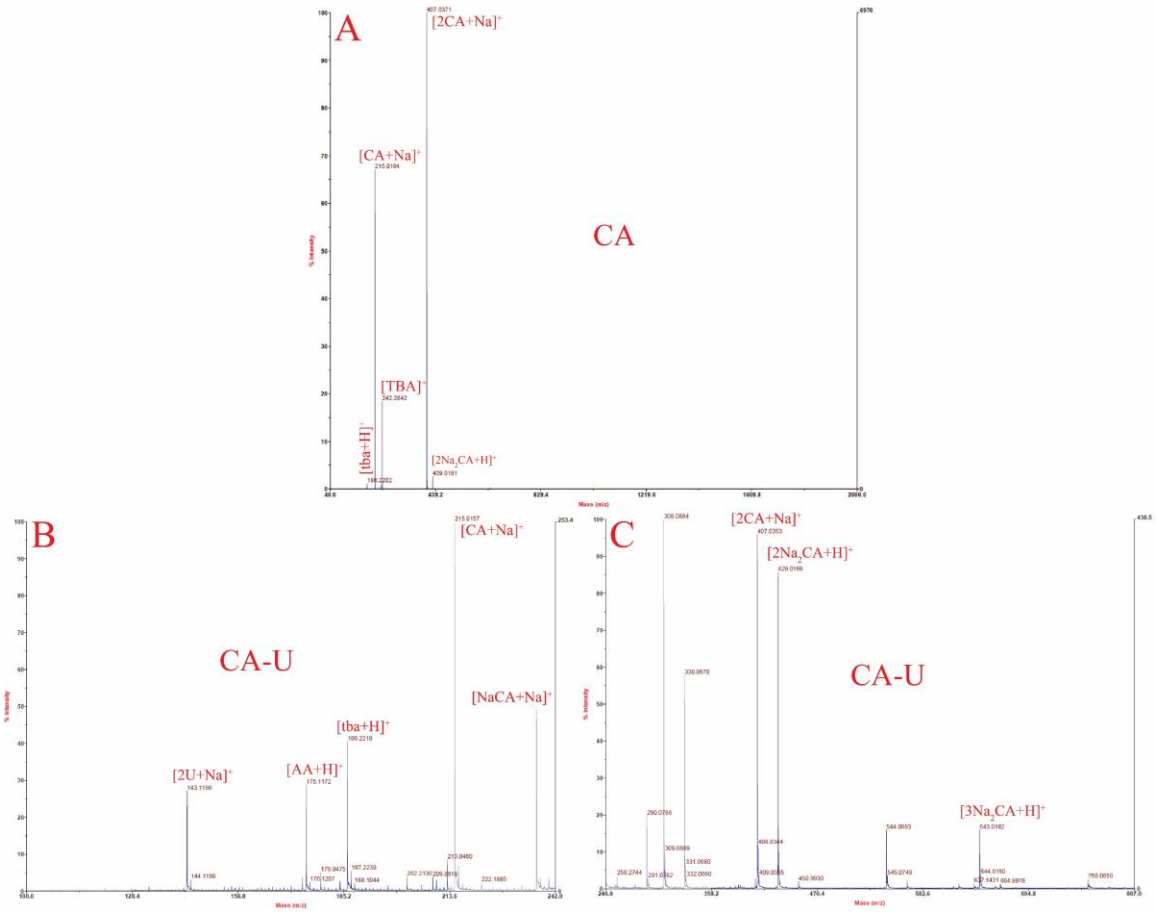

Figure D.24 Mass spectra of (A) CA and (B–C) CA–U precursor solutions from a *m/z* range of (B) 100–242 and (C) 246–807.

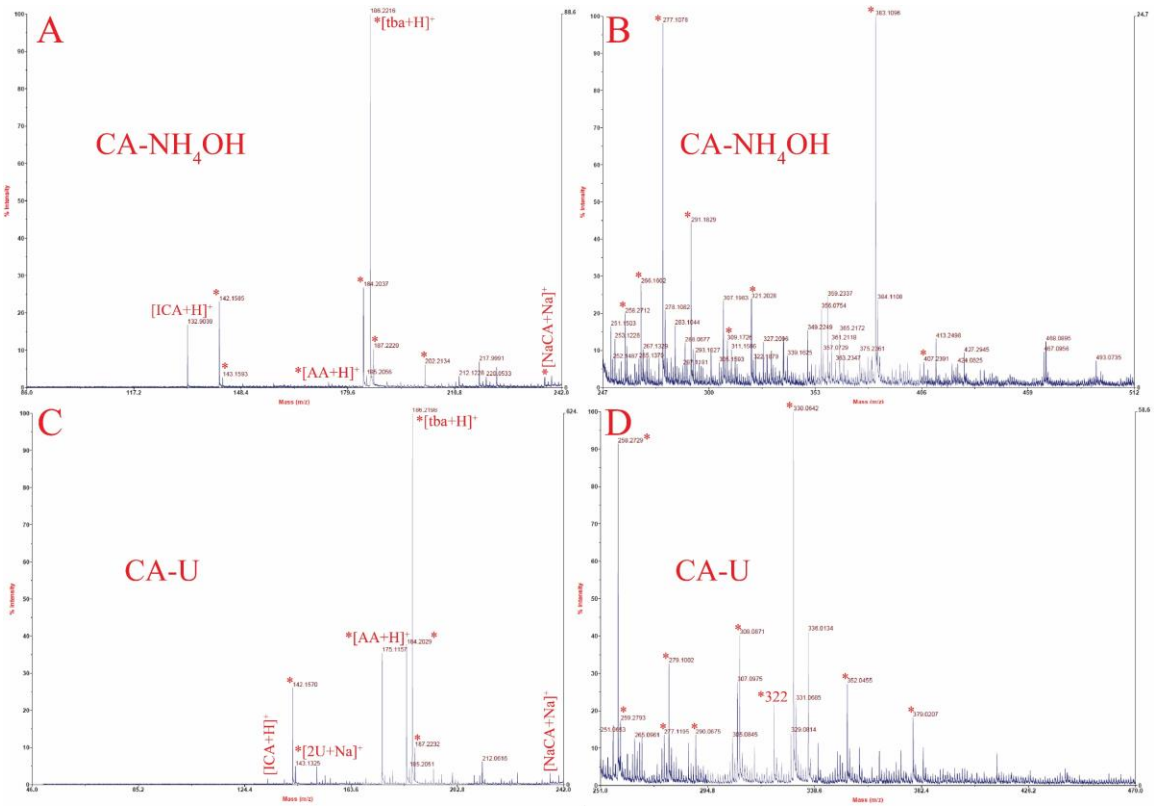

Figure D.25 Mass spectra of (A–B) CA–NH_4OH and (C–D) CA–U as-synth. fractions from *m/z* ranges of (A) 86–242, (B) 247–512, (C) 46–242, and (D) 251–470. An asterisk (*) next to a peak or peak assignment indicates that the peak was also observed in the precursor spectra.

Table D.1 Photovoltaic metrics for all device sets in Chapter 5 and Appendix D.

Precursor	Fraction	Conc. (mg mL^{-1})	Solvent System	Sens. Time	η (%)	J_{SC} (mA cm^{-2})	V_{OC} (V)	FF (%)
Bare TiO_2	–	–	–	–	$0.04_8 \pm 0.01_5$	0.184 ± 0.027	0.463 ± 0.042	54.75 ± 4.73
CA–NH_4OH	As-synth.	5 mg mL^{-1}	Acetone	2 h	$0.28_4 \pm 0.02_7$	0.827 ± 0.043	0.512 ± 0.007	67.05 ± 3.50
				24 h	$0.22_5 \pm 0.02_3$	0.732 ± 0.083	0.498 ± 0.005	61.94 ± 1.81
			Acetone/EtOH	2 h	$0.28_0 \pm 0.03_0$	0.823 ± 0.049	0.513 ± 0.004	66.19 ± 3.45
				24 h	$0.21_5 \pm 0.01_1$	0.709 ± 0.019	0.495 ± 0.003	61.15 ± 2.87
		10 mg mL^{-1}	Acetone	2 h	$0.26_9 \pm 0.02_0$	0.796 ± 0.037	0.507 ± 0.004	66.57 ± 3.37
				24 h	$0.22_8 \pm 0.00_8$	0.733 ± 0.012	0.512 ± 0.001	60.77 ± 1.67
			Acetone/EtOH	2 h	$0.30_1 \pm 0.03_2$	0.864 ± 0.049	0.514 ± 0.004	67.57 ± 3.37
		30 mg mL^{-1}	Acetone	2 h	$0.29_5 \pm 0.03_2$	0.850 ± 0.054	0.508 ± 0.005	68.23 ± 4.29
				24 h	$0.19_9 \pm 0.01_5$	0.617 ± 0.025	0.498 ± 0.001	64.68 ± 2.01
			Acetone/EtOH	2 h	$0.28_7 \pm 0.02_1$	0.807 ± 0.047	0.500 ± 0.004	71.09 ± 1.31
				24 h	$0.19_9 \pm 0.02_0$	0.635 ± 0.030	0.485 ± 0.004	64.51 ± 3.89
	As-synth. Aged		Acetone	2 h	$0.23_2 \pm 0.03_2$	0.695 ± 0.062	0.500 ± 0.007	66.43 ± 3.67
	As-synth. Aged		Acetone/EtOH		$0.28_2 \pm 0.04_7$	0.842 ± 0.071	0.511 ± 0.009	65.10 ± 4.59
	As-synth. Therm. Evap.		Acetone		$0.09_7 \pm 0.01_6$	0.373 ± 0.069	0.451 ± 0.018	57.91 ± 1.68
	As-synth. Rotovap.				$0.16_1 \pm 0.00_9$	0.583 ± 0.057	0.490 ± 0.006	56.69 ± 3.10
	As-synth. Therm. Treat.				$0.20_7 \pm 0.01_8$	0.631 ± 0.034	0.497 ± 0.005	65.93 ± 2.90
	Dial.	5 mg mL^{-1}	Acetone	2 h	$0.28_9 \pm 0.03_6$	0.828 ± 0.058	0.516 ± 0.007	67.49 ± 4.19
			Acetone/EtOH		$0.30_2 \pm 0.03_0$	0.862 ± 0.066	0.517 ± 0.008	67.83 ± 2.97
		10 mg mL^{-1}	Acetone		$0.32_3 \pm 0.03_3$	0.897 ± 0.059	0.521 ± 0.012	69.00 ± 2.14
			Acetone/EtOH		$0.31_9 \pm 0.04_1$	0.906 ± 0.077	0.516 ± 0.006	67.94 ± 2.48

CA–NH_4OH	Dial.	30 mg mL^{-1}	Acetone	2 h	$0.27_8 \pm 0.01_1$	0.826 ± 0.058	0.510 ± 0.006	66.25 ± 4.04
				24 h	$0.23_9 \pm 0.01_6$	0.743 ± 0.032	0.500 ± 0.002	64.30 ± 1.70
			Acetone/ EtOH	2 h	$0.33_7 \pm 0.03_4$	0.962 ± 0.054	0.517 ± 0.006	67.49 ± 3.54
	Retent.	1 mg mL^{-1}	Acetone	2 h	$0.10_1 \pm 0.01_7$	0.330 ± 0.043	0.471 ± 0.002	64.34 ± 2.88
		5 mg mL^{-1}			$0.10_0 \pm 0.01_5$	0.317 ± 0.037	0.474 ± 0.011	66.44 ± 3.54
			Acetone/ EtOH		$0.09_0 \pm 0.00_5$	0.294 ± 0.012	0.473 ± 0.006	64.46 ± 0.91
	Retent. + Dial.	1 mg mL^{-1} + 1 mg mL^{-1}	Acetone	2 h	$0.14_1 \pm 0.01_2$	0.474 ± 0.030	0.492 ± 0.001	60.61 ± 2.68
		1 mg mL^{-1} + 2.5 mg mL^{-1}			$0.21_9 \pm 0.00_8$	0.649 ± 0.036	0.517 ± 0.013	65.24 ± 2.72
		1 mg mL^{-1} + 5 mg mL^{-1}			$0.26_4 \pm 0.01_0$	0.767 ± 0.064	0.521 ± 0.011	66.19 ± 1.64
		1 mg mL^{-1} + 10 mg mL^{-1}			$0.34_0 \pm 0.02_7$	0.932 ± 0.042	0.529 ± 0.004	68.95 ± 2.85
		1 mg mL^{-1} + 30 mg mL^{-1}			$0.28_0 \pm 0.02_2$	0.812 ± 0.070	0.524 ± 0.003	65.86 ± 1.32
		1 mg mL^{-1} + 30 mg mL^{-1}	Acetone/ EtOH		$0.38_4 \pm 0.02_1$	1.083 ± 0.059	0.535 ± 0.002	66.26 ± 0.80
		5 mg mL^{-1} + 1 mg mL^{-1}	Acetone	2 h	$0.07_9 \pm 0.00_1$	0.267 ± 0.005	0.466 ± 0.002	63.43 ± 0.88
		5 mg mL^{-1} + 2.5 mg mL^{-1}			$0.12_2 \pm 0.00_8$	0.376 ± 0.019	0.479 ± 0.002	67.76 ± 1.30
		5 mg mL^{-1} + 5 mg mL^{-1}			$0.16_5 \pm 0.01_4$	0.488 ± 0.039	0.492 ± 0.002	68.71 ± 1.48
		5 mg mL^{-1} + 10 mg mL^{-1}			$0.22_8 \pm 0.00_7$	0.653 ± 0.015	0.507 ± 0.004	68.70 ± 0.80
		5 mg mL^{-1} + 30 mg mL^{-1}			$0.22_2 \pm 0.01_2$	0.633 ± 0.029	0.509 ± 0.002	68.69 ± 0.72
		5 mg mL^{-1} + 30 mg mL^{-1}	Acetone/ EtOH		$0.32_9 \pm 0.02_9$	0.913 ± 0.052	0.521 ± 0.001	69.10 ± 2.16
Arg	As-synth.	10 mg mL^{-1}	EtOH	12 h	$0.06_2 \pm 0.00_7$	0.190 ± 0.007	0.541 ± 0.008	59.86 ± 3.88
	As-synth. Filt.				$0.05_5 \pm 0.00_3$	0.173 ± 0.005	0.548 ± 0.009	57.99 ± 1.80
	Dial.				$0.04_7 \pm 0.00_5$	0.171 ± 0.009	0.472 ± 0.012	57.76 ± 2.11
	Retent.				$0.10_9 \pm 0.00_9$	0.297 ± 0.016	0.551 ± 0.005	66.36 ± 2.09
	As-synth.	30 mg mL^{-1}			$0.07_6 \pm 0.00_2$	0.196 ± 0.003	0.611 ± 0.002	63.25 ± 0.47
	Pellet	~8 mg mL^{-1}	DMSO		$0.06_1 \pm 0.00_1$	0.193 ± 0.004	0.510 ± 0.003	61.80 ± 0.43

CA–U	As-synth.	10 mg mL^{-1}	Water	2 h	$0.01_7 \pm 0.00_5$	0.106 ± 0.021	0.359 ± 0.029	42.60 ± 3.11
	As-synth. Aged				$0.04_2 \pm 0.01_4$	0.178 ± 0.043	0.421 ± 0.019	54.94 ± 5.81
	Dial.				$0.02_5 \pm 0.00_8$	0.127 ± 0.023	0.394 ± 0.023	48.13 ± 5.84
	Dial. Aged				$0.03_5 \pm 0.01_4$	0.163 ± 0.044	0.416 ± 0.018	49.96 ± 6.21
	Retent.				$0.01_9 \pm 0.00_6$	0.110 ± 0.029	0.380 ± 0.018	45.10 ± 1.60
	Retent. Aged				$0.04_2 \pm 0.01_1$	0.176 ± 0.037	0.430 ± 0.004	55.43 ± 3.50
GSH–F	As-synth.	Unknown	Form-amide/ Water	24 h	$0.08_0 \pm 0.01_4$	0.266 ± 0.028	0.490 ± 0.013	61.05 ± 3.90
	As-synth. Aged				$0.07_1 \pm 0.01_3$	0.250 ± 0.039	0.477 ± 0.007	59.05 ± 2.15
	As-synth. Aged Films				$0.04_2 \pm 0.00_3$	0.168 ± 0.010	0.444 ± 0.017	56.43 ± 1.74
	As-synth. 200 °C				$0.03_5 \pm 0.01_1$	0.202 ± 0.031	0.397 ± 0.013	43.34 ± 5.06
	Dial.				$0.06_7 \pm 0.01_5$	0.230 ± 0.025	0.479 ± 0.022	59.96 ± 7.80
	Dial. Aged				$0.05_8 \pm 0.00_8$	0.208 ± 0.022	0.463 ± 0.004	59.65 ± 2.08
	Dial. Aged Films				$0.04_0 \pm 0.00_4$	0.157 ± 0.011	0.443 ± 0.010	57.61 ± 2.24
	Dial. 200 °C				$0.05_1 \pm 0.00_2$	0.212 ± 0.002	0.444 ± 0.006	54.53 ± 1.99
	Retent.	10 mg mL^{-1}	Water		$0.05_7 \pm 0.00_8$	0.225 ± 0.030	0.452 ± 0.012	56.25 ± 2.27
	Retent. Aged				$0.04_4 \pm 0.00_9$	0.187 ± 0.028	0.440 ± 0.004	53.75 ± 2.58
	Retent. Aged Films				$0.01_4 \pm 0.00_3$	0.078 ± 0.008	0.375 ± 0.013	45.62 ± 4.33
	Retent. 200 °C				$0.04_1 \pm 0.01_0$	0.193 ± 0.023	0.434 ± 0.009	48.89 ± 4.93
Coal	Retent.	10 mg mL^{-1}	Water	24 h	$0.00_2 \pm 0.00_1$	0.029 ± 0.012	0.216 ± 0.037	37.22 ± 1.54

Appendix E: Solar Simulator Setup and Operation†

†This appendix derives, in part, from material contained in the MS thesis entitled "*Dye Sensitized Solar Cells: Optimization of Grätzel Solar Cells Towards Plasmonic Enhanced Photovoltaics*" by J. Essner (Kansas State University, 2011). The information presented herein has been used with permission from the author.

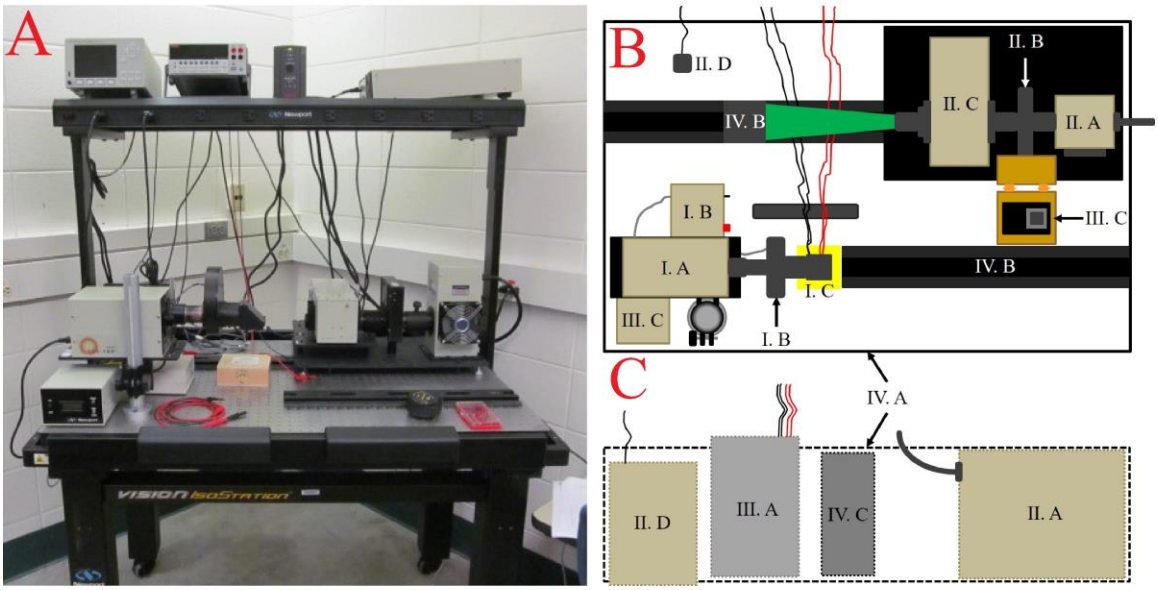

Figure E.1 (A) Photograph of the solar simulator system employed in all the studies discussed within this dissertation. (B–C) Schematical representation of the components comprising the solar simulator system shown in panel A. Specifically, panels B (solid lines) and C (dashed lines) represent the instrumentation/modules on the lower breadboard and upper shelf, respectively, where the provided identifiers correspond to the elements listed in Table E.1.

Solar Simulator System Components

The solar simulator system, shown in Figure E.1, both (A) photographically and (B) schematically, was sourced solely from Newport® Corporation and consists of the various (major) components listed in Table E.1. At the heart of the system are two separate light sources employed for producing the desired types of light common to solar cell characterizations, specifically, (I) broadband and (II) monochromatic light. The former,

Table E.1 Major components comprising the solar simulator system.

I. Solar simulator (broadband light)	**III. Characterization instrumentation**
A. 100 W Xe arc lamp and housing	A. Keithley SourceMeter™
B. Shutter and power supply	B. Laptop (not shown in Figure E.1)
C. AM1.5G filter with 90° beam turner	C. Certified Si reference cell
II. Monochromatic light	**IV. Miscellaneous**
A. 300 W Xe arc lamp, housing, and power supply	A. Vision IsoStation Workbench
B. Motorized filter wheel and filters	B. 24" optical rails and rail carrier
C. Motorized dual-grating monochromator	C. Uninterrupted power supply
D. Power meter and detector	

which is a class ABB Newport® Oriel® LCS-100™ solar simulator (94011A-ES), consists of a 100 W Xe (ozone free) arc lamp (I.A), a motorized shutter (I.B), and, the key component, an air mass (AM) 1.5G filter affixed within a 90° beam turner (I.C). This precalibrated setup is certified (by Newport's Photovoltaic Calibration and Test Laboratory) to produce a collimated 100 mW cm^{-2} beam of simulated solar radiation at a specified distance from the beam turner. The vital element, the AM1.5G filter, is a unique optical filter specially designed to mimic the electromagnetic radiation of the sun (*i.e.*, ultraviolet, visible, infrared) incident on the Earth's surface at an angle of 48.2° (relative to the Zenith angle) and after atmospheric absorption by greenhouse gases (*e.g.*, CO_2, H_2O, O_3, O_2). Figure E.2 depicts the exact function of this filter and the origin of the filter's name, AM1.5G. Specifically, Figure E.2A schematically shows the origin of select air mass designations while panels B and C display solar radiation spectra above the atmosphere,

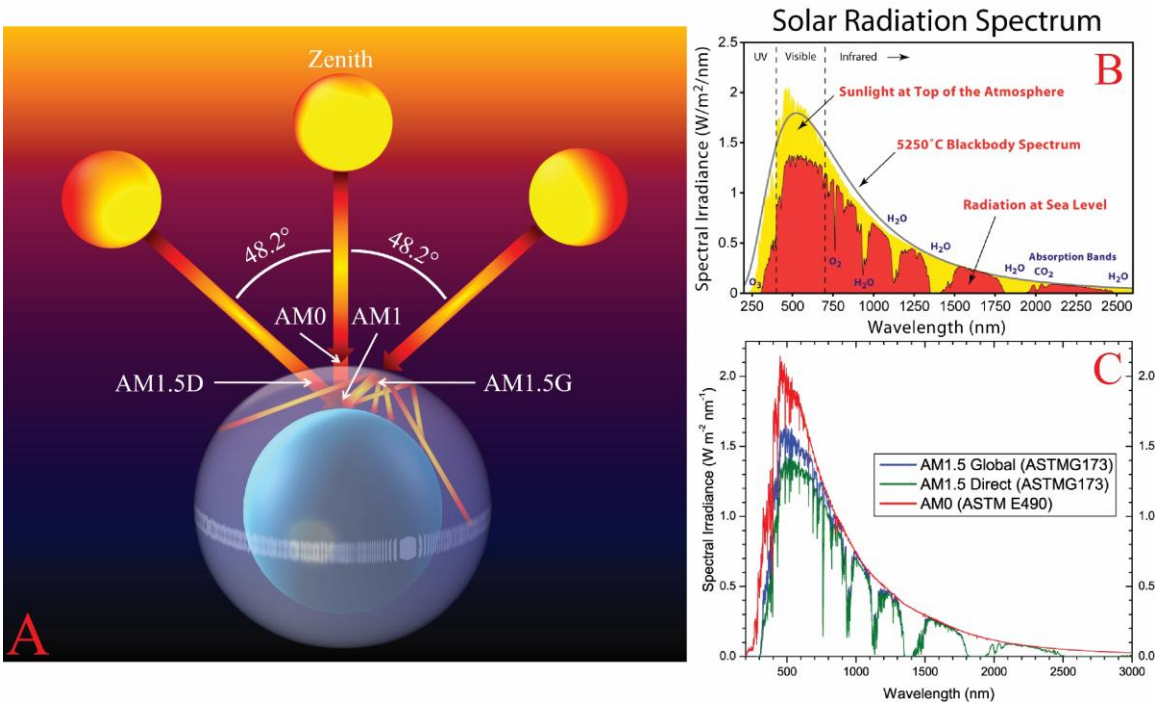

Figure E.2 (A) Schematic representation of the origin of various air mass (AM) classifications, specifically, AM0, 1, 1.5D, and 1.5G, which are the solar radiation at the top of the Earth's atmosphere at the Zenith angle, solar radiation at the Earth's surface at the Zenith angle, direct solar radiation at the Earth's surface at a 48.2° angle (relative to Zenith), and both direct and diffuse solar radiation at the Earth's surface at a 48.2° angle (relative to Zenith), respectively. The solar radiation spectra arising from AM0 and AM1.5 conditions are shown in yellow and red, respectively, in panel B, with simulated spectra of these conditions (*i.e.*, AM0, AM1.5D, AM1.5G) provided in panel C. AM1.5G filters employed in photovoltaic characterizations are designed to mimic the blue "AM1.5 Global" spectrum shown in panel C. Panels B and C were used with permission from references 1 and 2, respectively. Copyright © 2007 Robert A. Rohde (panel B) and Copyright © 2010 Christiana Honsberg and Stuart Bowden (panel C; original work and data from SMARTS modeling program used at the National Renewable Energy Laboratory).

below the atmosphere, and simulated solar radiation for these air mass (*i.e.*, AM0, AM1.5D, AM1.5G) conditions, where the latter is the spectrum the filter is designed to mimic.[1-2] Due to the variability in solar irradiance on the Earth's surface from fluctuating

atmospheric conditions, the systematic characterization of photovoltaic devices necessitated the development of standardized solar radiation spectra and incident power. These standardized light intensities are designated as AM0, 1, 1.5, and 2 for outside the atmosphere at the Zenith angle (red spectrum in Figure E.2C), on the Earth's surface at the Zenith angle, on the Earth's surface at a 48.2° angle (relative to Zenith), and on the Earth's surface at a 60.1° angle (relative to Zenith), respectively. Furthermore, AM1.5 solar radiation has two distinctions, specifically, AM1.5D (green spectrum in Figure E.2C), which only includes direct radiation, and AM1.5G, where "G" stands for global, which includes both direct and diffuse radiation (blue spectrum in Figure E.2C). The solar intensity of AM1.5G sunlight is calculated to be ~970 W m^{-2} but, due to the aforementioned variations in intensity from changing atmospheric conditions, the value is standardized to 1000 W m^{-2}, although the most widely employed value is 100 mW cm^{-2}, commonly referred to as 1 sun. To ensure that the simulated solar light is within its certified 100 mW cm^{-2} output prior to each use, the system is armed with a calibrated (by VLSI Standards, Inc., using a master reference cell certified by the National Renewable Energy Laboratory) Newport® Oriel® silicon reference cell and meter (91150V; III.C) whose performance metrics are certified to fall within a specific range under 1 sun illumination. Since the solar simulator unit is suspended above the breadboard table via attachment to a pole with an inset track that permits alteration of the vertical distance between the light source and solar cell, the certified Si reference cell allows the height to be adjusted as the lamp ages such that the system remains calibrated at 100 mW cm^{-2}. Additionally, the system is equipped with a neutral density filter set (FS-ND), that includes eight filters, for conducting low-light intensity measurements that mimic solar conditions less than 1 sun

such as intense cloud cover or small angle incidence (*i.e.*, sunrise, sunset). A final important component of the broadband light setup is the motorized safety shutter, which enables the incident light to be interrupted during data collection to assess how devices, specifically, their photocurrent and photovoltage, behave under rapidly changing illumination.

The other light source arrangement, which generates monochromatic light, consists of a (II.A) power supply (OPS-A500) to drive a housed (67005) 300 W ozone-free Xe arc lamp (6258), whose collimated irradiation is directed through 280, 550, or 1000 nm longpass filters (10CGA-280, -550, and -1000, respectively), secured in a (II.B) motorized, 6-position filter wheel (74010), prior to wavelength selection with a (II.C) Newport® CS 130 dual grating monochromator (CS130-USB-1-MC). The separation of broadband light into its monochromatic components is crucial for understanding observed device performance, specifically, the photocurrent, since irradiating the device with monochromatic light allows the exact origin of the photocurrent to be elucidated via external quantum efficiency measurements (described in Appendix G). To conduct such measurements, the power density at each wavelength must be measured, a task that is accomplished with a (II.D) Newport® power meter (1936-R) equipped with a UV silicon detector (918D-UV-OD3R). Both the monochromator and power meter are controlled with Newport's TracQ™ Basic Data Acquisition and Spectroscopy software (version 6.5).

The system also consists of a (III.A) Keithley 2400 SourceMeter™ for biasing the devices and measuring the resultant photocurrent (PVIV-1A), Oriel® I-V Test Station software for collecting and analyzing all *J-V* data (part of the PVIV package), (IV.B) multiple optical rails (PRL-24) and a rail carrier (PRC-3) with micrometer-driven (SM-50) translation stages (433), and all necessary hardware and accessories. Lastly, all the

aforementioned components are mounted to a (IV.A) Newport® Vision IsoStation breadboard-topped workbench (VIS3048-IG2-125A), as shown in Figure E.1, sporting front and rear support bars (VIS-HG-48), an overhead shelf with built-in power strips (VIS-ATS-48), and a sliding lower shelf (VIS-S1430; not shown in Figure E.1). The laptop computer (III.B) and uninterrupted power supply (IV.C) were sourced separately.

Solar Simulator System Setup and Calibration

Once the solar simulator system was procured, it was fully assembled (as shown in Figure E.1) and the lamps were aligned and calibrated. As previously mentioned, the Newport® Oriel® LCS-100™ solar simulator is certified to produce a uniform, 100 mW cm^{-2} beam of collimated, simulated solar radiation at a designated distance, therefore, this setup only required proper calibration of the height of the simulator above the breadboard with the Si reference cell. On the other hand, since the housed 300 W ozone-free Xe arc lamp was not precertified, the lamp required alignment and calibration, where the uniformity of the incident beam is absolutely critical to safe and stable operation, as well as appropriate characterization. Figure E.3 schematically shows potential beam irradiances emanating from the lamp. Ideally, the incident radiation from the arc lamp would be of equal power across the entire beam face (perfectly uniform/collimated) as visualized in Figure E.3A. In reality though, there is a power maximum at the center of the beam and the beam power drastically decreases as a function of distance from the apex (Figure E.3B). Thus, the goal is to align the lamp and internal mirrors in the housing in such a manner that the maximum power is nominally the same across a substantially larger area (Figure E.3C).

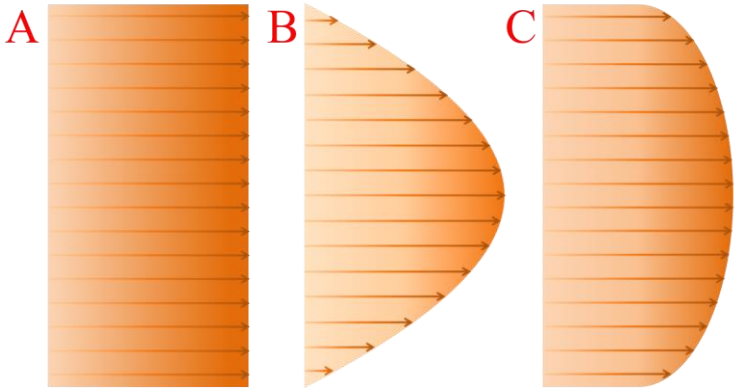

Figure E.3 (A) Ideally, an incident beam of light irradiating from the lamp would possess uniform power across the entire beam. (B) Realistically though, the power magnitude of the incident beam is more conically shaped; that is, a Gaussian distribution with high power at the center and decreasing power away from the apex. (C) Therefore, the goal is to align the lamps and collimate the emanating light such that a more uniform power distribution (*i.e.*, dome-shaped) is achieved.

To accomplish this (*i.e.*, maximize beam uniformity), four critical parameters were optimized: (i) the position of the lamp arc, (ii) the reflector mirror position, (iii) the distance between the arc and the condenser lens, and (iv) device placement, that is the distance from the lamp and position within the collimated beam. Specifically, the first steps for alignment were to position the arc in the center of the reflector mirror and the condenser lens through horizontal and vertical adjustments of the arc lamp mount using the appropriate knobs on the outside of the lamp housing. Once the lamp was roughly centered in the reflector mirror, the condenser lens was slid as close as possible to the lamp housing and peering down the condenser tube (with the lamp off!), the arc was further centered in the back reflector mirror and the condenser lens. This was done by adjusting the vertical and horizontal positions on the lamp, as well as the x, y, and z axes of the reflector mirror until the inverted arc image (seen in the reflector mirror) was overlain and aligned nicely with the actual arc.

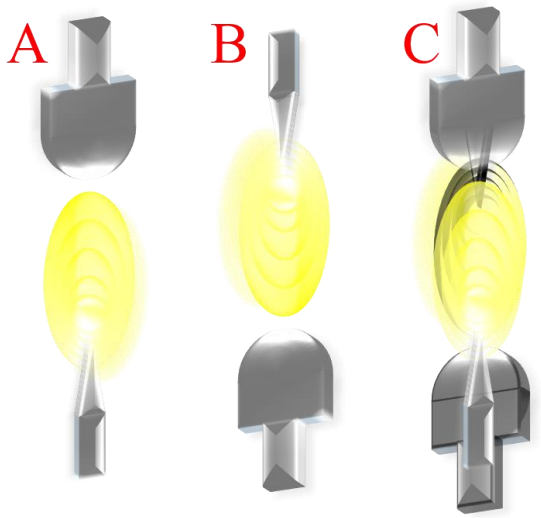

Figure E.4 For proper alignment of the 300 W arc lamp, the (A) actual arc and the (B) arc image created by the back reflector mirror need to be (C) superimposed in such a manner that the "hot spots" of the electrodes (tip of point electrode) do not lie directly over the larger curved anode.

The ideal placement of the inverted arc image over the arc can be seen in Figure E.4 (A - arc, B - inverted arc image, C - superimposed arc and arc image). For ideal alignment, the inverted arc image (outlined in black) would be perfectly superimposed over the actual arc but this would put the arc hot spots (point electrode - cathode) directly over the curved electrode (anode) and would cause the lamp to overheat. Therefore, the inverted arc image was superimposed over the arc such that the arc hot spots were just inside the anode and anode image. The hot spots were situated far enough from each other to keep them from directly overlapping but they were placed close enough so that they did not fall onto the anode or anode image. This placement allowed for the brightest points of the arc and the arc image to overlap such that a near circular beam was irradiated from the lamp housing (condenser lens).

With the inverted arc image aligned nicely over the actual arc, the lamp was turned on and fine tuning of the beam uniformity was conducted. Before fine tuning though, the

condenser lens was slid forward to diverge the beam and using the monochromatic-capable power meter and detector, a suitable distance from the lamp was chosen to yield the highest power density while still providing a large enough beam area to encompass devices undergoing testing. Once the distance from the lamp was set, the other three parameters could be slightly adjusted to bring the beam uniformity as close to unity as possible. To assess the wavelength-dependent beam uniformity, power readings as a function of wavelength were recorded in both the x (horizontal) and y (vertical) directions using the power meter and the rail carrier/translation stage. After each uniformity test, slight adjustments in the reflector mirror position, lamp position, and/or condenser lens position were made and the uniformity was re-assessed. Note, tuning in the y-direction also affects the x-direction uniformity so both axes must be aligned simultaneously. Lastly, this entire process must be repeated upon installation of a replacement lamp.

Solar Simulator Operation

The appropriate lamp(s) for the desired characterization(s) to be conducted should be turned on at least 30 minutes prior to commencing measurements; the 100 W solar simulator system is for collection of illuminated, broadband *J-V* curves while the 300 W lamp is for monochromatic power and short-circuit current density measurements for external quantum efficiency (EQE) calculations. The details of these measurements and their results are described in Appendix G. If EQE measurements will be conducted, this lamp should be powered on first as it requires a massive power dump to initiate the arc, a current surge that *could* negatively impact other instrumentation or components on the same circuit if they are powered on. Note, all instrumentation, except the power supply for controlling the 300 W lamp, is plugged into the power strips along the front and back of

the upper shelf of the IsoStation breadboard-topped workbench; the power supply for controlling the 300 W lamp is plugged directly into a wall outlet due to the power surge required to ignite the arc. The two plugs providing power to the power strips are plugged into an uninterrupted power supply (UPS) so that surges do not destroy any instrumentation and the UPS is plugged directly into a wall outlet.

To power on the 100 W lamp, flip the switch on the back and allow the lamp to warm up; for lamp shutdown, simply toggle the same switch. Conversely, powering on the 300 W lamp is a little more complex. First, the lamp's power supply must be turned on using the large, black "Power" switch on the far right of the front of the power supply. The power supply was previously setup upon initial installation, following the instructions in the appropriate manual, so the supply should be prepared for use once on. Allow the supply to power up, which should take <30 s, and then press the "Lamp Mode" button (elliptical button on the bottom left) to verify that it is in constant power mode; the power and power limit should be set at 300 and 330 W, respectively. Firmly press the square "Lamp" button once to initiate the arc; a small click or pop should be heard if the arc was initiated. Additionally, if the lamp is on, illumination should be visible through the cracks of the lamp housing. The power applied to the lamp will rapidly rise to around 250 W and then slowly climb to 290–300 W as the lamp warms up. Once the lamps are on, the other components can be powered up. Specifically, the monochromator (via a metal toggle switch on the back of the housing), the power meter and detector (via a black push button on the front of the meter), and the source unit (via a grey push button on the front). All of these components will take 1–2 min to fully power on. Additionally, the shutter attached to the 100 W solar simulator could be powered on, however, it will have to be shut back

off to collect *J-V* curves under dark conditions, therefore, the shutter is usually left off until collection of curves under illumination.

Once the lamps and all other components are powered on and warmed up, the reference Si solar cell needs to be characterized to ensure the system is properly calibrated. The black and red wires (two black and two red; one of each for "4-Wire Sense", or "Sen", and the other for "Input/Output", or "I/O") should be removed from the back of the source unit (if they are still plugged in) and the single gray wire with four banana plugs on one end should be plugged in. The plugs are appropriately labeled for their designated location but, for clarity, the male "Sen" plugs go in the two female receptacles on the left while the male "I/O" plugs, with the black resistor box, go in the two female receptacles on the right; the central bulge on the banana clips, where the single wire bundle comes into the clips, should face to the right when looking at the back of the source unit. The other end of the wire is plugged directly into the reference Si cell housing (there is only one alignment where the wire properly interfaces with the Si cell receptacle) and the reference cell is placed in the appropriate location beneath the beam turner attached to the solar simulator housing/shutter assembly; the system is now ready for a calibration check. The laptop and appropriate software for the solar simulator will control all instrumentation and testing. The software for collecting *J-V* curves (Oriel® I-V Test Station) should be opened and the appropriate recipe should be loaded. Note, multiple preprogrammed recipes already exist for characterizing the reference cell and dye-sensitized solar cells (with different upper voltage limits), as well as collecting external quantum efficiency (described below), however, new recipes may be created where the bias direction (forward *vs* reverse; typically the latter is employed), voltage limits (depends on device architecture), the scan rate, the number of

data points collected, and the voltage dwell time are all adjusted. Dark and illuminated scans should be conducted on the reference cell; for the latter, the shutter should be turned on prior to collection by flipping the switch on the back of the shutter power supply module. The software has built-in functions to automatically analyze the *J-V* curves and calculate all relevant device metrics, which can be viewed on different tabs within the software, however, the generated files should be saved as text (.txt) files and then imported into Excel for further analysis. Since the device metrics can be viewed in the software, the files for the reference cell only need to be saved (*i.e.*, no further analysis is typically necessary) and the metrics can be directly compared to those specified for the reference cell when illuminated with 100 mW cm^{-2}. If all metrics fall within the specified ranges then the solar simulator is properly calibrated, however, if the values are outside of these ranges, adjustments to the height of the solar simulator off the breadboard need to be made until all metrics are within the specified ranges. Note, as the lamp ages, the solar simulator will slowly have to be lowered closer to the breadboard to keep the system within calibration. Eventually the system will not be able to be lowered any further so cells being characterized will have to be raised up closer to the simulator such that the irradiance is nominally 100 mW cm^{-2} (*i.e.*, the reference cell stays within the certified values). Once system calibration is verified, the reference cell should be safely stored away in its appropriate box, the grey wire should be removed, and the black and red wires are then put back in the source unit. The system is now ready to collect *J-V* curves of devices slated for characterization. To characterize individual devices, the black wires are connected to separate alligator clips attached to the cathode while the red wires are attached to separate alligator clips affixed to the photoanode.

To conduct external quantum efficiency (EQE) measurements, the power density at each wavelength of interest should first be collected. To ensure proper calibration of the lamp employed for these measurements, the EQE of the reference cell should be periodically collected, however, since the power density is collected during each measurement session, changes in these values provide a reliable indication if the lamp is aging. Furthermore, due to the nature of these measurements, as long as the power density and short-circuit current values are collected at the same distance from the lamp, minute changes to the power density over time are inconsequential. Based on the present calibration/alignment, the following steps should be followed for EQE collection. The center hash on the translation stage should be placed at 10.5" on the translation track and the vertical micrometer should be adjusted to 50 mm. Two bolts are then screwed into the translation stage, specifically, in the outer screw holes in the 3rd row down from the top, and the detector is carefully placed atop these screws (after removing the black plastic cover) such that the back of the detector is flush with the translation stage. A thick, black posterboard is arced over the translation track, keeping it flush against the monochromator housing, to create a tunnel for blocking as much stray light as possible. Wavelength-dependent power densities are then collected under dark and illuminated conditions using the Newport® TracQ™ Basic software, which is currently preprogrammed to collect power densities from 300 to 800 nm at a 10 nm interval with a one second dwell time at each wavelength using only "grating 2" in the monochromator and conducting a filter change from the 280 nm to the 550 nm longpass filter at the 550 to 560 nm grating transition. Note, the USB plugs for both the monochromator and power meter need to be plugged into the computer prior to initiating the software. Additionally, the built-in monochromator shutter

should be closed and opened via the software for the collection of dark and illuminated power densities, respectively. The generated files should be saved as text files (*i.e.*, .txt) for easy viewing and importing into Excel for further analysis, the software should be closed, and the detector should be carefully set aside, replacing the plastic cover for protection.

For collection of wavelength-dependent short-circuit current values of devices, the center hash of the translation stage should be shifted to 10” on the track and the vertical micrometer should be adjusted to 35–38 mm to account for differences in detector and device position within the beam. Note, this positioning places the cells nominally in the same beam area that the power densities were collected, although, minor adjustments may need to be done. The device, with the black and red leads still connected, is carefully shifted over to the translation stage, turning the device vertical, and placing a bolt through the top binder clip and mounting the cell directly to the translation stage by screwing the bolt into the top center screw hole. This latter step should be done cautiously as overtightening the bolt could force the binder clip open, causing catastrophic electrolyte leakage, while under tightening the bolt may cause the device to undesirably shift prior to or during measurements. Specifically, the bolt should be snuggly hand-tightened only to an extent that the mounted device has very little horizontal sway; keeping the aforementioned bolts (that support the detector) in place will help reduce this potential sway. Short-circuit current values (illuminated conditions implied) are then collected at a 10 nm interval from 300 to 800 nm using the Oriel® I-V Test Station software with the desired EQE recipe loaded, controlling the monochromator (*i.e.*, gratings, filters) with the Newport® Mono Utility (version 5.0.4) software. Note, different EQE recipes are already set up for

collecting a variety of data points (*e.g.*, 5, 10, 15, 30) per wavelength and, upon opening the Mono Utility software, the appropriate number of gratings should be selected (*i.e.*, 2) and the desired filter change at 550 nm must be input in the software every time. Upon completion of the data collection, the power densities should be re-collected such that the before and after values can be averaged and employed for data analysis. When all EQE characterizations are complete, the lamp should be shut off by firmly pressing the "Lamp" button once, however, the power supply for the lamp should not be turned off until the fan on the lamp housing conducts its cooling cycle and automatically powers down. For additional detailed operation of the individual components, as well as replacing the arc lamps, consult the provided user manuals.

References

1. Rohde, R. A. Solar Spectrum. 2007 https://en.wikipedia.org/wiki/Sunlight#/media/File:Solar_spectrum_en.svg (accessed 11/25/2020).
2. Honsberg, C.; Bowden, S. Standard Solar Spectra. 2010 http://www.pveducation.org/pvcdrom/appendicies/standard-solar-spectra/ (accessed 11/25/2020).

Appendix F: Detailed Preparation and Operation of Sensitized Solar Cells

Preparation of Substrates for use as Photovoltaic Electrodes

The industry standard substrate that is employed, for both the photoanode and cathode, in rigid, sensitized solar cells is soda-lime glass coated with a transparent conductive oxide (TCO), typically indium- or fluorine-doped tin oxide (ITO or FTO). Since the latter is known to possess a higher thermal stability, FTO-coated glass is the substrate of choice for the works described herein. Specifically, TEC™ 7 and TEC™ 8 (MS001695) FTO-coated glass were sourced from Pilkington Glass (Toledo, OH) and GreatCell Energy® (formerly Dyesol; Queanbeyan, Australia), respectively, where the number associated with each TEC™ product (*i.e.*, "7", "8") represents the sheet resistance of the FTO coating (*i.e.*, 7, 8 Ω sq.$^{-1}$). To ready the FTO-coated glass (referred to simply as "FTO") for electrode preparation, large plates (12" x 12") are first cut into nine smaller squares (4" x 4") with a laboratory glass cutting table (GC0101) procured from MSE Supplies (Tucson, AZ), after which each 4" x 4" square is then cut into 24 electrode-sized pieces (21/32" x ~1"). The cut glass should then be cleaned by sequentially sonicating the substrates for 60 min in a dilute solution of Alconox® detergent (0.5 wt%), an ethanolic solution of 0.1 M HCl, isopropanol, and acetone. After cleaning with detergent and ethanolic HCl, the glass needs to be thoroughly rinsed with water before proceeding to the next cleaning step and, after sonication in acetone, the substrates should be dried upright at 50–70 °C. The substrates should then undergo a $TiCl_4$ treatment to deposit a thin layer (*i.e.*, nanometers thick) of TiO_2 through the hydrolysis of $TiCl_4$ by placing them in a 40 mM aqueous $TiCl_4$ solution for 40 min at 70 °C (FTO side up). The deposition of this thin TiO_2 layer has been

demonstrated to be a crucial step in electrode preparation as the layer helps the thicker, photoactive layer better adhere to FTO and behaves as a blocking layer, preventing charge recombination between FTO and the electrolyte, a well-documented source of parasitic losses to performance.[1-4] Note, a well-trained hand can distinguish the FTO side from the bare glass side by lightly dragging a spatula across both sides, where the latter will result in little to no drag, however, measuring the electrical resistance with an ohm meter provides conclusive evidence for the FTO-coated side, as the nonconductive, bare-glass side is highly insulating. After the $TiCl_4$ treatment, the treated substrates need to be thoroughly rinsed with water and EtOH and dried upright at 50–70 °C. Note, the $TiCl_4$ treatment is not necessary for substrates to be employed as counter electrodes so cleaned FTO is used directly in the preparation of these, without any additional treatment(s).

Photovoltaic Photoanode Preparation

The intended area of TiO_2 application is first defined by placing either Scotch™ brand tape (two layers thick, ~60 μm per layer) or adhesive-backed, removable Cricut® Premium Vinyl™ (one layer thick, ~100 μm) onto the FTO side of the substrates as application masks; in the case of the former, a mask that is approximately 0.5–1.0 cm^2 is formed with four pieces of tape to generate a "window" and a second layer of tape is applied over the existing layer, whereas, for the latter, the adhesive-backed, removable masks are simply placed directly onto the substrate. The vinyl masks are typically fabricated with outer dimensions of 1" x 0.620" (or ~25 mm x 15.8 mm) and a 1 cm^2 (1 cm x 1 cm) centered window, cut from a 12" x 48" roll of black Cricut® Premium Vinyl™ - Removable using Cricut Explore Air™ 2 or Cricut Maker® machines. A small amount of commercial transparent titania (TiO_2) paste (*e.g.*, GreatCell Energy® 18NR-T – MS002010, Sigma-

Aldrich – 791547) is then placed along any edge of the defined window and the paste is carefully spread across the mask in a single fluid pass with uniform pressure using a modified doctor blade approach (*e.g.*, a small glass stir rod turned sideways). Alternatively, in-house TiO_2 paste can be generated following well-established protocols,[5-7] however, this route often requires methodical refinement of the paste composition prior to use to obtain the desired consistency for easy application. After the deposition of TiO_2 paste, the masks should be cautiously removed to avoid perturbation of the applied paste and minimize adhesive transfer to the substrate, especially in the vicinity of the paste. The films should then be relaxed at room temperature in the dark for approximately 24 h, followed by drying in a programmable oven at 125 °C and 200 °C for 24 and 6 h, respectively. The dried films are transferred to a muffle or tube furnace and annealed at 525 °C for 1 h using a ramp rate of 1 °C min^{-1} to the sinter the TiO_2 nanoparticles into an interconnected, mesoporous network. Note, the films must be in direct contact with the ceramic base as any air gap between the substrates and the ceramic will result in poor film yield due to cracking and delamination. After the 1 h sintering period, the furnace is shut off and allowed to cool naturally with the films inside. Once at room temperature, if the films are opaque and white, the TiO_2 layer is poorly adhered to the substrate, which will lead to cracking/flaking or worse, delamination upon the slightest stress, meaning these films are unusable, however, if the preparation is performed properly, the resultant films will be semitransparent (*i.e.*, non-opaque) with a slight blue hue.

A second $TiCl_4$ treatment (40 mM at 70 °C for 30–40 min, TiO_2 side up) can then be conducted as this additional treatment is known to enhance performance by improving photoanode electronic properties,[3, 8] although, it has also been demonstrated that the

observed enhancement is sensitizer dependent.[9] If a second treatment is conducted, afterwards, the films should be carefully rinsed with water and EtOH, dried at 100–120 °C, and annealed at 500 °C for 1 h following the exact same protocol as the first annealing step. Again, if all steps are carefully and properly performed, the films should retain their semitransparency and blue hue. High quality films can be stored in the dark for months until needed.

To finalize the photoanode preparation, the high-quality TiO_2 films are then submersed in a solution of the desired sensitizer; the experimental conditions employed here (*i.e.*, solvent system, sensitizer concentration, adsorption time) are highly dependent on the exact sensitizer, therefore, if a published protocol is not followed, these parameters require optimization as part of the course of study. For devices employing the industry standard dye, N719 (procured from GreatCell Energy® – MS003190 or Sigma-Aldrich – 703214), TiO_2 films are sensitized for 12–24 h (some papers report < 4 h sensitization time) using a 0.5 mM solution of the dye dissolved in 1:1 v/v acetonitrile:t-butyl alcohol.

Photovoltaic Cathode (Counter Electrode) Preparation

Industry standard platinum (Pt) counter electrodes are prepared on precleaned FTO-coated glass by placing strips of Scotch™ brand tape (one or two layers thick) along the long edges of the glass to generate a "trough" and commercial Pt paste (*e.g.*, GreatCell Energy® PT-1 – MS006210, Sigma-Aldrich – 791512) is applied via the doctor blade technique. After carefully removing the tape layers, the films should be dried at 70–100 °C for 24 h and then fired at 450 °C for 1 h in a muffle furnace. The prepared Pt films can be stored for months before use and can also be reliably used in multiple devices as long as the Pt

film is still visibly intact and uniform; that is, if the spacer or electrolyte start to remove sections of the Pt film, the electrical discontinuity will start to show in device performance.

Electrolyte Preparation

In most instances, a commercial electrolyte solution containing the industry standard I^-/I_3^- redox couple (*e.g.*, Iodolyte AN-50 sourced from Solaronix, Aubonne, Switzerland) is employed for ease and to avoid any necessary optimizations of the electrolyte composition. The provided example electrolyte (Iodolyte AN-50) consists of a propriety blend of iodine, a lithium salt (likely, lithium iodide), an iodide-containing ionic liquid (*i.e.*, 1,2-dimethyl-3-propylimidazolium iodide), and a pyridine derivative dissolved in acetonitrile. Alternatively, in-house electrolyte blends can be prepared, however, similar to employing in-house paste formulations, if reported electrolyte compositions, such as those described in these reviews,[10-12] are not being employed then compositional optimizations must be undertaken.

Photovoltaic Device Assembly

Full devices are assembled by sandwiching a DuPont™ Surlyn® 25 or 60 μm spacer (Meltonix 1170-25 or 1170-60; sourced from Solaronix, Aubonne, Switzerland) between a sensitized TiO_2 photoanode and a Pt counter electrode, where the spacer has a precut window with inner dimensions slightly larger than the sensitized TiO_2 film and outer dimensions at least 1/8" greater than the inner measurements; that is, the spacer material should be ~1/16" wide on all four sides. These low melting point spacers are designed to effectively "glue" the two electrodes together upon mild heating, sealing the device, however, once sealed, the created void still needs to be filled with electrolyte. The easiest way to accomplish this is to drill two small holes in the Pt electrodes prior to device

assembly and, while the electrode "sandwich" is still warm from melting the spacer, electrolyte solution is continually pipetted onto one of the holes as the device is rapidly cooled to draw the electrolyte into the void, however, this approach can still lead to air bubbles within the spacing between the electrodes, an undesirable scenario that can negatively impact performance. This issue can be circumvented by employing a microfluidic setup sourced from IDEX® Health & Science. Specifically, NanoPort™ assemblies are epoxied over each hole in the Pt-coated substrate and microfluidic tubing is interfaced with the attached assemblies, with two microfluidic shut-off valves placed in line with the tubing; all tubing connections are made with the appropriate microfluidic adaptors. To fill the device, one valve is kept closed and a vacuum is pulled through the other, open valve. After pulling vacuum for ~5 min, the open valve is closed while still pulling vacuum, an electrolyte-filled syringe (completely purged of air) is attached to the other valve, and this valve is rapidly opened so that the electrolyte solution is drawn in by the vacuum. This methodology provides efficient filling, however, the aforementioned process may have to be carefully repeated multiple times to get the gap completely filled and devoid of air bubbles. Additionally, the required components are costly. An alternate, facile approach, that is both inexpensive and effective, is to sandwich the spacer between the electrodes with two 1" binder clips placed on the long sides of the device, leaving the spacer unmelted, and depositing electrolyte into the void by slightly relieving the pressure from one binder clip such that a small-bore needle can be carefully slid into the gap to slowly inject electrolyte, expelling excess electrolyte and air upon clamping the electrodes back together. While this latter methodology is the cheapest and simplest approach, the binder clips do not provide the necessary pressure to keep the device fully sealed for

extended (>1 day) studies of device performance, thus, if temporal stability studies are desired, the substrate interfaces of the sandwiched device should be liberally coated in the strongest epoxy available after assembly to seal off all possible (microscopic) gaps for electrolyte losses via evaporation of the volatile solvents. Additionally, while epoxying, the device should be held together with a clamp that provides stronger pressure than small binder clips (*e.g.*, plastic-coated c-clamp). Even if one of the two former filling approaches are employed, fully sealing the device with epoxy, most importantly, the drilled filling holes, is a wise decision to ensure any temporal stability studies undertaken can be conducted worry-free, alleviating any concerns of the device catastrophically failing due to electrolyte evaporation. Note, while devices can be refilled if they leak, the performance typically plummets upon refilling which is an undesirable outcome when attempting to conduct temporal stability studies. Regardless of the filling technique employed, the external areas of the sealed device should be carefully wiped down with an EtOH-soaked Kimwipe™ to remove any residual electrolyte and potential light scattering contaminants.

Photovoltaic Device Architecture and Operation

As detailed above, sensitized semiconductor-based solar cells typically consist of a mesoporous network of thermally fused, interconnected TiO_2 (or ZnO) nanoparticles sensitized with a photocurrent-producing chromophore (a dye or fluorescent nanoparticles (NPs) such as semiconductor quantum dots (QDs), carbon nanodots (CNDs), or nanoclusters (NCs)) as the photoanode and a catalytically active cathode (*e.g.*, Pt) with a redox-active electrolyte (*e.g.*, I^-/I_3^-) sandwiched between the two electrodes, an architecture that is schematically depicted in Scheme F.1. Assuming proper band alignment between the sensitizer/semiconductor and redox couple/sensitizer (shown schematically in

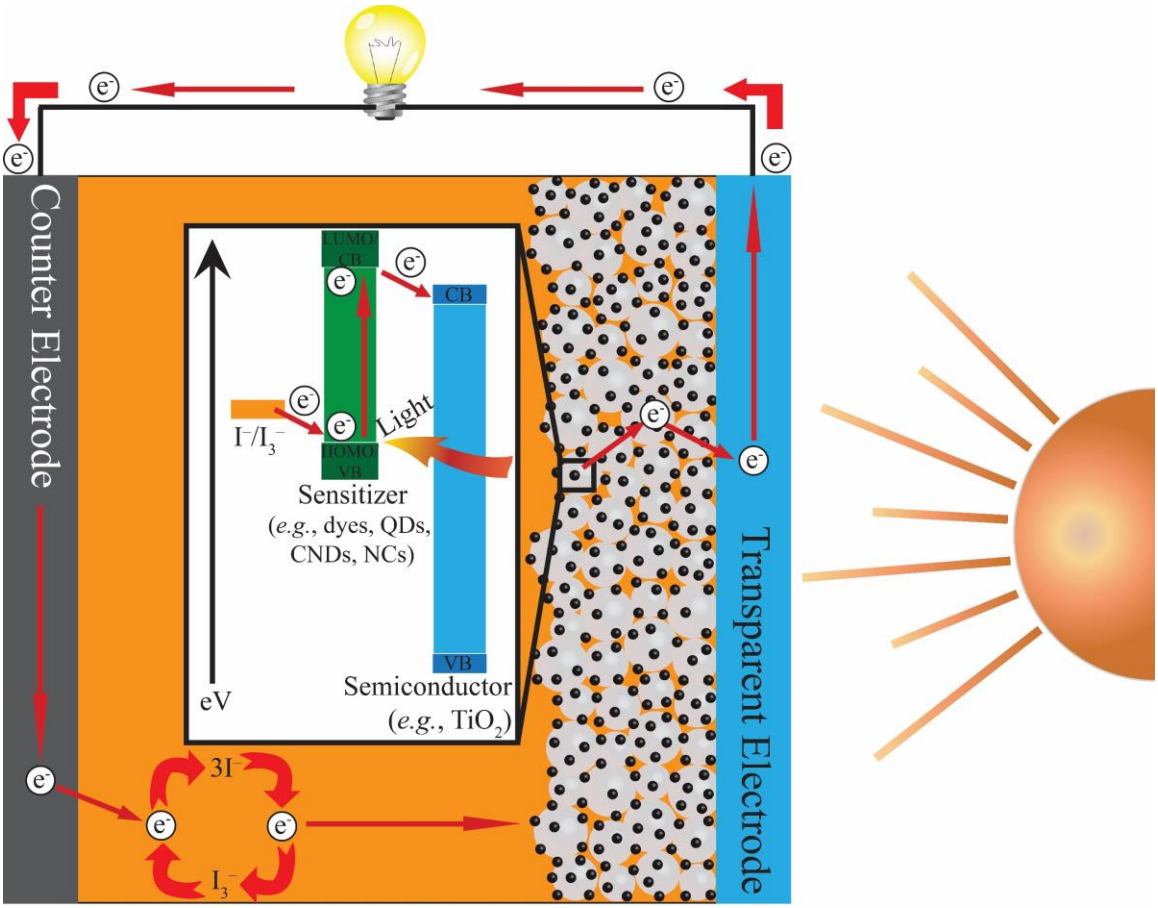

Scheme F.1 Schematic representation of the components of a fully assembled sensitized solar cell.

the inset of Scheme F.1) the following processes should occur: the chromophoric sensitizer will absorb incident light of the appropriate wavelength, exciting electrons from the highest occupied molecular orbital (HOMO) or valence band (VB) to the lowest unoccupied molecular orbital (LUMO) or conduction band (CB). The excited state electrons will then be injected into the semiconductor, oxidizing the sensitizer in the process, and the electrons randomly percolate through the interconnected network to the transparent electrode, where they are collected and leave the device to conduct external work such as illuminating a light bulb. The electrons re-enter the device through the cathode or counter electrode where they reduce the oxidizing agent of the redox couple (*e.g.*, I_3^-) to generate its reducing agent

counterpart (*e.g.*, I^-). The electron-carrying reducing agents then diffuse across the electrolyte gap between the electrodes and, upon reaching the electrolyte/sensitizer interface, reduce the oxidized sensitizer, regenerating it, as well as the oxidizing agent of the redox couple, such that another absorption event may occur to initiate the entire process again.

References

1. Ito, S.; Liska, P.; Comte, P.; Charvet, R. L.; Pechy, P.; Bach, U.; Schmidt-Mende, L.; Zakeeruddin, S. M.; Kay, A.; Nazeeruddin, M. K.; Gratzel, M., Control of Dark Current in Photoelectrochemical (TiO_2/I^--I_3^-) and Dye-sensitized Solar Cells. *Chem. Commun.* **2005**, 4351–4353.

2. Ito, S.; Murakami, T. N.; Comte, P.; Liska, P.; Grätzel, C.; Nazeeruddin, M. K.; Grätzel, M., Fabrication of Thin Film Dye Sensitized Solar Cells with Solar to Electric Power Conversion Efficiency over 10%. *Thin Solid Films* **2008**, *516*, 4613–4619.

3. Vesce, L.; Riccitelli, R.; Soscia, G.; Brown, T. M.; Di Carlo, A.; Reale, A., Optimization of Nanostructured Titania Photoanodes for Dye-sensitized Solar Cells: Study and Experimentation of $TiCl_4$ Treatment. *J. Non-Cryst. Solids* **2010**, *356*, 1958–1961.

4. M. Sharif, N. F.; Shafie, S.; Ab. Kadir, M. Z. A.; Hasan, W. Z. W.; Mustafa, M. N.; Samaila, B., The Effect of Titanium (IV) Chloride Surface Treatment to Enhance Charge Transport and Performance of Dye-sensitized Solar Cell. *Results Phys.* **2019**, *15*, 102725.

5. Opara Krašovec, U.; Berginc, M.; Hočevar, M.; Topič, M., Unique TiO_2 Paste for High Efficiency Dye-sensitized Solar Cells. *Sol. Energy Mater. Sol. Cells* **2009**, *93*, 379–381.

6. Al-Attafi, K.; Nattestad, A.; Dou, S. X.; Kim, J. H., A Comparative Study of TiO_2 Paste Preparation Methods using Solvothermally Synthesised Anatase Nanoparticles in Dye-sensitised Solar Cells. *Appl. Sci.* **2019**, *9*, 979.

7. Shakeel Ahmad, M.; Pandey, A. K.; Abd Rahim, N., Advancements in the Development of TiO_2 Photoanodes and its Fabrication Methods for Dye Sensitized Solar Cell (DSSC) Applications. A Review. *Renew. Sustain. Energy Rev.* **2017**, *77*, 89–108.

8. Sommeling, P. M.; O'Regan, B. C.; Haswell, R. R.; Smit, H. J. P.; Bakker, N. J.; Smits, J. J. T.; Kroon, J. M.; van Roosmalen, J. A. M., Influence of a $TiCl_4$ Post-treatment on

Nanocrystalline TiO_2 Films in Dye-sensitized Solar Cells. *J. Phys. Chem. B* **2006**, *110*, 19191–19197.

9. Du, Z.; Zhang, H.; Bao, H.; Zhong, X., Optimization of TiO_2 Photoanode Films for Highly Efficient Quantum Dot-sensitized Solar Cells. *J. Mater. Chem. A* **2014**, *2*, 13033–13040.

10. Wu, J.; Lan, Z.; Lin, J.; Huang, M.; Huang, Y.; Fan, L.; Luo, G., Electrolytes in Dye-sensitized Solar Cells. *Chem. Rev.* **2015**, *115*, 2136–2173.

11. Gorlov, M.; Kloo, L., Ionic Liquid Electrolytes for Dye-sensitized Solar Cells. *Dalton Trans.* **2008**, 2655–2666.

12. Sharma, K.; Sharma, V.; Sharma, S. S., Dye-sensitized Solar Cells: Fundamentals and Current Status. *Nanoscale Res. Lett.* **2018**, *13*, 381.

Appendix G: Interpretation and Analysis of Photovoltaic Data†

†This appendix derives from material contained in the MS thesis entitled "*Dye Sensitized Solar Cells: Optimization of Grätzel Solar Cells Towards Plasmonic Enhanced Photovoltaics*" by J. Essner (Kansas State University, 2011) and should be cited as: Essner, J., Dye Sensitized Solar Cells: Optimization of Grätzel Solar Cells Towards Plasmonic Enhanced Photovoltaics. Department of Chemistry, Kansas State University, 2011. The information presented herein has been used with permission from the author.

J-V Curves and Extracted Performance Metrics

The benchmark characterization for PV devices is the collection of current-voltage (*I-V)* curves under dark and illuminated conditions. For these measurements, the applied voltage on the device is systematically modulated and the resulting current is monitored, where the device can be either forward- or reverse-biased; that is, sweeping the voltage from negative to positive or positive to negative. Although, certain device architectures such as perovskite-based PVs can present with strong hysteresis between forward- and reverse-biasing. In our lab, devices are typically reverse-biased, sweeping the voltage from 0.75 V to -0.2 V but the exact voltage range depends on the device architecture, mainly, the employed sensitizer. The measured device current is typically reported in milliamps (mA), however, the collected current is dependent on the active area of the device, therefore, to normalize the photocurrent, the values are divided by the active area to yield current density (*i.e.*, mA cm^{-2}) and current density-voltage (*J-V*) curves.

J-V curves collected under illuminated conditions are the cornerstone of all PV measurements. Typically, devices are illuminated under the industry standard irradiance of 1 sun (or 100 mW cm^{-2}), although higher or lower power densities can be employed for

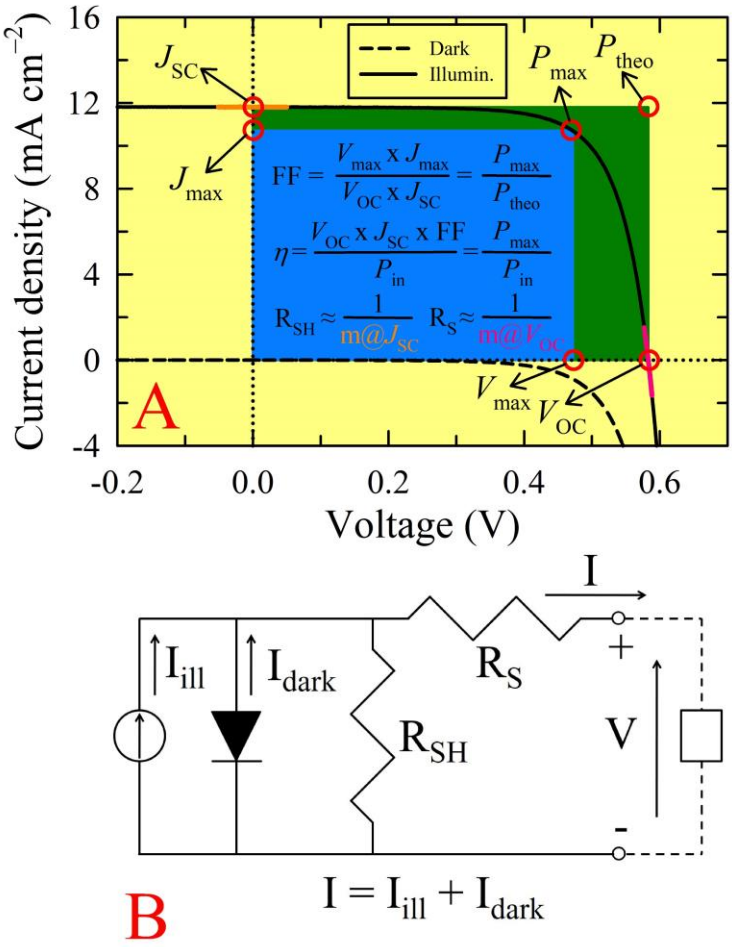

Figure G.1 (A) Schematic of representative *J*-*V* curves of a photovoltaic device collected under dark and illuminated conditions with major device metrics and their origins shown, specifically, short-circuit current density (J_{SC}), open-circuit voltage (V_{OC}), theoretical power output (P_{theo}), maximum power output (P_{max}), current density at P_{max} (J_{max}), and voltage at P_{max} (V_{max}). Additionally, the equations for calculation of fill factor (FF) and efficiency (η), as well as the approximation of shunt (R_{SH}) and series (R_S) resistances, are also provided in the inset. Such photovoltaic devices can be modeled by simple equivalent circuits such as that shown in panel B.

targeted high- or low-light conditions. Regardless of the intensity of the incident light, well-behaved devices should yield *J*-*V* curves comparable to that schematically shown in Figure G.1. A number of critical device metrics are then extracted from the illuminated curve,

specifically, the short-circuit current density (J_{SC}), current density at the maximum power (J_{max}), open-circuit voltage (V_{OC}), the photovoltage at the maximum power (V_{max}), fill factor (FF), shunt resistance (R_{SH}), series resistance (R_S), the theoretical power density (P_{theo}), and the maximum power density (P_{max}), which is equivalent to efficiency (η) when devices are illuminated under 100 mW cm^{-2}. The exact origin of these metrics from the illuminated *J-V* curve are shown in Figure G.1.

The J_{SC} arises when the applied voltage on the device is zero and is the maximum possible current that the cell can generate, while the V_{OC} occurs when there is not any current flow through the device and is the maximum obtainable voltage of the cell. Therefore, since current times voltage equals power, the product of these maximal photocurrent and photovoltage values yields the maximum theoretical power output (P_{theo}) that a device can generate. To provide a better context for discussing the other device metrics, specifically, FF and efficiency, an understanding of the (parasitic) device resistances (R_{SH} and R_S) and their origins is first necessary; R_{SH} arises from an absence of alternate current pathways (*i.e.*, power losses) in the device while R_S results from the combined (interfacial) charge transfer resistances throughout the entire device. Ideally, R_{SH} is large, meaning there are little to no alternate pathways for the current to flow other than the desirable pathway, which translates to very little power losses occurring throughout the device. Conversely, in the ideal scenario, R_S is extremely low due to minimal electrical resistance to charge transport through the device. These resistances can be approximated from the slopes of the *J-V* curve near zero current and zero volts, respectively. Specifically, R_{SH} is approximated by calculating the inverse of the *J-V* slope around J_{SC} (m@J_{SC}; orange line in Figure G.1A) while R_S is approximated by calculating the inverse of the *J-V* slope

about V_{OC} (m@V_{OC}; pink line in Figure G.1A). Thus, in the ideal scenario, devices produce essentially no slope near J_{SC} and an extremely large slope near V_{OC} yielding high shunt (*i.e.*, 1 / an infinitesimal slope = large value) and low series (*i.e.*, 1 / a prodigious slope = small value) resistances, respectively. In this theoretical scenario of a flawless device, an ideal *J-V* curve, represented by the green box in Figure G.1A, would arise, however, due to inherent charge-carrier losses from these unavoidable but minimizable parasitic resistances, the *J-V* curve deviates from the quintessential state, yielding a curve comparable to that shown (solid black line in Figure G.1A).

The charge-carrier losses stemming from non-ideal resistances that are observed in device *I-V* responses, under both dark and illuminated conditions, can be better visualized by representing the various device components with equivalent circuit models, as shown in Figure G.1B. Under dark conditions, the ideal device behaves like a diode, producing current, I_{dark}, while, under illumination, the device generates photocurrent, I_{ill}, which is modeled as an additional current-producing component in the circuit model. Thus, the total current produced by the device, *I*, is equal to the sum of I_{dark}, I_{ill}, and I_{SH}. Again, in an ideal device, R_{SH} is near infinite and R_S is near zero, resulting in the total current produced equivalent to the sum of just I_{dark} and I_{ill}, as evident in the circuit model. Specifically, if R_S is large, then charge transport through the circuit (*i.e.*, the device) is hindered, thereby decreasing *I* and the overall efficiency of the device (discussed below). Likewise, if R_{SH} is infinitesimal, then the device possesses undesirable, alternate pathways for charge transport which would result in a voltage drop across the circuit (*i.e.*, lower photovoltage) and, again, decreased device efficiency.

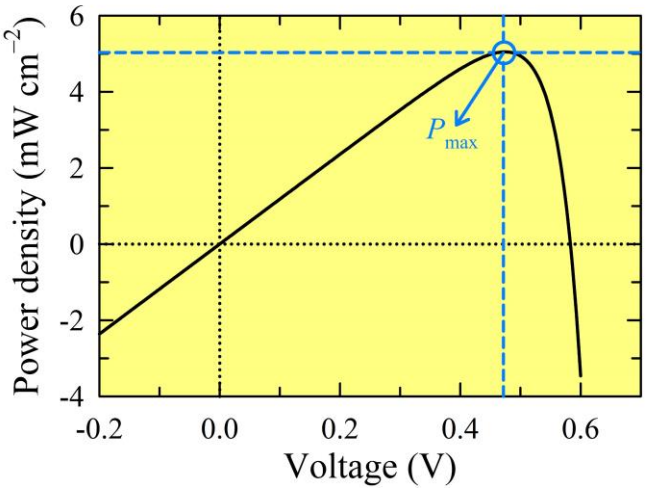

Figure G.2 The maximum power density output of a device can be determined by plotting the product of the current and voltage values *vs* the original voltage values. A near parabolic curve should be obtained where the apex of the curve equates to the maximum power output.

The aforementioned deviations from the ideal *J*-*V* curve give rise to other vital PV metrics utilized to characterize device performance, specifically, J_{max}, V_{max}, FF, P_{max}, and η. Since the product of current and voltage equals power, the corresponding photocurrent and photovoltage values can be multiplied together to yield power and the resulting power values can be plotted *vs* the applied voltage, which should produce a curve comparable to that shown in Figure G.2, where the vertex is equivalent to P_{max} and the specific photocurrent and photovoltage values that give rise to this power are represented by J_{max} and V_{max}, respectively. Then, using these determined parameters, the FF of the device can be calculated with the following formula:

$$FF = \frac{J_{max} \times V_{max}}{J_{SC} \times V_{OC}} = \frac{P_{max}}{P_{theo}}$$

Therefore, a device's FF is simply the ratio of the maximum power output (P_{max}) to the theoretical maximum power output (P_{theo}), which is essentially the ratio of the area of the

blue square to the area of the green square shown in Figure G.1A. Thus, FF provides a metric for the extent that the parasitic resistances are influencing the device; that is, low R_{SH} produces a decrease to J_{max} while high R_S yields a diminished V_{max}, scenarios that lead to poor FFs.

The final device metric, and undoubtedly the most critical in terms of device characteristics since it is the benchmark of device performance, is the power conversion efficiency (η), which is defined as the ratio of the maximum power output (P_{max}) to the power of the incident radiation (P_{in}) and is derived as such:

$$\eta\ (\%) = \frac{FF\ \times\ J_{SC}\ \times\ V_{OC}}{P_{in}} \times 100$$

$$\eta\ (\%) = \frac{J_{max}\ \times\ V_{max}}{P_{in}} \times 100$$

$$\eta\ (\%) = \frac{P_{max}}{P_{in}} \times 100$$

Given this, if devices are illuminated with the industry standard irradiance (*i.e.*, 100 mW cm^{-2}), the efficiency is simply equivalent to P_{max}.

While the *J-V* curves generated under illuminated conditions provide the majority of information pertinent to the observed device performance, *J-V* curves generated under dark conditions also provide vital information about charge transport, specifically, these curves can be used to determine the cathodic current of the device; that is, undesirable back reactions occurring within the device. This is accomplished by plotting the dark current over a specified voltage range, such as that highlighted by the red box in Figure G.3, on a log scale *vs* the applied voltage, which should yield a (relatively) straight line as shown in the inset. Comparisons of the resulting lines (*i.e.*, positioning of the lines on the y-axis) and

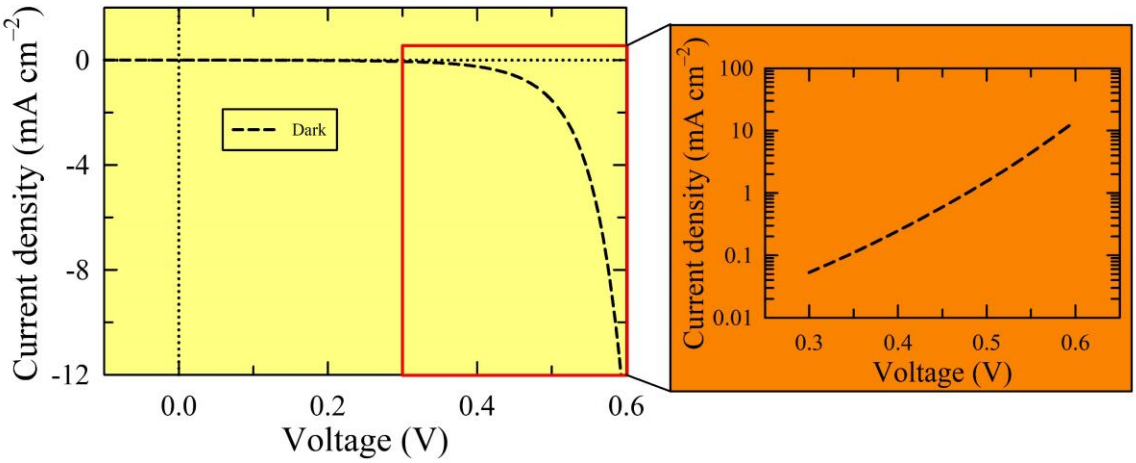

Figure G.3 Critical information regarding charge transport properties can be inferred from the *J-V* response under dark conditions by plotting the dark current density on a log scale *vs* a specified voltage range.

their corresponding slopes elucidate crucial details about the cathodic current and the charge transport properties of the device.[1]

External Quantum Efficiency

Of particular interest to device operation is the exact origin of the observed photocurrent. Specifically, since photocurrent is generated through incident electromagnetic radiation on the device's photoactive layer, it is useful to know which wavelengths within the electromagnetic spectrum are responsible for the production of photocurrent. Such characterizations are known as incident photon-to-current conversion efficiency (IPCE) or external quantum efficiency (EQE) measurements. Simplistically, EQE is the percentage of incident photons at each wavelength that are converted to harvested charge carriers; that is, converted electrons that are not lost to parasitic recombination and leave the device to do external work. For example, a wavelength-specific EQE of 50% indicates that for every electron produced and harvested, two photons of that wavelength were required. A schematic of a representative EQE spectrum for a dye-sensitized solar cell is provided in

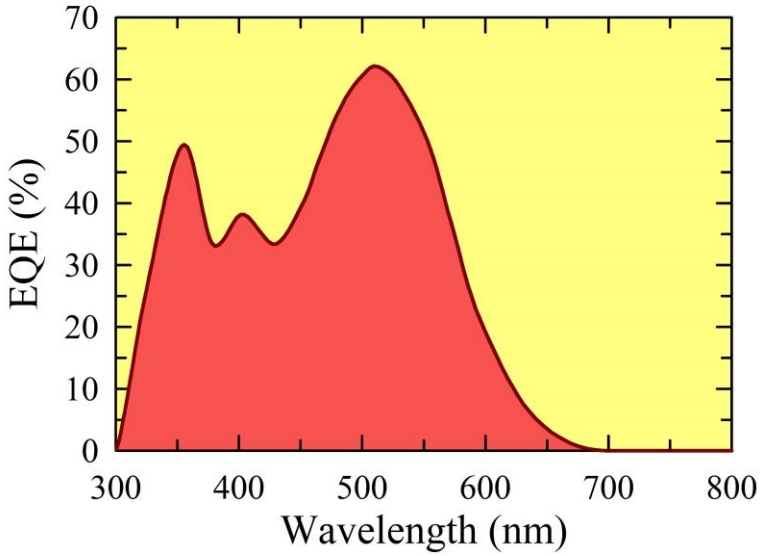

Figure G.4 Schematic representation of external quantum efficiency (EQE) for a device with a dye-sensitized semiconductor photoanode. EQE is a direct measure of how efficiently the device converts incident photons to electrons, and then current, at each wavelength. Ideally, the observed EQE peaks will correspond to the characteristic UV-vis absorption peaks of the photoactive sensitizer.

Figure G.4. While the derivation of EQE is quite complex,[2] the resulting formula for calculation of EQE only requires the wavelengths (λ_x) tested and the J_{SC} and P_{in} values that result from each wavelength probed, typically in μA cm^{-2} and μW cm^{-2}, respectively, as shown in the following equation:

$$EQE\ @\ \lambda_x\ (\%) = \frac{J_{SC}\ @\ \lambda_x\ (\mu A\ cm^{-2})}{P_{in}\ @\ \lambda_x (\mu W\ cm^{-2})} \times \frac{1240}{\lambda_x\ (nm)} \times 100$$

Therefore, to assess the EQE, the short-circuit current density and incident power at each wavelength (J_{SC} @ λ_x and P_{in} @ λ_x, respectively) are measured with a source measure unit or potentiostat and a monochromatic-capable power meter and detector, respectively, and the resultant values are analyzed with the above equation. In general, the EQE spectrum should correlate well with the absorption spectrum of the photoactive electrode, assuming all absorbing species/centers are capable of generating photocurrent (to some extent).

Specifically, the EQE spectral profile for a dye-sensitized solar cell employing the industry standard dye, N719, should strongly correlate with the UV-vis absorption spectrum of the sensitized film. Additionally, an EQE peak could also be present for the employed semiconductor such as the peak at ~350 nm in the schematic graph, which is attributable to the TiO_2 film.

Chronoamperometry and Chronopotentiometry

Two powerful techniques that allow the measurement of device stability and charge transport properties, particularly in photosensitizer-driven solar cells, are chronoamperometry and chronopotentiometry. For both temporal techniques the device is illuminated for a set time period and the irradiance is briefly interrupted (usually with a shutter) at designated intervals to observe how the respective photocurrent or photovoltage behaves under rapidly changing light conditions. Specifically, for chronoamperometry, the device is biased at 0 V and the short-circuit current (J_{SC}) is monitored during these illuminated/dark periods (Figure G.5). The stability of the device's photocurrent is easily visualized from the chronoamperogram; if the measured current density during the illuminated period remains virtually unchanged then the device is stable. The critical information that comes from chronoamperometry is whether photocurrent production is diffusion-limited due to slow charge-carrier transport through the electrolyte. If the device is not diffusion-limited, indicated by steady photocurrent during the illumination period, then the redox mediators are able to regenerate the sensitizer (*i.e.*, reduction of oxidized sensitizer) at the same rate that it is being excited and injecting electrons into the semiconductor support (*i.e.*, sensitizer oxidization). Conversely, when the device is diffusion-limited, a decay in photocurrent will be visible as shown in the second two

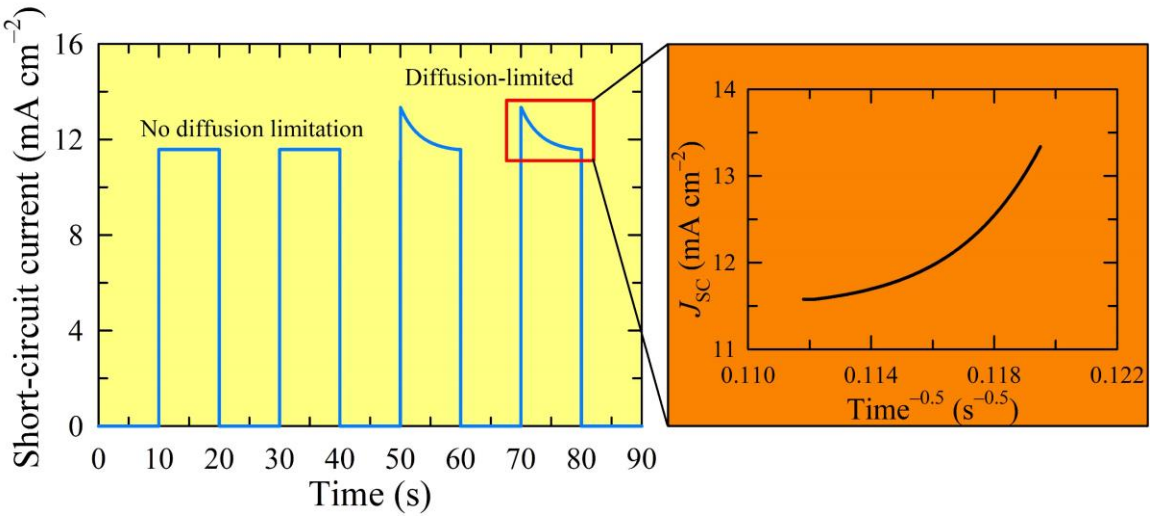

Figure G.5 Chronoamperometry provides vital information about device charge transport, namely, temporal stability of photocurrent, whether the photocurrent production is limited by diffusion, and, if so, what the diffusion coefficient of the electrolyte is. As the illumination is continually interrupted, a stable device will have the same current response during each illumination period; that is, a drop in photocurrent will not be observed over multiple dark/illuminated cycles. Conversely, if a decay in photocurrent is visible during each illumination period then the device's photocurrent production is limited by electrolyte diffusion. In this scenario, the photocurrent decay can be plotted *vs* time$^{-0.5}$ as shown in the outset plot and the apparent diffusion coefficient can be extracted from an appropriate fitting of the curve.

illumination periods of Figure G.5. Such a scenario arises as follows: upon illumination, the sensitizer species are excited and start to inject electrons into the semiconductor. The now oxidized sensitizer species are instantly regenerated by the redox couple present at the sensitizer/electrolyte interface, allowing continuity of the process. However, as the reducing agent of the redox couple that is in direct contact with the photoanode is quickly depleted, the oxidized sensitizer species now have to wait for more reducing agent to diffuse across the electrode gap to the photoanode before regeneration can occur. In other words, the sensitizer species are being oxidized faster than the redox couple can reduce

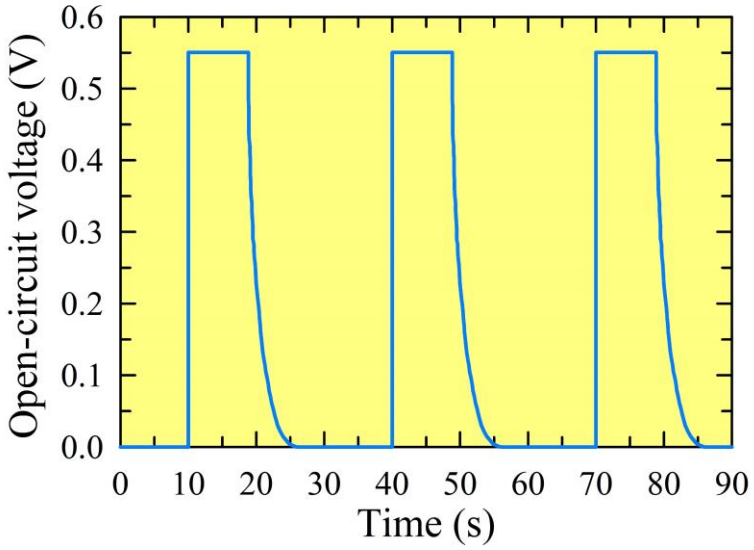

Figure G.6 Similar to chronoamperometry, chronopotentiometry can provide critical information regarding device stability and charge transport properties, specifically, the decay in the photovoltage can be used to determine the recombination lifetime of electrons within the electrolyte.

them, leading to the consumption of reducing agent before it can penetrate deeply into the semiconductor support network, a scenario that leaves many sensitizer species, particularly those deep within the network, in an oxidized state, rendering them effectively useless. As this process occurs over time, there is a buildup of ineffective, oxidized sensitizer species resulting in a decrease in photocurrent. Eventually, these processes, specifically, the diffusion limitation, reach equilibrium and the photocurrent no longer decays, reaching steady-state operation. The critical information that can be extracted from this photocurrent decay is the apparent diffusion coefficient of the redox couple. To do so, the photocurrent decay is plotted *vs* the inverse square root of time ($t^{-0.5}$) and, if a linear dependence is present, then the apparent diffusion coefficient of the redox couple can be extracted from a linear regression analysis (Figure G.5).[1]

Conversely, in chronopotiometry, the open-circuit voltage is monitored while the incident light is repeatedly interrupted at set intervals. However, similarly to chronoamperometry, chronopotiometry can be used to determine the stability of the photovoltage of the device (Figure G.6). The critical information that can be extracted from the chronopotentiogram is the recombination lifetime of electrons with oxidized species in the electrolyte through the photovoltage decay upon interrupting the illumination.[3-4]

Electrical Impedance Spectroscopy

One of the most powerful characterization tools for probing the charge transport properties of photovoltaic devices is electrical impedance spectroscopy (EIS). EIS can be performed under any bias within the working range of the solar cell and under any illumination conditions but conventional conditions are open-circuit (*i.e.*, zero current flow) and an incident power of zero or 100 mW cm^{-2}. In EIS, a harmonically modulated small-amplitude voltage is superimposed over the bias voltage (*i.e.*, open-circuit) which allows a small AC current to flow.[5] The resultant current is monitored over a predetermined frequency range and the impedance at each of the frequencies is calculated. A typical EIS spectrum, called a Nyquist Plot (Figure G.7A), is a plot of the real impedance (x-axis) *vs* the negative value of the imaginary impedance (y-axis). For photosensitizer-driven devices, typically three semicircles will appear, although the 3rd semicircle in the mHz region, which is the finite-Warburg impedance of electrolyte mass transport, can often vanish into the 2nd semicircle or may not be visible for devices with small electrode gaps.[5-6] The first semicircle, which represents the charge transfer resistance at the counter electrode, is usually in the kHz region while the 2nd semicircle, which represents the charge transfer resistances throughout the semiconductor and at the semiconductor/sensitizer/electrolyte interfaces, is usually in

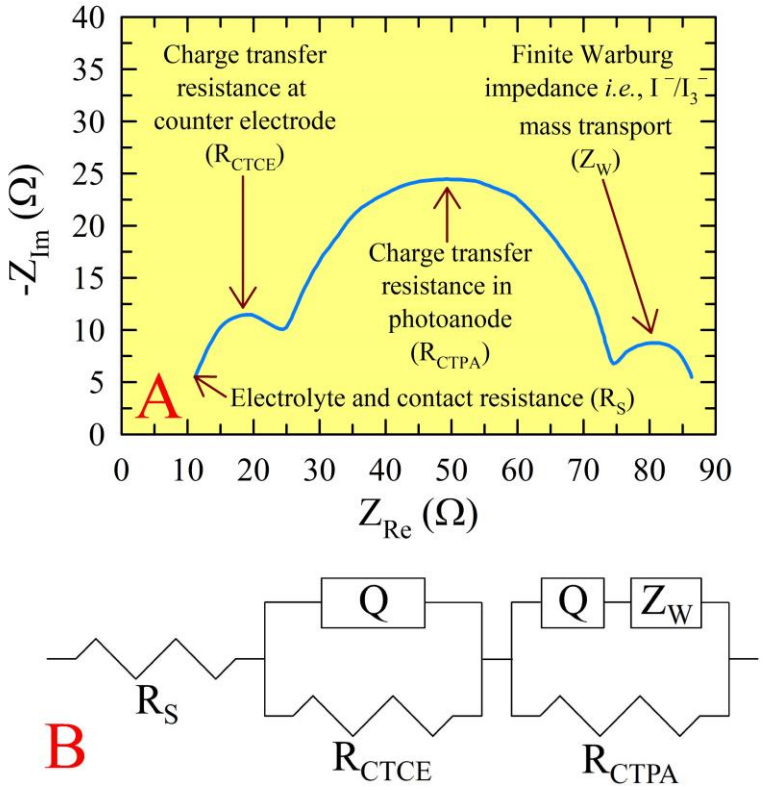

Figure G.7 (A) Schematic representation of a Nyquist plot obtained from the electrical impedance spectroscopic characterization of a dye-sensitized solar cell. The resulting Nyquist plot from such characterizations will typically consist of three semicircles which arise from: (i) the charge transfer resistance at the counter electrode (kHz region), (ii) the charge transfer resistance in the photoanode (Hz region), and (iii) the finite Warburg impedance (mHz region). The semicircles will be shifted to the right, or to higher resistance values, depending on the electrolyte and contact resistance. Plotting the same data in a Bode phase plot and extracting the peak frequency of the 2nd semicircle provides information about the electron lifetime within the semiconductor film. (B) The Nyquist plot can also be modeled by a resistor and two RC circuits in series, with one RC circuit containing a finite-Warburg Impedance element, Z_W. R_S corresponds to the resistance of the electrolyte and the electric contacts while the two RC circuits (Q = capacitor, C, of variable capacitance) represent the charge transfer resistances at the counter electrode/electrolyte interface (R_{CTCE}) and the dye/semiconductor/electrolyte (photoanode) interface (R_{CTPA}) as well as the double layer capacitances at each interface (Q).

the Hz region. Additionally, the electron lifetimes in the semiconductor layer can be determined through EIS by plotting the data in a Bode phase plot and extracting the peak frequency of the 2nd semicircle. Furthermore, using the appropriate software, the EIS data can be fit to an equivalent circuit (Figure G.7B). The resistance that arises from the electrolyte and the electrical contacts can be represented by a simple resistor labeled, R_S. The first and second semicircles are represented by simple RC circuits (a resistor and a capacitance component) in series. Both the first and 2nd semicircles require a capacitor of variable capacitance, represented by Q. This component arises from double layer capacitance at both the cathode/electrolyte (1st semicircle) and photoanode/electrolyte (2nd semicircle) interfaces. The resistors for the 1st semicircle (R_{CTCE}) and the 2nd semicircle (R_{CTPA}) correspond to the charge transfer resistances at the respective interfaces; that is, for the 1st semicircle, R_{CTCE} = charge transfer resistance at the counter electrode, while for the 2nd semicircle, R_{CTPA} = charge transfer resistance at the photoanode. Combining R_S, R_{CTCE}, and R_{CTPA} together yields the overall series resistance of the solar cell obtained from *J-V* analyses. To account for the third semicircle, the Z_W component, which models the finite-Warburg impedance of the electrolyte mass transport, needs to be incorporated. If the circuit model did not contain the Z_W component then only two semicircles would arise. Even with this component included, the 3rd semicircle is often not visible due to the thin nature of the device (not diffusion-limited) and/or the 2nd semicircle overlapping the 3rd; that is, the diffusion component is masked by the 2nd semicircle.[1, 5-6]

References

1. Sauvage, F.; Di Fonzo, F.; Li Bassi, A.; Casari, C. S.; Russo, V.; Divitini, G.; Ducati, C.; Bottani, C. E.; Comte, P.; Graetzel, M., Hierarchical TiO_2 Photoanode for Dye-sensitized Solar Cells. *Nano Lett.* **2010**, *10*, 2562–2567.

2. Kamat, P. V., Incident Photon to Charge Carrier Efficiency of Solar Cells. https://www3.nd.edu/~kamatlab/synthetic%20secrets/IPCE%20derivation.pdf (accessed March 20, 2021).

3. Schlichthorl, G.; Huang, S. Y.; Sprague, J.; Frank, A. J., Band Edge Movement and Recombination Kinetics in Dye-sensitized Nanocrystalline TiO_2 Solar Cells: A Study by Intensity Modulated Photovoltage Spectroscopy. *J. Phys. Chem. B* **1997**, *101*, 8141–8155.

4. Schlichthorl, G.; Park, N. G.; Frank, A. J., Evaluation of the Charge-collection Efficiency of Dye-sensitized Nanocrystalline TiO_2 Solar Cells. *J. Phys. Chem. B* **1999**, *103*, 782–791.

5. Kern, R.; Sastrawan, R.; Ferber, J.; Stangl, R.; Luther, J., Modeling and Interpretation of Electrical Impedance Spectra of Dye Solar Cells Operated under Open-circuit Conditions. *Electrochim. Acta* **2002**, *47*, 4213–4225.

6. Lai, Y. H.; Lin, C. Y.; Chen, H. W.; Chen, J. G.; Kung, C. W.; Vittal, R.; Ho, K. C., Fabrication of a ZnO film with a Mosaic Structure for a High Efficient Dye-sensitized Solar Cell. *J. Mater. Chem.* **2010**, *20*, 9379–9385.

VITA

Jeremy B. Essner was born in 1985 in St. Louis, Missouri to Donald and Theresa Essner. He grew up in the St. Louis area and attended De Smet Jesuit High School, graduating in 2004. As a St. Louis native, he is a diehard Cardinals fan.

After graduating high school, he attended Benedictine College in Atchison, Kansas, receiving a Bachelor of Science in Chemistry in 2008. During this time, he worked on a variety of research projects involving organic synthesis, heavy metal monitoring and remediation in local waters, and the electrochemical synthesis of nanomaterials. Upon graduation, he moved to Manhattan, Kansas to pursue higher education at Kansas State University. Under the direction of Professor Jun Li, he explored plasmonic enhancement of dye-sensitized solar cells, receiving his Master of Science in Chemistry in 2011 (thesis title: "Dye Sensitized Solar Cells: Optimization of Grätzel Solar Cells Towards Plasmonic Enhanced Photovoltaics").

In 2011, he moved back to St. Louis and accepted an intern position at Anheuser-Busch Brewing Company, working as a lab technician whose primary responsibilities were monitoring product characteristics, both quantitively and qualitatively via instrumentation and taste panels, respectively. Then, in the fall of 2012, he returned to graduate school to pursue a doctorate in Chemistry under the direction of Professor Gary Baker at the University of Missouri-Columbia, where he explored functional nanomaterials (*e.g.*, nanocarbons) and novel electrolyte systems (*e.g.*, deep-eutectic-solvent-based electrolytes), with an emphasis on their applications in mesoporous, metal-oxide-based photovoltaic solar cells. He defended his dissertation on the purification of fluorescent carbon dots in the fall of 2020. Throughout his graduate studies, he has published 22 (and

counting) peer-reviewed journal articles on luminescent nanoparticles, functional nanomaterials, and alternate energy, with over 800 citations of his work to date and an h-index of 13. He has won multiple awards, including the Discovery Scholar Award (2008), the Timothy R. Donoghue Scholarship (2008), the Kansas Space Grant Consortium Fellowship (2010), and, most recently, the MU Chemistry Department's Breckenridge/Lyons Outstanding Graduate Research Award (2017). His current research interests include designer ionic liquid and deep eutectic solvents, luminescent and functional nanomaterials, such as quantum dots and perovskites, and the application of these in sustainable energy, particularly, photovoltaic solar cells.

His passions include servant leadership, personal and professional development, fishing, hunting, MU football, and, chiefly, brewing his own beer.